University of Exeter

College of Life and Environmental Science

MSc by Research Geography

Impacts of Revised Geologic Forcing Factors on the Phanerozoic Carbon Cycle

Submitted by Joshua James Williams to the University of Exeter

as a thesis for the degree of

Masters by Research in Geography

July 2016

……

Table of Contents

List of Figures

List of Tables

Acknowledgements

First and foremost, I would like to thank my lead supervisor, Professor Tim Lenton, for his continual enthusiasm, support and guidance throughout the course of this project – his direction and advice, as well as useful critiques of early versions of the manuscript, have proved invaluable.

I would also like to give thanks to Dr Ben Mills for his continual contributions and assistance with the model code, as well as additional guidance and suggestions on how to further and improve the project. Thanks also to Dr Stuart Daines for his help in setting up the COPSE model, and to Dr Chris Boulton for his programming assistance throughout the year.

In addition, I would like to thank Anne Nicholls for all of the administrative work within the Earth System Science research group that has allowed this project to run extremely smoothly throughout the year.

I could not have asked for a better office environment in which to conduct this research, and so thanks must go to all those who have made this year so enjoyable, namely Nick W, Nick D, Nina, Matt, Jon, Chris, Tom, Ellie, James, Laura, Nathan, Fanny, Martin, Tobia, Alice, Arwen and Sarah. I wish you all the best with your current projects and future research.

Many thanks to the examiners Professor Graham Shields-Zhou and Dr Paul Halloran who raised informative suggestions that have certainly led to improvements in the thesis.

Finally, I would like to thank my parents, Louise and Ian Williams, for their continual and unerring support for the course of my studies at both undergraduate and postgraduate level.

Abstract

Traditionally, biogeochemical models are forced by the $^{87}Sr/^{86}Sr$, $\delta^{13}C$ and/or $\delta^{34}S$ isotopic records. This study builds on existing work to present a forwards model for the entire Phanerozoic that aims instead to predict these isotopic variations, as well as the key environmental variables of global temperature, pCO_2, pO_2 and ocean sulphate concentration.

The main geologic forcings; tectonic uplift, degassing, and basaltic area, of the COPSE biogeochemical model are revised following recent updates to the geologic record. In addition, a simple weatherability function is developed to account for the latitudinal location of large igneous province basalt. Further revisions are made to the model seafloor weathering and phosphorus weathering fluxes.

A simplified strontium isotope system is adopted, which successfully reproduces the broad-scale Phanerozoic $^{87}Sr/^{86}Sr$ record, providing a test of the model predictions. The model also successfully predicts proxy data for both $\delta^{13}C_{carb}$ and $\delta^{34}S$.

The updated model predictions of temperature and pCO_2 are improved for the Early-Palaeozoic, which is characterised by a gradual cooling trend. However the duration of the Permo-Carboniferous glaciation is underestimated. This is attributed to an arbitrary reduction in the C:P burial ratio of plant biomass to account for the evolution of lignolytic organisms, although their impact has been questioned in recent research.

Revision of the geologic forcings leads to an improved prediction of Phanerozoic pO_2 that shows better agreement with other biogeochemical models in the Mesozoic, a period in which the original COPSE model probably overestimated the atmospheric oxygen concentration.

Following the initial model updates, the complexity of the model is increased through the creation of a dynamic land area forcing, accounting for the incomplete preservation of large igneous provinces, and coupling the seafloor weathering function to both temperature and spreading rates. Whilst having clear impacts upon modelled temperature, pCO_2 and pO_2, such updates invalidate the $^{87}Sr/^{86}Sr$ prediction. This is addressed by increasing the complexity of the strontium isotope system through the inclusion of rubidium

decay and a dynamic sediment strontium subsystem, however the $^{87}Sr/^{86}Sr$ prediction remains invalidated for large parts of the Phanerozoic. As such, a simplified strontium isotope system is seen to offer the best approximation of the Phanerozoic record.

1. Introduction

1.1. Phanerozoic Biogeochemical Modelling

The Phanerozoic, stretching from 541Ma to the present day, is an eon characterised by dramatic changes in the Earth System, with such changes intertwined with biotic evolution (Berner et al., 2007). On such a geologic timescale, the long-term carbon cycle acts as the major long-term regulatory mechanism for atmospheric CO_2 and O_2 concentrations, and thus global temperature. Over the course of the Phanerozoic, variations in the key geologic and biologic factors affecting the long-term carbon cycle have drawn the Earth System into extended intervals of both glaciation, for example in the Late Ordovician, Permo-Carboniferous and Cenozoic, (i.e. Crowley, 1998; Rothman, 2002; Isbell et al., 2003; Fielding et al., 2008; Frank et al., 2008; Vandenbroucke et al., 2010; Finnegan et al., 2011) and greenhouse conditions, notably the Cambrian and Early-Ordovician as well as the End-Permian and Triassic (i.e. Renne et al., 1995; McElwain et al., 1999; Berner and Kothavala, 2001; Kidder and Worsley, 2004; Sun et al., 2012). Moreover, the Phanerozoic saw the second major rise in atmospheric O_2 (i.e. Lenton, 2001), paving the way for the evolution of complex floral and faunal life.

Throughout the past three decades, modelling of elemental cycles has helped further our knowledge of the Phanerozoic history of atmospheric CO_2 and O_2 (i.e. Walker et al., 1981; Berner et al., 1983; Berner, 1991; 1994; 2006; Kump and Arthur, 1997; Berner and Kothavala, 2001; Bergman et al., 2004; Arvidson et al., 2006), with modelling of the long term carbon cycle a major focus as it plays a dominant role in controlling the levels of atmospheric CO_2 and O_2 on a multi-million year timescale (Berner, 2004a).

The use of one-dimensional heat balance equations to study climate goes back to the work of Budyko (1969) and Sellers (1969), with North et al (1981) providing an in depth review of this literature. Walker et al (1981) used this energy balance approach to develop a negative feedback based model in order to investigate the mechanisms acting as to stabilise Earth's temperature, with a focus upon the dependence of the rate of silicate weathering on surface temperature.

Such feedback understandings, alongside the early carbon and sulphur cycle modelling of Garrels and Lerman (1981; 1984), Berner et al (1983) and Berner and Canfield (1989), amongst others, were brought together by Berner (1991; 1994) to form GEOCARB, a simple carbon cycle model for the Phanerozoic. GEOCARB is mathematically simpler than BLAG (Berner et al., 1983), but more complex with respect to geologic and biologic processes (Berner, 1991).

Through the concept of the 'surficial system' (Berner, 1994; 1999; 2004a) consisting of the reservoirs of the short term carbon cycle, GEOCARB offers a simple approach to carbon mass balance modelling (Berner, 2004a). By combining these reservoirs, processes involved in the short term carbon cycle are avoided in the modelling (Berner, 2004a), thus allowing the model to use a steady-state approach. As the weathering and degassing fluxes of carbon over a multi-million year timescale are much larger than the amount that can be stored in the 'surficial system', it can be assumed that the input and output fluxes of carbon are essentially balanced (i.e. Berner, 1991; 1994). This greatly simplifies theoretical modelling of the long term carbon cycle, and so for each timestep, whilst the input and output fluxes may change, they re-adjust during the timestep to reach a new steady-state (Berner, 2004a).

Carbon cycle modelling is argued, however, to be more complex than simply the balance between degassing and continental weathering (Francois et al., 2005). As such, GEOCARB has been extended (i.e. Berner, 1994; 2006a,b; 2009; Berner and Kothavala, 2001) multiple times from the original (Berner, 1991) model. Such extensions include the introduction of the oxygen-dependence of carbon and sulphur isotope fractionation (Berner, 2006a), as well as the separation of the crustal reservoir into volcanic and non-volcanic rocks (Berner, 2006b).

The COPSE model of Bergman et al (2004) combines the geochemical carbon cycle of GEOCARB with the 'Redfield Revisited' modelling of Lenton and Watson (2000a; 2000b), a feedback-based model of oceanic nutrients and atmospheric O_2, as well as a simple sulphur-cycle model (Kump and Garrels, 1986). The result is a zero-dimensional biogeochemical box model that represents the co-evolution of the biotic and abiotic components of the Earth System through the modelling of the carbon, oxygen, sulphur and phosphorus

cycles, as well as processes describing the evolution and subsequent impact of terrestrial biology (Bergman et al., 2004).

Since the initial COPSE model, the model has been furthered through considering the enhancement of weathering by early non-vascular land plants (Lenton et al., 2012), as well as through the use of improved geological data (i.e. Van Der Meer et al., 2014) to update the representation of tectonic driving factors (Mills et al., 2014a,b) within the model.

1.2. The Geologic Time Scale

It is not uncommon for different studies to use varying timescales, as well as stage nomenclature, with respect to quantifying environmental change across the Phanerozoic (Gradstein et al., 2012a). Moreover, as developments in, for example, dating techniques take place, major developments in the geologic time scale have occurred over time (Gradstein et al., 2012a), and so the definition of stage boundaries can vary between studies, as displayed, using the Ordovician as an example, in Table 1.1.

Stage Boundary	Time (Ma)			
	Webby et al (2004)	Sadler and Cooper (2004)	Sadler et al (2009)	Cooper and Sadler (2012)
Ordovician Onset	489.0	488.3	490.9	485.4
Tremadocian/Floian	479.0	478.6	483.7	477.7
Floian/Dapingian	471.0	471.8	473.9	470.0
Dapingian/Darriwilian	468.0	468.1	470.5	467.3
Darriwilian/Sandbian	460.5	460.9	460.9	458.4
Sandbian/Katian	454.2	455.8	456.0	453.0
Katian/Hirnantian	444.7	445.6	444.7	445.2
End Ordovician	443.0	443.7	443.4	443.8

Table 1.1: Summary of the difference in dates for the global Ordovician stage boundaries as given by four studies. The most recent dates, from the 2012 Geologic Time Scale (Gradstein et al., 2012b), are given in the final column by Cooper and Sadler (2012).

Moreover, the definition of geologic sub-stages can differ; for example the sub-stages of the Ordovician as displayed in Table 1.2.

Global Subdivisions	British Subdivisions
Tremadocian	Tremadoc
Floian	Arenig
Dapingian	Llanvirn
Darriwilian	Llandeilo
Sandbian	Caradoc
Katian	Ashgill
Hirnantian	

Table 1.2: Summary of the difference in nomenclature for Ordovician stage boundaries between the 'Global Subdivisions' following (Cooper and Sadler, 2012), and the 'British Subdivisions', as given by (Finney, 2005). Please note, these subdivisions do not match temporally, and are displayed purely in order of occurrence, from earliest through to the latest Ordovician.

To avoid confusion, this study follows the 2012 Geologic Time Scale (Gradstein et al., 2012b) regarding the nomenclature and dating of stage boundaries through the Phanerozoic, as displayed in Figure 1.1 (Gradstein, 2012). Stages and subdivisions of the Phanerozoic time scale are defined by their lower boundaries at GSSPs (Global Boundary Stratotype Sections and Points) (Gradstein and Ogg, 2012; Cooper and Sadler, 2012; Gradstein et al., 2012a), which provide a means for global correlation.

The GEOLOGIC TIME SCALE 2012

Geologic TimeScale Foundation

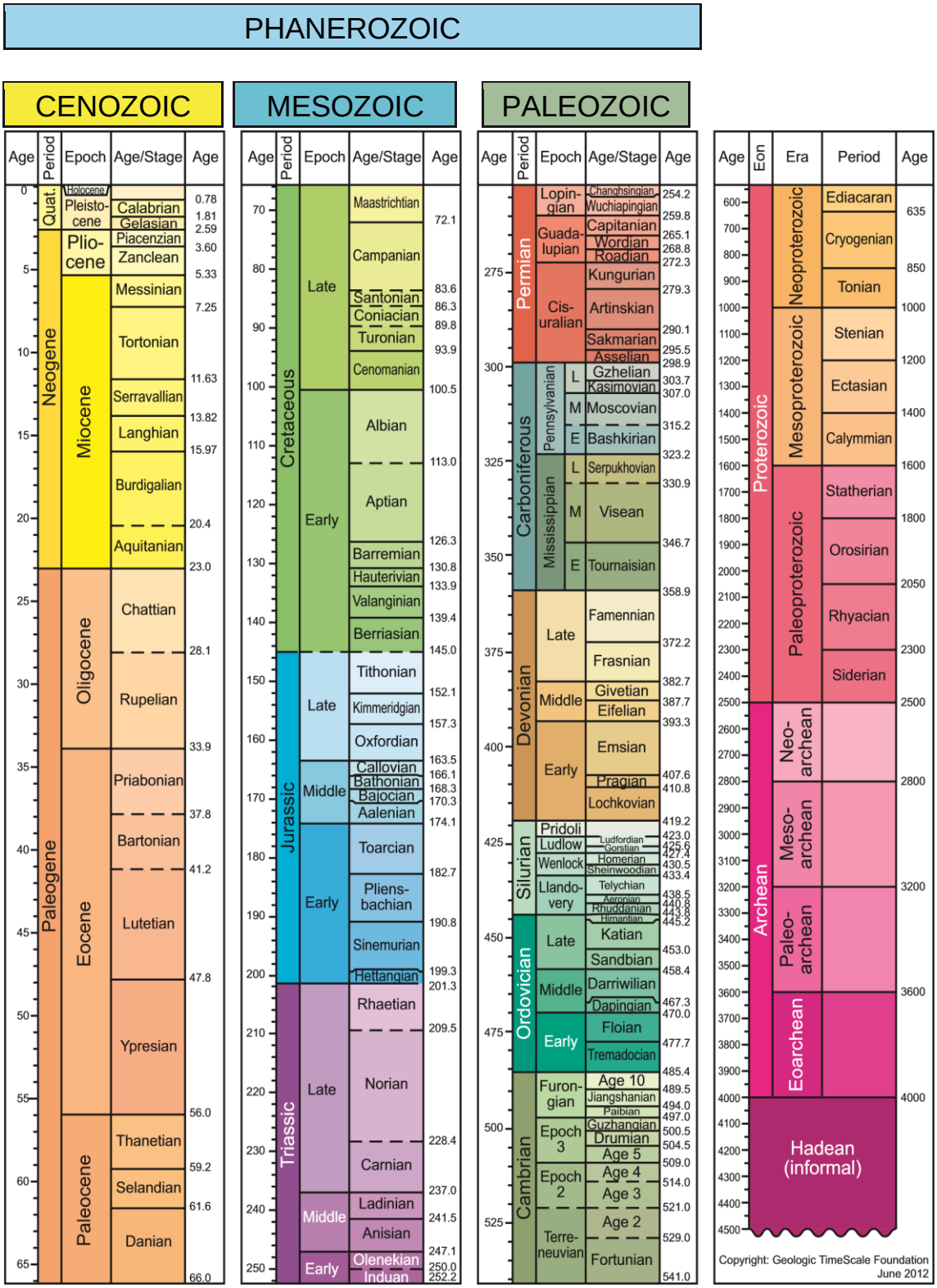

Figure 1.1: The 2012 Geologic Time Scale, taken from Gradstein et al (2012a).

1.3. Project Rationale

1.3.1. Originality and Justification of Research

In a thorough critique of the biogeochemical models of the time, Boucot and Gray (2001) argue that the models do not satisfactorily account for the geological information, insufficient geological and biological data has been gathered to impart reliability to model constructs, and whilst many models assume a positive correlation between atmospheric CO_2 and surface temperature, none agree on atmospheric CO_2 levels through time. In addition, traditionally biogeochemical models of the Phanerozoic are forced by isotopic records, for example $^{87}Sr/^{86}Sr$, $\delta^{13}C$ and $\delta^{34}S$.

The GEOCARB models (Berner, 1991; 1994; Berner and Kothavala, 2001) are driven by $\delta^{13}C$ and $\delta^{34}S$, and until GEOCARBSULF (Berner, 2006a,b; 2009), their uplift forcing was driven by $^{87}Sr/^{86}Sr$. As an alternative approach, COPSE (Bergman et al., 2004) predicts $\delta^{13}C$ and $\delta^{34}S$, although uplift remains derived from the $^{87}Sr/^{86}Sr$ record. This was updated by Mills et al (2014b), who included a simple strontium isotope system within the COPSE model, however their study is limited to the Mesozoic and Cenozoic.

Given the abundance of geological and biological data available (Berner, 2004a), this study looks to further the use of published geological data as a basis for forcing the COPSE model throughout Phanerozoic time. This differs from the approach of early biogeochemical models in that it allows the prediction of proxy records, for example carbon and strontium isotopes, that can subsequently be compared to published data in order to validate the model predictions, and furthers the work of Mills et al (2014b) by extending the geologically-derived forcing throughout the entire Phanerozoic.

As a result, this study displays originality through presenting a forwards model that is not constrained by isotopic data, and aims instead to predict these isotopic variations, as well as the key environmental variables of global temperature, atmospheric CO_2 and O_2, and oceanic sulphate concentration. Moreover, the geological forcings presented in this study have either been updated following recent advances in our understanding, or are entirely original attempts to improve the predictions of the zero-dimensional COPSE model

using factors that are usually reserved for more complicated modelling approaches.

1.3.2. Aims

- To derive and improve the representation of the key geologic factors affecting the long term carbon cycle within the COPSE model.
- To attempt to reproduce the broad scale structure of the strontium isotope record over Phanerozoic time.
- To examine the effects of the updated model forcings upon model predictions of global temperature, atmospheric CO_2 and O_2, and ocean sulphate concentration.
- To investigate whether increasing the complexity of model forcings and the strontium isotope system leads to improved model predictions.

2. The Long Term Carbon Cycle

2.1. Background

The cycle of carbon is essential for the regulation of Earth's climate, the maintenance of life, and to the composition of the atmosphere and oceans (Berner, 2004a). There is, however, a clear difference between the long and short term carbon cycles (i.e. Berner, 1997, 1998, 2004a; Archer, 2010).

The short term carbon cycle involves the transfer of carbon between the atmosphere, hydrosphere, biosphere, and soils (Berner, 1998), and describes the natural processes that control atmospheric carbon dioxide concentrations on timescales of tens of thousands of years. Over millions of years, carbon still undergoes constant cycling and recycling via the short term cycle (Berner, 2004a), but added to this is a new set of processes as a result of the exchange of carbon between rocks and the various reservoirs at or near the Earth's surface.

Such processes include silicate weathering, acting as to sequester carbon from the atmosphere, leading to its burial in ocean sediments (i.e. Walker et al., 1981; Francois and Walker, 1992; Berner, 1998; Amiotte-Suchet et al., 2003; Berner, 2004a), and the volcanic degassing of CO_2, acting as the major long term source of carbon to the atmosphere.

The overall impact of the long term carbon cycle is to act as a thermostat for global temperatures (Walker et al., 1981) through its regulation of the atmospheric CO_2 concentration, as well as determining, especially for the Phanerozoic, the atmospheric O_2 concentration through organic carbon burial.

2.2. Silicate and Carbonate Weathering

The chemical weathering of Ca and Mg-bearing silicate minerals, essentially the dissolution of continental rocks, acts as the primary sink for atmospheric CO_2 over geologic time (i.e. Walker et al., 1981; Brady and Gislason, 1997; Amiotte-Suchet et al., 2003; Berner, 2004a) through providing a pathway for carbon to exit the fast surface carbon cycle and return to the solid Earth.

Silicate weathering and its effect on the long term carbon cycle is best described through the following chemical equations. Firstly, continental silicate rocks react with carbon dioxide in the presence of water to yield positively charged Ca^{2+} (or Mg^{2+}) and negatively charged bicarbonate (HCO_3^-) ions (Equation 2.1) (Lenton and Watson, 2011).

$$2CO_2 + 3H_2O + CaSiO_3 \rightarrow Ca^{2+} + 2HCO_3^- + H_4SiO_4 \quad (2.1)$$

The dissolved species produced as a result of Equation 2.1 are carried to the ocean via groundwater and riverine transport (i.e. Berner, 2004a), whereby the dissolved Ca^{2+} and HCO_3^- precipitate, mainly biogenically, as calcium carbonate ($CaCO_3$), described in Equation 2.2, with the silicic acid (H_4SiO_4) forming biogenic silica as described in Equation 2.3.

$$Ca^{2+} + 2HCO_3^- \rightarrow CaCO_3 + CO_2 + H_2O \quad (2.2)$$

$$H_4SiO_4 \rightarrow SiO_2 + 2H_2O \quad (2.3)$$

Subsequently, the calcium carbonate and biogenic silica are buried in marine sediments, acting to store carbon over long periods of geologic time in the lithosphere (i.e. Berner, 1998; 2003; 2004a).

This chain of reactions can be simplified into a single, overall, reaction as described in Equations 2.4 and 2.5. This follows the work of Ebelmen (1845) and Urey (1952), and following Berner (2004a) is referred to as the Ebelmen-Urey reaction(s).

$$CaSiO_3 + CO_2 \rightarrow CaCO_3 + SiO_2 \quad (2.4)$$

$$MgSiO_3 + CO_2 \rightarrow MgCO_3 + SiO_2 \quad (2.5)$$

This overall reaction, whereby $CaSiO_3$ is taken as the simplest possible chemical formula for igneous rocks, is a key reaction of the long term carbon cycle and represents the transfer of carbon from the atmosphere to the rock record by means of weathering and marine carbonate sedimentation (Berner, 2004a). More simply, weathering of continental silicate rocks removes carbon from the atmosphere (in the form of carbon dioxide) which is then stored in marine sediments.

Unlike silicate weathering, however, carbonate weathering has little effect on atmospheric CO_2 concentrations (Amiotte-Suchet et al., 2003). The process of carbonate weathering is described as follows (Berner et al., 1983):

$$CaCO_3 + CO_2 + H_2O \rightarrow Ca^{2+} + 2HCO_3^- \quad (2.6)$$

This reaction is the reverse of Equation 2.2, and thus carbonate weathering and transport of Ca^{2+} and HCO_3^- ions to the ocean results in no net atmospheric exchange of carbon dioxide (Berner, 2004a), as the CO_2 uptake is balanced by CO_2 fluxes released to the atmosphere by carbonate precipitation in the oceans (Equation 2.2) on geological timescales (Amiotte-Suchet et al., 2003).

2.3. Degassing

The loss of carbon to marine sediments via continental silicate weathering and subsequent transport is a carbon sink. Whilst this sink is small, should there be no compensatory carbon source, given enough time it would act as to remove the atmosphere-ocean-biosphere of all its carbon (Walker et al., 1981; Berner, 1998).

Most of the carbon stored as $CaCO_3$ in marine sediments, therefore, is assumed to be recycled, through plate tectonics (Berner and Canfield, 1989; Berner, 2003), from sedimentary rocks that subducted and subsequently released their CO_2 in the reverse Ebelmen-Urey reaction (Ebelmen, 1845; Urey, 1952; Berner, 1998; Berner, 2004a) – right to left in Equations 2.4/2.5. This represents the return of carbon to the atmosphere-ocean-biosphere (Berner, 1998) through both volcanism (i.e. Van Der Meer et al., 2014) and metamorphic degassing following the thermal breakdown of carbonates at depth (Berner, 1998; 2004a; Kerrick, 2001; Edmond and Huh, 2003; Mills et al., 2014b).

Metamorphic degassing is driven by the subduction of oceanic crust at continental margins (Kerrick, 2001), with the input of mantle CO_2 associated with crustal production at mid ocean ridges (Mills et al., 2014b), as well as with large igneous province (LIP) emplacement. This transformation is known as metamorphism as it occurs at temperatures at which rocks begin to deform and change chemically into metamorphic rocks (Newton et al., 1980; Berner, 2003; Edmond and Huh, 2003). Metamorphism, under great heat and pressure, acts

to convert carbon back into carbon dioxide molecules, which are then forced up from the depths of the earth and released into the atmosphere (Walker et al., 1981; Edmond and Huh, 2003).

Roughly 50% of the CO_2 flux to the atmosphere-ocean-biosphere is attributed to spreading centres/mid ocean ridges (Archer, 2010; Mills et al., 2014b). Whilst the time taken to move carbon from a subduction zone to a spreading centre via plate motion (Lenton and Watson, 2011) is variable and poorly known, higher spreading rates and stronger $CaCO_3$ subduction are generally associated with increased degassing and thus periods of elevated atmospheric CO_2 (Berner et al., 1983; Brady and Gislason, 1997).

As such, on timescales of 10^7-10^8 years (Van Der Meer et al., 2014), degassing through direct volcanic input, metamorphic degassing at mid ocean ridges (i.e. Kerrick, 2001) and LIP emplacement (i.e. Mills et al., 2014b) act as the major source of CO_2 to the atmosphere, and thus the major source of carbon to the atmosphere-ocean-biosphere. Consequently, the global climatic evolution of the Earth can be described as the result of the long term balance between continental silicate weathering and solid earth degassing (Walker et al., 1981; Godderis et al., 2008). This is displayed graphically in Figure 2.1.

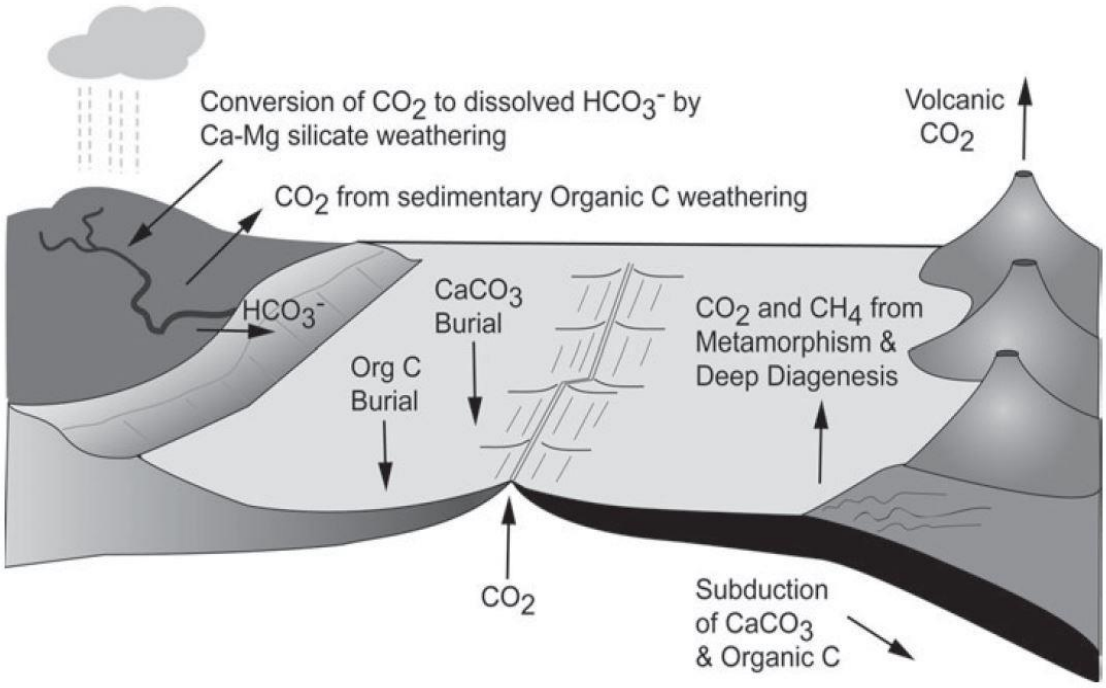

Figure 2.1. Graphical diagram illustrating the long term carbon cycle (following Berner, 1999; 2004a).

2.4. Balancing the Long Term Carbon Cycle and Feedback Mechanisms

The supply of carbon to and from each of the reservoirs in the Earth system must be very closely in balance over time (Walker et al., 1981). Minor imbalances between CO_2 sources and sinks would cause rapid fluctuations in atmospheric CO_2 levels and global temperatures (Brady and Gislason, 1997), and deviation from modern CO_2 drawdown rates of even a few percent can cause atmospheric CO_2 concentrations to be reduced well below reasonable values over a period of millions of years (Berner and Caldeira, 1997; Taylor and Lasaga, 1999).

Degassing rates, and thus the atmospheric CO_2 source, are variable, hence the continental silicate weathering flux must respond to such variability in order to maintain the balance of the long term carbon cycle.

Furthermore, as the Sun converts hydrogen to helium, its core becomes denser and hotter, increasing the rate of thermonuclear fusion (Caldeira and Kasting, 1992). Therefore, solar models predict that the Sun has increased in luminosity over time, from values ~18-25% lower than the present day in the Archaean (Sagan and Mullen, 1972; Newman and Rood, 1977; Le Hir et al., 2014). Not only does this require a mechanism to keep Earth's temperature at a habitable value for early life (i.e. Prokaryotes, Archaea), but as increasing solar luminosity warms the Earth, a mechanism is required to cool the Earth (Lovelock and Whitfield, 1982).

Crucially, the rate of silicate weathering is temperature-dependent, with the rate increasing with temperature (and vice versa), thus acting to stabilise atmospheric CO_2 and temperature through a negative feedback (i.e. Walker et al., 1981; Berner et al., 1983; Kump and Arthur, 1997; Berner, 1998).

A feedback loop is a chain of cause and effect which can be traced in a closed circuit, such that a perturbation to one part eventually causes a further change in that same process (Lenton and Watson, 2011). Positive feedbacks are seen as self-amplifying or destabilising, whereas negative feedbacks, such as the silicate weathering feedback, are viewed as stabilising. This is displayed in Figure 2.2.

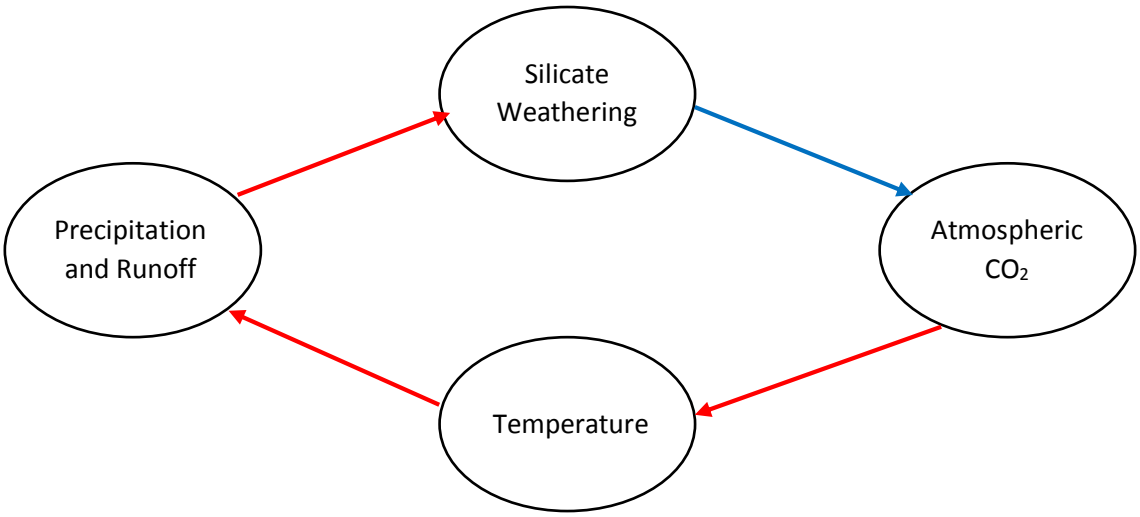

Figure 2.2. Feedback diagram of the silicate weathering negative feedback. Red arrows indicate a positive response whereas blue arrows indicate a negative response.

Following Figure 2.2, in the context of a faint young sun, reduced solar luminosity in early Earth history would have reduced temperature, thus reducing silicate weathering, resulting in a higher atmospheric greenhouse gas concentration acting as to keep the Earth warm (Walker et al., 1981). As increasing solar luminosity warms the Earth, silicate rocks should weather more readily, reducing atmospheric CO_2 (Lovelock and Whitfield, 1982), buffering Earth's temperature against this change (Walker et al., 1981).

This feedback acts as a 'thermostat', controlling and stabilising the atmospheric CO_2 concentration. The main idea behind this is that with increased temperature, not only does the chemical rate of reaction increase, but the hydrologic cycle also accelerates, further increasing the rate of chemical weathering (Walker et al., 1981).

Any change in the rate of chemical weathering or degassing can alter the 'set point' of the thermostat, for example should uplift increase, thus increasing the area of rock exposed to erosion and reducing soil shielding, chemical weathering increases, thus reducing atmospheric CO_2 (Walker et al., 1981). In a steady state, once the thermostat has had time to equilibrate, CO_2 consumption by silicate weathering must once again balance the rate of CO_2 degassing (Berner, 1997; 1998).

As Berner (1997; 1998) argues, the actual rate of CO_2 removal from the atmosphere by silicate weathering, on a multimillion year timescale, is not an independent parameter and must be essentially equal to the supply of CO_2 from degassing. Consequently, the increased weathering as a result of, in this

instance, enhanced uplift must be matched by a process acting to decelerate global weathering. A drop in atmospheric CO_2 would be such a process – following Figure 2.2 it would result in a reduction in temperature, a slowing of the hydrologic cycle, and thus a reduction in silicate weathering rate such that it once again balances degassing (Berner, 1997). In this sense, increased uplift causes an increased 'weatherability' (i.e. Kump and Arthur, 1997) of the Earth, which is compensated for by a cooler climate and reduced atmospheric CO_2 content.

This permits the climate, on timescales of tens to hundreds of millions of years, to drift between icehouse climates (i.e. Kirschvink, 1992) characterised by polar ice sheets and greenhouse periods (Katz et al., 2008), when the Earth would have felt tropical from the equator to the poles (i.e. Zachos et al., 2003; 2005; 2006). Such variability comes as a result of perturbations to the long term carbon cycle, which in turn alter the silicate weathering thermostat, for examples through changes in uplift, degassing, palaeogeographic configuration, biology and lithology. These perturbations and their impacts are discussed in Chapter 3.

Moreover, the balance between silicate weathering and CO_2 degassing defines the multimillion year atmospheric CO_2 base level (i.e. Godderis et al., 2008), and around this, fluctuations are allowed at shorter timescales (i.e. Berner, 1991; Godderis and Francois, 1995; Berner, 2006; Donnadieu et al., 2006), an example of which would be the dramatic onset of glaciation in the Late Ordovician (i.e. Lenton et al., 2012; Pohl et al., 2014).

2.5. The Long Term Carbon Cycle and Atmospheric Oxygen

As well as atmospheric CO_2, the long term carbon cycle controls atmospheric O_2 concentrations on geologic timescales (Bergman et al., 2004; Berner, 1999; 2004a; 2006; 2009), especially for the Phanerozoic for which organic carbon burial is a more important source of atmospheric oxygen than hydrogen loss to space (i.e. Lyons et al., 2014) or pyrite burial.

Oxygen is ultimately formed by photosynthesis, but the majority of this is just as quickly consumed (i.e. Garrels and Lerman, 1981; Berner and Canfield, 1989). When organic carbon is respired, it consumes the same amount of oxygen as

was produced when the organic carbon was first synthesised through photosynthesis (Holland, 1984). Therefore, in order to generate oxygen that can build up in the atmosphere, organic carbon must be protected from being re-oxidised, thus allowing it to escape this short term recycling.

This is done so through burying organic carbon in sediments beneath the seafloor, in a process known as organic carbon burial, and can be described through Equations 2.7 and 2.8 (Berner, 1998; 2004a).

$$CO_2 + H_2O \rightarrow CH_2O + O_2 \quad (2.7)$$

$$CH_2O + O_2 \rightarrow CO_2 + H_2O \quad (2.8)$$

Equation 2.7 represents 'net photosynthesis' (photosynthesis – respiration), resulting in the burial of organic matter (taken as CH_2O) and the production of oxygen (Berner, 1998; 2004a). The reverse equation, 2.8, represents 'georespiration' (Berner, 1998; 2004a), or the oxidation of old organic carbon in rocks, occurring either by the oxidative weathering of organic matter in uplifted sedimentary rocks, or by the decomposition of organic matter to reduced-carbon-containing gases, followed by the oxidation of these gases once they are emitted to the atmosphere (Berner, 2004a).

Carbon can also be buried as carbonate rocks (i.e. $CaCO_3$), however this does not affect the amount of oxygen left behind as the carbon is buried in an oxidised form (i.e. Berner, 2003).

The process of 'georespiration' provides a balance (Berner, 1999), which if not present would result in the biosphere holding the ability to double the atmospheric oxygen concentration in roughly 2 million years. The long term carbon cycle must not only balance with respect to CO_2, but also to O_2.

Further mechanisms acting to balance the oxygen flux as a result of organic carbon burial are changes in sulphur and phosphorus burial (Van Cappellen and Ingall, 1994; 1996).

When there are excursions in carbon isotopes (discussed in chapter 4), there are usually complementary excursions in the isotopes of sedimentary sulphur, which exists in both an oxidised form, gypsum ($CaSO_4$), and a reduced form, pyrite (FeS_2) (Berner and Raiswell, 1983). These forms are analogous to the oxidised and reduced forms of sedimentary carbon; $CaCO_3$ and CH_2O. If

sulphur is weathered in the form of gypsum and buried in the form of pyrite, it will leave behind some oxygen in the same manner as the burial of reduced organic carbon (Canfield, 2005; Halevy et al., 2012). According to carbon and sulphur isotopes, at times of high organic carbon burial, the rate of reduced sulphur burial tends to be low, offsetting the source of oxygen to the atmosphere that would arise from the organic carbon burial alone (Berner, 2006a), thus providing evidence for an oxygen regulating mechanism.

The 'VCI feedback' (Van Cappellen and Ingall, 1994; 1996) states that phosphorus, a major limiting nutrient (i.e. Lenton, 2001; Planavsky et al., 2010; Mills et al., 2014a), is more easily released from sediment under anoxic or dysoxic conditions. Therefore, there could be a strong dependency of the marine C:P burial ratio of organic matter on bottom water anoxia, which in turns is a function of the atmospheric oxygen concentration, thus creating a negative feedback on atmospheric oxygen. A scarcity in oxygen would result in anoxic bottom water conditions, increasing the organic carbon content in sediments through altering C:P burial ratio, in turn resulting in a greater amount of oxygen left behind to bring the atmospheric oxygen content back up (Van Cappellen and Ingall, 1994; 1996).

Similarly to CO_2, however, the atmospheric oxygen content can be perturbed, for example through changes in the chemical weathering flux (i.e. Mills et al., 2014a) altering the supply on phosphorus to the ocean, thus enhancing productivity and so organic carbon burial (i.e. Planavsky et al., 2010), increasing atmospheric oxygen.

The rise of vascular plants is argued to have resulted in a dramatic increase in atmospheric oxygen, from ~12% (by volume) during the early Palaeozoic (~570-400Ma) to ~21% (by volume) at 340Ma (Lenton, 2001). Such a rise in atmospheric oxygen, however, is balanced through a negative feedback based by which increasing oxygen results in an increasing frequency and intensity of vegetation fires (Lenton, 2001), which is argued to have regulated atmospheric oxygen to within a range of 15-25% (by volume) over the last 350Ma.

2.6. Summary

In summary, the long term carbon cycle can be described as the balance between continental silicate weathering and CO_2 degassing, and acts as to set the multimillion year atmospheric CO_2 base level. Perturbations to this cycle are balanced by a negative silicate weathering feedback, as a result of the dependence of the rate of silicate weathering, and thus the sequestration of atmospheric CO_2, on temperature.

The long term carbon cycle is also of vital importance to atmospheric O_2 through organic carbon burial, which acts as the major source of atmospheric O_2 over geological time. This oxygen source is mediated through 'georespiration', pyrite burial, the 'VCI feedback' and a negative fire feedback.

3. Factors Affecting the Long Term Carbon Cycle

3.1. Introduction

The long term carbon cycle is balanced between the degassing CO_2 sources of volcanism and metamorphic processes, and the weathering sink of CO_2 through the liberation of Ca^{2+}/Mg^{2+} ions and their subsequent transport to the ocean and burial as $CaCO_3$/$MgCO_3$ (Mills et al., 2014b). These sources and sinks of CO_2 are affected by changes in tectonic processes, as well as the impact of biology (i.e. Lenton et al., 2012; Porada et al., 2014), and thus such factors exert a major control on atmospheric CO_2, and so climate, over geologic time.

3.2. Tectonic and Geologic Factors

3.2.1. Uplift

Uplift is driven by plate tectonics and acts to accelerate chemical weathering through multiple processes (i.e. Raymo and Ruddiman, 1992; Crowley, 1998). The terrestrial surface of the Earth is an importance interface for global biogeochemical material fluxes between the various reservoirs of the Earth system (Hartmann et al., 2011). Uplift of the continents provides a fresh supply of silicate material available for chemical weathering (i.e. Kump et al., 1999; Frank et al., 2008; Cramer et al., 2011; Mills et al., 2014b). This enhanced exposure and weathering consequently results in a reduction in atmospheric CO_2 (i.e. Raymo and Ruddiman, 1992; Kump et al., 1999; Frank et al., 2008).

Changes in the elevation of land masses may have further, indirect, effects on chemical weathering (Crowley, 1998). Uplift generally results in high relief, which results in steep slopes and thus enhanced erosion (Berner, 2004a), which further uncovers primary minerals and exposes them to the atmosphere. Moreover, uplift has impacts on local weather and climate (Crowley, 1998), an example at present being the impact of the Himalayas on the Asian monsoon (i.e. Kutzbach et al., 1989; Molnar et al., 2010). An increase in precipitation at elevation enhances chemical weathering (Berner, 2004a), with weathering exacerbated at greater elevations through glacial processes.

All of these impacts lead to an enhanced silicate weathering flux and faster uptake of atmospheric CO_2 (Berner, 2004a). Uplift is also intrinsically linked with

further tectonic and geologic factors that affect the long term carbon cycle; degassing (i.e. Herrmann et al., 2010), lithology (i.e. Bluth and Kump, 1991; Nardin et al., 2011; Mills et al., 2014b) and continental configuration (i.e. Hartmann et al., 2014).

3.2.2. Volcanism

The rate of volcanic degassing varies through time (i.e. Berner, 1990; Tajika and Matsui, 1993), and volcanism has impacts upon climate and the long term carbon cycle that vary over different timescales.

Volcanic outgassing offers the key long term source of atmospheric CO_2 (i.e. Mills et al., 2014b; Van Der Meer et al., 2014). CO_2 has a much longer atmospheric residence time than SO_2 (Bond and Wignall, 2014), and so whilst individual eruptions may inject a very small amount of CO_2 relative to the atmospheric reservoir, the cumulative impact of sustained volcanic outgassing is to maintain the atmospheric CO_2 source.

Further, ocean-continent subduction zones manifest as chains of continental arc volcanoes (Lee et al., 2013). Continental arc magmas are argued to be more likely than island arc magmas to intersect sedimentary carbonates, as $CaCO_3$ tends to deposit in shallower and mid-depth waters (Milliman, 1993). Under the high temperatures of the magma, such carbonates undergo metamorphosis and decarbonise, resulting in significant CO_2 release (i.e. Chadwick et al., 2007; Lee et al., 2015; McKenzie et al., 2016).

Despite this, volcanism can lead to long term cooling due to the weatherability of volcanic rocks (explored in section 3.2.3) (i.e. Hartmann et al., 2014; Mills et al., 2014b), as well as the uplift of volcanic arcs as a result of the sinking of oceanic plates (Van Der Meer et al., 2014; Zagorevski et al., 2016). Such uplift leads to enhanced erosion (i.e. Allegre et al., 2010), as explored in the previous section. Therefore whilst, for example, continental arc volcanism leads to enhanced CO_2 outgassing, the high elevations of such arcs may also enhance orographic precipitation and change global atmospheric circulation patterns, thus acting as to enhance weathering efficiency, sequester CO_2 and

consequently dampen the climatic warming response to volcanic activity (Lee et al., 2015).

Large Igneous Provinces (LIPs) are typically defined as volumetrically large (>100,000km^2) magmatic provinces erupted or emplaced rapidly, commonly in less than 5 million years (i.e. Ernst, 2007; Horton, 2015). Pulses of LIPs are associated with supercontinental break-up (Ernst and Bleeker, 2010), with an average LIP frequency of ~20 million years (Ernst, 2007). Whilst the eruption of LIPs is accompanied by a massive CO2 input over a geologically short timescale (< 10^6 years) (Mills et al., 2014b), LIPs are dominantly composed of theolitic basalt. Basaltic rocks are extremely weatherable (i.e. Dessert et al., 2003; Mills et al., 2014b) and thus LIP magmatism contributes significantly to the silicate weathering flux (i.e. Hartmann et al., 2014), acting as to cool the climate.

Consequently, whilst volcanic and metamorphic outgassing make up the major source of atmospheric CO_2 on a geologic time scale, periods of enhanced arc and LIP volcanism can in fact result in long term climate cooling due to their enhancement of the silicate weathering.

3.2.3. Lithology

The lithologic composition of the continental crust can change through time (Bluth and Kump, 1991; Nardin et al., 2011), via plate tectonics, orogenesis and volcanism. As a consequence, it is important to account for changes in the relative exposures of different lithologies when considering changes in the long term carbon cycle and biogeochemical cycles in the geologic past (Taylor and Lasaga, 1999).

The present global uptake of atmosphere and soil CO_2 is estimated to be composed of 40% carbonate weathering, and 60% silicate weathering (Amiotte-Suchet et al., 2003).

Amongst all silicate rocks, basalts, which are emplaced by volcanic processes, have a significant influence upon the rate of CO_2 uptake by chemical weathering (Amiotte-Suchet et al., 2003). This is due to the fact that basaltic rocks are prone to rapid chemical weathering (i.e. Dessert et al., 2001; Berner,

2004a; 2006; Mills et al., 2014b; Horton, 2015), up to 8 times as fast as shield rocks (Dessert et al., 2003; Nardin et al., 2011) and notably faster than granites or other acidic igneous and metamorphic rocks (i.e. Meybeck, 1987; Taylor and Lasaga, 1999; Berner, 2004a).

Basaltic rocks are rich in Ca and Mg silicates (Berner, 2006b; Young et al., 2009), and thus the weathering of volcanic rocks is an important component of the total global silicate weathering flux (Berner, 2006b). At present, the continental surface lithology is roughly composed of 11% volcanic rocks (Nardin et al., 2011), which contributes to an estimated 25-35% of the total CO_2 uptake by silicate weathering (Gaillardet et al., 1999; Dessert et al., 2003).

Moreover, such rapid chemical weathering rates indicate that basaltic weathering is especially important with regards to its impacts upon the long term carbon cycle, and thus atmospheric CO_2 concentrations over geologic time (Taylor and Lasaga, 1999; Berner, 2004a). Consequently, episodes of intense basaltic volcanism in the past could have resulted in net atmospheric CO_2 removal, despite the associated outgassing (Berner, 2004a).

3.2.4. Palaeogeography and Continental Configuration

In addition to variations in uplift, volcanism and lithology, palaeogeography has rapidly been recognised as a major factor controlling the long term variability in atmospheric CO_2 through its capacity to affect continental silicate weathering (Godderis et al., 2014), as well as the oceanic circulation (i.e. Wilde, 1991; Herrmann et al., 2004).

The local climate of a location undergoing chemical weathering can vary as a function of both climatic change, as well as changes in the position and size of the continents (Berner, 2004a; Godderis et al., 2012). Palaeolatitude and relative continental positioning have major impacts upon the hydrological cycle (i.e. Godderis et al., 2014; Maher and Chamberlain, 2014; Mills et al., 2014b) through their impact upon temperature and runoff (Probst and Tardy, 1989). Rock mineral dissolution is dependent on the availability of water, and thus on the continental area located within humid climatic belts, as well as on

temperature, and so on the latitudinal distribution of the continents (Godderis et al., 2014).

Low, equatorial latitudes are characterised by high temperature and runoff. Consequently, continental silicate weathering is greatest in warm, low latitudes (Moore and Worsley, 1994), with a continental configuration favouring the warm and humid tropical zone resulting in enhanced CO_2 consumption through rock weathering (i.e. Boucot and Gray, 2001; Nardin et al., 2011; Melchin et al., 2013).

As a result, it is important to consider both the latitudinal distribution of rock types (Amiotte-Suchet et al., 2003) as well as orogenic belts (Moore and Worsley, 1994) when considering the impact of continental weathering upon the long term carbon cycle. Furthermore, the geographic position of mountain belts has further impacts upon local weather systems – high weathering rates in the Himalayas are facilitated by the Asian monsoon, which is a function of their geographic location (Molnar et al., 2010; McKenzie et al., 2014). The size of continents is also an important consideration. Larger continents, especially those with coastal mountains (Berner, 2004a), are likely to have extremely dry interiors, with low weathering rates regardless of their palaeolatitudanal location, as exemplified by Pangaea (Kutzbach and Gallimore, 1989). As such, the impact of continental configuration upon rock weathering is also suggested to be dependent upon how the land masses are dispersed, as well as their respective latitudes (Otto-Bliesner, 1995).

Throughout the Phanerozoic there have been remarkable changes in continental configuration (Varga et al., 2012), and the interplay between palaeogeography and the long term carbon cycle may potentially offer a first-order forcing on climate over such geologic time (Godderis et al., 2014).

3.3. Biologic Factors

3.3.1. Land Plants

3.3.1.1. Land Plant Evolution

Cryptospores are considered to have been produced by the earliest terrestrial flora that likely consisted of non-vascular plants (i.e. Gray et al., 1985; Wellman et al., 1998; 2015). Recent work has put forward the argument that the earliest plants had evolved by at least the Mid-Late Ordovician (i.e. Rubinstein et al., 2010; Le Hir et al., 2011; Raevskaya et al., 2016) through the evidence of such cryptospore assemblages, with the discovery of these assemblages dated to the Dapingian in Argentina (Rubinstein et al., 2010) and the Katian in Siberia (Raevskaya et al., 2016). Further, as bryophytes lack abundant tissues that are resistant to microbial attack (Wellman, 2010), they do not fossilise easily, resulting in a negligible fossil record. As such, the earliest land plants are postulated to have potentially evolved as early as the Late Cambrian to Mid-Ordovician (Kenrick et al., 2012).

Early plants underwent continual evolution and diversification through the Mid-Late Ordovician, Silurian and Devonian (Le Hir et al., 2011; Lenton et al., in press), with vascular plants evolving and spreading across the land surface from the Early-Mid Silurian (Lenton, 2001).

The Devonian saw the spread of rooted vascular plants (Berner, 1997), with evidence of a progressive increase in the size and depth of roots from the Silurian to Early-Devonian (Retallack, 1997). Arborescence resulted in a further increase in maximum root depths (Algeo and Scheckler, 1998), with the first trees, Archaeopterids (Lenton, 2001), extending from tropical to boreal palaeolatitudes (Algeo and Scheckler, 1998) and resulting in the development of the first forests by ~385Ma (Lenton et al., in press). The seed habit was developed by the Late-Devonian (Le Hir et al., 2011) and resulted in a further increase in land colonisation (Algeo and Scheckler, 1998). Such advances in plant physiology and morphology led to an intensification of pedogenesis and thus a large increase in the thickness and extent of soils (Berner, 1997; Algeo and Scheckler, 1998).

Following the Palaeozoic, the dominance shifted from lycopsids and pteridophytes to gymnosperms in the Mesozoic, with a subsequent shift to angiosperm-dominance in the Tertiary (Robinson, 1990).

3.3.1.2. The Biotic Enhancement of Weathering

Land plants accelerate the chemical weathering of silicate minerals (i.e. Berner et al., 2003; Berner, 2004a). All plants require rock-derived minerals (for example Phosphorus, Potassium, Magnesium, Iron and Calcium) for growth (Lenton et al., 2012). As such, natural selection may well have driven the evolution of rock weathering mechanisms as plants that acted as to amplify the weathering of rocks benefitted by acquiring such rock bound nutrients (Lenton, 1998; 2001).

Prior to the evolution of vascular plants, early lichens and bryophytes are suggested to have accelerated the chemical weathering of rock relative to bare rock surfaces (i.e. Lenton et al., 2012; Porada et al., 2013; 2014; 2016). Whilst this hypothesis that the origin and diversification of early land plants largely increased weathering rates is not unanimously supported (i.e. Quirk et al., 2015), both ecophysiological modelling (i.e. Porada et al., 2013; 2014; 2016) and physical weathering experiments (Lenton et al., 2012) indicate that non-vascular plants considerably enhance silicate weathering rates over abiotic background levels.

The rhizines of lichen and the rhizoids of bryophytes break up the rock surface, followed by dissolution of minerals through the action of different organic acids, for example oxalic acid (Porada et al., 2014), and chelating agents released by the organisms (Porada et al., 2016). Weathered material is subsequently transported from the rock, thus allowing organisms to access deeper, non-weathered layers of rock, advancing as a ‘weathering front’ through the materials (Porada et al., 2014). The resulting impact of such processes is a potential enhancement of chemical weathering by ~1-2 orders of magnitude above the abiotic background rate (Porada et al., 2016).

It is generally assumed that an increase in plant size, as well as a wider geographic distribution, further promotes chemical weathering processes (Algeo

and Scheckler, 1998; Berner, 2004a; Le Hir et al., 2011), and so the evolution of vascular plants resulted in accelerated rock weathering compared to that of the lichens, bryophytes and algae that precluded them (Berner, 2004a). Vascular plants have evolved various mechanisms, as well as symbiotic relationships (i.e. Simon et al., 1993; Lenton, 2001), to enhance the release of essential nutrients from rocks (Lenton et al., 2012), and thus enhance chemical weathering as follows:

- Soils act as to retain water and maintain aqueous contact with rock surfaces and mineral grains, thus maximising weathering (Lenton, 2001). Furthermore, plants anchor clay-rich soils, reducing erosion and thus allowing the retention of water and so continued weathering of primary minerals (Berner, 1997). In the absence of vegetation, rapid erosion can expose bare bedrock such that less weathering occurs due to the shorter water-rock contact time (Berner, 2004a).
- On a regional scale, plants re-circulate water through transpiration followed by rainfall (Berner, 1997). This enhancement of the hydrological cycle (Lenton, 2001) can result in increased precipitation, which increases the weathering rate.
- Respiration of roots and organisms in soil results in increased soil pCO_2 (Lenton, 2001), and thus acidifying soil water.
- Organic litter that accumulates in soils undergoes microbial decomposition to form organic and carbonic acids (Berner, 1997; 2004a), providing additional acidity for mineral dissolution.
- Plants, as well as symbiotic mycorrhizal fungi, secrete organic acids and chelates that attack primary minerals in order to gain nutrients (Berner, 1997; 2004; Lenton; 2001), causing enhanced chemical weathering.
- Roots act as to split rocks through physical weathering (Lenton, 2001).
- The soluble products of weathering are removed by plants, which enhances the weathering reactions that produce them through Le Chatelier's principle (Lenton, 2001).

Such processes are estimated to have vastly increased global rock weathering rates. At present, the land biosphere is estimated to increase weathering rates by at least an order of magnitude relative to bare rock (Schwartzman and Volk,

1989), with the breakdown of nutrient containing silicate minerals enhanced by factors of 2-10 (Lenton et al., 2012).

It has also been argued that progressively stronger biological effects on weathering have evolved over time (Schwartzman and Volk, 1991; Lenton and Watson, 2011). Following the shift in floral dominance from the Palaeozoic to Mesozoic (Robinson, 1990), biotic enhancement may have caused weathering rates to further increase – Royer et al (2014) argue that angiosperm dominated ecosystems would result in a six fold increase in chemical weathering over minimally vegetated ecosystems.

3.3.1.3. The Impact of Biotic Weathering Enhancement on Climate

The spread and evolution of land plants impacted upon many Earth System processes (Berner, 1997). Enhanced chemical weathering results in enhanced removal of CO_2 from the atmosphere, as displayed in the reactions introduced in chapter 2**.** As such, the impacts of land plants have been postulated to have contributed to drawing the Earth System into glaciation, for example during the End-Ordovician (Lenton et al., 2012; Porada et al., 2016) and the Permo-Carboniferous (i.e. Berner, 1997; 1998). From the Early to Late-Devonian, atmospheric CO_2 levels are estimated to have fallen from ~6300ppmv to 2100ppmv (Le Hir et al., 2011), primarily as a result of this acceleration of weathering of silicate rock by the development of deep rooted vascular plants (Berner, 1998).

Furthermore, a biological negative feedback exists between atmospheric CO_2 and land plants (Berner, 2004a). Plants fix more carbon at elevated CO_2, provided their growth is not limited by light, water or nutrients – Andrews and Schlesinger (2001) state a 33% increase in weathering rate when CO_2 is increased from 360 to 570ppm.

Following the expansion of vascular plants in the Devonian, the Earth System was thus drawn into the Permo-Carboniferous glaciation (i.e. Berner, 1997; Le Hir et al., 2011; Zhuang et al., 2014), the most extensive and long-lived glaciation of the Phanerozoic.

An important factor, bringing a further decrease in atmospheric pCO_2 (see section 2.5), is the enhanced burial of organic matter in sediments (i.e. Berner 1997), as evidenced by the vast coal swamps of the Carboniferous and Early-Permian, c. 330-260Ma. As previously discussed, this burial of organic carbon is also the major source of atmospheric O_2 on geologic time (i.e. Berner and Canfield, 1989; Berner, 1998; 2003; 2004a).

By extracting phosphorus, a major limiting nutrient (Planavsky et al., 2010; Lenton et al., 2012), from continental rocks and converting it to bioavailable forms (Lenton, 2001), plants stimulate terrestrial and marine productivity and so organic carbon burial, resulting in an increase in atmospheric O_2 (i.e. Lenton, 2001; Lenton et al., in press). Moreover, early plant material is argued to have a much higher C:P burial ratio than marine biomass (Lenton et al., in press), due to carbon-rich but nutrient-poor structural compounds such as lignin (i.e. Robinson, 1990), acting as to further enhance organic carbon burial.

As a consequence, the evolution of land plants has recently been argued to have driven a mid Palaeozoic oxygenation (Lenton et al., in press), as well as a dramatic increase in atmospheric O_2 from c. 12% to 21% (by volume) by c. 340Ma (Lenton, 2001). The latter is evidence by the presence of fossil charcoal in the stratigraphic record between the Late-Silurian (Glasspool et al., 2004) and the Mid-Devonian (i.e. Rowe and Jones, 2000; Cressler, 2001), which suggests an atmospheric O_2 level >15% (by volume) at this time (Lenton, 2001).

4. Isotopic Background

4.1. Carbon Isotopes

Carbon exists in three isotopes, ^{12}C, ^{13}C and ^{14}C (i.e. Libby, 1946; Craig, 1953), of which the stable isotopes, ^{12}C and ^{13}C, are fractionated by biological processes (i.e. Roeske and O'Leary, 1984; Farquhar et al., 1989; Guy et al., 1993). Patterns in the fractionation of these isotopes are expressed as deviations using delta (δ) notation – as the variations are so small, they are expressed in ‰ (parts per thousand) rather than % (parts per hundred). The formula for relating an isotopic ratio to a δ value is as follows:

$$\delta = (1 - R_{sample})/R_{standard}) * 1000‰ \quad (4.1)$$

In nature, the stable ^{12}C isotope (~98.89%) is far more abundant than ^{13}C (~1.11%) (Munnecke et al., 2010), and the isotopic compositions of $CaCO_3$ and organic carbon have remained remarkably stable over geologic time (Archer, 2010; Lenton and Watson, 2011).

During photosynthesis, the enzyme rubilose bi-phosphate carboxylase, commonly abbreviated to rubisco (i.e. Lorimer, 1981; Farquhar et al., 1989; Guy et al., 1993), that binds to CO_2 preferentially fixes the lighter ^{12}C isotope roughly 2.5%, or 25‰, more than often than if it were strictly down to chance (Hayes et al., 1999; Munnecke et al., 2010). The overarching impact is that organic carbon is thus isotopically light by about -25‰ (Hayes et al., 1999; Archer, 2010), and so in recent geological settings, organic ^{13}C depletions of -25‰ to -30‰ are routinely interpreted as evidence for oxygenic photosynthesis.

Secular variations in the $\delta^{13}C$ of marine carbonate reflect changes in the ratio of organic carbon (C_{org}) to inorganic carbon (C_{carb}) when one or the other (or both) is removed from participating in the carbon cycle through burial as organic matter or sedimentary carbonate (Holland, 1984; Frank et al., 2008) – shifts in $\delta^{13}C$ values are thus related to major changes in carbon cycling in the world's oceans (Marshall et al., 1997). Both $\delta^{13}C_{org}$ and $\delta^{13}C_{carb}$ depend on the isotopic composition of DIC in seawater; therefore any change in this should equal parallel changes in both $\delta^{13}C_{org}/\delta^{13}C_{carb}$ (Munnecke et al., 2010).

Despite this, due to the fact that $\delta^{13}C_{org}$ values are potentially affected by a large number of different primary and secondary processes, their values are often highly variable and so their stratigraphic use is limited compared to $\delta^{13}C_{carb}$ values (Delabroye and Vecoli, 2010; Munnecke et al., 2010). Investigations into $\delta^{13}C_{org}$ are mostly carried out should rock samples not contain enough carbonate for $\delta^{13}C_{carb}$ measurements (i.e. Underwood et al., 1997).

Enhanced (+) $\delta^{13}C_{carb}$ values occur when increased isotopically light ^{12}C is sequestered (Frank et al., 2008), and are often explained in terms of either enhanced bioproductivity (i.e. Brenchley et al., 1994; Canfield, 1994; Wenzel and Joachimski, 1996; Brenchley et al., 2003; Frank et al., 2008; Cherns et al., 2013; Rasmussen et al., 2016) and/or enhanced organic carbon burial (i.e. Veizer et al., 1999; Cramer and Saltzman, 2005; Frank et al., 2008; Cherns et al., 2013). Organic carbon burial is a critical process in the Earth system (i.e. Berner and Canfield, 1989; Berner, 1991; 1994; 2004a; Montanez, 2016; Nelsen et al., 2016) as it influences atmospheric CO_2 and O_2, and thus climate (i.e. Berner, 2004a). Since the $\delta^{13}C_{carb}$ record is of the ^{13}C in carbonate, it should get heavier if there is enhanced organic carbon burial as it represents what is left behind by biological processes, which preferentially fix the lighter ^{12}C.

Consequently, positive $\delta^{13}C_{carb}$ excursions are interpreted as representing periods of cooling and/or enhanced oxygen production. Moreover, an expected consequence of enhanced CO_2 uptake by enhanced biological production is a drop in atmospheric pCO_2 as the reservoir of available reduced carbon shrinks (Frank et al., 2008; Yan et al., 2009).

Examples of such excursions are prevalent throughout the Phanerozoic – the early Palaeozoic alone witnessed numerous excursions (Cherns et al., 2013), several of which were >+5‰ in magnitude. During the Ordovician period, the Guttenberg Isotopic Carbon Excursion (GICE) and Hirnantian Isotopic Carbon Excursion (HICE) (i.e. Marshall et al., 1997; Kaljo et al., 2004; Kaljo et al., 2007; Bergstrom et al., 2009; Ainsaar et al., 2010; Bergstrom et al., 2010; Cooper and Sadler, 2012; Holmden et al., 2013; Bauert et al., 2014) saw positive $\delta^{13}C_{carb}$ excursions ranging from +2.20‰ during the GICE (Bauert et al., 2014) to between +4-7‰ at the peak of the HICE (Marshall et al., 1997).

Regarding the Phanerozoic, continuous $\delta^{13}C$ curves are not yet available for any single continent (Cooper and Sadler, 2012) and as such our temporally greatest reconstructions are as a result of synthetic curves, complied from a number of regional curves (i.e. Saltzman and Thomas, 2012).

4.2. Strontium Isotopes

Strontium has four isotopes; ^{84}Sr, ^{86}Sr, ^{87}Sr and ^{88}Sr (Munnecke et al., 2010), of which only ^{87}Sr is radiogenic, produced by the decay of ^{87}Rb. The strontium isotope ratio of seawater is characterised by 3 major sources, with two major isotopic end-members (i.e. Burke et al., 1982; Qing et al., 1998; Halverson et al., 2007; Shields, 2007); the riverine and hydrothermal reservoirs. Further, due to the lengthy residence time of strontium in seawater compared to the oceanic mixing time (~10^3 years) (i.e. McArthur et al., 2012), the oceans are thoroughly mixed on timescales that are short relative to rates of strontium gain/loss, and thus the strontium isotope ratio of seawater is globally uniform at any given time (i.e. Qing et al., 1998; Shields, 2007; Munnecke et al., 2010; McArthur et al., 2012).

The first major source of strontium to seawater is via mantle input, through hydrothermal alteration of the seafloor (i.e. Burke et al., 1982; Allegre et al., 2010) and submarine low-temperature alteration of basalts (Qing et al., 1998; Allegre et al., 2010). Such exchange between seawater and the oceanic crust, along mid-oceanic ridges, supplies strontium to the ocean that inherits the isotopic composition of its magmatic precursor (Shields, 2007), with estimated $^{87}Sr/^{86}Sr$ ratios of ~0.703 (Shields, 2007) to 0.7035 (Palmer and Elderfield, 1985; Qing et al., 1998). This hydrothermal flux is believed to be proportional to seafloor spreading rates, with additionally enhanced mantle contributions from plumes and superplumes (Qing et al., 1998). More recently, however, Allegre et al (2010) have proposed that ~60% of the mantle-like input of strontium is actually from intensive weathering on volcanic islands and island arcs, with the remaining 40% from ridge crest hydrothermalism and low temperature seafloor basalt alteration.

The alternate isotopic end-member is contributed via the riverine input of strontium liberated by continental weathering (i.e. Halverson et al., 2007; Shields, 2007), supplying a relatively radiogenic flux of strontium to the oceans. ^{87}Rb decays to ^{87}Sr over time (McArthur et al., 2012), and as a result there are clear isotopic differences within the igneous rock reservoir (Francois and Walker, 1992). Old shield/sialic rocks are important sources of radiogenic strontium (Burke et al., 1982; Francois and Walker, 1992; Shields, 2007) due to high Rb abundance combined with the long time elapsed since their differentiation from mantle material (Francois and Walker, 1992), as well as the great mean age of the upper continental crust (Shields, 2007). Shield rocks have $^{87}Sr/^{86}Sr$ ratios falling into the range of ~0.710-0.730 (Brass, 1976; Holland, 1984; Francois and Walker, 1992), with a mean value estimated at 0.716 (Goldstein and Jacobsen, 1988) and 0.7178 (Shields, 2007).

Conversely, young volcanics/mafics are more mantle-like, with $^{87}Sr/^{86}Sr$ ratios in the range of 0.704-0.706 (Burke et al., 1982; Holland, 1984; Francois and Walker, 1992). As a consequence, whilst increased continental erosion should theoretically increase the strontium isotope ratio of seawater (Qing et al., 1998), an enhancement in the weathering of young volcanics or basalts may in reality act as to cause a reduction in the strontium isotope ratio of seawater (Taylor and Lasaga, 1999), which is sensitive to the global fraction of volcanic vs non-volcanic weathering (Royer et al., 2014). Moreover, to balance the marine strontium cycle, Berner (2006b) argued that basaltic volcanic weathering on land may represent a flux that is ~3 times that of basaltic seawater exchange.

The dissolution of carbonate rocks and evaporitic sulphates is an additional major source of strontium to the ocean due to the high strontium contents of these minerals (Brass, 1976; Shields, 2007). However, the isotopic signature of this largely carbonate source today is assumed to be close to that of average Phanerozoic seawater (~0.7077-0.708), and so changes in the rates and isotopic composition of the carbonate weathering flux are widely disregarded in interpretations of oceanic $^{87}Sr/^{86}Sr$ trends. Despite this, the $^{87}Sr/^{86}Sr$ ratio of the carbonate weathering flux is argued to have evolved over time (Shields, 2007). Moreover, different carbonate rock types may have differing $^{87}Sr/^{86}Sr$ signatures, reinforcing the argument that this flux of strontium to the ocean represents an important consideration when assessing long-term trends.

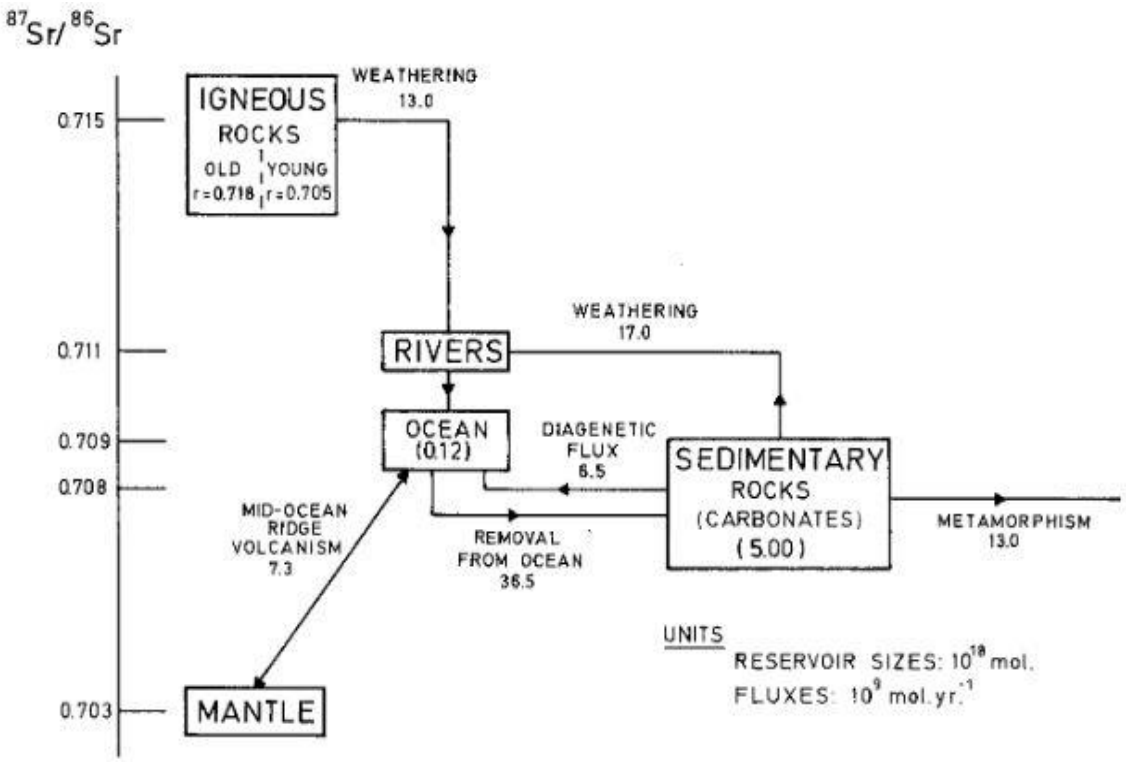

Figure 4.1: Simple model of the present day strontium isotope system, with the y axis representing an approximation of the $^{87}Sr/^{86}Sr$ ratios of the various reservoirs (from Francois and Walker, 1992).

The combination of continental silicate weathering (~0.7178) and carbonate weathering (~0.7077) produces a modern day riverine value of 0.7124 (Palmer and Edmond, 1989; Peucker-Ehrenbrink and Miller, 2006), which when combined with the alternate hydrothermal end member, produces a modern day seawater strontium isotope ratio of 0.709176±0.000003 (Allegre et al., 2010). Over time, due to the large isotopic difference between strontium sources, changes in this value are argued to track long term changes in the weathering of Earth's surface and the relative importance of the hydrothermal flux (i.e. Burke et al., 1982; Francois and Walker, 1992; Qing et al., 1998; Halverson et al., 2007; Shields et al., 2003; Shields, 2007; Allegre et al., 2010; Vollstaedt et al., 2014), as summarised in Figure 4.1.

However, as eluded to previously, tracing past strontium isotope ratios of rivers is difficult as it depends not only on the isotopic evolution of the upper continental crust, but also on the relative susceptibility to weathering, age and strontium content of the various minerals that make up the exposed part of the crust (Shields, 2007). As a consequence, the actual circumstances leading to strontium isotope variation probably involve a variety of factors, such as variation in the lithologic composition of the crust exposed to weathering, the

configuration and topography of continents, variation in climate and the extent of volcanic activity (Burke et al., 1982).

Despite this, changes in the $^{87}Sr/^{86}Sr$ ratio of seawater over time can be used as a proxy indicator of changes in the global tectonic system (Veizer et al., 1999; Munnecke et al., 2010), with the Phanerozoic curve characterised by large fluctuations, as displayed in Figure 4.2.

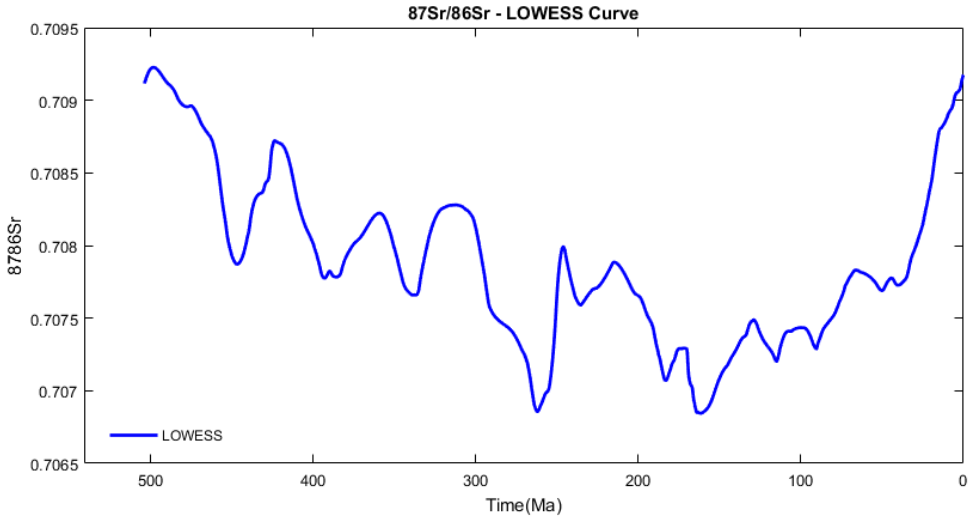

Figure 4.2: LOWESS $^{87}Sr/^{86}Sr$ curve, reproduced after McArthur et al (2012).

As well as curves spanning the Phanerozoic (i.e. Prokoph et al., 2008; McArthur et al., 2012), high resolution records exist of distinct geologic intervals spanning the Neoproterozoic (Halverson et al., 2007), as well as the Cambrian (Montanez et al., 1996; Denison et al., 1998), Ordovician (i.e. Denison et al., 1998; Qing et al., 1998; Shields et al., 2003; Young et al., 2009; Saltzman et al., 2014), Silurian (i.e. Denison et al., 1997; Fryda et al., 2002; Cramer et al., 2011) and Devonian (i.e. Denison et al., 1997; Fryda et al., 2002).

4.3. Sulphur Isotopes

Sulphur exists in four stable isotopes, ^{32}S, ^{33}S, ^{34}S and ^{36}S (Strauss, 1997; 1999; Johnston, 2011; Nehlich, 2015), with abundances estimated at 94.93%, 0.76%, 4.29% and 0.02% respectively (Johnston, 2011). The isotopic compositions of both redox states of Sulphur, oxidised as dissolved sulphate or reduced as sedimentary pyrite, are indicators for changes in past geochemical, geological and biological environments (Strauss, 1997; 1999), and analyses of

the Sulphur isotope record can elucidate changes in the burial rates of both oxidised and reduced Sulphur.

The ratio of ^{34}S to ^{32}S displays variations through a number of organic and inorganic processes within the Earth System, and is commonly expressed as $\delta^{34}S$ (Strauss, 1997). As with Carbon isotopes, $\delta^{34}S$ is calculated following Equation 4.1.

The Sulphur isotope composition of the ocean is seen as uniform over geologic time, as the residence time of Sulphur is much greater than the mixing time of the ocean (Nehlich, 2015). As such, the Sulphur isotope record displays geologic scale fluctuations (i.e. Paytan et al., 1998; Paytan and Gray, 2012) on the order of 10^8 years, with shorter term (10^7 year) variation superimposed upon the long term trend (Strauss, 1999).

Oceanic $\delta^{34}S$ is controlled by the relative proportions of the inputs and outputs of sulphides and sulphates to the ocean, and their isotopic compositions (Bottrell and Newton, 2006; Paytan and Gray, 2012). Riverine input is typically characterised by low $\delta^{34}S$ ratios of 0-10‰ (Paytan and Gray, 2012), with notable variation between rock-types (Nehlich, 2015). Volcanism and hydrothermal activity offer additional small sources of Sulphur to the ocean, with $\delta^{34}S$ values close to 0‰ (Canfield, 2004; Paytan and Gray, 2012).

Output fluxes occur via the deposition of evaporates and other sulphate-containing minerals, with $\delta^{34}S_{evaporite}$ roughly equal to $\delta^{34}S_{seawater}$, and/or the deposition of sulphides, with $\delta^{34}S_{pyrite}$ roughly equal to 15% (Paytan and Gray, 2012).

Microbial sulphate reduction (MSR) is commonly seen as the key ‘catalyst’ in the marine Sulphur cycle (Leavitt et al., 2013). This is an energy-yielding anaerobic process (Canfield, 2001), occurring in reducing conditions, and essentially acts as to reduce sulphates to sulphides, which are scavenged by iron to form pyrite (Canfield, 2001; 2004; Leavitt et al., 2013). Pyrite thus typically acquires strongly negative $\delta^{34}S$ values due to the preferential utilisation of ^{32}S by sulphate-reducing microbes (Strauss, 1999).

As a consequence of the strong fractionation involved in MSR, the Sulphur-isotope ratios of seawater sulphate are higher than any of the input sources to

the ocean (Paytan and Gray, 2012), with present seawater $\delta^{34}S$ taken as 21±0.2‰.

The balance between the oxidation of sulphides to sulphates and pyrite burial influences the geologic isotopic record (Leavitt et al., 2013), with weathering fluxes also stated to have an effect (Kah et al., 2004). As pyrite is characterised by strongly negative $\delta^{34}S$ values (Strauss, 1999), increased pyrite burial drives isotopic compositions to positive $\delta^{34}S$ values (^{34}S-enriched) (Kah et al., 2004). Conversely, enhanced weathering reduces $\delta^{34}S$ values, as the riverine flux, whilst an input of Sulphur to the ocean, commonly has a lower $\delta^{34}S$ value than that of seawater (Paytan and Gray, 2012).

4.4. Oceanic Sulphate

Oceanic dissolved sulphate, SO_4^{2-}, is a major reservoir of the Sulphur cycle (Nehlich, 2015), and is the second-most abundant anion in seawater (Paytan and Gray, 2012). The long term variation in the concentration of oceanic sulphate is of interest, as it acts as a proxy record of the oxygenation of the Earth System (Algeo et al., 2015).

Enhanced reduction of sulphate under anoxic conditions reduces the oceanic sulphate reservoir (Canfield, 2004). In contrast, through the progressive oxygenation of the Earth System, sulphide-oxidation has increased, leading to a corresponding increase in marine sulphate concentration (Kah et al., 2004).

The concentration of oceanic sulphate displays a two-step increase from the Neoproterozoic to present (Algeo et al., 2015). Low concentrations characterised the Neoproterozoic, rising sharply at the Ediacaran-Cambrian boundary, before rising for a second time during the Permian (Algeo et al., 2015).

Only slight variation has occurred over the past 250Ma, although short-term drawdowns in oceanic sulphate concentration over ~2Myr timescales have characterised intervals of enhanced ocean anoxia, intense MSR, and enhanced pyrite burial (Algeo et al., 2015).

5. The COPSE Model

5.1. COPSE Original

5.1.1. Background

The COPSE model is a biogeochemical Earth System box model for the Phanerozoic, based upon modelling the carbon, oxygen, phosphorus and sulphur cycles (Bergman et al., 2004), in addition to partial cycles of nitrogen and calcium, with the strontium cycle added later by Mills et al (2014b). The model is forced with geological drivers; uplift, rock weathering and degassing, as well as processes describing the biotic enhancement of weathering following the evolution of terrestrial vascular plants. Figures 5.1**,** 5.2 and 5.3, as well as the accompanying Table 5.1, display the model schemes for the phosphorus

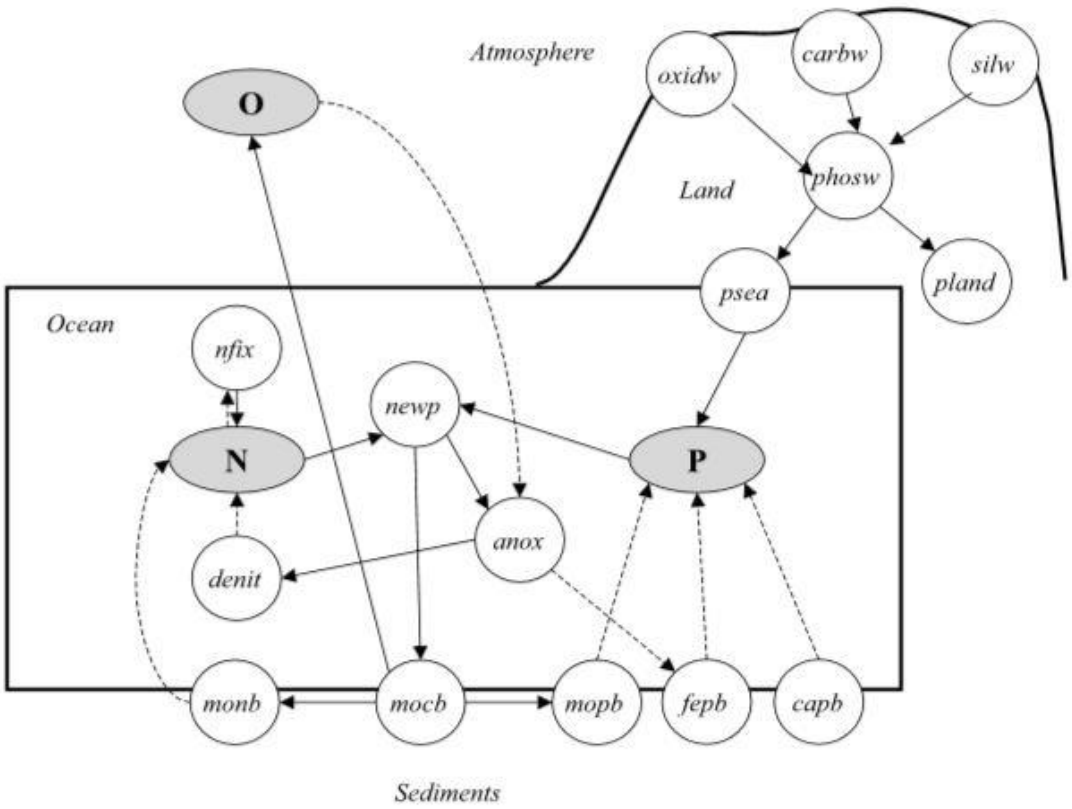

Figure 5.1. COPSE model scheme for the phosphorus and nitrogen cycles, with atmospheric and oceanic oxygen denoted as 'O', and oceanic phosphate and nitrate as 'P' and 'N' respectively. Fluxes ending with 'w' denote weathering, and those ending with 'b' denote burial. The proportions of phosphate derived from weathering that is delivered to the land and oceans are denoted as 'pland' and 'psea' respectively. Bottom water anoxia is presented by 'anox', with nitrogen fixation and denitrification represented by 'nfix' and 'denit'. Marine new production is denoted by 'newp'. Solid arrows represent a positive relationship, and dashed arrows a negative relationship. For a full overview of fluxes and reservoirs, see Table 5.1 and Bergman et al (2004).

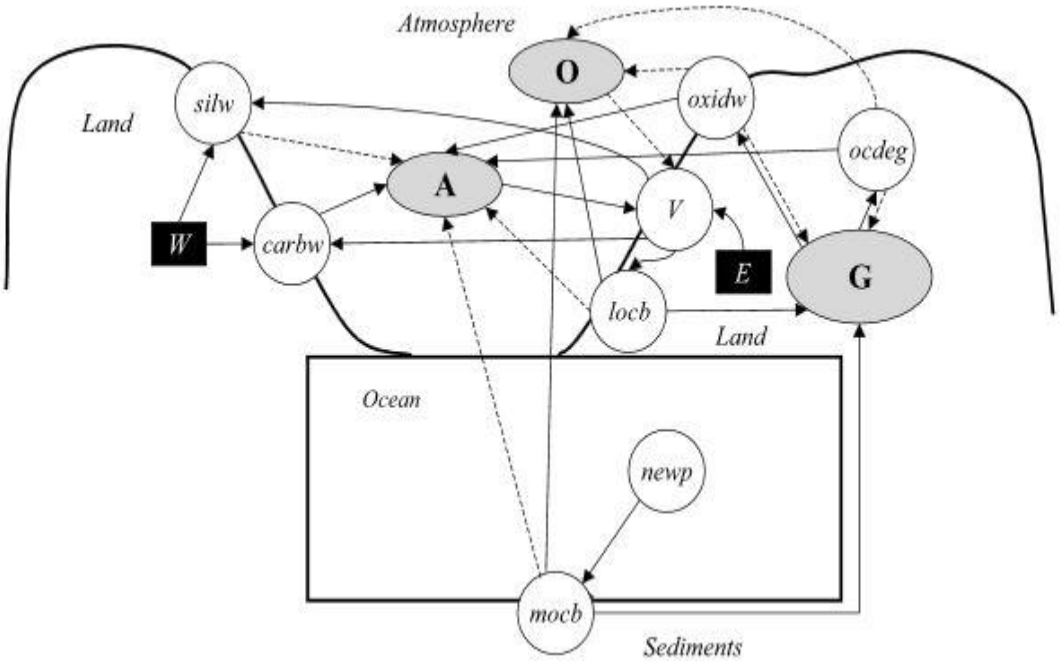

Figure 5.2. COPSE model scheme for the organic carbon and oxygen cycles, with atmospheric and oceanic oxygen and CO_2 denoted as 'O' and 'A' respectively, and 'G' referring to crustal organic carbon. Additional fluxes include terrestrial vegetation, 'V', and the degassing of organic carbon, 'ocdeg'. The evolution of land plants and subsequent enhancement of weathering are denoted by the forcings 'E' and 'W' respectively. For a full overview of flues and reservoirs, see Table 5.1 and Bergman et al (2004).

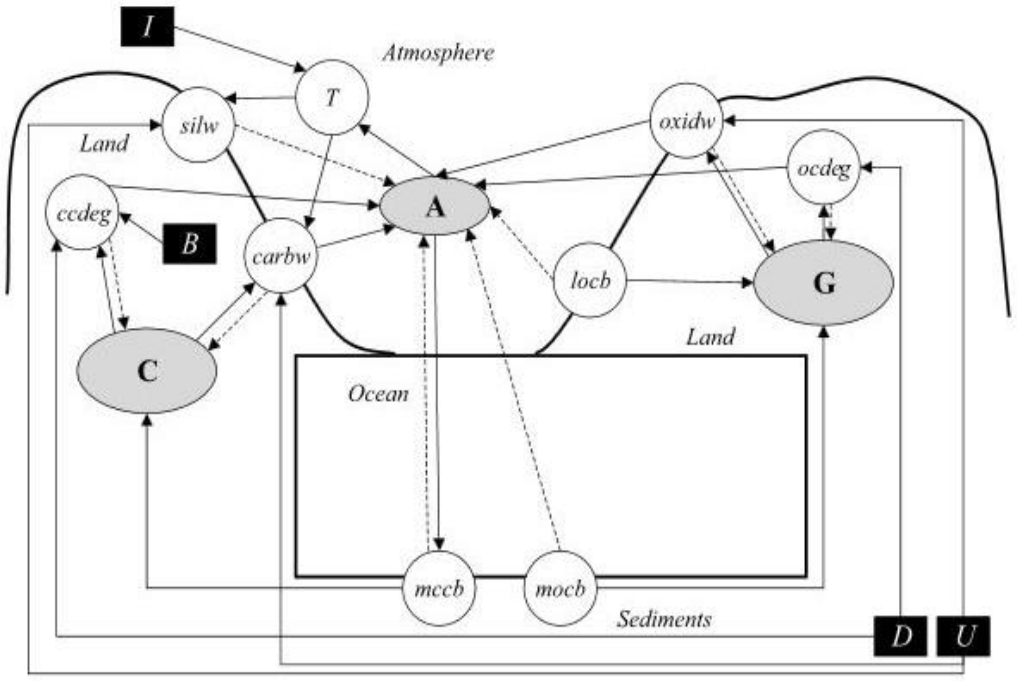

Figure 5.3. COPSE model scheme for the carbon cycle and inorganic forcings, with crustal carbonate carbon denoted by 'C'. The temperature parameter is described as 'T', with the forcings of uplift, 'U', volcanic and metamorphic degassing, 'D', solar insolation, 'I', and apportioning of carbonate burial between deep and shallow seas, 'B', also displayed. For a full overview of flues and reservoirs, see Table 5.1 and Bergman et al (2004).

Reservoir	Description
O	Atmospheric and oceanic O_2
N	Oceanic nitrate
P	Oceanic phosphate
A	Atmospheric and oceanic CO_2
G	Crustal organic carbon
C	Crustal carbonate carbon
Flux	**Description**
oxidw	Oxidative weathering
carbw	Carbonate weathering
silw	Silicate weathering
phosw	Phosphorus weathering
pland	Phosphorus flux to land
psea	Phosphorus flux to the oceans
newp	Marine new production
anox	Oceanic anoxic fraction
nfix	Nitrogen fixation
denit	Denitrification
monb	Marine burial flux of organic nitrate
mocb	Marine burial flux of organic carbon
mopb	Marine burial flux of organic phosphate
fepb	Iron-sorbed inorganic phosphate burial
capb	Calcium-bound inorganic phosphate burial
locb	Terrestrial organic carbon burial
mccb	Marine carbonate carbon burial
V	Terrestrial vegetation
ocdeg	Degassing of organic carbon
ccdeg	Degassing of carbonate carbon
Forcing	**Description**
E	Land plant evolution
W	Biotic enhancement of weathering
U	Tectonic uplift
D	Volcanic and metamorphic degassing
I	Solar insolation
B	Apportioning of carbonate burial between deep and shallow seas

Table 5.1. Summary of reservoirs, fluxes and forcings used in the COPSE model, as displayed in Figures 5.1 through 5.3. See Bergman et al (2004) for a more detailed overview.

and nitrogen cycles (Figure 5.1), organic carbon and oxygen cycles (Figure 5.2), and the carbon cycle with inorganic forcings (Figure 5.3).

The present day is taken as the pre-industrial state of the Earth System, and the model starts at 600Ma, before tending towards this state (Bergman et al., 2004).

For a thorough overview of model equations, the reader is referred to Bergman et al (2004).

5.1.2. Original Model Forcings

As displayed in Table 5.1, COPSE original is forced by six external forcings; tectonic uplift, volcanic and metamorphic degassing, the apportioning of carbonate burial between deep and shallow seas, land plant evolution and the subsequent biotic enhancement of weathering, and time-dependent solar insolation (Bergman et al., 2004). Solar insolation is used in the calculation of time-dependent global temperature following the energy balance equations of Caldeira and Kasting (1992), rather than an explicit forcing.

The remaining five forcings (U, D, B, E and W) are normalised to present day values, such that at 0Ma, U, D, B, E, W = 1 (Bergman et al., 2004), with the range of magnitudes defined in Table 5.2.

Forcing	Range of Values over the Phanerozoic
U	0.53-1.17
D	0.98-1.73
B	0.75 (Cambrian to Late Jurassic) - 1.00 (Present)
E	0.00 (Cambrian) - 1.00 (Permian to Present)
W	0.00 (Cambrian) - 1.00 (Late Cretaceous to Present)
I	4.4% increase over the Phanerozoic

Table 5.2. Range of normalised values for the six external model forcings of COPSE original, simplified from Bergman et al (2004) Table 2.

The Phanerozoic change in the normalised magnitude of physical forcings U, D and I are displayed in Figure 5.4, with a graphical representation of the biological forcings E, W and B displayed in Figure 5.5.

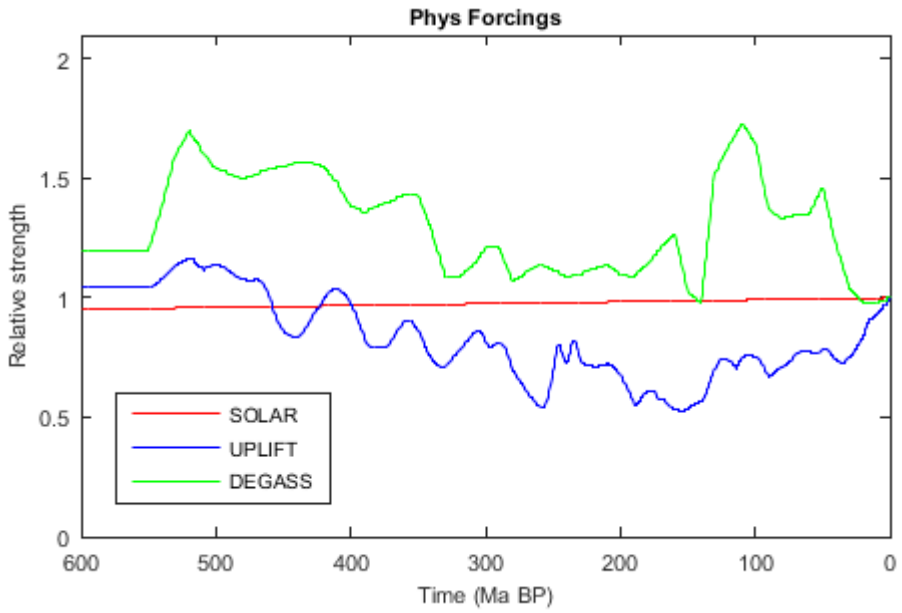

Figure 5.4. Phanerozoic variation in the normalised physical forcings; uplift, degassing and solar insolation, present in COPSE original.

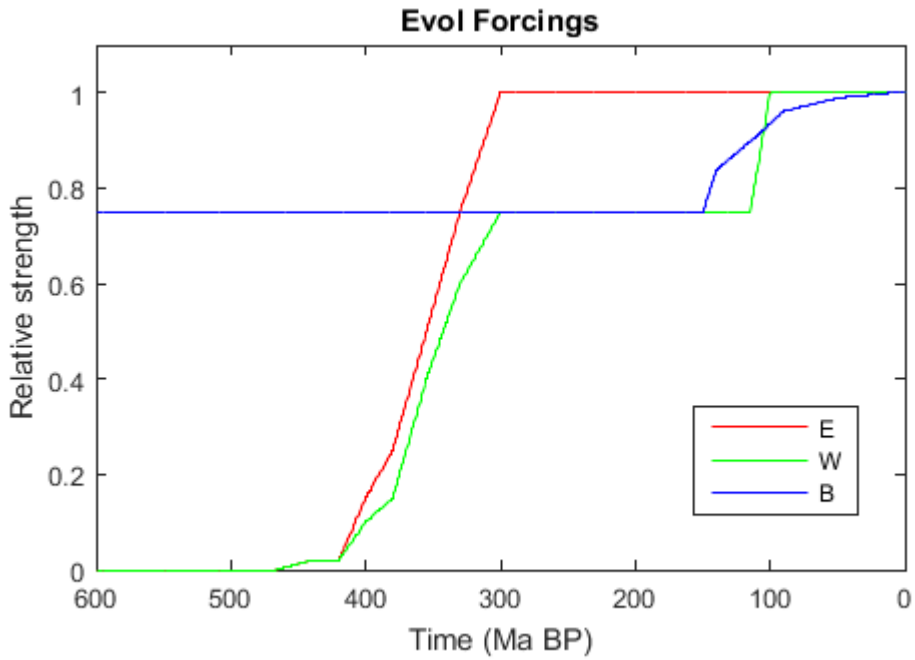

Figure 5.5. Phanerozoic variation in the relative strength of the evolutionary forcings; E, W and B, present in COPSE original.

5.1.2.1. Tectonic Uplift (U)

In COPSE original, tectonic uplift over the Phanerozoic is calculated using the seawater strontium isotope data of the LOWESS curve of McArthur et al (2001) from 509Ma to present. For the earlier Cambrian, the seawater strontium isotope data of Burke et al (1982) is used. In subsequent updates to the COPSE model, Mills et al (2014b) use sediment abundance data (Ronov, 1994) in order to predict the $^{87}Sr/^{86}Sr$ record for the Mesozoic and Cenozoic.

As discussed in Section 3.2.1., increased uplift acts as to increase continental weathering rates through its impact on relief (i.e. Berner, 2004a), exposure of silicate minerals (i.e. Kump et al., 1999), and impacts upon local weather and climate (i.e. Crowley, 1998). Consequently, uplift has a linear relationship with weathering, following Berner (1994) and Lenton and Watson (2000a, 2000b).

5.1.2.2. Degassing (D)

The approach to calculating a degassing forcing for the Phanerozoic follows the BLAG model (Berner et al., 1983), whereby it is assumed that a linear correlation exists between degassing and seafloor spreading rates. Decarbonation occurs due to the subduction of sediments, and so an increase in seafloor spreading, and hence subduction rates, acts as to increase decarbonation and thus CO_2 outgassing (Bergman et al., 2004).

5.1.2.3. Burial Depth of Marine Carbonates (B)

This forcing refers to the impact of the rise of calcareous plankton in the Mid-Mesozoic upon carbonate degassing (Bergman et al., 2004). Calcareous plankton are largely deposited in deep waters and so their rise is believed to have increased the amount of carbonate susceptible to subduction and thermal decomposition (Volk, 1989).

Following Berner (1991), B=0.75 until 150Ma, after which it increases until B=1.00 at the present day.

5.1.2.4. Evolution and Spread of Vascular Plants (E)

The biological forcing 'E' attempts to capture the evolution and spread of vascular plants, and is used in the calculation of land productivity (Bergman et al., 2004). Before the evolution of vascular plants, E=0, and through the rise and diversification of vascular plants, mainly during the Devonian and Carboniferous (i.e. Berner, 1997; Algeo and Scheckler, 1998; Lenton, 2001), E rises to equal 1 in the Late-Carboniferous.

5.1.2.5. Biotic Enhancement of Weathering (W)

Following 'E', and as discussed in Section 3.3, the rise of vascular land plants is argued to have accelerated the rate of chemical weathering of continental rocks (i.e. Berner et al., 2003; Berner, 2004a; Le Hir et al., 2011). 'W' acts as to enhance continental weathering rates as the land biosphere evolves over the Phanerozoic.

By definition, when E=0, W=0, however whilst E=1 in the Late Carboniferous (Bergman et al., 2004), W is equal to 0.75 at this stage, only equalling 1 in the Late Cretaceous following the rise of an angiosperm dominated land biosphere (Robinson, 1990).

5.1.3. Global Temperature and Atmospheric CO_2

Atmospheric CO_2 is taken as a fraction of the total atmospheric and ocean CO_2, 'A'. The present reservoir is given by A_0, with $A_0 = 3.193*10^{18}$mol (Bergman et al., 2004). Calculating the CO_2 content with respect to the present atmospheric level (PAL) follows Equation 5.1:

$$pCO2PAL = \frac{A}{A_0} \quad (5.1)$$

This can be considered as the normalised value of CO_2. To calculate the physical concentration of atmospheric CO_2, pCO2PAL must be multiplied by the pre-industrial concentration of 280ppm:

$$pCO2atm = pCO2PAL * (280 * 10^{-6}) \quad (5.2)$$

Mean global surface temperature is represented by 'T', with the present temperature (T_0) taken as 15^0C (Bergman et al., 2004). Over the Phanerozoic, 'T' is calculated using the energy balance model approach of Caldeira and Kasting (1992), which accounts for the changing albedo with temperature, the greenhouse warming effect, and the increase in solar luminosity over time. A correction factor of $+0.194^0$C is applied to return the temperature to 15^0C at the present day.

5.1.4. Isotope Systems

An advantage of the COPSE model is that rather than use the carbon and sulphur isotope records as forcings, the model calculates $\delta^{13}C_{carb}$ and $\delta^{34}S$ (of evaporitic sulphate) values, which can subsequently be compared to published isotopic data (Bergman et al., 2004).

For $\delta^{13}C_{carb}$, the isotopic composition of each of the carbon reservoirs (A, G and C) is traced, with assumed fractionation as a result of burial fluxes and biologic productivity (i.e. Frank et al., 2008; Munnecke et al., 2010), though weathering processes are assumed not to cause fractionation.

Following other sulphur cycle models, $\delta^{34}S$ fractionation is assumed for pyrite burial but not gypsum burial, with sulphur-weathering also assumed not to fractionate.

5.2. Published Updates to the COPSE Model

The 2015 version of the COPSE model involves various alterations, both to the model functions and forcings. This section will largely focus on the updated model forcings, and additional flux, reservoir and isotopic updates deemed to be essential to this study. For an overview of the full change list, the reader is referred to the supplementary information of Mills et al (2014b), which includes a thorough list of updated model functions.

Changes to the tectonic forcings and fluxes, as well as the implementation of a simple strontium isotope system, are discussed in Mills et al (2014b), with the inclusion of the effects of early non-vascular plants on weathering and climate discussed in Lenton et al (2012).

5.2.1. Forcing Updates

5.2.1.1. Tectonic Uplift

The updated representation of Phanerozoic tectonic uplift is taken as the $f_R(t)$ function of GEOCARB 3 (Berner and Kothavala, 2001). This is defined as the effect of mountain uplift on chemical weathering, and is normalised relative to the present. The sediment abundance data of Ronov (1994) is used to estimate the abundance of terruginous sediments over time as a measure of palaeo-erosion (Berner and Kothavala, 2001), which is combined with the relationship between physical erosion and chemical weathering as presented by Gaillardet et al (1999) to calculate $f_R(t)$, as displayed in equations (6) through (9) of Berner and Kothavala (2001).

Figure 5.6 displays a comparison between the original and updated COPSE uplift forcings, and their variation across the Phanerozoic.

Using such a parameter overcomes issues with strontium isotope-based approximations of tectonic uplift. As discussed in Section 4.2, the marine strontium isotope record is not necessarily purely a measure of the overall rate of the global silicate weathering flux (i.e. Burke et al., 1982; Francois and Walker, 1992; Shields, 2007), as it can also be affected by the $^{87}Sr/^{86}Sr$ ratio of the rocks undergoing weathering themselves.

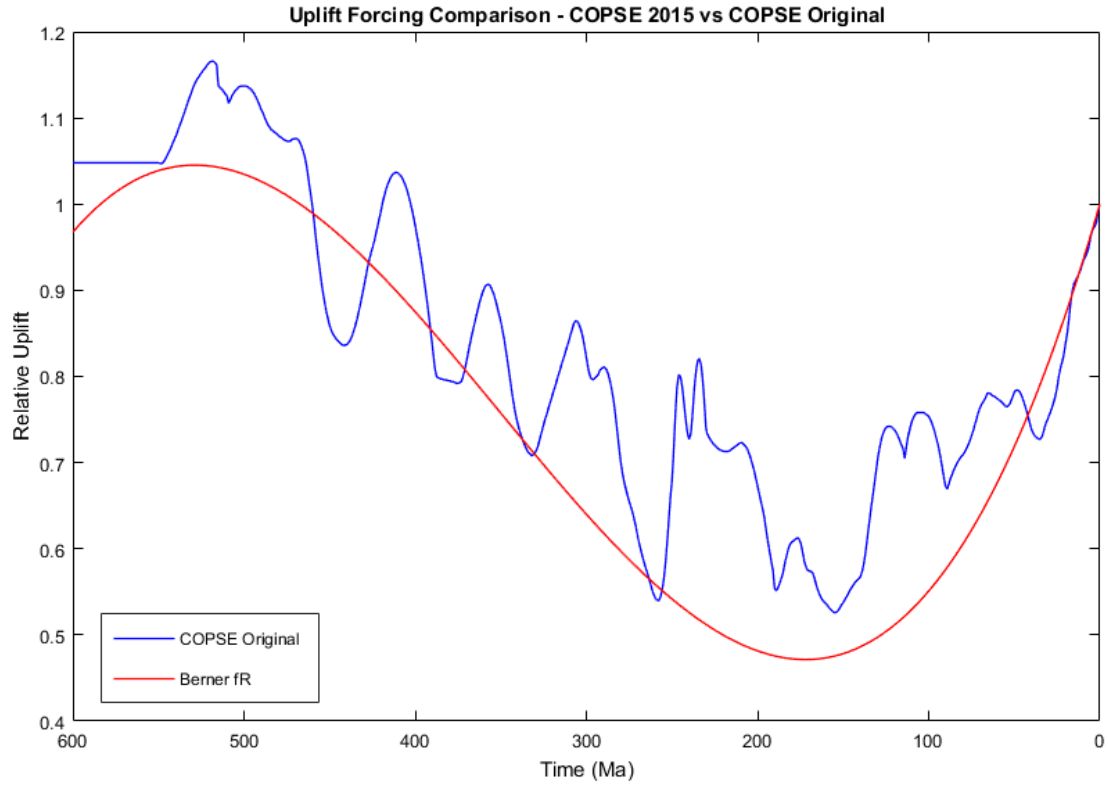

Figure 5.6. Comparison between tectonic uplift forcings available for use in the COPSE model.

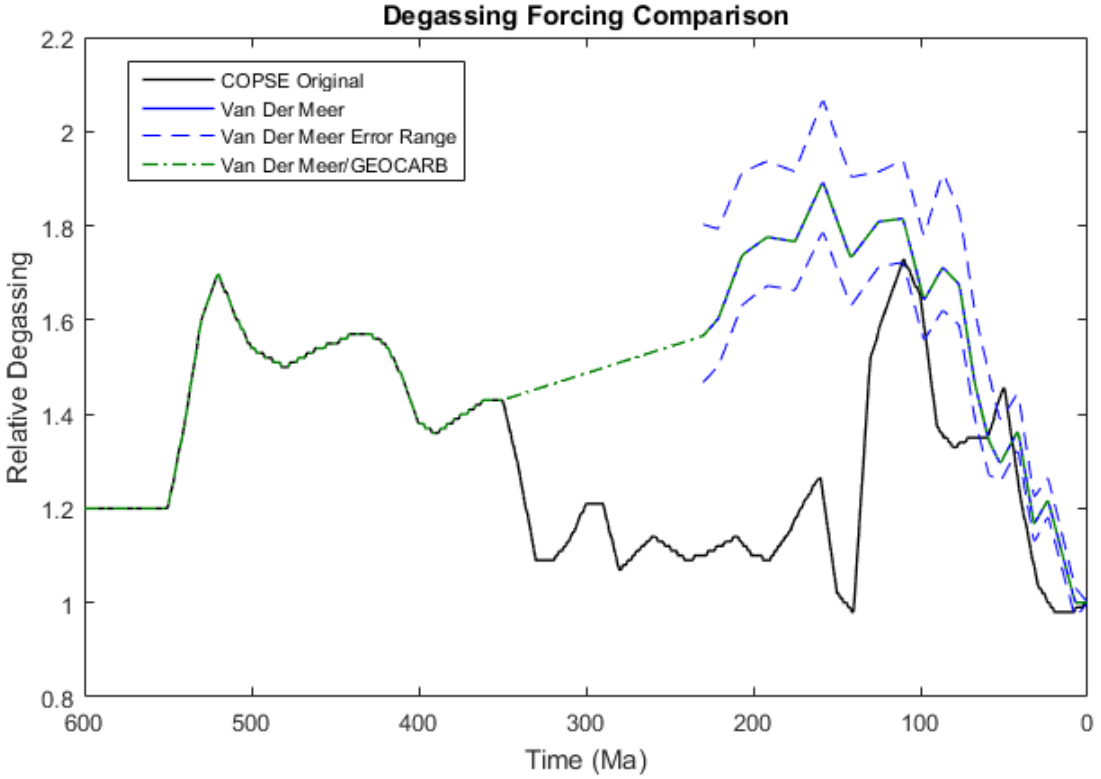

Figure 5.7. Comparison between degassing forcings available for use in the COPSE model.

Furthermore, as this forcing is no longer based upon the strontium isotopic record, a simple strontium isotope system can now be included in the COPSE model to offer additional comparative capability with published isotopic data (see Section 5.2.3.).

5.2.1.2. Degassing

Van Der Meer et al (2014) offer an updated reconstruction of combined arc and ridge CO_2 degassing over the past 230Ma based upon a reconstruction of subduction zone lengths. COPSE uses this as the sole degassing forcing when focusing on the Mesozoic (i.e. Mills et al., 2014b), whereas for studies of the Phanerozoic this is combined with the GEOCARB degassing forcing from COPSE original.

A comparison between the original and updated forcings is displayed in Figure 5.7.

5.2.1.3. Palaeogeography (PG)

As discussed in Section 3.2.4, palaeogeography is recognised as a major control on continental rock weathering (i.e. Berner, 2004a; Godderis et al., 2014). To approximate this in COPSE, the GEOCLIMtec normalised runoff factor is taken from Godderis et al (2014) (Figure 7). This simulation uses a rising solar constant and palaeogeography as its sole forcings, and so the 'PG' forcing accounts purely for the impact of palaeogeography on runoff, which in turn is taken to enhance weathering.

PG' is used as a multiplier in COPSE weathering flux calculations for both the weathering of carbonates and silicates, and is displayed in Figure 5.8.

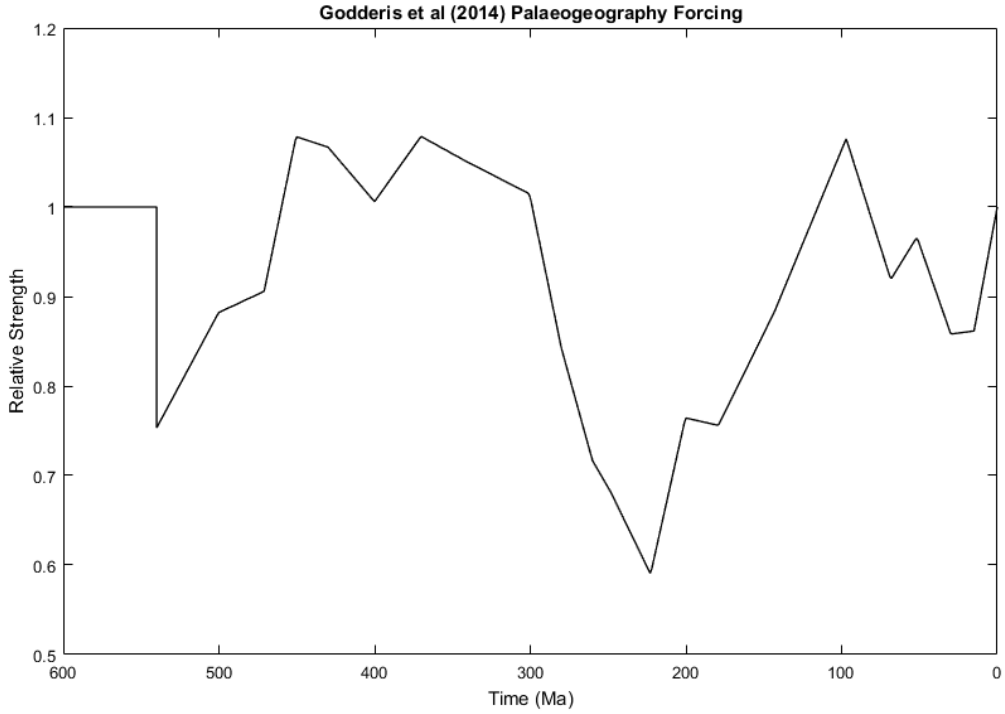

Figure 5.8. Godderis et al (2014) palaeogeography multiplier, 'PG', from 600Ma to present, measured relative to the present day.

5.2.1.4. Land Area

Rather than keep land area constant as in COPSE original, land area now follows GEOCARB (Berner, 1994; Berner and Kothavala, 2001), with normalised land area for the Phanerozoic based on data from Ronov (1994), displayed in Figure 5.9.

As palaeolithological maps are generally unavailable, silicate area is usually assumed to be proportional to continental area (Francois et al., 2005). Despite this, Berner (1994) argues that changing land area should not be used to calculate silicate weathering, as Phanerozoic land area changes generally involved sea level fluctuations that acted to expose/cover areas underlain by relatively non-weatherable clays.

After Mills et al (2014b), silicate weathering is split into granite and basaltic weathering components (see sections 5.2.1.6, 5.2.2.1). As basaltic and carbonate areas are input as distinct forcings (see sections 5.2.1.5, 5.2.1.6), land area is used to calculate granitic area, which is in turn used in the calculation of the granitic weathering component of the silicate weathering flux.

5.2.1.5. Carbonate Area

Carbonate area follows GEOCARB (Berner, 1994; Berner and Kothavala, 2001), with the areal data derived from the work of Bluth and Kump (1991). The carbonate area forcing is equivalent to that displayed in Berner (1994) Figure 1, and reproduced in Figure 5.9.

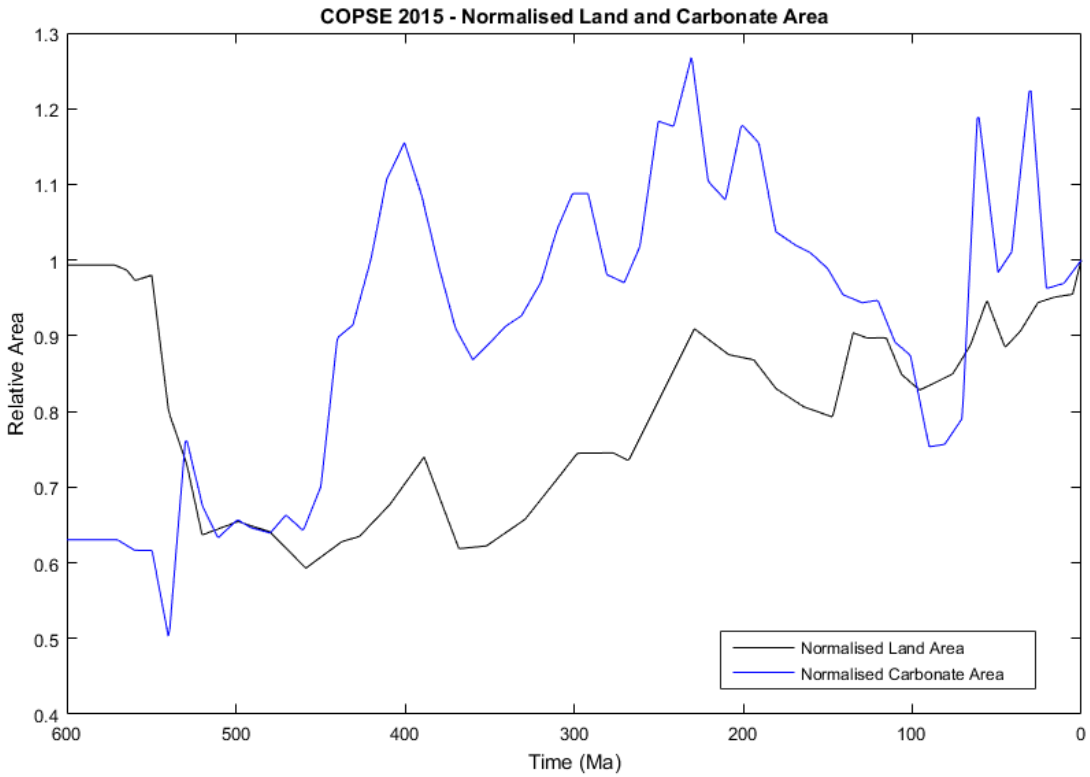

Figure 5.9. Normalised land and carbonate area forcings from 600Ma to present, displayed relative to the present day.

5.2.1.6. Basalt Area

Basalt area is estimated over the Mesozoic as discussed in Mills et al (2014b), whereby it is directly estimated from geologic data regarding the timing and size of large igneous provinces (LIPs), as well as the rate of island arc basalt production.

Mills et al (2014b) collate a database of known LIPs, and following emplacement, assume these LIPs decay exponentially. LIPs with an estimated initial areal extent of $>10^6 km^2$ are taken to be major events, for which individual decay constants are calculated such that their present areas are recovered.

A single decay constant is calculated for all additional, minor, LIPs, chosen such that the total LIP area recovers to $4.8*10^6 km^2$ at present, following Dessert et al (2003) and Allegre et al (2010). Present day total basalt area is calculated to equal $6.8*10^6 km^2$ (Dessert et al., 2003), with $2.0*10^6 km^2$ contributed by island arcs and ocean island basalts (Allegre et al., 2010).

Only continental flood basalts are assumed to influence terrestrial weathering rates. Regarding the marine contribution, 87% of the total ocean island basalt/island arc basalt at present contributed by island arcs (Allegre et al., 2010). As island arcs are driven by subduction of the crust, Mills et al (2014b) assume island basalt area scales with the global subduction rate, as estimated from 230Ma to present by Van Der Meer et al (2014). Prior to 230Ma, this is kept constant due to a lack of data.

Estimating original LIP volume, however, is notoriously difficult (Bond and Wignall, 2014). To account for this, and for incomplete preservation, Mills et al (2014b) assume an uncertainty range of -20% to +50% on initial LIP area estimation. A further uncertainty comes from the assumption of constant decay over time – it is more likely that decay rates were largely affected by the palaeogeographic location of the LIPs over time (i.e. Godderis et al., 2014; Mills et al., 2014b), however this method offers a reasonable first order attempt for a zero-dimensional biogeochemical modelling study.

5.2.2. Updated Fluxes

5.2.2.1. Silicate Weathering

The silicate weathering flux is partitioned into basaltic and granitic weathering components. As discussed in section 3.2.3, not only can the lithologic composition of the exposed continental crust vary through geologic time (Bluth and Kump, 1991; Nardin et al., 2011), but the type and areal coverage of the basaltic component of the silicate weathering flux has a large influence on terrestrial weatherability (i.e. Taylor and Lasaga, 1999; Dessert et al., 2001; 2003; Berner, 2004a; 2006; Mills et al., 2014b).

Basalts are taken to represent the highly reactive volcanic silicate weathering component (Mills et al., 2014b), with granite acting as to represent all non-volcanic terrestrial silicate minerals.

Silicate weathering is subsequently calculated by adding the basaltic and granitic weathering fluxes. The reader is referred to Bergman et al (2004) and Mills et al (2014b), including supplementary materials, for a full list of model equations.

5.2.2.2. Seafloor Weathering

Oceanic crust formation can act as both a source, through degassing, and sink, through seafloor weathering, of Carbon to the Earth System (Gillis and Coogan, 2011), with this sub-section of the long term carbon cycle acting as to bring mantle Carbon into the crust and hydrosphere through mid ocean ridge volcanism, and drawing seawater Carbon back into the crust via carbonate precipitation. These carbonates are eventually subducted back into the mantle.

Seafloor weathering, the process of low temperature basalt alteration and carbonate precipitation in the upper oceanic crust has been proposed as a climate-weathering feedback (i.e. Brady and Gislason, 1997; Gillis and Coogan, 2011; Coogan and Gillis 2013; Mills et al., 2014a; Farahat et al., 2014; Abbot et al., 2015), acting as an important sink for atmospheric CO_2 over geologic time.

A low temperature hydrothermal circulation driven by the cooling of the oceanic lithosphere occurs through the upper oceanic crust, away from the ridge axis (Coogan and Gillis, 2013), leading to fluid fluxes into and out of the ocean. This ‘off-axis’ hydrothermal circulation leads to fluid-rock reactions within the crust, that act as to change the composition of the formation fluid and lead to secondary mineral precipitation (Coogan and Gillis, 2013).

Extensive Calcium-leaching (Brady and Gislason, 1997) via the breakdown of igneous minerals in the oceanic crust (Coogan and Gillis, 2013) generates alkalinity and drives the precipitation of secondary carbonate minerals, most often calcite and aragonite (both crystalline forms of $CaCO_3$) (Gillis and Coogan, 2011), which consume the generated alkalinity.

This is argued to have a pronounced effect on the long term carbon cycle, especially if the breakdown of igneous minerals in the oceanic crust is linked to atmospheric CO_2 (Brady and Gislason, 1997; Coogan and Gillis, 2013). Evidence exists from the Late Mesozoic (Coogan and Gillis, 2013) and the Cretaceous (Gillis and Coogan, 2011) to support this.

However, not only is there considerable uncertainty in the rate of Ca-leaching and CO_2 consumption by seafloor weathering (Brady and Gislason, 1997), there is also an ongoing debate as to which processes or parameters are the most important in controlling the rate of reaction between hydrothermal fluids and the crust (Gillis and Coogan, 2011).

Seafloor weathering is represented in the COPSE model following Mills et al (2014a), based upon the CO_2-dependence of seafloor weathering as put forward by Brady and Gislason (1997), as shown in Equation 5.3. They argue that this dependence may constitute a feedback whereby enhanced CO_2 production via seafloor spreading would be compensated for by an acceleration in the seafloor weathering flux.

$$sfw = k_{sfw} * D * (pCO_2)^a \quad (5.3)$$

Relative seafloor spreading rate is assumed to be linked directly to degassing, 'D', as the updated degassing forcing represents the combined arc and ridge flux reconstructed from subduction zone lengths (Van Der Meer et al., 2014).

The present day seafloor weathering rate, k_{sfw}, is taken as $1.75*10^{12}$ mol/yr (Mills et al., 2014b). The relative atmospheric CO_2 concentration is denoted by 'pCO_2', with 'a' representing the power of the seafloor weathering dependence on atmospheric CO_2 (Brady and Gislason, 1997). This is taken as 'a=0.23', however there are considerable uncertainties with this value (Mills et al., 2014a; 2014b).

5.2.3. The Strontium Isotope System

Mills et al (2014b) add a simple strontium isotope system to the COPSE model, following the work of Francois and Walker (1992) and Vollstaedt et al (2014). As discussed in Section 4.2, the strontium isotope ratio of seawater at any given time offers a proxy for the relative rates of terrestrial weathering and hydrothermal activity (i.e. Burke et al., 1982; Veizer, 1988; Francois and Walker, 1992; Shields, 2007; Allegre et al., 2010; Munnecke et al., 2010).
Young volcanic rocks (in this case, basalts) are assumed to have an $^{87}Sr/^{86}Sr$ ratio of 0.705, with old igneous rocks (granites) given the ratio of 0.718 by Francois and Walker (1992), changed to 0.715 by Mills et al (2014b).

Mantle input is assumed to be linked proportionally to the degassing rate, 'D', and has an $^{87}Sr/^{86}Sr$ ratio of 0.703.

The decay of ^{87}Rb to ^{87}Sr is considered, and is represented clearly in the modelled system (Mills et al., 2014b). This decay influences seawater $^{87}Sr/^{86}Sr$ values over geologic time (i.e. McArthur et al., 2012) as it is responsible for the differing $^{87}Sr/^{86}Sr$ values of different rock types – the different strontium reservoirs have very different Rb/Sr molar ratios (Francois and Walker, 1992), and since ^{87}Sr is produced by the decay of ^{87}Rb, they therefore have very different $^{87}Sr/^{86}Sr$ ratios.

Rubidium decay is represented as shown in Equation 5.4, following Francois and Walker (1992):

$$(87Sr/86Sr)_t = (87Sr/86Sr)_0 + (87Rb/86Sr) * (1 - e^{\lambda t}) \quad (5.4)$$

Equation 5.4 essentially acts as to equate the $^{87}Sr/^{86}Sr$ ratio at a given time 't' to the initial $^{87}Sr/^{86}Sr$ ratio of the reservoir multiplied by the $^{87}Rb/^{86}Sr$ ratio of the reservoir, with λ equal to $1.4*10^{11}yr^{-1}$, the decay constant of ^{87}Rb (Francois and Walker, 1992). The initial $^{87}Sr/^{86}Sr$ ratio is taken as 0.69898 for the time of formation of the Earth, following Papanastassiou and Wasserburg (1968).

This strontium system is designed to function from 230Ma through to the present. As such, the initial oceanic $^{87}Sr/^{86}Sr$ value is set to 0.708 in accordance with the geologic data, with initial sedimentary carbonate $^{87}Sr/^{86}$

Sr set to 0.714 at 230Ma such that the model returns to the present day value (Mills et al., 2014b).

For the full equations of the strontium system as utilised in Mills et al (2014b), readers are directed to the supplementary information of their study, as well as to Francois and Walker (1992).

5.2.4. Effect of Early Non-Vascular Plants

The work of Lenton et al (2012) looked to update the COPSE model to investigate the impact of non-vascular plant colonisation during the Ordovician on the long term carbon cycle and climate, with the aim of simulating the Late-Ordovician glacial period.

The biologic forcings EVO and W were perturbed, following the results of physical weathering experiments, from values of 0 at 475Ma to values of 0.15 and 0.75 respectively at 460Ma following a linear rise, with the forcings being held constant thereafter. Enhanced phosphorus weathering was invoked to match the $\delta^{13}C_{carb}$ record, and so the EPSILON forcing, representing an enhancement of nutrient weathering, was spiked between 460-456Ma and 447-443Ma.

As a result, the enhancement of weathering by early non-vascular plants provides a mechanism drawing the climate into the Hirnantian glaciation, as well as reproducing the GICE and HICE $\delta^{13}C_{carb}$ excursions.

6. Methodology

6.1. Creating a New Baseline Model

In order to achieve the aim of reproducing the broad scale structure of the strontium isotope record over Phanerozoic time, the geologic forcing factors are updated to create a new baseline model setup.

Revised tectonic uplift and basalt area forcings, as well as a new parameterisation of the impact of palaeogeography on the weatherability of LIPs, are constructed within this study. An updated degassing forcing is constructed from the subduction zone lengths of Mills et al (in press).

Due to the inherent uncertainties involved with the creation of forcing factors representative of tectonic uplift, volcanic degassing and basaltic area over Phanerozoic time, error ranges of ±20% (uplift and degassing) and +50%/-20% (basaltic area) are applied to account for this. Moreover, such maximum and minimum values allow for the investigation into the effects on the Phanerozoic long term carbon cycle of enhanced or decreased geologic forcing magnitude.

6.1.1. Updated Model Forcings

6.1.1.1. Tectonic Uplift

The uplift forcing is initially updated from the GEOCARB 3 fR forcing of Berner and Kothavala (2001), as discussed in Section 5.1.2.1, to the GEOCARBSULF fR forcing of Royer et al (2014) (Figure 1D). This parameter is defined as the effect of relief on chemical weathering at a given time relative to the present day (Royer et al., 2014), and was initially estimated following $^{87}Sr/^{86}Sr$ data, although more recent versions of GEOCARB use rock abundance data, as is used in the Royer et al (2014) uplift forcing.

This update of the representation of tectonic uplift differs from that of Berner and Kothavala (2001) in that whilst both display uplift over the course of a Wilson Cycle and both estimate high uplift from the Late-Proterozoic through the Ordovician, the updated Royer fR predicts a consistently increased effect of relief upon chemical weathering throughout the rest of the Phanerozoic, as displayed in Figure 6.2.

However, such an uplift forcing, essentially a cubic fit to erosion rates (i.e. Berner and Kothavala, 2001; Hay et al., 2006) is not entirely representative; times of enhanced uplift largely correlate with supercontinental accumulation, for example Rodinia, Pannotia, Gondwana, and Pangaea (Meert, 2012; Nance and Murphy, 2013; Nance et al., 2014), and reduced uplift with periods of supercontinental breakup. Furthermore, increased uplift is also associated with orogenic events, with Table 6.1 giving an overview of those of the Phanerozoic.

Orogeny	Period (Ma)	Source(s)
Cadomian	670-520 650-550	Guerrot and Peucat (1990) Linnemann et al (2008)
Taconic	550-440	Moore and Worsley (1994) Kump et al (1999) Ganis and Wise (2008) Herrmann et al (2010)
Caledonian	500-400 490-390 420-390	Mckerrow et al (2000) Jahn (2004)
Acadian	375-325	Murphy et al (1999) Murphy and Keppie (2005)
Variscan/Hercynian	380-300	Jahn (2004)
Alleghanian	325-260	Maher et al (1994) Simancas et al (2005) Engelder and Whitaker (2006)
Cimmerian	210-180 250-200	Zanchi et al (2009)
Alpine	120-0 100-0 65-2.5	Schmid et al (2004) Rosenbaum et al (2002)

Table 6.1. Orogenic events of the Phanerozoic.

To better account for these processes whilst retaining the ability to predict the strontium isotope record, an updated uplift forcing is calculated by producing a smoothed fit (LOWESS (i.e. Cleveland, 1981; Trexler and Travis, 1993)) to the combined relative sediment abundance data, supplied by Mills (pers. comm.), of Berner (2004a) and Hay et al (2006), as displayed in Figure 6.1.

The abundance of sediment over the Phanerozoic is a direct reflection of erosion rates (Hay et al., 2006), as periods characterised by high deposition rates were periods of uplift and erosion of the continents (Wold and Hay, 1990). Whilst there is clear variation in sediment abundance over shorter timescales, it is assumed that such variations are not due to short-term variations in uplift. On

a planetary scale, as post-glacial rebound is not considered, uplift is unlikely to vary by such magnitudes over such short geological timescales. At ~480Ma, the uppermost two data points, although both indicating high sediment abundance, differ by over half the normalised level. Whilst this could indicate a dramatic short-term change in uplift, as these data points are from the two different sources, it is argued that such differences are as a result of variations in sampling methods and locations of these datasets. As is clear in Figure 6.1, moving average and LOESS fits are more sensitive to local variation which, as stated, may not be representative of the long-term trend. Moreover, the LOWESS fit largely bisects the moving average and LOESS fits, and is thus argued to offer the approximation most representative of all three. Consequently, the LOWESS fit is argued to be the most representative on a Phanerozoic timescale.

As this study focuses on long-term changes over the Phanerozoic, it is assumed that a smoothed fit to this sediment abundance data is representative of the long-term variations in uplift. This assumption is supported by the peak in sediment abundance coinciding with the peak in orogenic activity and supercontinental assembly, as displayed in Figure 6.1.

This updated uplift forcing is then compared to prior estimates in Figure 6.2.

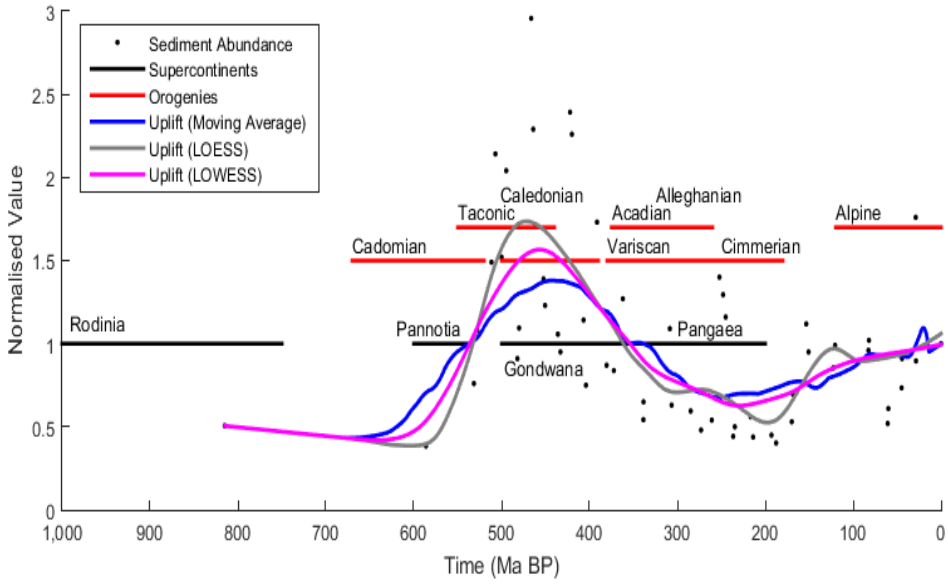

Figure 6.1. Updated uplift forcing, fitted to the sediment abundance data of Berner (2004a) and Hay et al (2006), compared to orogenic and supercontinental events over the past 1000Ma.

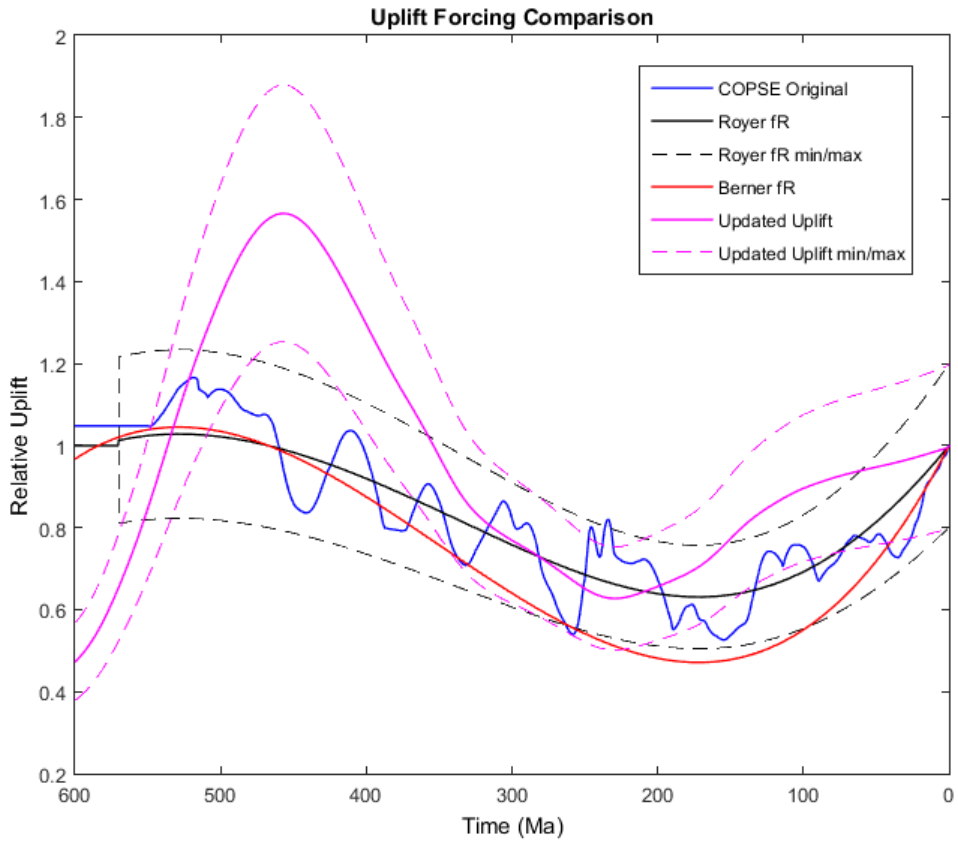

Figure 6.2. Comparison between the uplift forcings of COPSE original (Bergman et al., 2004), GEOCARB 3 (Berner and Kothavala, 2001), Royer et al (2014) and the updated sediment abundance fit produced in this study.

6.1.1.2. Degassing

Initially, the COPSE degassing forcing was updated in a similar manner to tectonic uplift, through utilising the GEOCARBSULF fSR forcing of Royer et al (2014) (Figure 1K). The fSR parameter defines the seafloor creation rate relative to the present, and as seafloor spreading rates have a strong control upon both volcanic and metamorphic degassing rates (Royer et al., 2014), it can be taken to represent CO_2 degassing. This variable, however, is argued to be poorly constrained (Berner, 2004a), as it is inferred from the volume of intact seafloor. As little of the oceanic crust is older than 180Ma due to subduction and recycling, for periods prior to this seafloor spreading rates must be inferred from changes in sea level (i.e. Berner et al., 1983).

A further updated CO_2 degassing forcing, displayed in Figure 6.3**.**, is calculated following the subduction zone reconstruction of Mills et al (in preparation).

Subduction zone lengths were acquired from Mills (pers. comm.), and as subduction zone length is a first-order control on the degassing of CO_2 at volcanic arcs (Mills et al., 2016), this data is taken as representative of the long term degassing trend over the Phanerozoic.

A benefit of this forcing update is that it provides a subduction zone based estimate for the entirety of the Phanerozoic, unlike the reconstruction of Van Der Meer et al (2014) which only covers the Mesozoic.

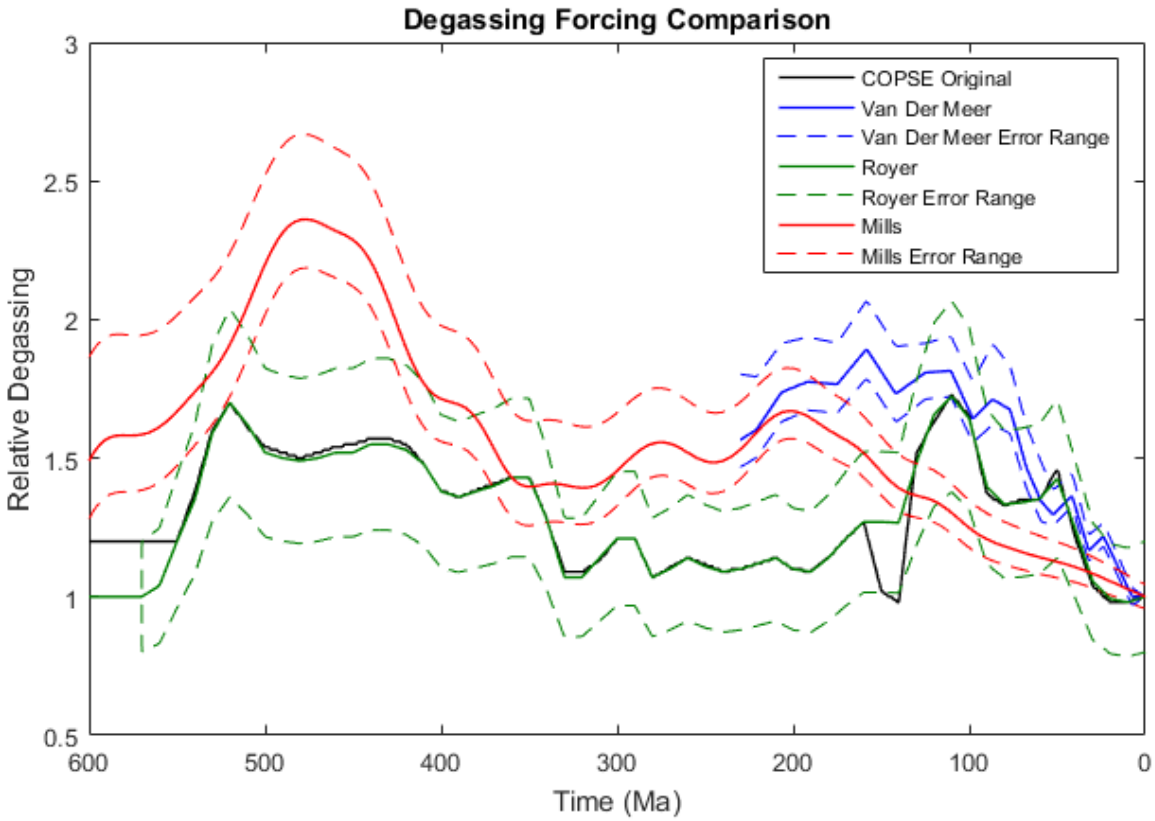

Figure 6.3. Comparison between the degassing forcings of COPSE original (Bergman et al., 2004), Royer et al (2014), Van Der Meer et al (2014) and Mills et al (in preparation).

6.1.1.3. Reconstructing Basaltic Area

Following the work of Mills et al (2014b), surmised in Section 5.2, basaltic area over the Phanerozoic is reconstructed using the LIP record. This study looks to further the reconstruction by considering an LIP-based basalt area forcing over the course of the Phanerozoic, rather than just the Mesozoic as presented in Mills et al (2014b).

The LIP database of Mills et al (2014b) is extended back to the Bir El Khzaim Event of 850Ma, such that a more accurate representation of the basaltic area at the onset of the Phanerozoic is presented, rather than simply presuming present day extent. Further, two additional LIPs are added to the Mesozoic, the Sierra Madre Occidental and Qiangtang Panjal events. The full database is displayed in Table 6.2. As with the study of Mills et al (2014b), only continental flood basalts are assumed to affect terrestrial chemical weathering rates.

The same ‘major’ events defined by Mills et al (2014b) are taken to have individual decay constants to recover their present areas. Despite additional events having estimated areas $>10^6 km^2$ (see Table 6.2), as their present areas are unknown they are included within the ‘minor’ events for which a single decay constant, calculated as 0.01484876, is used to recover the present LIP area of $4.8*10^6 km^2$ (Dessert et al., 2003; Mills et al., 2014b).

Whilst the ocean island basalt/island arc contribution of Mills et al (2014b) is kept constant beyond 230Ma due to a lack of global subduction rate data beyond this point, with the updated degassing forcing of Mills et al (in preparation), this contribution is calculated back to 750Ma, before which it is kept constant. The areal extent of the individual LIPs and the ocean island basalt contribution is displayed in Figure 6.4. Subsequently, the total reconstructed areal extent of basalt through the Phanerozoic is shown in Figure 6.5.

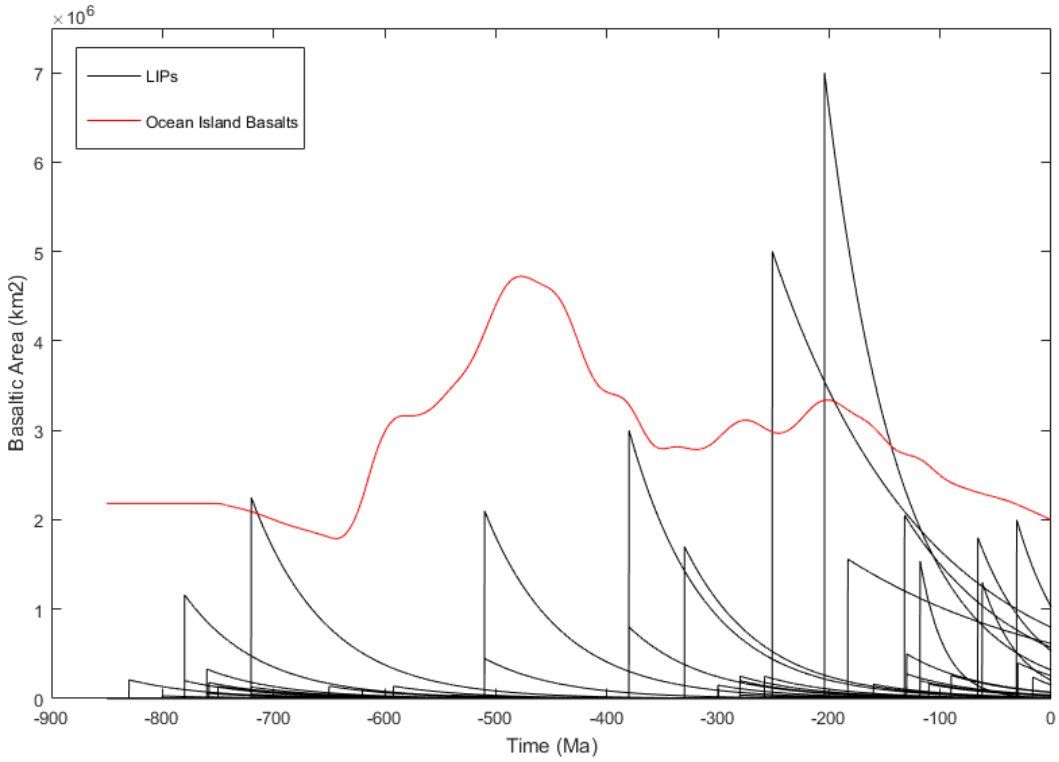

Figure 6.4. Reconstruction of basaltic area from 850Ma to present, with the black curves displaying the contribution of individual LIPs, and the red curve showing the contribution from ocean island basalts, assumed proportional to subduction zone lengths as described in Section 6.1.1.2.

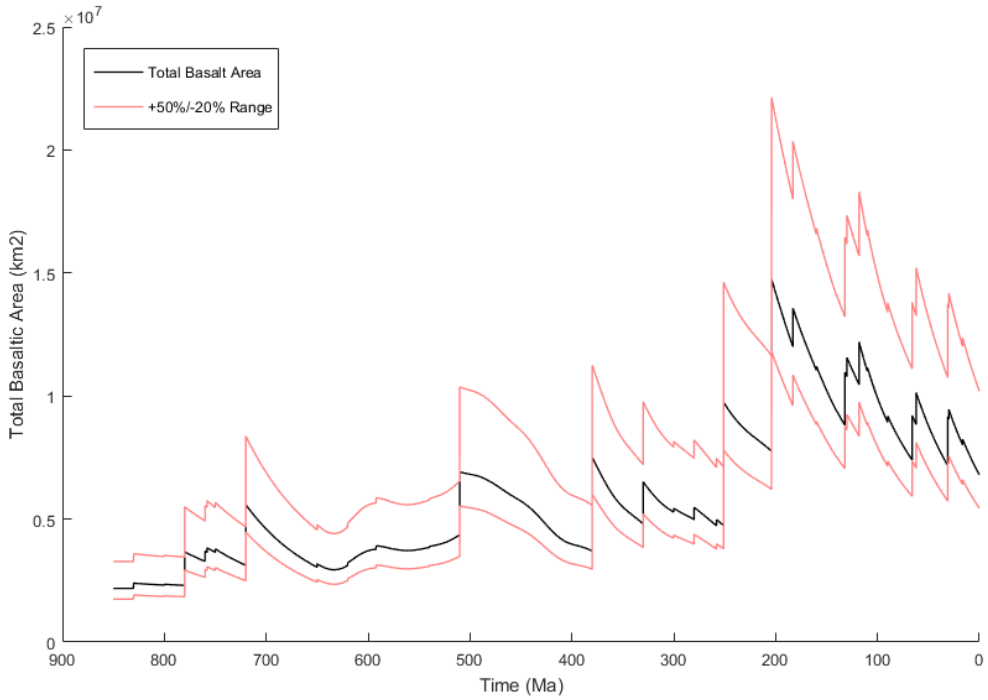

Figure 6.5. Reconstruction of total basaltic area from 850Ma to present, combining both the LIP and ocean island basalt contributions. The red curves display the +50%/-20% error range applied to the average forcing following Mills et al (2014b).

Time of Emplacement (Ma)	Name of Province	Continental Area (km^2)	References
16.5	Columbia River	240000	-
30	Sierra Madre Occidental*	400000	Bryan and Ferrari, 2013
31	Afro-Arabia	2000000	-
62	North Atlantic Igneous Province	1300000	-
66	Deccan Traps	1800000	-
90	Madagascar Event	260000	-
110	Marie Byrd Land Event	160000	-
118	Kerguelen Plateau	1540000	-
118	Rajmahal/Sylhet Province	200000	-
130	Queen Elizabeth Islands	275000	-
130	High Arctic Large Igneous Province	500000	-
132	Comei-Bunbury LIP	100000	-
132	Parana-Etendeka Event	2050000	-
140	South West Greenland Trap	20000	-
160	North West Australian Margin	160000	-
183	Karoo-Ferrar Event	1560000	-
204	Central Atlantic Magmatic Province	7000000	-
251	Siberian Traps	5000000	-
258	Emeishan Event	250000	-
280	Qiangtang Panjal*	40000	Ernst and Buchan, 2001; Zhai et al., 2013
280	Himalaya-Neotethys Event	200000	-
280	Tarim Block Event	250000	-
300	European-Northwest Africa Event	150000	-
330	Tianshan*	1700000	-
380	Yakutsk-Vilyui*	800000	-
380	Kola-Dneiper*	3000000	-
400	Panzhihua*	5000	Ernst and Buchan, 2001; Ernst, 2014
510	Antrim Event*	450000	Ernst, 2014
510	Kalkarindji*	2100000	Glass and Phillips, 2006

Time of Emplacement (Ma)	Name of Province	Continental Area (km^2)	References
540	Wichita Mountains Event*	40000	-
575	Late Central-Iapetus Event*	7000	-
592	Middle Central-Iapetus Event*	140000	-
620	Early Central-Iapetus Event*	105000	-
650	Volyn Event*	140000	Ernst and Buchan, 2001; Ernst, 2014
720	Gannakouriep Event*	30000	Ernst and Buchan, 2001; Ernst, 2014
720	Franklin Province	2250000	-
720	Dovyren-Kingash*	130000	-
720	Mutare*	50000	-
750	Muggamurra Event*	140000	Ernst and Buchan, 2001; Ernst, 2014
758	Mundine Well Event*	180000	Ernst and Buchan, 2001; Ernst, 2014
760	Shaba and Ogcheon Event*	330000	Ernst and Buchan, 2001; Ernst, 2014
760	Malani Event*	20000	Ernst, 2014
760	Mt. Rogers Event*	60000	McClellan and Gazel, 2014
780	Gunbarrel Event*	200000	Ernst and Buchan, 2001; Ernst, 2014
780	Kangding Event*	1160000	Ernst, 2014
800	Niquelandia*	30000	Correia et al., 2012; Ernst, 2014
830	Willouran-Gairdner Event*	210000	Ernst and Buchan, 2001; Ernst, 2014
850	Bir El Khzaim Event*	520000	Ernst and Buchan, 2001; Ernst, 2014

Table 6.2. Database of Continental Large Igneous Provinces from 850Ma to present, developed following Mills et al (2014b). Provinces marked '*' have been added to the original database, and their references provided. References marked '-' are present within the supplementary information of Mills et al (2014b), to which the reader is directed.

The uncertainties regarding this approach have been briefly discussed in Section 5.2.1.6, and largely result from the incomplete preservation of LIPs, as well as the assumption of an exponential decay for each province, independent of its palaeogeographical location at any given time (Bond and Wignall, 2014; Mills et al., 2014b). Due to such incomplete preservation, an error range of +50%/-20% is given following Mills et al (2014b), as initial LIP areas, especially for earlier provinces, are much likely underestimates.

6.1.1.4. Palaeogeographic Weatherability of LIPs

One of the main uncertainties with the reconstruction of Phanerozoic basaltic area from LIPs is that the exponential decay assumed for each province does not accurately represent the change in weatherability of LIPs as a function of their changing palaeogeographic location over time.

As such, to account for this, the changing spatial distribution of continental LIPs was mapped following the maps of Ernst (2014), displayed in Figure 6.7, and the palaeomaps of Scotese (2015), the temporal resolution of which is summarised in Table 6.3.

The natural surface of the Earth is complicated (Yang et al., 1999), and so in order to conduct measurements of the Earth's surface, the Earth must be represented as an ellipsoid or sphere that approximates the natural body of the Earth.

The palaeomaps of Scotese (2015) offer a chance to reconstruct LIP latitude through time as present national and continental boundaries are reconstructed through the Phanerozoic. These maps are displayed in Mollweide projection. This is a pseudocylindrical, equal-area projection (i.e. Snyder, 1987; Yang et al., 1999; Grafarend and Krumm, 2006; Varga et al., 2012) that is normally used as a world map (Snyder, 1987), as shown in Figure 6.6.

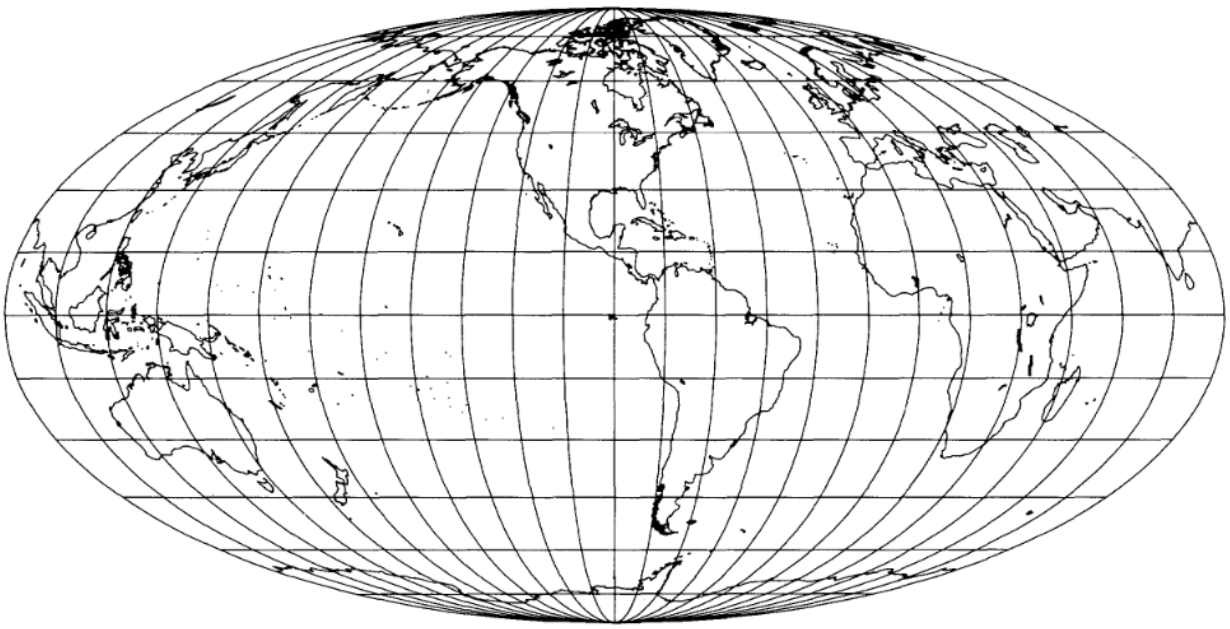

Figure 6.6. Example of the Mollweide projection, taken from Snyder (1987)

Georectification of the palaeomaps to a standard Mollweide projection, in this case using a first order polynomial transformation, is necessary in order for the maps to hold real-world scale geometry.

Due to the ‘time slice’ nature of the palaeomap catalogue, linear change in continental, and thus LIP, motion is assumed between maps, and so shorter term variation is not captured by this forcing. It is, however, representative on a geologic time scale.

The present area of LIPs are mapped from the maps of Ernst (2014) (Figure 6.7), and are re-projected from a Robinson projection to a Mollweide projection in order to be compatible with the palaeomaps.

Following this, the average palaeolatitude of each continental flood basalt mapped by Ernst (2014) is manually tracked to an accuracy of 15^0. This is deemed appropriate as a result of multiple uncertainties. Firstly, on a Mollweide projection, latitude is displayed as straight parallel lines, however these are not equally spaced (Snyder, 1987). For example, regions along the equator are stretched 23% in the North/South direction relative to the East/West Direction (Snyder, 1987).

Moreover, there are additional inherent assumptions that the LIPs are equally thick across their surface area, and that this area does not change over time. Consequently, an accuracy of 15^0 is argued to be acceptably coarse to account for these uncertainties, as well as the user error with the mapping.

For the LIPs with multiple ‘sections’ at present (i.e. CAMP), each section was mapped independently, before calculating an average latitude which was assumed representative of the entire province.

An average LIP latitude was subsequently calculated at each 20Myr timestep (following the temporal resolution of the palaeomaps), and is displayed in Figure 6.8. However, this is not appropriate as a forcing as there is no weighting for LIP area, i.e. small events are given equal weighting as major events.

To overcome this, a weighted average latitude must be calculated whereby each LIP is assigned a fraction of the total LIP area at any given time, such that the average latitude of global LIP basaltic area is calculated rather than simply the average latitude of LIPs irrespective of their basalt content.

A weighted average latitude is calculated as displayed by equations 6.1 and 6.2:

$$\bar{x}_w = \frac{\sum f_i * x_i}{\sum f_i} \quad (6.1)$$

Equation 6.1 displays the standardised function for calculating a weighted average, whereby 'f_i' refers to a weighting factor, and 'x' to the parameter for which the weighted average is being calculated. In the case of LIP latitude, this can be described as follows:

$$\overline{LIP}_w(t) = \frac{\sum average\ LIP\ latitude(t) * fractional\ area(t)}{\sum fractional\ area\ (t)} \quad (6.2)$$

Here, the weighted average LIP latitude at time 't' is calculated with the fractional area at time 't' as the weighting factor. As before, for the LIPs with multiple 'sections', the weighted average latitude of each of these LIPs is calculated, and this is then applied to the overall, global, calculation. Each section is mapped, and a present area is calculated, which is then converted into a percentage of the total present area.

Assuming that these sections retain their areal ratio over time, a weighted average can be calculated whereby the percentage of the total present area is used as the weighting factor. The weighted average latitude of LIPs over the Phanerozoic is also displayed in Figure 6.8.

Whilst a weighted average is far more representative, a major uncertainty remains in that the maps of Ernst (2014) do not include all of the LIPs used in the calculation of basalt area. In actual fact, 12 of the 57 LIPs are not mapped, resulting in only ~79% coverage – therefore for certain periods of the Phanerozoic, especially those whereby an extensive period of time elapses over the course of which LIPs are not contributing to the calculation of this latitudinal forcing (i.e. the Panzhihua and Antrim Events between 510 and 380Ma), the weighted average latitude may not be representative of the actual palaeogeographical configuration of LIP basalt at this time.

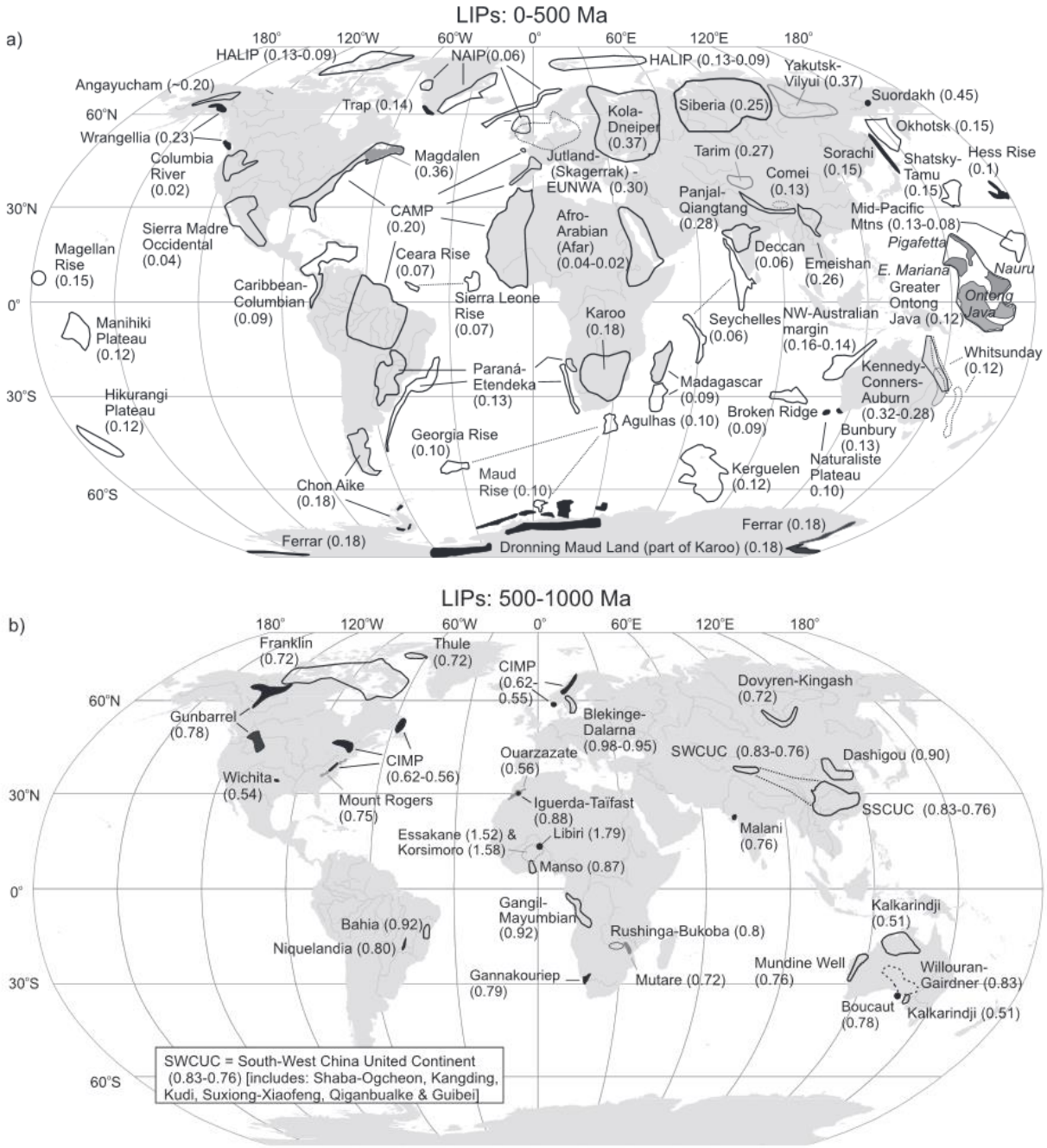

Figure 6.7. Global maps, in Robinson projection, displaying the suggested present location of LIPs, emplaced between (a) the present day and 500Ma, and (b), 500Ma and 1000Ma (Ernst, 2014).

Geologic Time Period	Time (Ma)
Neoproterozoic – Middle Ediacaran	600
Neoproterozoic – Late Ediacaran	560
Cambrian-Precambrian	540
Middle Cambrian	520
Late Cambrian	500
Early Ordovician	480
Middle Ordovician	460
Early Silurian – Llandovery	440
Late Silurian – Ludlow	420
Early Devonian – Emsian	400
Late Devonian – Frasnian	380
Devono-Carboniferous	360
Middle Mississippian	340
Late Mississippian	320
Late Pennsylvanian	300
Early Permian – Artinskian	280
Middle Permian – Capitanian	260
Middle Triassic – Anisian	240
Late Triassic – Carnian	220
Triassic/Jurassic Boundary	200
Early Jurassic – Toarcian	180
Late Jurassic – Oxfordian	160
Early Cretaceous - Berriasian	140
Early Cretaceous – Early Abtian	120
Early Cretaceous – Late Albian	100
Late Cretaceous – Campanian	80
Palaeocene	60
Late Middle Miocene	40
Early Miocene	20
Modern World	0

Table 6.3. Catalogue of palaeomaps used to calculate the change in LIP latitude over the Phanerozoic, following Scotese (2015). Geologic time intervals also from Scotese (2015).

Despite this, as no other such maps exist at the time of writing, it is argued that this methodology offers the current best estimate for LIP basalt palaeolatitude over the course of the Phanerozoic.

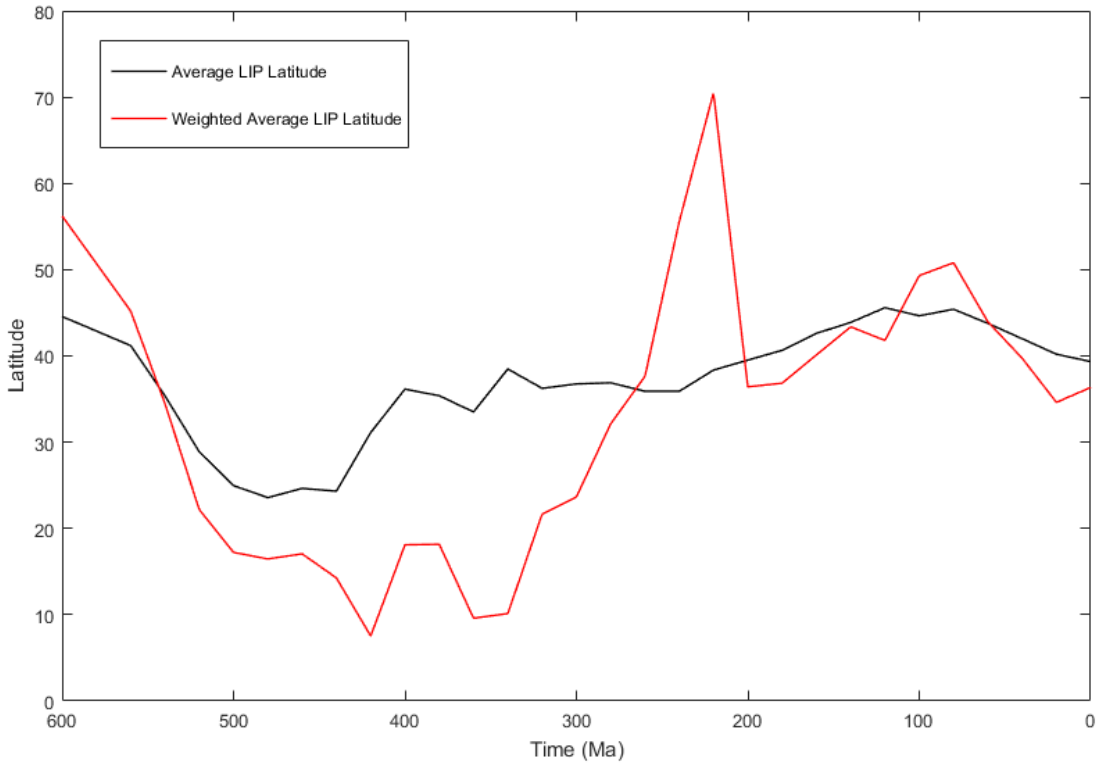

Figure 6.8. Comparison between average LIP latitude and weighted average LIP latitude over the Phanerozoic.

To account for the latitudinal position of basalt through the Phanerozoic, the weighted average latitude is used to calculate a multiplication factor, 'W_{lip}', by which the basalt weathering flux is multiplied. This factor is derived following the relative runoff function of the BLAG model (Berner et al., 1983), as displayed in Equation 6.3, where '$R(T)/R(T_0)$' is taken as relative runoff, '$T\text{-}T_0$' as the difference in temperature between any time (T) and the present day (T_0 = 15^0C), and 'A' is a constant:

$$\frac{R(T)}{R(T_0)} = 1 + A(T - T_0) \quad (6.3)$$

Relative runoff can subsequently be used as the multiplication factor 'W_{lip}'.

As this function is being used to represent the latitudinal weathering dependency of basalt, temperature at time 't' (T) is therefore taken as the

temperature at the weighted average latitude of basalt at time 't', denoted as 'T_{lip}'. This is calculated following Figure 6.9, from Francois and Walker (1992), and converted from Kelvin to degrees Celsius. A function relating latitude to temperature is extracted from this plot and is subsequently used to calculate the temperature at the weighted average latitude of basalt at any given time through the Phanerozoic.

Following this, Equation 6.3 can be amended to Equation 6.4:

$$W_{lip} = 1 + A(T_{lip} - 15) \quad (6.4)$$

Finally, the constant 'A', or 'slope factor', is taken following the work of Probst and Tardy (1989), who calculate the relative runoff for drainage basins in three different hydroclimatological regions; subarctic cold regions, temperature and subtropical warm regions, and humid and very humid regions. A similar three-region approach has been taken to study the climate variability across the Late-Permian ocean (Roscher et al., 2011).

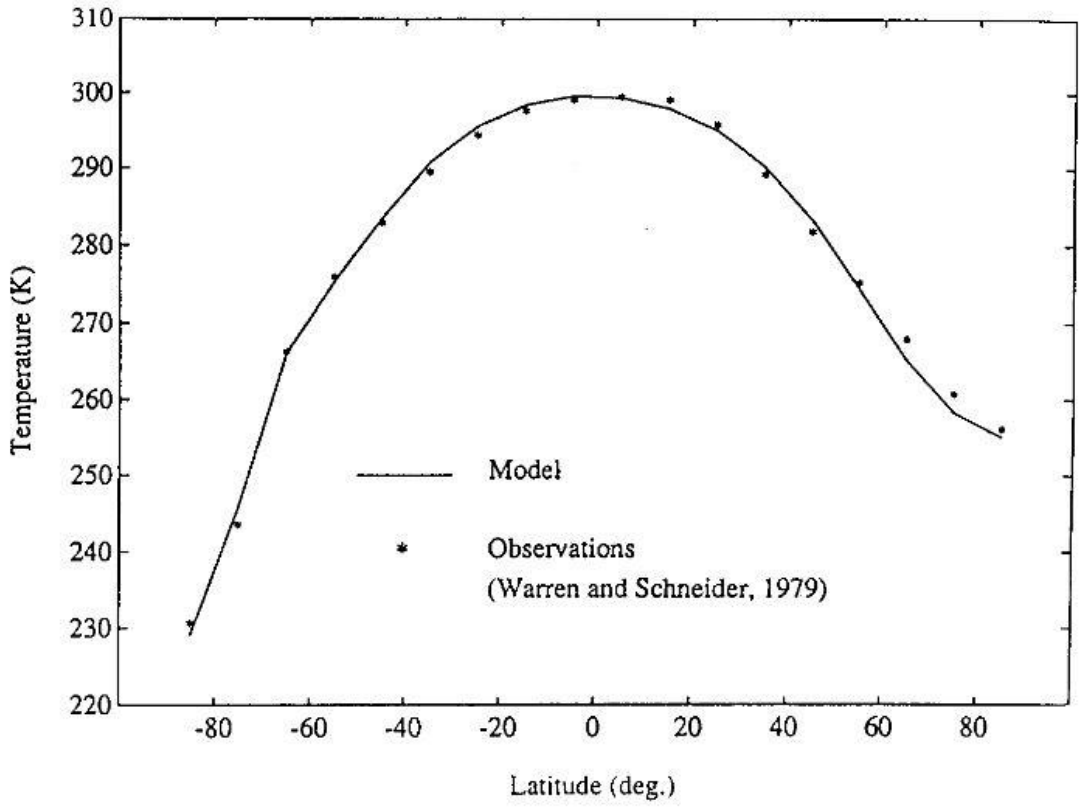

Figure 6.9. Temperature-Latitude relationship, taken from Francois and Walker (1992)

Whilst an extremely rough assumption, these regions are taken to represent the latitudinal bands 90^0-60^0, 60^0-30^0, and 30^0-0^0 respectively. For each of these bands, the constant 'A' is taken from Table 2 of Probst and Tardy (1989); 0.016, 0.031 and 0.098 respectively, as displayed in Equations 6.5 through 6.7 where 'LIP WAL' refers to LIP weighted average latitude:

$$W_{lip} = 1 + 0.016(T_{lip} - 15) \quad (90^0 \geq \text{LIP WAL} > 60^0) \quad (6.5)$$

$$W_{lip} = 1 + 0.031(T_{lip} - 15) \quad (60^0 \geq \text{LIP WAL} > 30^0) \quad (6.6)$$

$$W_{lip} = 1 + 0.098(T_{lip} - 15) \quad (30^0 \geq \text{LIP WAL} \geq 0^0) \quad (6.7)$$

In order to use this latitudinal dependent multiplication factor for the basaltic weathering flux, the Godderis et al (2014) palaeogeography forcing 'PG' is removed from the calculation, and the runoff temperature dependence of basalts is set to constant.

As eluded to, this method of calculating the 'weatherability' of LIPs throughout the Phanerozoic is subject to multiple assumptions and uncertainties. A major assumption is that latitude is the only factor affecting the weatherability of LIPs. In reality, the local climate of the weathering location can also vary due to the size and position of the continents (Berner, 2004a) – larger continents are characterised by dry interiors (Kutzbach and Gallimore, 1989), and so LIPs located within the interior of large continents, or supercontinents, are likely to be slowly weathered, irrespective of their latitudinal location (i.e. Berner, 2004a; Godderis et al., 2012). Moreover, continental configuration affects both oceanic (Crowley, 1998) and atmospheric (Berner, 2004a) circulations, both of which in turn affect local climates and thus weathering rates – neither of these are accounted for in this parameter.

An improvement would be to calculate an average distance of each LIP from the coast for each palaeomap, however such an improvement would require palaeomaps with accurate spatial data rather than the hand-drawn maps of Scotese (2015), and given that the maps are in Mollweide projection, linear distances are subject to distortion, furthering affecting the accuracy of such measurements.

Additionally, it is counter-intuitive that this parameter is used in the calculation of basaltic weathering, yet basaltic area remains largely approximated by

exponential decay (except for those provinces with known present areas). In reality, variability in the weatherability of LIPs would alter their decay curves, or patterns, over time. However, to calculate an independent decay curve for each LIP for the Phanerozoic is entirely beyond the scope of this study, especially given the fact that firstly, present areas for the majority of LIPs are largely unknown, and secondly that this weatherability forcing is a first-order attempt at quantifying the impact of palaeogeographic locational variability of LIPs, and so any decay curves calculated using it would also be subject to large uncertainties.

Despite these uncertainties, it has been argued that moving a land mass from pole to equator results in great changes in temperature and runoff, and thus the weathering flux (Worlsey and Kidder, 1991), and an average low-latitude position is likely to promote silicate weathering (Godderis et al., 2012). Moreover, given the available data, this is argued to offer the most accurate approach currently available to constrain the impact of changing palaeogeography on rock weathering.

6.1.2. Updated Model Fluxes

6.1.2.1. Seafloor Weathering

As discussed in Section 5.2.2.2, COPSE uses a seafloor weathering function based upon this suggested CO_2 dependence of seafloor weathering. As high seafloor spreading rates are associated with increased atmospheric pCO_2 (Berner et al., 1983), and the Van Der Meer et al (2014) based degassing forcing is derived from subduction zone lengths, relative seafloor spreading is implied to be directly linked to degassing and a power law based approximation of its dependence upon atmospheric CO_2. This is multiplied by the present seafloor weathering rate of $1.75*10^{12}$mol/yr (Mills et al., 2014b) to give a relative flux, as denoted in Equation 6.8 (repeated from Section 5.2.2.2):

$$sfw = k_{sfw} * D * (pCO_2)^a \quad (6.8)$$

Not only, however, do major uncertainties exist with this approximation, especially with the value of ‘a’ (taken as a=0.23), but experiments demonstrate that temperature exerts a major control on mineral dissolution rates (i.e. Brady

and Gislason, 1997; Farahat et al., 2013) through increased rate of reaction (Coogan and Gillis, 2013). Therefore, increased seafloor temperatures are argued to increase Ca-leaching from rock, leading to enhanced carbonate precipitation and so CO_2 removal (i.e. Wheat et al., 2000; Wheat and Fisher, 2008; Gillis and Coogan, 2011). A change in temperature of between 10-15^{0}C has been suggested to roughly double the rate of seafloor weathering (Brady and Gislason, 1997).

As a result, the seafloor weathering function has been updated to account for this temperature dependence, as displayed in Equations 6.9 and 6.10 (Mills, pers. comm.):

$$sfw_t = e^{0.0608T} \quad (6.9)$$

$$sfw = sfw_t * k_{sfw} \quad (6.10)$$

The temperature dependence of seafloor weathering, 'sfw_t', assumes the same activation energy, 42KJ/mol, as terrestrial basalts, with 'T' taken as the model temperature in degrees Celsius. This is then multiplied by the present seafloor weathering rate to give a relative flux.

This derivation considers the seafloor weathering flux as a temperature relationship, thus also considering the solar flux. As it has been argued that an increase in solar luminosity played a part in shifting global weathering from a seafloor-dominated flux to a terrestrial-dominated flux (Mills et al., 2014a), such consideration is required to more accurately parameterise the seafloor weathering flux.

Seafloor weathering also plays a role in regulating the $^{87}Sr/^{86}Sr$ ratio of seawater (Qing et al., 1998; Allegre et al., 2010), with the low temperature alteration of seafloor basalts providing a source of non-radiogenic strontium with values estimated in the range of 0.703-0.7035 (Palmer and Elderfield, 1985; Qing et al., 1998; Shields, 2007).

6.1.2.2. Phosphorus Weathering

The fraction of phosphorus liberated from the weathering of different rock types is updated following Compton et al (2000) and Hartmann et al (2014), with the values obtained from Mills (pers. comm.), displayed in Table 6.4.

The silicate weathering fraction is the sum of the fraction of phosphorus liberated from basalt and granite weathering. The granitic flux is four times that of basalts, due to the fact that the granitic weathering flux is roughly two times that of the basaltic weathering flux, and that basalts contain much more Ca/Mg.

Rock Weathering Type	Fraction of Phosphorus Liberated
Carbonate Weathering	0.21
Oxidative Weathering	0.21
Basalt Weathering	0.12
Granite Weathering	0.46
Silicate Weathering (Basalt+Granite)	0.58

Table 6.4. Fraction of phosphorus liberated from the weathering of different rock types

6.1.3. The Strontium Isotope System

The strontium isotope system of Mills et al (2014b), as discussed in Section 5.2.3, is simplified for use over the whole Phanerozoic. As the modelled system is a vast simplification of reality, the aim is not to produce an exact replica of the ocean $^{87}Sr/^{86}Sr$ record, but to offer a prediction of the strontium isotope curve across the entire Phanerozoic that lies within an acceptable range of published data. Moreover, as with Mills et al (2014b), certain features of the predicted curve may correlate with published curves, thus allowing insight into past weathering regimes.

Following the work of Dessert et al (2003) and Mills et al (2014b), the contribution of basaltic and granitic strontium fluxes equate to their respectively contributions to global silicate weathering, with the fraction of continental strontium obtained from basalt weathering thus taken as 0.35.

In order to predict the strontium isotope record for the entire Phanerozoic, the modelled strontium system is initially simplified, before the impacts of increasing its' complexity are investigated.

Rubidium decay is removed, and the carbonate strontium component is non-dynamic. In addition, to be consistent with the updated seafloor weathering function, mantle strontium is decoupled from degassing.

That the carbonate (sediment) strontium component be set as non-dynamic for the baseline runs may appear to be an oversimplification – as discussed in section 4.3, the flux of strontium to the oceans from the weathering of carbonates represents a major source of oceanic strontium (Brass, 1976) that has experienced variation in its isotopic signature over geological time (Shields, 2007). This approach is justified as the ethos of the updated baseline model is to approximate the long-term trends in the Phanerozoic $^{87}Sr/^{86}Sr$ record using a simplified strontium system, before increasing the complexity of both the model forcings and fluxes, as well as the strontium isotope system, and assessing for improvements in model predictions. Moreover, whilst the $^{87}Sr/^{86}Sr$ ratio of the carbonate weathering flux will evolve over time (Shields, 2007), current modelled strontium isotope systems use fixed isotopic compositions for each strontium source (i.e. Francois and Walker, 1992; Mills et al., 2014b). To develop a model strontium system with evolving isotopic compositions through the Phanerozoic is beyond the realms of this study.

Despite this, as the carbonate weathering flux offers the largest source of strontium to the ocean, the impact of its addition to the model is investigated in Section 8.

The mantle flux is given a minor update following the work of Allegre et al (2010), whereby it is partitioned into ridge crest hydrothermalism, accounting for 27% of the flux and taking an $^{87}Sr/^{86}Sr$ ratio of 0.7035, and arc islands/ocean island basalts, which account for the remaining 73% of the flux and have an $^{87}Sr/^{86}Sr$ ratio of 0.703, as displayed in Figure 6.10.

As the starting strontium isotope ratios of Mills et al (2014b) are only applicable to a system beginning at 230Ma, these are altered to reflect the starting values for the Phanerozoic. As the model begins spinning up at 600Ma, oceanic strontium is given the value of 0.7077 following the LOWESS curve of McArthur et al (2012).

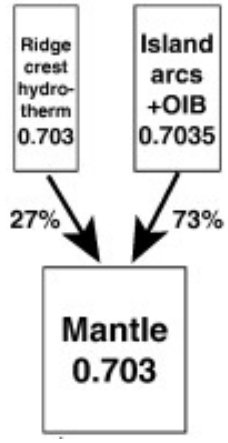

Figure 6.10. Updated mantle strontium partitioning, following Allegre et al (2010)

Following Mills et al (2014b), sediment strontium is used as a tuning parameter such that the predicted strontium isotope curve returns to the present day value, 0.709 (i.e. Hodell et al., 1990). In order to do so, sediment strontium must be set to 0.708. This is both lower than the value (0.714) used by Mills et al (2014b), as well as the average value (0.712) for chemical weathering of the continental crust and its sedimentary cover (Palmer and Edmond, 1989; Peucker-Ehrenbrink and Miller, 2006; Zhao et al., 2009). Despite this, it does fall into the lower estimates of published ranges, for example that of Ohno et al (2008) (0.70797-0.71285).

6.1.4. Plant Forcings

The ‘E’ and ‘W’ forcings of COPSE original are included within the updated model, however the value of the k_{15} parameter, representing the pre-plant weathering rate, is altered from its original value of 0.15 to an updated value of 0.25 (Mills, pers. comm.).

The plant forcings of Lenton et al (2012), namely perturbations in ‘E’ and ‘W’ as well as transient increases in the phosphorus weathering flux, are not included within the baseline run, though can still be used to investigate the impact of early land plants on Ordovician climate under updated model predictions.

6.2. Summary of the Updated Baseline Model

In summary, the updated baseline model uses the following parameters; uplift is calculated from a fit to sediment abundance data from Berner (2004a) and Hay et al (2006), and degassing from the subduction zone lengths of Mills et al (in preparation). Both of these forcings have a +/-20% error range.

Basaltic area is reconstructed via the LIP record back to 850Ma, and an error range of +50/-20% is applied following Mills et al (2014b), with a larger positive error to account for the potential incomplete preservation of LIPs. Granite area is set as constant at present day value due to the uncertainties surrounding its estimating over the Phanerozoic, and carbonate area follows the work of Berner and Kothavala (2001).

The updated geologic forcings are displayed in Figure 6.11.

To account for the changing weatherability of LIPs, they are mapped over the Phanerozoic, and a 'weathering multiplier' is calculated based upon the weighted average location of basalt at any given time, in turn affecting basaltic weathering rates.

The fraction of phosphorus liberated from different sources of weathering is updated following Compton et al (2000) and Hartmann et al (2014).

Seafloor weathering is linked to temperature, with multiple studies suggesting this is a key controlling factor through its effect on chemical rate of reaction (Brady and Gislason, 1997; Coogan and Gillis, 2013; Farahat et al., 2013).

The strontium isotope system of Mills et al (2014b) is simplified, with rubidium decay removed and sediment strontium fluxes set to constant. Mantle strontium fluxes are updated following Allegre et al (2010), however to remain consistent with seafloor weathering, are decoupled from seafloor spreading rates. The starting strontium isotope values are altered to reflect those at 600Ma (McArthur et al., 2012), with sediment strontium set to 0.708 to return the system to the present day.

Finally, the k_{15} parameter of COPSE original is revised from 0.15 to 0.25 (Mills, pers. comm.) resulting in an enhanced pre-plant weathering flux.

6.3. Monte Carlo Setup

Following the methodology of Royer et al (2014), a Monte Carlo simulation is used to investigate the range of possible model results as a result of the error ranges of the three major geologic forcings; uplift, degassing and basaltic area, as displayed in Figures 6.12 through 6.14.

The model is run 100 times, with a random forcing strength assigned for each geologic forcing independently for each run, as described by Equations 6.11 through 6.13.

$$U_{rand} = U_{min} + (U_{max} - U_{min}) * q \quad (0 \leq q \leq 1) \quad (6.11)$$

$$D_{rand} = D_{min} + (D_{max} - D_{min}) * r \quad (0 \leq r \leq 1) \quad (6.12)$$

$$BA_{rand} = BA_{min} + (BA_{max} - BA_{min}) * s \quad (0 \leq s \leq 1) \quad (6.13)$$

Results are displayed as a mean value, with the associated deviations displayed around the mean representing the range of possible results.

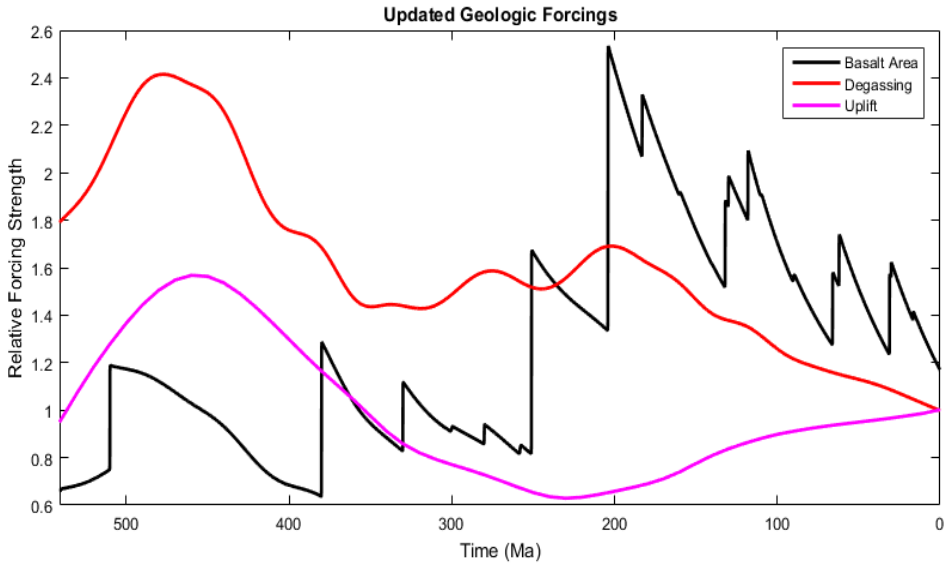

Figure 6.11. Revised geologic forcings used in the updated baseline model

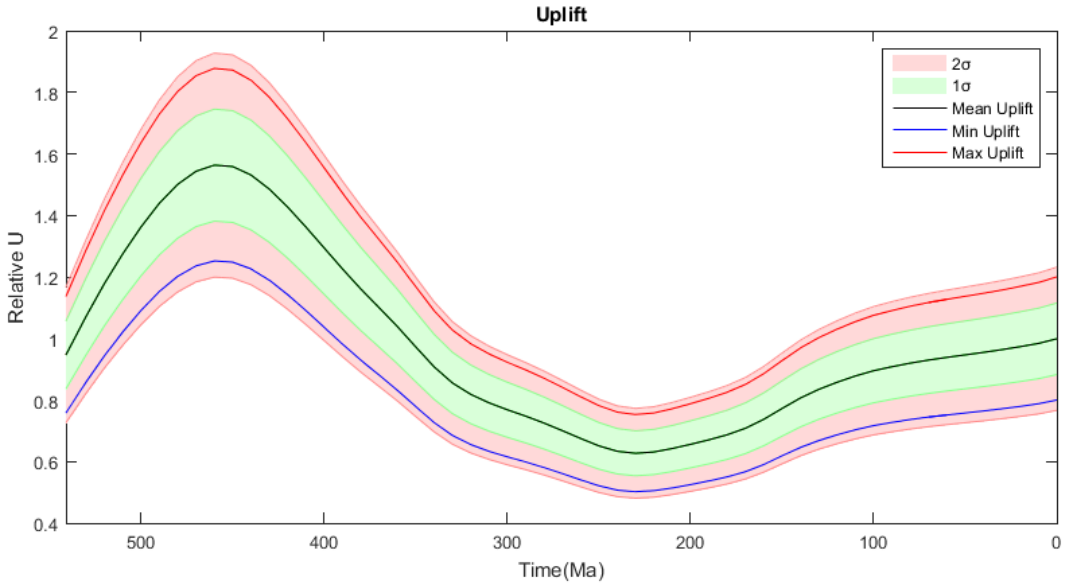

Figure 6.12. Range of uplift values used in the Monte Carlo simulation.

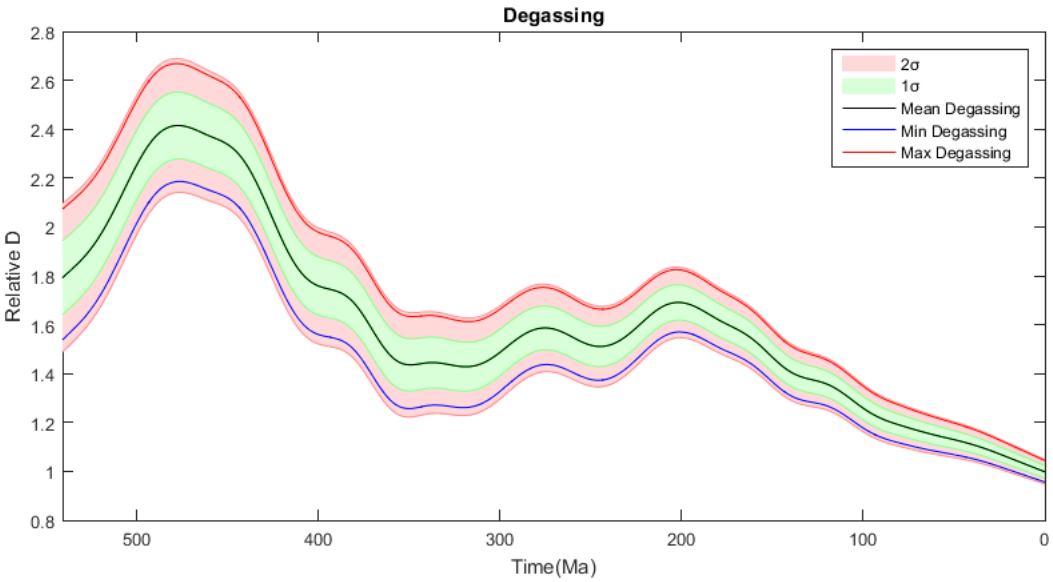

Figure 6.13. Range of degassing values used in the Monte Carlo simulation.

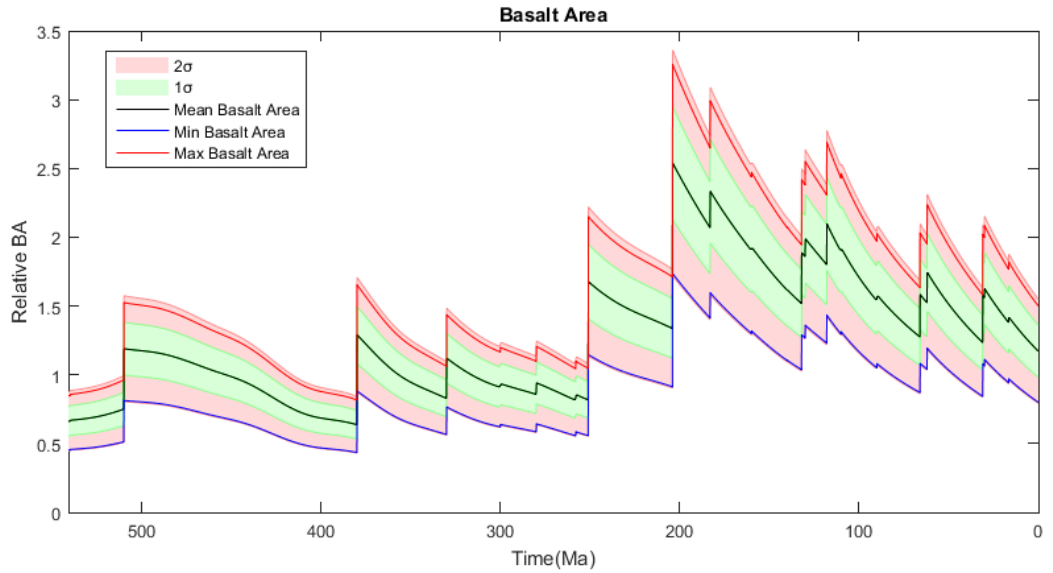

Figure 6.14. Range of basalt area values used in the Monte Carlo simulation.

7. Results and Discussion

Although the general pattern of the evolution of the Earth System over the Phanerozoic displays some similarity, there are considerable differences between the updated model and COPSE original, and these updated trends are validated by good predictions against the long term $^{87}Sr/^{86}Sr$, $\delta^{13}C$, and $\delta^{34}S$ isotopic records. Whilst shorter term isotopic and climatic variability is not necessarily well-represented by model predictions, the aim of this study is to produce an updated model of the long term Carbon cycle, that is validated by predictions against the main long term Phanerozoic isotopic proxy records.

This section first looks to assess and discuss the long-term results for the Phanerozoic, starting with temperature, CO_2 and O_2, followed by isotopic analyses. Whilst there are clear discrepancies between the updated model and both published data and COPSE original for the Mesozoic and Cenozoic, the major aim of this study is to capture the long term trends in Phanerozoic with a focus on the Palaeozoic. As such, these periods are not discussed in as much detail as the Palaeozoic.

7.1. Baseline Results for the Phanerozoic

7.1.1. Temperature and CO_2

The major long term predicted trends in temperature and pCO_2 differ to that of COPSE original, as displayed in Figures 7.1 and 7.2. A steady decline in pCO_2 takes place until ~380Ma, after which the model undergoes a dramatic transition to icehouse conditions, with a concurrent decrease in global temperature. Both temperature and pCO_2 show a large increase between 300-200Ma, before a subsequent fall to cooler conditions for the remainder of the Phanerozoic.

Atmospheric pCO_2 starts at >20PAL in the earliest Cambrian, with a concurrently high temperature of 22^0C, before a drawdown at ~510Ma, likely relating to the emplacement of the Kalkarindji and Antrim LIPs resulting in an enhanced basaltic weathering flux, and thus CO_2 drawdown. This corresponds to a ~1.2^0C of global cooling. These estimates of high pCO_2 are consistent with the general consensus that the Cambrian was characterised by the highest

pCO_2 levels of the Phanerozoic (i.e. Berner and Kothavala, 2001), in the region of 15PAL. Such high CO_2 levels were required to keep the planet warm under reduced solar luminosity (i.e. Kasting, 1989), although they were at such levels that greenhouse conditions prevailed.

This Cambrian greenhouse has been argued to have been fuelled by extensive tectonic outgassing (McKenzie et al., 2014). This is consistent with the updated degassing forcing of Mills et al (in preparation), with Cambrian degassing between 1.5 and 2 times the present level.

Our understanding of the climate of the Ordovician has undergone a paradigm shift (Rasmussen et al., 2016), from hypotheses of an extended greenhouse interval to modern ideas of a period characterised by global cooling and abrupt glaciation. As a consequence, there exists a range of published pCO_2 estimates from both model and proxy data, in general between 8-22PAL (i.e. Yapp and Poths, 1992; 1996; Berner, 1997; 2006a; Berner and Kothavala, 2001; Bergman et al., 2004; Tobin et al., 2005; Finnegan et al., 2011; Lenton et al., 2012). This change in understanding is well-reflected in the updated model results.

COPSE original displays an increase in both pCO_2 and temperature through the Ordovician (Bergman et al., 2004), consistent with traditional understanding of Ordovician climate. In contrast, the updated model predicts a gradual decline in both pCO_2, from ~15PAL to ~12PAL, and temperature throughout the period, consistent with the trend of the $\delta^{18}O$-based palaeotemperature curve of Trotter et al (2008), although the magnitude of cooling is predicted to be much greater, as well as the palaeotemperature estimates of Vandenbroucke et al (2010).

Whilst additional earlier cool intervals have been postulated (Rasmussen et al., 2016), the updated model does not recognise the Hirnantian glaciation (i.e. Boucot and Gray, 2001), as is clear in Figure 7.3, despite the enhancements made to the geologic forcing.

This Hirnantian glaciation resulted in a fall in atmospheric pCO_2, to as low as an estimated 5PAL (Rothman, 2002; Vandenbroucke et al., 2010; Pohl et al., 2015), and accompanied global cooling on the order of ~3.5 (Lenton et al., 2012) to 6^{o}C (Vandenbroucke et al., 2010; Melchin et al., 2013).

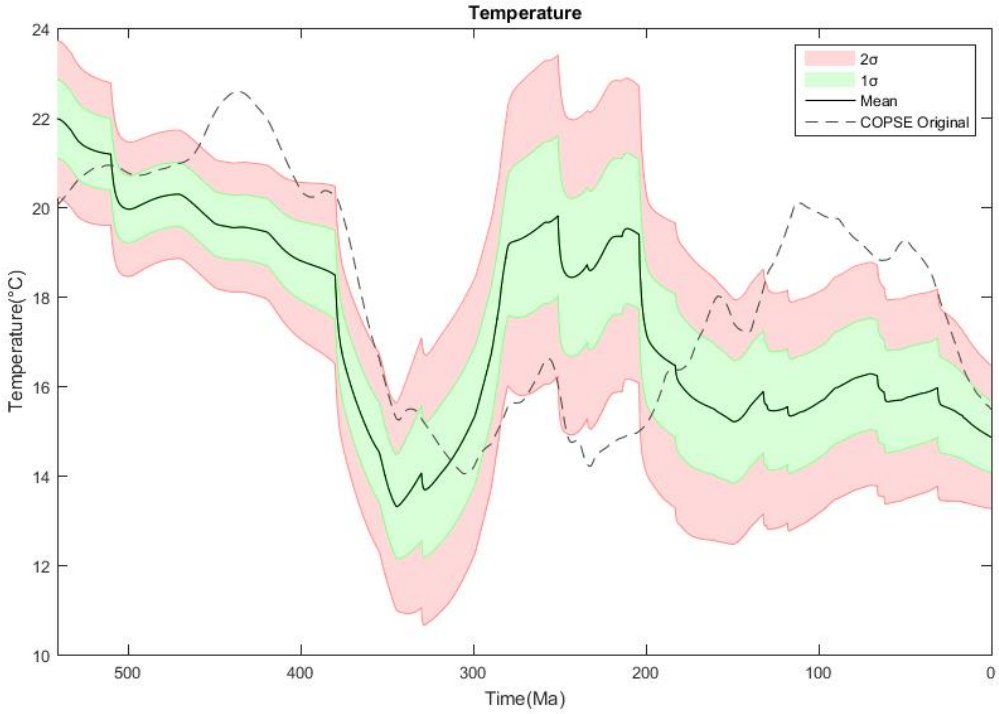

Figure 7.1. Phanerozoic temperature prediction of the updated COPSE model compared to COPSE Original (Bergman et al., 2004), following a Monte Carlo simulation of 100 runs. The error range is denoted as ±1 and ±2 standard deviations (σ) from the mean.

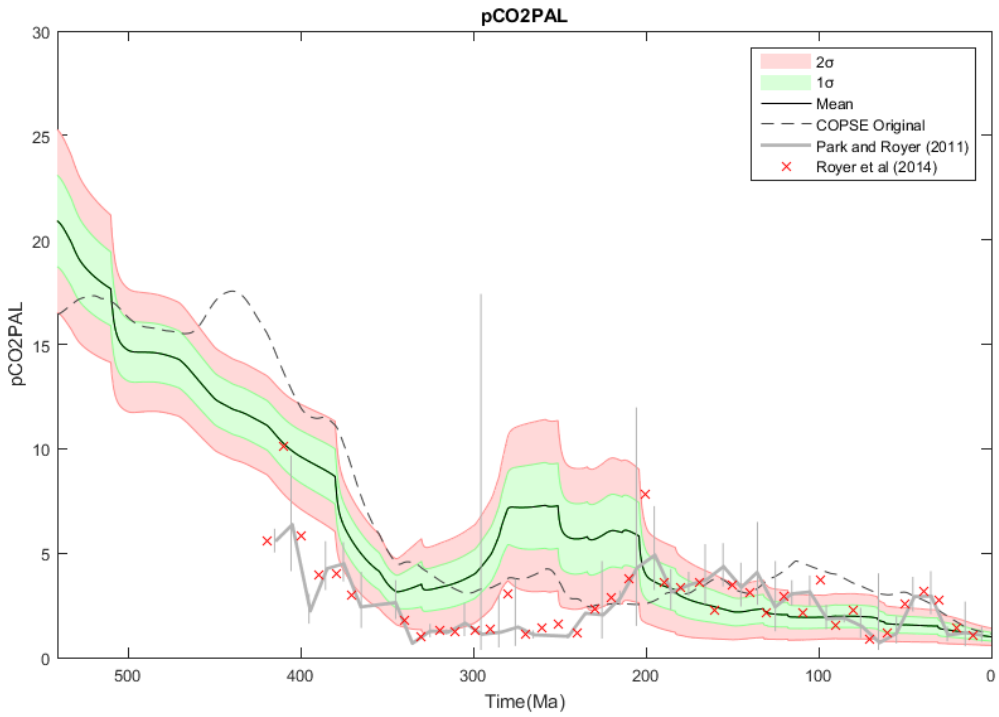

Figure 7.2. Phanerozoic pCO_2 prediction of the updated COPSE model compared to COPSE Original (Bergman et al., 2004) and the proxy data of Park and Royer (2011) and Royer et al (2014), following a Monte Carlo simulation of 100 runs. The error range is denoted as ±1 and ±2 standard deviations (σ) from the mean.

Such an abrupt climatic cooling caused the expansion of a Southern Hemisphere Gondwanan ice mass (i.e. Sutcliffe et al., 2000; Ghienne et al., 2014; Paris et al., 2015) and Northern Hemisphere sea ice (Pohl et al., 2014), and an associated fall in sea level (Haq and Schutter, 2008).

Many authors have argued for a geological trigger of the Hirnantian glaciation, with hypotheses of enhanced uplift during the Taconic and Caledonian orogenies (i.e. Kump et al., 1999) enhancing the exposure of continental lithology to silicate weathering, mass volcanism (i.e. Huff, 2005; 2008; Buggisch et al., 2010; Sell, 2011; Sell et al., 2013), an enhanced basaltic weathering flux (Nardin et al., 2011), potential as a result of a mantle superplume (i.e. Barnes, 2004; Lefebvre et al., 2010), as well as the movement of the continents, and hence lithology undergoing weathering, through the ITCZ (Nardin et al., 2011).

These geological forcing factors, however, are argued to be much better represented in the updated model. The uplift forcing displays a peak in the Ordovician, consistent with the height of the Taconic Orogeny (i.e. Moore and Worsley, 1994; Ganis and Wise, 2008). In addition, past basaltic area is calculated from the LIP record, and such LIPs are mapped over time to account for the proposed impact of continental drift.

Consequently, the updated model results are consistent with the suggestion of Lenton et al (2012) that geologic models seem insufficient to lower pCO_2 to the 8PAL threshold (i.e. Pohl et al., 2014; 2015) required for Ordovician icehouse initiation, although the length of the timestep of the model may also act as to overlook short-term climate dynamics (i.e. Boucot and Gray, 2001).

As such, it is argued that the enhancement of weathering by early non-vascular plants (i.e. Lenton et al., 2012) is required to draw the Ordovician climate into icehouse conditions. Whilst the updated geologic forcings clearly draw the temperature and pCO_2 to levels similar to those postulated as a ‘threshold’ for icehouse initiation, 8-10PAL pCO_2 (i.e. Poussart et al., 1999; Herrmann et al., 2004; 2010; Pohl et al., 2014; 2015), the impact of early non-vascular plants on Ordovician climate looks to be required to push the climate system past such a threshold.

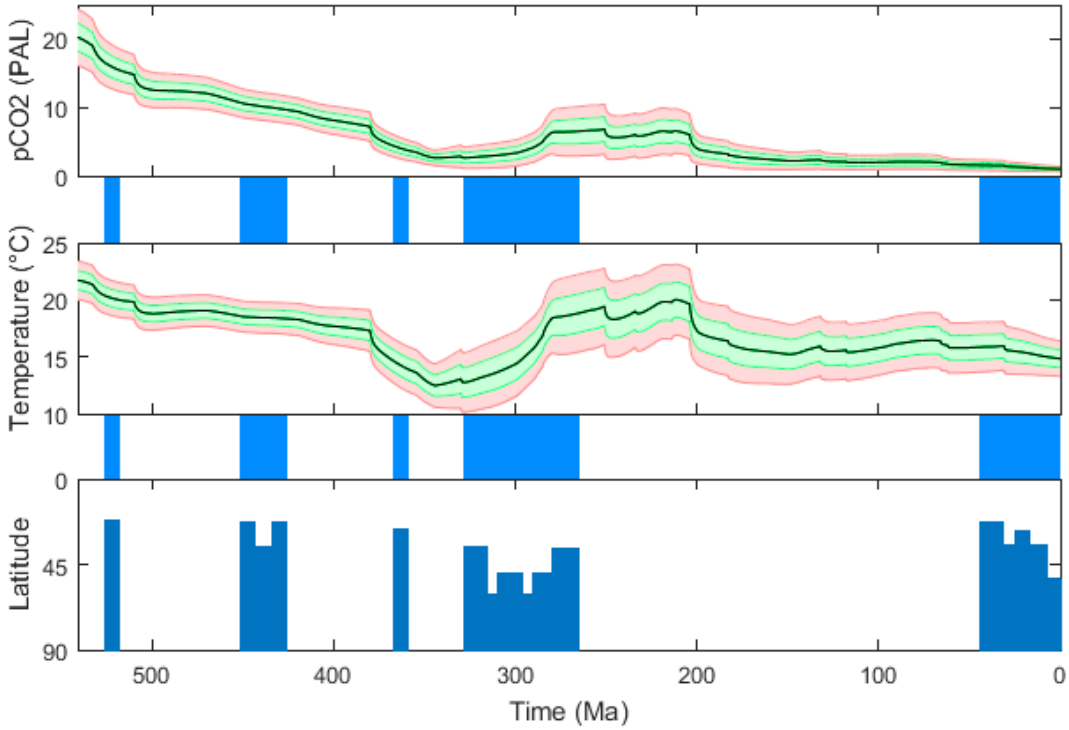

Figure 7.3. Phanerozoic temperature and pCO_2 predictions of the updated COPSE model compared to the glaciation data of Crowley (1998).

Figures 7.4 and 7.5 display the impact upon temperature and pCO_2 respectively of the incorporation of the Ordovician non-vascular plant weathering enhancements of Lenton et al (2012). These enhancements draw pCO_2 to levels of 8.5-9PAL without transient phosphorus weathering pulses, with an accompanying temperature fall to ~17^{0}C. With the addition of ephemeral episodes of enhanced phosphorus weathering, pCO_2 falls to 6.3PAL and 4.5PAL at the Guttenberg and Hirnantian isotopic carbon excursions, with temperature falling to ~15^{0}C and ~13.4^{0}C in accompaniment. Such values show high similarity with those of Lenton et al (2012), firstly suggesting that weathering enhancements by early non-vascular plants may still be necessary in order to initiate glaciation in the Ordovician, even under enhanced uplift and basaltic weathering, and secondly that, given the similarity of the values, negative feedbacks within the model appear strong enough such that it is extremely difficult to force temperature and pCO_2 below certain levels at any given time under realistic model forcings.

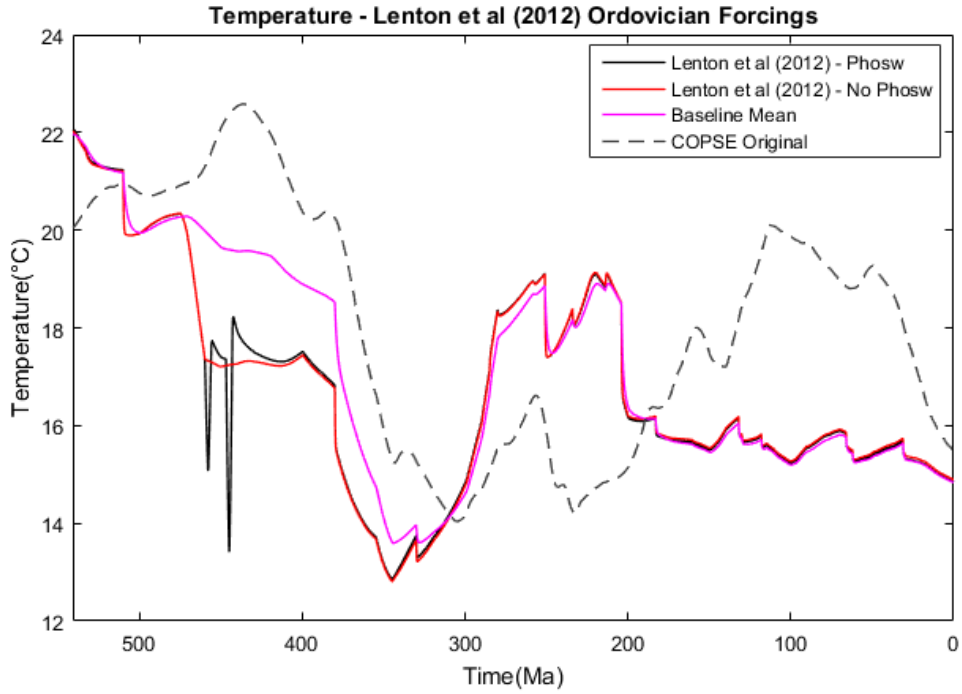

Figure 7.4. Mean Phanerozoic temperature predictions of the updated COPSE model following the incorporation of the Ordovician plant forcings of Lenton et al (2012), with and without transient phosphorus weathering pulses, compared to the updated mean baseline run and COPSE Original.

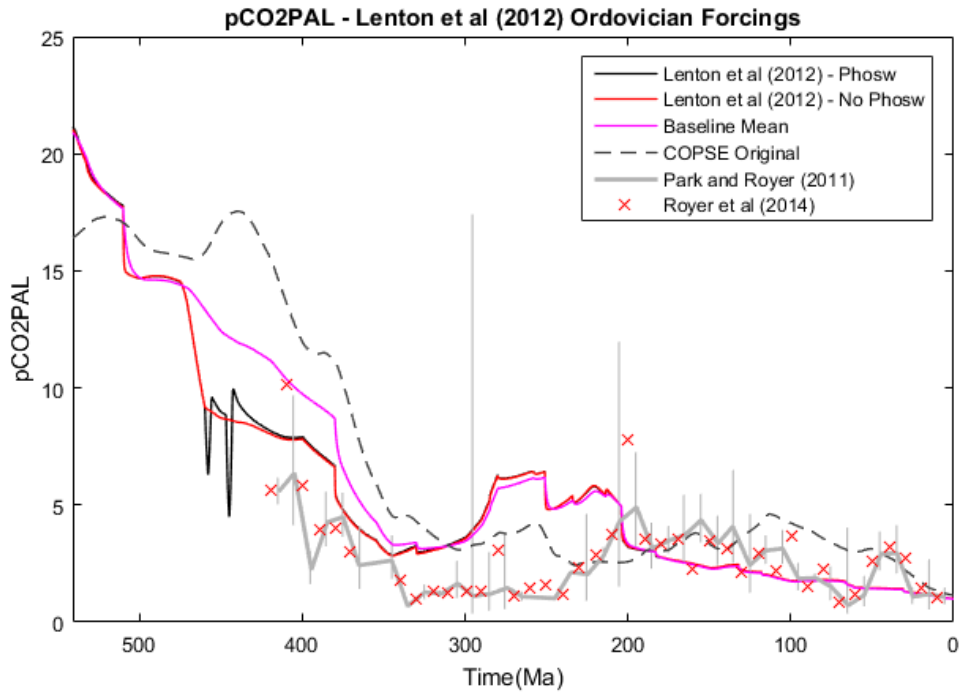

Figure 7.5. Mean Phanerozoic pCO_2 predictions of the updated COPSE model following the incorporation of the Ordovician plant forcings of Lenton et al (2012), with and without transient phosphorus weathering pulses, compared to the updated mean baseline run and COPSE Original.

The decreasing trend of the Ordovician continues through the Silurian, with pCO_2 reaching <10PAL. This shows consistency with some proxy pCO_2 estimates, although the majority of the data points lie below the predicted mean curve, though these estimates are characterised by large uncertainties, especially this early in the Phanerozoic (i.e. Breecker et al., 2010; Breecker and Retallack, 2014; Royer, 2014). There are, however, suggestions that icehouse conditions may have prevailed, to an extent, into the Silurian (i.e. Cooper et al., 2014), consistent with the lower pCO_2 estimates of the proxy data. This 'Early Palaeozoic Icehouse' hypothesis (Page et al., 2007) suggests a 20-30Myr period of icehouse conditions (i.e. Munnecke et al., 2010; Finnegan et al., 2011; Melchin et al., 2013; Gambacorta et al., 2016) with multiple episodes of glaciation and deglaciation with only partial ice sheet retreat, stretching from the Early-Katian through much of the Llandovery. Despite this, as the Hirnantian glaciation is missed by the model, such cooler conditions, as well as increasing temperature and pCO_2 associated with the recovery are not represented.

Conversely, it can be argued that despite this, the long term cooling trend of the Early Palaeozoic is well represented, and capturing such long term variation is the major aim of the model.

The physical mechanisms by which vascular plants enhance weathering rates have been explained previously in Section 3.3. The result of this dramatic enhancement of global rock weathering is a major drawdown in atmospheric CO_2 (Berner, 1997; 1998; Algeo and Scheckler, 1998; Lenton, 2001). This is well-represented in the updated COPSE model, with mean pCO_2 falling from ~8PAL to a minimum of ~3PAL by ~340Ma. These values are consistent with published estimates derived from the carbon isotope record (i.e. Mora et al., 1991; 1996; Yapp and Poths, 1992; 1996), which range from 3-5PAL for the Late-Devonian/Early-Carboniferous.

Such cooling is predicted by the updated COPSE model in tandem with the drop in pCO_2, with mean global temperatures falling from ~18^0C to ~13^0C by ~340Ma. This is consistent with an observed $\delta^{18}O$ shift from -5‰ to -1‰ at the Devonian/Carboniferous boundary, attributed to the growth of continental ice sheets (Crowley and Baum, 1991) and the cooling of tropical surface waters (Veizer et al., 1986) during the onset of the Permo-Carboniferous glaciation (i.e. Veevers and Powell, 1987; Crowley and Baum, 1992; Isbell et al., 2003;

Scheffler et al., 2003; Poulsen et al., 2007; Fielding et al., 2008; Frank et al., 2008; Royer, 2014).

The Permo-Carboniferous glaciation, the most prevalent icehouse in the Phanerozoic (Scheffler et al., 2003), is generally considered to have lasted from ~340-260Ma (Veevers and Powell, 1987; Frank et al., 2008; Royer, 2014), although the exact time and extent is debated (Poulsen et al., 2007; Frank et al., 2008). Moreover, the conventional view that the Permo-Carboniferous was a single long, protracted event has been challenged in recent research that argues for a series of shorter, 1-8Myr discrete glacial events (Isbell et al., 2003; Fielding et al., 2008) separated by periods of warmer climate.

The end-result is a major icehouse interval. A minimum in both temperature and pCO_2 is predicted by the updated COPSE model at ~340Ma, after which there is a gradual rise to 300Ma, before a rapid increase in both temperature and pCO_2 by ~290Ma. This is consistent with Last Glacial Maximum sized ice sheets in the Serpukhovian (Barham et al., 2012) and the associated positive $\delta^{18}O$ trend, with the mean predicted pCO_2 agreeing well with published estimates of 2-3PAL (Rothman, 2002). Whilst some argue for atmospheric CO_2 levels as low as 0.7-2.0PAL (Crowley and Berner, 2001), once glacial conditions had been established, it is argued that large ice sheets could be maintained up to 4-6PAL, with the latter in the case of low obliquity (Zhuang et al., 2014), as a result of the non-linear land/ice albedo feedback (North, 1984; Baum and Crowley, 1991).

Despite such consistencies with published data, the modelled length of the Permo-Carboniferous glaciation is much shorter than many estimates, with evidence of major ice sheets existing to at least 290Ma (Isbell et al., 2003; Fielding et al., 2008), and a permanent ice-free world argued un-established until 260Ma (Jones and Fielding, 2004). This is observed in COPSE original whereby a post-glacial peak in temperature occurs at ~250Ma, however Figure 7.3 shows that the updated model underestimates the length of this icehouse interval.

The model may predict such a short icehouse period for a variety of reasons. Firstly, the average latitude of continental flood basalts rises above 30^0 at ~290Ma (Figure 6.8), thus resulting in the decline in basaltic weathering seen in

Figure 7.6. In addition, total basaltic area is falling through this interval, with only minor LIPs, the Tarim Block, Qiantang Panjal and Himalaya-Neotethys, emplaced at 280Ma, such that the fraction of volcanic rocks (xvolc) remains low through the Permian (Figure 7.7). Moreover, the continental configuration of the Permian was characterised by the Pangaea supercontinent stretching from almost pole-to-pole (i.e. Gibbs et al., 2002; Schneebeli-Hermann, 2012). This landmass was characterised by high aridity, and thus low weathering rates, in the continental interior, therefore suggesting silicate weathering rates may have decreased, contributing to increasing atmospheric pCO_2.

However, as observed in Figure 7.6, although basalt weathering decreases, the granitic weathering component of the global silicate weathering flux increases, causing a global increase in silicate weathering through the Early-Permian. Therefore, an alternative driver is required.

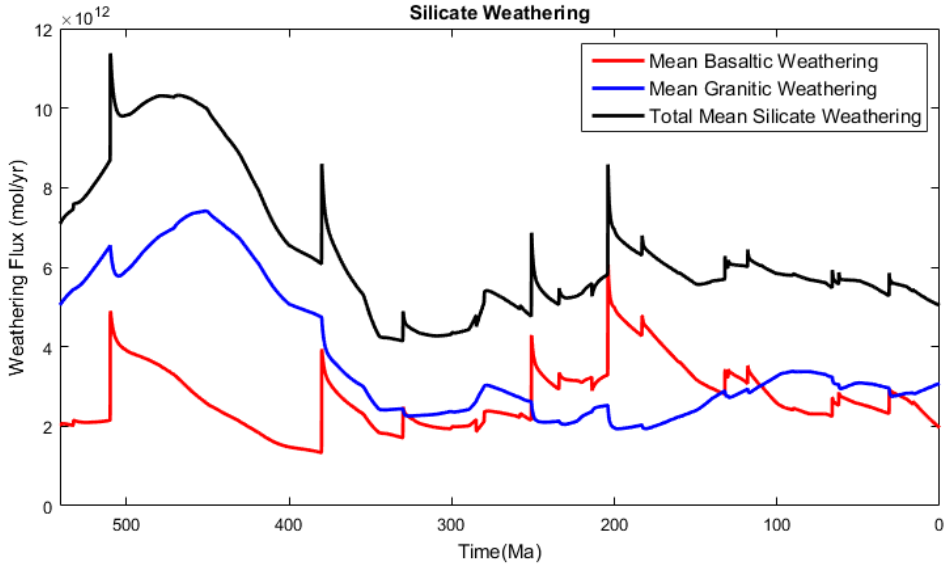

Figure 7.6. Mean Phanerozoic predictions of the basaltic and granitic weathering fluxes, as well as the total silicate weathering flux, following a Monte Carlo simulation of 100 runs.

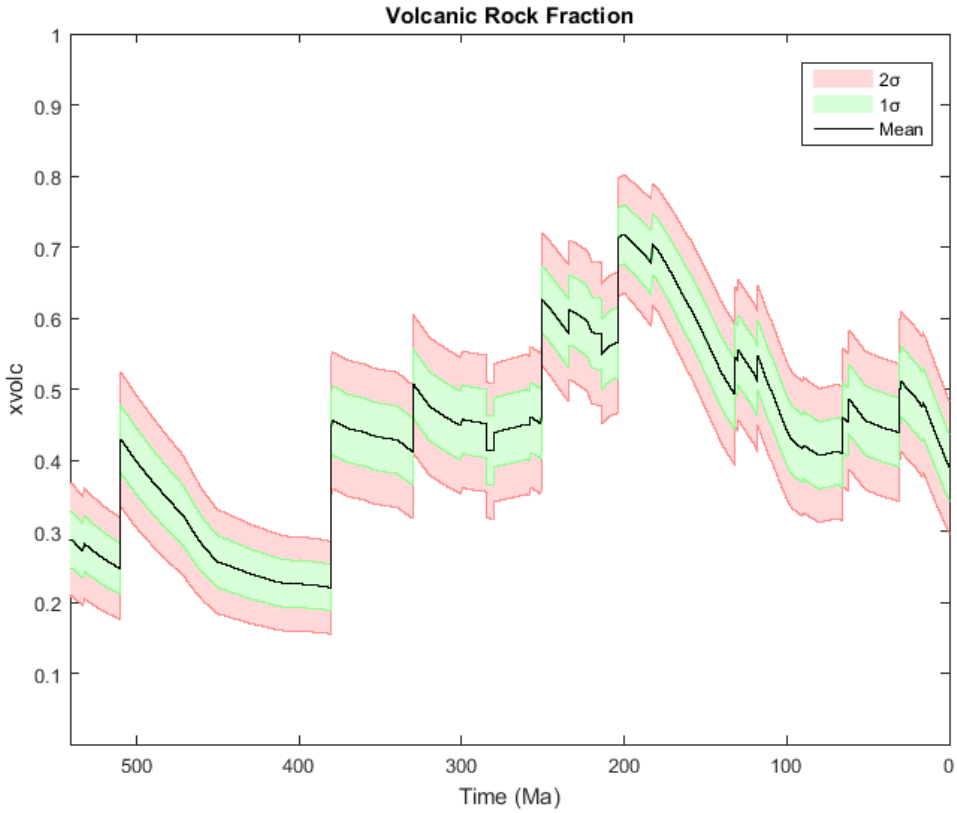

Figure 7.7. Phanerozoic fraction of volcanic rock (xvolc) prediction of the updated COPSE model, following a Monte Carlo simulation of 100 runs. The error range is denoted as ±1 and ±2 standard deviations (σ) from the mean.

First and foremost, the updated degassing and uplift forcings (Figure 6.11) show an increase in volcanic outgassing from ~300Ma, with uplift falling to reach a minimum at the End-Permian/Early-Triassic. Consequently, whilst likely unable to explain all of the anomalous temperature increase, it is likely that an increased flux of CO_2 to the atmosphere combined with a reduction in the silicate weathering flux as a function of reduced uplift certainly played a role to some extent.

A sea-level low stand associated with the Permo-Carboniferous glacial maximum may have increased the exposure of CO_2-fixing carbonate-complexes to carbonate weathering (Scheffler et al., 2003), thus increasing atmospheric pCO_2. This is consistent with model predictions of a slight increase in carbonate weathering during the Early-Permian (Figure 7.8), although carbonate weathering is argued to have little effect on atmospheric CO_2 concentrations (Berner, 2004a).

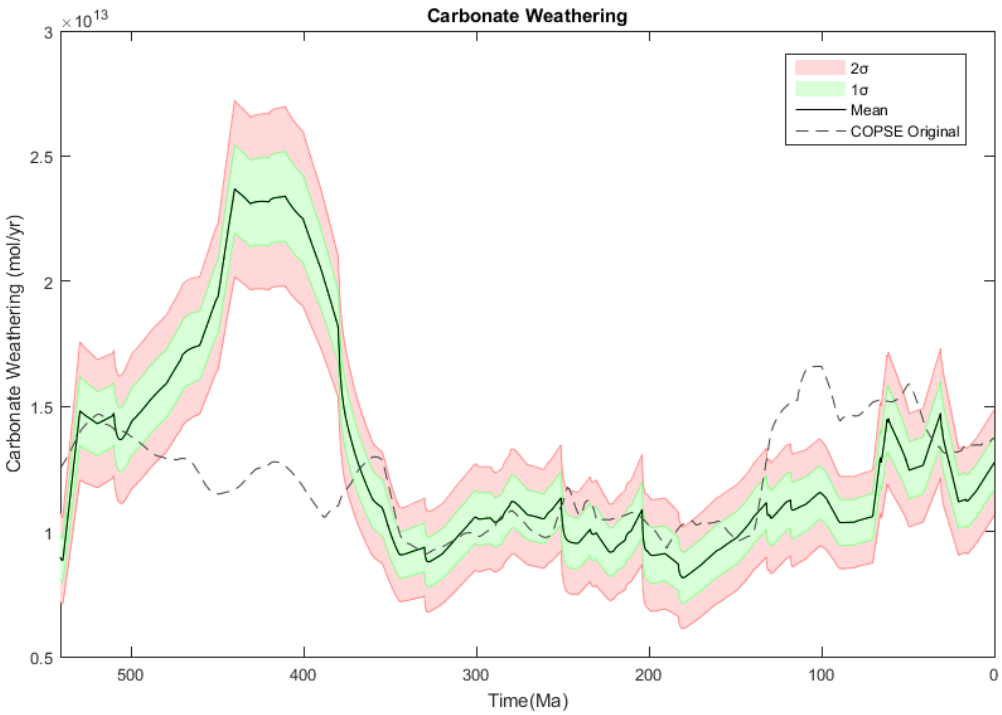

Figure 7.8. Phanerozoic carbonate weathering prediction of the updated COPSE model compared to COPSE Original (Bergman et al., 2004), following a Monte Carlo simulation of 100 runs. The error range is denoted as ±1 and ±2 standard deviations (σ) from the mean.

As seen in Figure 7.9, potentially the major factor causing such an early and dramatic rise in both pCO_2 and temperature is a large, steep fall in organic carbon burial. This is as a result of a reduction in the C:P burial ratio from 2000 to 1000, included within the COPSE Model to account for the evolution of lignin-degrading fungi (i.e. Robinson, 1990). As a consequence, a given flux of phosphorus weathering now supports less organic carbon burial (Lenton et al., in press), such that less carbon is removed from the atmosphere-ocean system, resulting in an increase in atmospheric pCO_2 and thus global temperature.

In reality, as is further discussed in the following section, recent research (Nelsen et al.,2016) argues that the evolution of lignolysis occurred much earlier than previously thought, and played much less of a role regarding organic carbon burial and atmospheric O_2 than has been suggested, with the unique climate of the Carboniferous promoting an abundance of coal swamps. As a consequence, the updated model can be further improved by revising trends in the C:P burial ratio of plant biomass over the Phanerozoic, and accounting for this in the model.

Despite concerns over the modelled length of the Permo-Carboniferous glaciation, there have been suggestions for an early deglaciation (Horton et al., 2012), beginning during the Late-Carboniferous (Montanez et al., 2007), with a rapid rise in pCO_2 to as high as 13PAL by the late Early-Permian. Such a rise in pCO_2 has been ascribed by various studies as a cause, at least in part, of the deglaciation (i.e. Crowley and Baum, 1992; Berner, 1994).

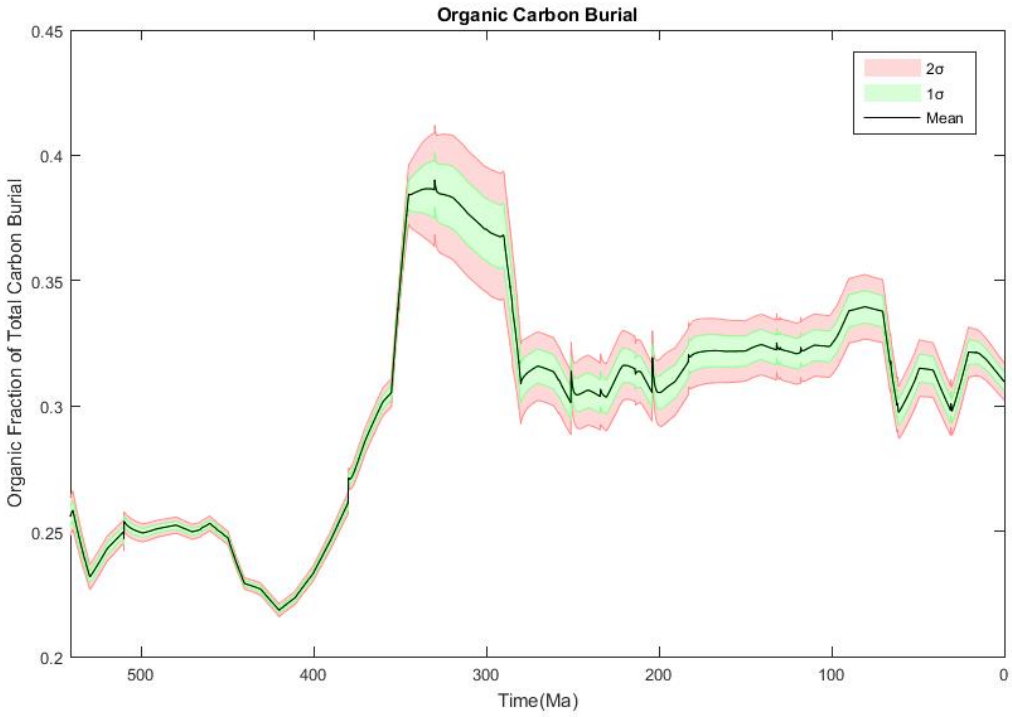

Figure 7.9. Phanerozoic organic carbon burial prediction of the updated COPSE model following a Monte Carlo simulation of 100 runs, represented as a fraction of total carbon burial. The error range is denoted as ±1 and ±2 standard deviations (σ) from the mean.

An increase in pCO_2 to 13PAL is greater than the model predictions, in which ~11PAL is the maximum value for the Permian. However, it is argued that deglaciation was maintained above 4PAL (Gibbs et al., 2002), and Permian pCO_2 was likely less than 10PAL (Poulsen et al., 2007), which is extremely consistent with the modelled pCO_2. Moreover, whilst this is much higher than the proxy estimates, Late-Palaeozoic pCO_2 estimates have an uncertainty of ±1200ppm (Montanez et al., 2007) and there is one data point of Royer et al (2014) that shows good correlation with the mean predicted curve.

Additionally, the modelled mean temperature increase of ~6-7^{0}C shows similarity with modelled deglaciation of a medium-sized ice sheet (Poulsen et al., 2007), the most consistent ice sheet size with geological data, as well as

with suggestions for a major post-glacial climate warming (Ziegler et al., 1997). Whilst the modelled temperature rises above that predicted by Poulsen et al (2007), Roscher et al (2011) argue for a minimum global average temperature of 18.2^{0}C as a threshold for a greenhouse/icehouse transition in the Late-Permian. The Late-Permian is widely recognised as a greenhouse climate, with reports of boreal forests in Antarctica (Taylor et al., 1992; Cuneo, 1996) and a lack of evidence for polar climates (Chumakov and Zharkov, 2003). As such, the modelled mean global average temperature of greater than 18.2^{0}C is thus consistent with this implication, with only the minimum predicted values reaching this threshold.

Such high temperatures are consistent with both negative shifts in the $\delta^{18}O$ and $\delta^{13}C_{carb}$ records (i.e. Kearsey et al., 2009; Shen et al., 2011; Joachimski et al., 2012), the implication of which is a ~6-10^{0}C rise in tropical SSTs and reduced SST gradients associated with significant temperature increases in high latitude sea surface water masses (Kiehl and Shields, 2005; Schneebeli-Hermann, 2012).

The Permian-Triassic boundary is characterised by the largest biological extinction event in Earth history (i.e. Erwin, 1994; Joachimski et al., 2012; Clarkson et al., 2015), in which 80-95% species became extinct (Benton et al., 2004) over a 200-700kyr interval (Huang et al., 2011; Shen et al., 2011). The cause of this extinction is debated, with Siberian Traps volcanism (i.e. Renne et al., 1995; Sun et al., 2012), ocean anoxia (Wignall and Hallam, 1992), and oceanic H_2S degassing (Kump et al., 2005) all postulated.

Climate warming is largely implicated as a cause (Kidder and Worsley, 2004), consistent with a shift in $\delta^{18}O$ (Sun et al., 2012). The updated COPSE model predicts high temperatures of 18.5-23^{0}C, and high pCO_2 levels of ~5-11PAL at the start of this interval, consistent with such implications.

The Siberian Traps LIP was emplaced at ~251Ma (Bowring et al., 1998), and the consequent CO_2 release has been attributed as major cause of the increased temperature during the End-Permian extinction (Sun et al., 2012). Degassing from LIP volcanism is not represented in the updated baseline model, however Mills et al (2014b) argue that such degassing does not significantly alter model predictions, resulting in only an ephemeral spike in

pCO_2 and temperature. The main result of the emplacement of the Siberian Traps is a fall in both pCO_2 and global temperature, given the increased basalt area and thus weathering (Romano et al., 2013).

The fall of pCO_2 by 2PAL and temperature by 2^0C is largely moderated by the fact that given the size of the Siberian Traps, its emplacement at a high latitude causes the mean latitude of LIP basalt to be assigned to the least weatherable 'band'. Consequently, whilst basalt weathering increases following its emplacement, the weatherability multiplier is reduced, offsetting, to an extent, this increase.

The updated COPSE model shows an increase in both temperature and pCO_2 through the Triassic, following a decline in basaltic weathering following the initial emplacement of the Siberian Traps, as seen in Figures 7.6 and 7.7. This is consistent, to an extent, with permanent water temperatures of $18\text{-}34^0C$, as estimated from $\delta^{18}O$ data (Korte et al., 2005). The Triassic/Jurassic boundary is argued to be characterised by a 4PAL increase in pCO_2, alongside a $3\text{-}4^0C$ global temperature increase (McElwain et al., 1999). Whilst the model doesn't predict such a rapid increase, the 2PAL/3^0C increase over the course of the Triassic shows some similarity to this estimate.

Similarly to the End-Permian, an extinction event occurred at the Triassic/Jurassic boundary (Belcher et al., 2010), with extensive volcanism associated with the break-up of Pangaea producing the Central Atlantic Magmatic Province (CAMP), the largest LIP of the Phanerozoic (Marzoli et al., 1999). As with the emplacement of the Siberian Traps, CAMP is argued to have initiated a 'super-greenhouse'. Whilst it can be argued that the updated model misses such a temperature/pCO_2 increase due to the non-consideration of LIP volcanism, when such degassing is considered the consideration of the weathering of basalts partially nullifies the pCO_2 rise, eventually bringing pCO_2 to a steady state lower than pre-CAMP levels (Mills et al., 2014b). Consequently, the long-term climate dynamics are well represented by a fall in pCO_2 by ~2.5-3.0PAL to ~4.0PAL, consistent with both the proxy data of Park and Royer (2011) and Royer et al (2014), as well as the model prediction of COPSE original. In tandem, global temperature falls by ~3^0C to ~$17.5\text{-}18.0^0C$.

Through the Jurassic, the updated model shows excellent agreement with both COPSE original and the CO_2 proxy data. Following Figure 7.7, intense LIP volcanism maintains pCO_2 and temperature at relatively constant levels (Dera et al., 2011). A discrepancy between COPSE original and the updated model occurs during the Cretaceous, whereby COPSE original predicts a ~2.5-3.0^{0}C increase in global temperature. This is likely as a result of the non-consideration of volcanic rock weathering – including such weathering has been seen to reduce Mesozoic pCO_2 and temperature in the GEOCARB model (Berner, 2006b), consistent with the updated COPSE model of this study.

The Eocene peak in temperature and pCO_2 (Royer, 2014), as seen in the proxy data (Park and Royer, 2011), is missed by the updated model, however the long term predicted pCO_2 trend bisects the proxy data during the Cenozoic, showing better agreement than COPSE original, and so it is argued that the long-term trend of this period is well-represented.

7.1.2. Atmospheric O_2

Whilst there is clear disagreement between model predictions of Phanerozoic atmospheric O_2, especially for the Early-Palaeozoic and Mesozoic (i.e. Berner and Canfield, 1989; Bergman et al., 2004; Arvidson et al., 2006; Berner, 2006a; 2009; Berner et al., 2007; Poulsen et al., 2015), it is argued that the predictions of atmospheric O_2 from COPSE are a major strength of the model.

The updated model curve, displayed in Figure 7.10, shows a long-term similarity with COPSE original, although there are key differences, notably a roughly doubling of Early-Palaeozoic atmospheric O_2, an increased Carboniferous O_2 maximum, with increased pO_2 over the Late-Palaeozoic and Early-Mesozoic, as well as reduced pO_2 over the Late-Mesozoic and Cenozoic.

Generally, Early-Palaeozoic atmospheric O_2 content is reconstructed with values well below 1PAL (Munnecke et al., 2010), although there is large variation within the published literature (i.e. Berner, 1999; Berner et al., 2004a; Algeo and Ingall, 2007). Both the updated COPSE model and COPSE original predict values greater than the 0.1PAL argued to be required for the survival of Cambrian fauna (Holland, 1984), however the updated COPSE model predicts

a higher atmospheric O_2 content than COPSE original throughout the Early-Palaeozoic, reaching ~0.5-0.6PAL compared to the 0.25PAL projected by COPSE original (Bergman et al., 2004).

This is likely due to the updated degassing forcing. The Ordovician was characterised by degassing levels ~2.2 times those of the present (Sheehan, 2001; Mills et al., in preparation). Increased CO_2 inputs from enhanced degassing results in an increase in silicate and phosphorus weathering fluxes. Such an increase in the phosphorus weathering flux in turn causes enhanced marine productivity and so organic carbon burial, therefore increasing pO_2 (Bergman et al., 2004).

In addition, the updated COPSE model is characterised by a sustained high level of pyrite burial through the Early-Palaeozoic as seen in Figure 7.11, also acting as to increase pO_2, consistent with the data of Prokoph et al (2008).

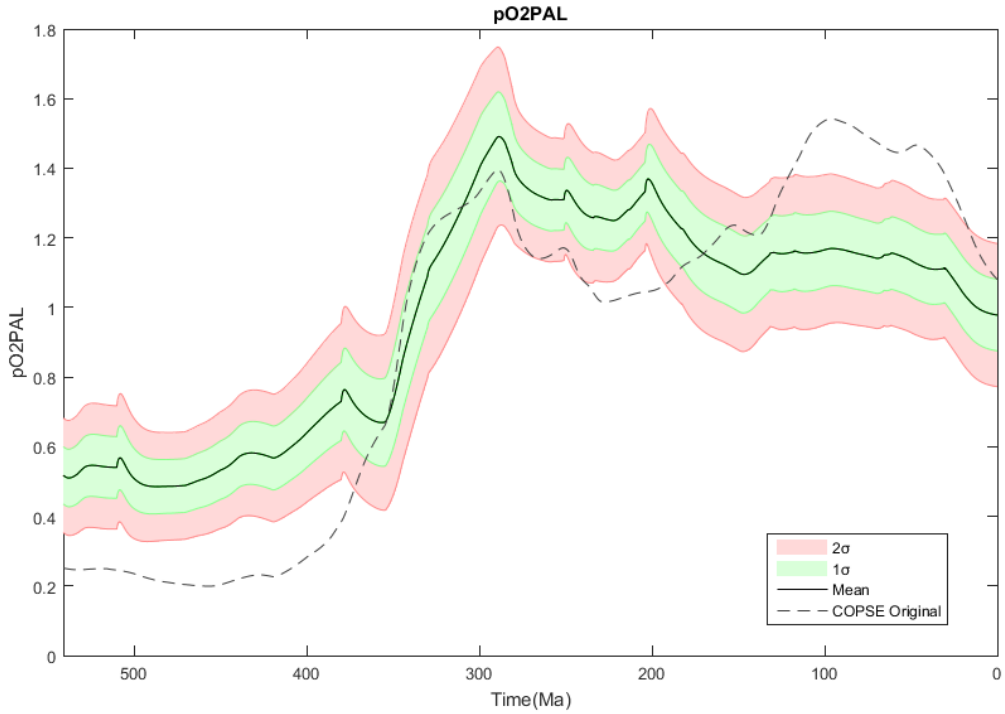

Figure 7.10. Phanerozoic pO_2 prediction of the updated COPSE model compared to COPSE Original (Bergman et al., 2004), following a Monte Carlo simulation of 100 runs. The error range is denoted as ±1 and ±2 standard deviations (σ) from the mean.

Since COPSE original, many studies have argued for an increase in Early-Palaeozoic pO_2 (i.e. Yan et al., 2009; 2012; Lenton et al., in press). This has been evidenced by a high abundance of organic carbon beneath Hirnantian horizons, pointing to enhanced organic carbon burial (Yan et al., 2009), Molybdenum-isotope data indicating oxygenation of the deep ocean (Dahl et al., 2010), and fossil charcoal suggesting atmospheric O_2 concentrations >15-17% between 420 and 400Ma (Glasspool et al., 2004; Scott and Glasspool, 2006).

Lenton et al (in press) attribute this oxygenation to early plants, arguing that a high coverage of cryptogamic vegetation (Porada et al., 2014) with a much higher C:P burial ratio than marine biomass acted to enhance the phosphorus weathering flux, which could support increased organic carbon burial due to the greater C:P ratio of the cryptogamic biomass. The plant forcings of Lenton et al (in press) are not included in the baseline model, which may offer an explanation as to why pO_2 remains less than that indicated by fossil charcoal in the Silurian.

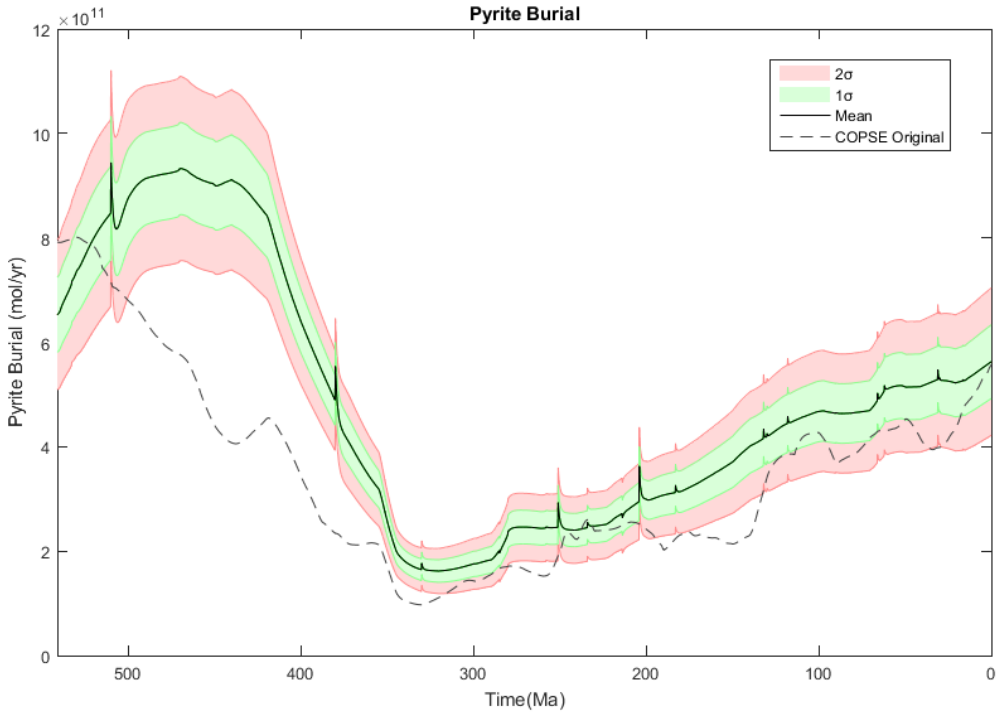

Figure 7.11. Phanerozoic pyrite burial prediction of the updated COPSE model compared to COPSE Original (Bergman et al., 2004), following a Monte Carlo simulation of 100 runs. The error range is denoted as ±1 and ±2 standard deviations (σ) from the mean.

Despite this, it is argued that for the Early-Palaeozoic, the updated COPSE model is much more consistent with current research than COPSE original. Moreover, other than COPSE, biogeochemical models are generally characterised by Early-Palaeozoic pO_2 levels approaching, or greater than, 1PAL (i.e. Berner and Canfield, 1989; Berner, 1999; Berner and Kothavala, 2001; Arvidson et al., 2006; Algeo and Ingall, 2007), as displayed in Figure 7.12. This lies far above the range indicated by geologic and proxy data (i.e. Dahl et al., 2010). Consequently, not only is the updated COPSE model an improvement over the original COPSE model with regards to atmospheric O_2 for this interval, it also offers a much more realistic prediction than alternative biogeochemical models.

A common prediction from biogeochemical models of the Phanerozoic is a dramatic increase in atmospheric O_2 in the Mid-Late Palaeozoic, between 400-300Ma, with the highest atmospheric O_2 concentrations in Earth history characterising the Carboniferous (i.e. Robinson, 1990; Lenton, 2001; Nelsen et al., 2016).

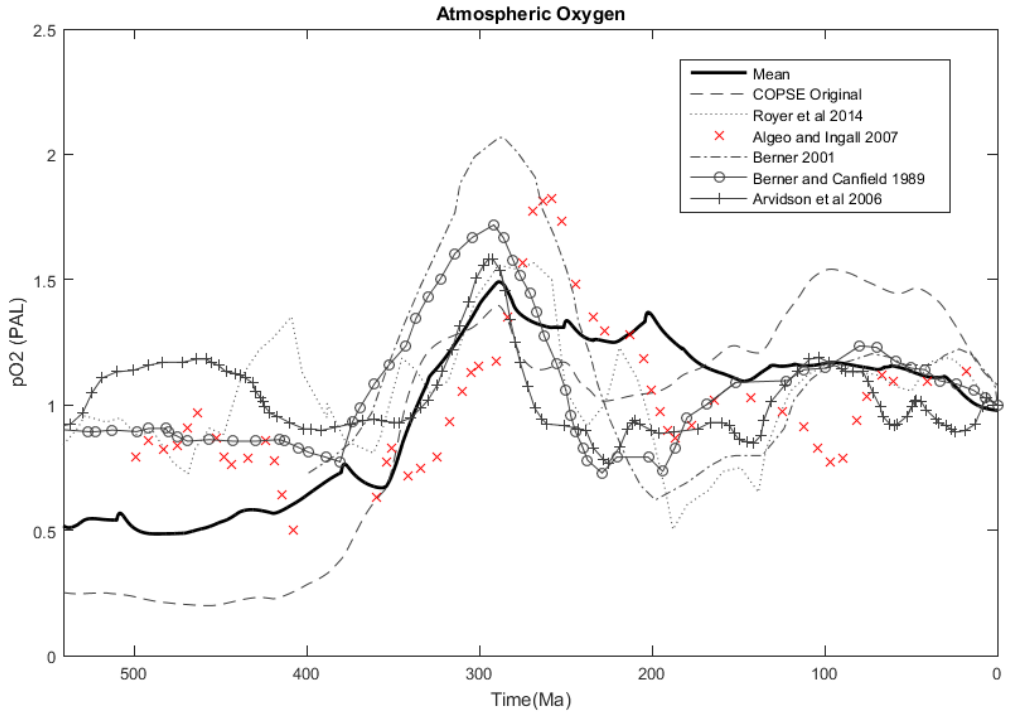

Figure 7.12. Mean Phanerozoic pO_2 prediction of the updated COPSE model compared to various biogeochemical modelling studies and the proxy data of Algeo and Ingall (2007), following a Monte Carlo simulation of 100 runs.

The major long term source of atmospheric O_2 in the Phanerozoic is organic carbon burial (i.e. Berner, 1997; 1998; 2004a), and as such the evolution of vascular land plants is arguably the most dominant factor affecting Phanerozoic pO_2. Not only do plants enhance phosphorus weathering, and thus increase organic carbon burial through enhanced marine productivity (Lenton, 2001), they also provide a supply of lignin-rich organic material to the terrestrial biosphere (i.e. Robinson, 1990; Berner et al., 2007). The Late Devonian and Carboniferous saw the highest rates of organic carbon burial in the Phanerozoic, reaching up to $6.5*10^{18}$ mol yr^{-1} (Montanez, 2016).

As only organic carbon that reaches burial is considered an O_2 source (Robinson, 1990), the traditional hypothesis explaining the dramatic rise in organic carbon burial through the Devonian and Carboniferous is based on an evolutionary gap between biodegradation-resistant lignin and lignolytic fungi (i.e. Robinson, 1990; Cleal and Thomas, 2005; Berner et al., 2007; Raven and Andrews, 2010). This is suggested to have resulted in a period when vast amount of lignin-rich plant material accumulated, as evidence by vast coal deposits (Berner, 1998), thus enhancing organic carbon burial and so increasing pO_2. Over time, through evolution, lignin production would then be reduced as taxa that can achieve equal strength and tissue development without investment in lignin have an energy advantage over their competitors, resulting in a decline in lignin through the Mesozoic (Robinson, 1990).

On the other hand, recent research argues that lignolytic fungi may have been present pre-Carboniferous, and that Palaeozoic coal abundance is as a function of a unique combination of ever wet tropical conditions and extensive depositional systems associated with the assembly of the Pangaea supercontinent. (Nelsen et al., 2016). Therefore, the expansion and radiation of extensive wetland forests in the tropics (Cleal and Thomas, 2005; Montanez, 2016) introduced a vast supply of organic material to the terrestrial realm, that was resistant to degradation due to the reduction of decay in the anoxic wetland environment (i.e. Moore, 1989).

Regardless of the precise cause of such an increase in organic carbon burial, there is a general agreement that pO_2 peaked during the Carboniferous. Fossil charcoal, dating as far back as the Silurian (Scott and Glasspool, 2006), provides evidence for wildfires, and thus an atmospheric O_2 content of >15%

(i.e. Rowe and Jones, 2000; Cressler, 2001; Lenton, 2001; Belcher and McElwain, 2008).

The updated model results are consistent with these interpretations. A pronounced rise in mean pO_2 is observed following the rise of vascular plants from ~0.7PAL to ~1.5PAL. This maxima is greater than that predicted by COPSE original, however it remains less than all other biogeochemical model predictions displayed in Figure 7.12. Such modelling indicates atmospheric O_2 may have increased to levels of 35% (i.e. Berner and Kothavala, 2001), however such high concentrations do not agree with the known existence of forests (Lenton, 2001). Increased atmospheric O_2 results in an increase in both the frequency and intensity of vegetation fires (i.e. Belcher and McElwain, 2008), thus reducing biomass and resulting in a shift to faster regenerating ecosystems (Lenton, 2001). As a consequence, it is argued that the updated COPSE model offers a better prediction of the Carboniferous pO_2 maxima than other biogeochemical models.

Following the Carboniferous pO_2 peak, biogeochemical models generally show a rapid decline in pO_2, as displayed in Figure 7.12. On the contrary, the updated COPSE model shows a minor decline through the Late-Palaeozoic and Mesozoic, with minor peaks at the Permian-Triassic boundary and the Triassic-Jurassic boundary, with pO_2 levels remaining consistently higher than other predictions.

This is consistent with fossil insect wing lengths. Increased pO_2 profoundly affected evolution (Royer, 2014), with the most pronounced interval of insect gigantism coinciding with the Carboniferous pO_2 peak (i.e. Graham et al., 1995; Berner et al., 2003; 2007; Clapham and Karr, 2012). During this interval insects were up to 10 times the size of similar extant groups (Royer, 2014), with wing spans up to 70cm (Graham et al., 1995; Dudley, 1998; Clapham and Karr, 2012).

Such insect gigantism is linked to hyperoxic conditions as O_2 concentration is a key physiological control on body size (i.e. Kaiser et al., 2007), particularly for groups like flying insects that have high metabolic O_2 demands (Clapham and Karr, 2012). Therefore, hyperoxia results in increased body size, and hypoxia

results in a reduced body size (i.e. Frazier et al., 2001), allowing fossil insect wing lengths to act as a proxy for atmospheric O_2 (Clapham and Karr, 2012).

When compared to the GEOCARBSULF model (Berner, 2006a; 2009), Clapham and Karr (2012) argue that insect size must have decoupled from O_2 concentration through the Jurassic and Cretaceous given that predicted O_2 concentration falls during this interval yet wing lengths increase, as shown in Figure 7.13. Dorrington (2012) scrutinises the hypotheses relating to alternative controls on body size put forward to explain this by Clapham and Karr (2012).

The updated COPSE model prediction provides a mean pO_2 curve that is much more consistent with the wing length data. There is no dramatic decline in Mesozoic pO_2, the secondary peak at ~200Ma is consistent with the increase in wing length during the Mid-Mesozoic, as is the gradual decline in pO_2 through the Late-Mesozoic and Cenozoic. Moreover, the secondary peak in pO_2 at the Triassic/Jurassic boundary is also consistent with suggestions with increased fire activity (Belcher et al., 2010; van de Schootbrugge, 2010), as evidenced by a dramatic increase in fossil charcoal in the Early-Jurassic (Belcher et al., 2010).

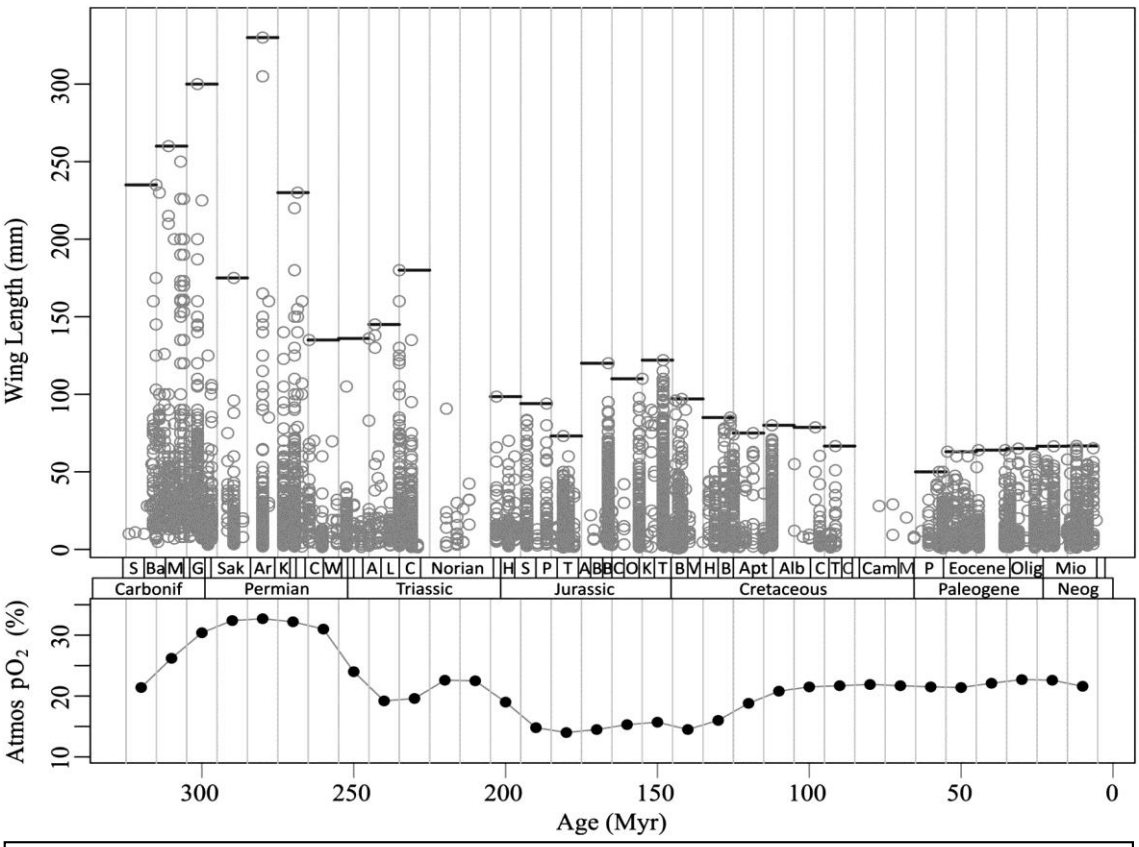

Figure 7.13. Phanerozoic trends in insect wing length compared to the pO_2 prediction of the GECARBSULF biogeochemical model (Berner, 2006a; 2009), taken from Clapham and Karr (2012).

Over the last ~150Ma, the updated COPSE model shows good agreement with other biogeochemical models, with predictions generally falling within two standard deviations of the mean, except for COPSE original which is characterised by a Cretaceous peak in pO_2 to levels greater than its prediction for the Carboniferous (Bergman et al., 2004). This is attributed to high degassing and the rise of angiosperms, which acted against the negative feedback loop associated with increased pO_2 suppressing vegetation biomass and thus weathering (Bergman et al., 2004). However, it is unlikely that the Late-Mesozoic/Cenozoic saw pO_2 reaching similar or greater levels than the Carboniferous peak as the unique climatic conditions of the Carboniferous (Nelsen et al., 2016) were no longer prevalent by the Cretaceous, and as discussed, over time lignin production declined, and the abundance of lignolytic organisms increased (Robinson, 1990), reducing organic carbon burial. In addition, the updated degassing forcing predicts reduced Cretaceous degassing compared to that of COPSE original, further suggesting the Mesozoic O_2 peak of the original COPSE model may be an overestimate.

As a consequence, the much lower organic carbon burial and reduced degassing, and thus the much lower pO_2 predicted by the updated COPSE model, offers a significant improvement over that of COPSE original, and brings the Late-Mesozoic/Cenozoic predictions in line with other biogeochemical models, although there remains considerable differences between models for this period (Berner, 2006a; Berner et al., 2007).

In summary, it is argued that the updated COPSE model offers a much improved pO_2 prediction for the entire Phanerozoic. Early-Palaeozoic pO_2 is greater than COPSE original, consistent with recent research, yet within the range indicated by proxy and geologic data, unlike other modelling studies. Similarly, a minor increase in pO_2 above COPSE original is observed at the Carboniferous maximum whilst remaining below the overestimates of alternative models. The Mesozoic prediction is consistent with both fossil wing length and charcoal proxy data, with a gradual decline to present levels through the Cenozoic consistent with other models and avoiding the issue of increased pO_2 through this interval that characterised COPSE original.

7.1.3. $^{87}Sr/^{86}Sr$

7.1.3.1. Long-Term Phanerozoic Trends

The model prediction, displayed in Figure 7.14, shows general agreement with the long-term trend of the LOWESS curve (McArthur et al., 2012), although clear differences exist, notably the consistently raised values from the Ordovician through Devonian, the modelled upward spike between ~300-250Ma, as well as the consistently heavier values from ~170-30Ma.

The long-term $^{87}Sr/^{86}Sr$ trend predicted by the model however, is argued to be largely successful, with the majority of the LOWESS proxy dataset falling within two standard deviations of the predicted mean curve. This includes excellent agreement from the Mid-Devonian through Carboniferous, the Early to Mid-Mesozoic, and the Mid to Late-Cenozoic. There are four key periods of disagreement between the model and the proxy data, namely the Ordovician, Early-Devonian and Permian minima displayed in the proxy data, as well as the modelled Cretaceous increase.

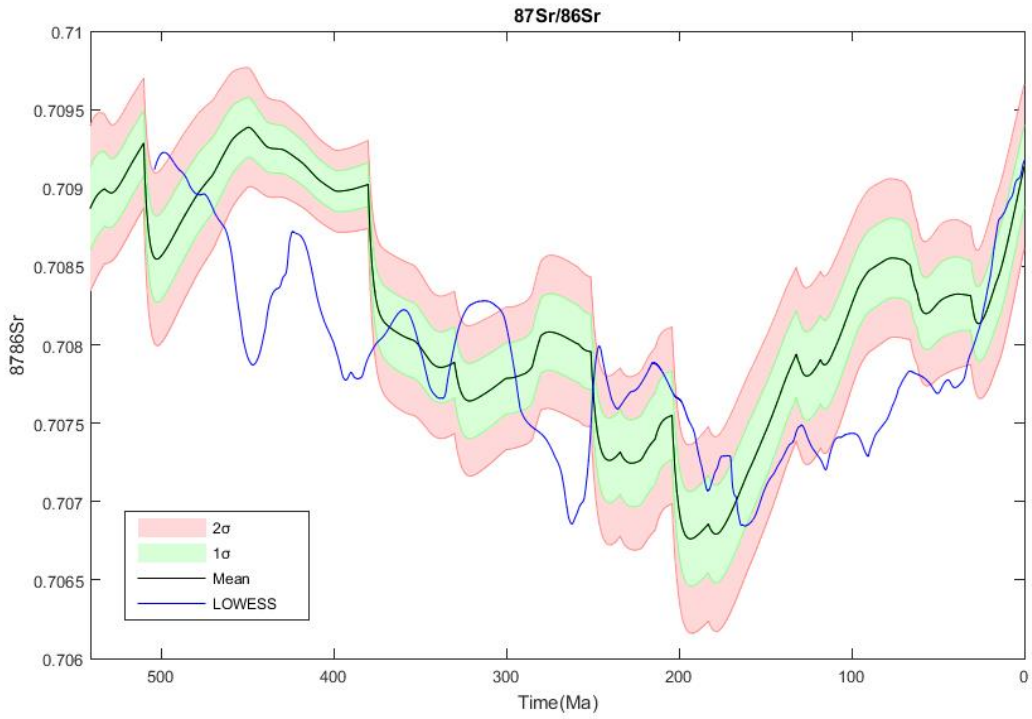

Figure 7.14. Phanerozoic $^{87}Sr/^{86}Sr$ prediction of the updated COPSE model compared to the LOWESS proxy dataset (McArthur et al., 2012), following a Monte Carlo simulation of 100 runs. The error range is denoted as ±1 and ±2 standard deviations (σ) from the mean.

The first three are likely linked to the basalt area forcing. By comparing the modelled strontium isotope curve to the proportion of volcanic rocks through the Phanerozoic, as displayed in Figure 7.15, it is clear that basalt area is a major control on the modelled $^{87}Sr/^{86}Sr$ curve. Clear decreases in $^{87}Sr/^{86}Sr$ accompany the emplacement of major LIPs (i.e. McArthur et al., 2001), notably the Kola-Dnieper and Yakutsk-Vilyui, Siberian Traps and CAMP events. Consequently, the lack of Ordovician, Early-Devonian and Permian LIPs in the model forcing likely explain why the model doesn't follow the proxy data. Despite this, such events are not present in the geologic data and other, unmodelled, factors likely had a role to play, which are discussed in the following section.

During the Cretaceous, the modelled curve lies far above that of the proxy data, argued to be as a result of the non-inclusion of the seafloor weathering flux (i.e. Gillis and Coogan, 2011; Coogan and Gillis, 2013). However, unlike the other periods of disagreement, the modelled curve follows the pattern of the LOWESS data, which provides confidence in the simplified strontium isotope system, even though the precise values show clear disagreement.

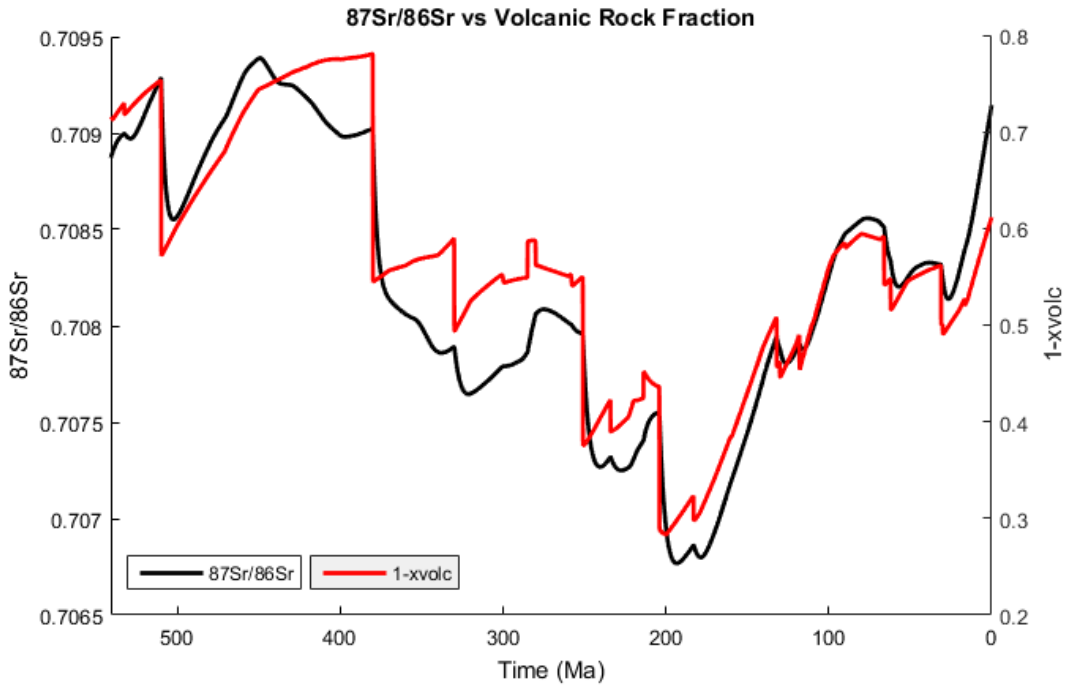

Figure 7.15. Mean Phanerozoic $^{87}Sr/^{86}Sr$ prediction of the updated COPSE model compared to the mean prediction of the volcanic rock fraction (displayed as 1-xvolc to aid comparison)

7.1.3.2. Shorter Term $^{87}Sr/^{86}Sr$ Dynamics

The Cambrian is predicted to be characterised by lower values than the stratigraphic record. Whilst this may be as a result of the model spin-up, the increased proportion of radiogenic Strontium in Cambrian oceans, rising from ~0.70845 (i.e. Derry et al., 1994; Braiser et al., 1996; Nicholas, 1996) to reach a peak of ~0.70910-0.70925 (McArthur et al., 2012), the highest value of the Phanerozoic and potentially of all geologic time (Denison et al., 1998), is argued to be caused by the uplift and weathering of metamorphic rocks formed during the Pan-African Orogeny (Montanez et al., 1996; McArthur et al., 2001; 2012). This orogeny is not well represented in the updated uplift forcing, with the Cambrian characterised by initially very low uplift.

Following the Cambrian, the model predicts a rise to a mean value of ~0.7094, compared to the Early Ordovician value of ~0.7090 (Saltzman et al., 2014), which then falls gradually throughout the Ordovician and Silurian, reaching ~0.7090 by the Early/Mid Devonian. This trend shows clear disagreement with the LOWESS data, maintaining levels close to or greater than both present day and Cambrian values until ~400Ma. Moreover, the shorter term Ordovician fall in $^{87}Sr/^{86}Sr$ is not represented, with the minimum lying far below two standard deviations of the predicted mean.

A gradual fall in the Early-Ordovician (Qing et al., 1998; Shields et al., 2003; Saltzman et al., 2014) is observed in the proxy data, attributed to reduced rates of tectonism during the waning of the Pan-African Orogeny (Qing et al., 1998; Shields et al., 2003), before a rapid fall to minimum values of ~0.7078 (Qing et al., 1998; Young et al., 2009; Saltzman et al., 2014; Edwards et al., 2015). That such a dramatic spike is missed by the model suggests a significant geologic event is not well represented, especially given that the minima coincides with the Hirnantian Glaciation (i.e. Finnegan et al., 2011; Lenton et al., 2012; Melchin et al., 2013). Several hypothesis exist regarding the onset of the Hirnantian Glaciation that may act as to explain the observed decline in $^{87}Sr/^{86}Sr$, and provide insight into why the model overlooks it.

The Ordovician is characterised by extensive mountain building episodes (Kump et al., 1999; Nardin et al., 2011), notably the Taconic Orogeny (Moore and Worsley, 1994; Kump et al., 1999; Ganis and Wise, 2008; Herrmann et al.,

2010) and the larger Caledonian Orogeny (McKerrow et al., 2000), which encompassed the Taconic, Penobscot (i.e. MacDonald et al., 2014) and Finnmarkian (Sturt et al., 1978) orogenies.

The Taconic Orogeny occurred over two phases, the first from 459-450Ma, and the second, main, phase from 450-443Ma (Ganis and Wise, 2008). It has been put forward that this orogenesis may have initiated a long term fall in atmospheric pCO_2 (Kump et al., 1999) through enhanced weatherability of silicate minerals. The tectonic uplift associated with such orogenesis is argued to have enhanced the exposure and erosion of relatively young lithology with non-radiogenic strontium isotope ratios (Young et al., 2009). This peak in uplift, however, is captured by the updated uplift forcing. Despite this, the baseline model run does not link the weathering of flood basalts to uplift. When continental flood basalt weathering is linked to uplift, as displayed in Figure 7.16**,** Ordovician mean $^{87}Sr/^{86}Sr$ falls slightly compared to the updated baseline model run, however the predicted trend remains at much greater values than the LOWESS data, with no downward spike.

Alternatively, an increase in hydrothermal activity would act as to increase the mantle input of non-radiogenic strontium into the ocean (Edwards et al., 2015). Whilst the Early Phanerozoic is characterised by a peak in subduction zone lengths (as seen in the updated degassing forcing), and thus by association seafloor spreading, in the simplified strontium isotope system employed in the baseline model, mantle input remains constant over time.

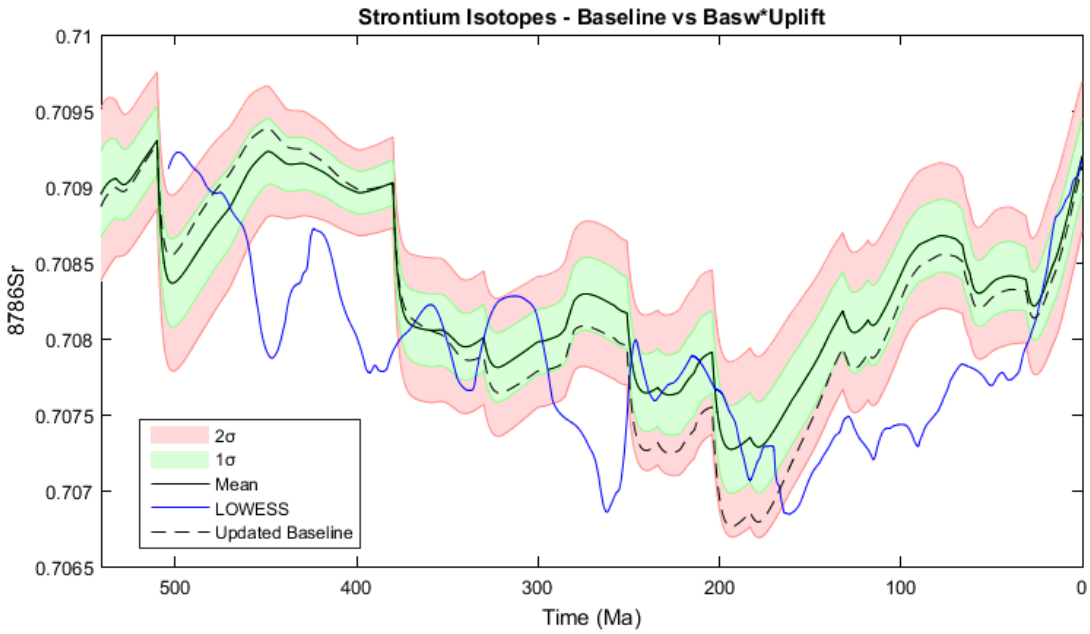

Figure 7.16. Phanerozoic $^{87}Sr/^{86}Sr$ prediction of the updated COPSE model with LIP basaltic area linked to uplift, compared to the updated baseline and LOWESS proxy dataset (McArthur et al., 2012), following a Monte Carlo simulation of 100 runs. The error range is denoted as ±1 and ±2 standard deviations (σ) from the mean.

As such, it is hypothesised that the increasing trend of the predicted curve, compared to the decreasing trend of the LOWESS data, is as a result of the simplified strontium isotope system. The increase in uplift, and hence supply of radiogenic ^{87}Sr, through the Ordovician is not balanced by the increase in degassing, and thus hydrothermal input.

Increasing the complexity of the system such that mantle input is linked to degassing, as in Mills et al (2014b), causes a major fall in the predicted strontium isotope curve, as displayed in Figure 7.17, and when combined with linking uplift to basaltic weathering, the prediction falls below minimum values for the Ordovician (Figure 7.18). Moreover, to retain consistency, should mantle input be linked to degassing, seafloor weathering must be linked to degassing.

These updates invalidate the predicted curve for other periods of the Phanerozoic, and so whilst it can be argued that they better represent reality, it is clear that a simplified approach best captures Early Phanerozoic trends and that updated approaches require multiple additional considerations that may be

beyond the scope of zero-dimensional modelling approaches over such long timescales.

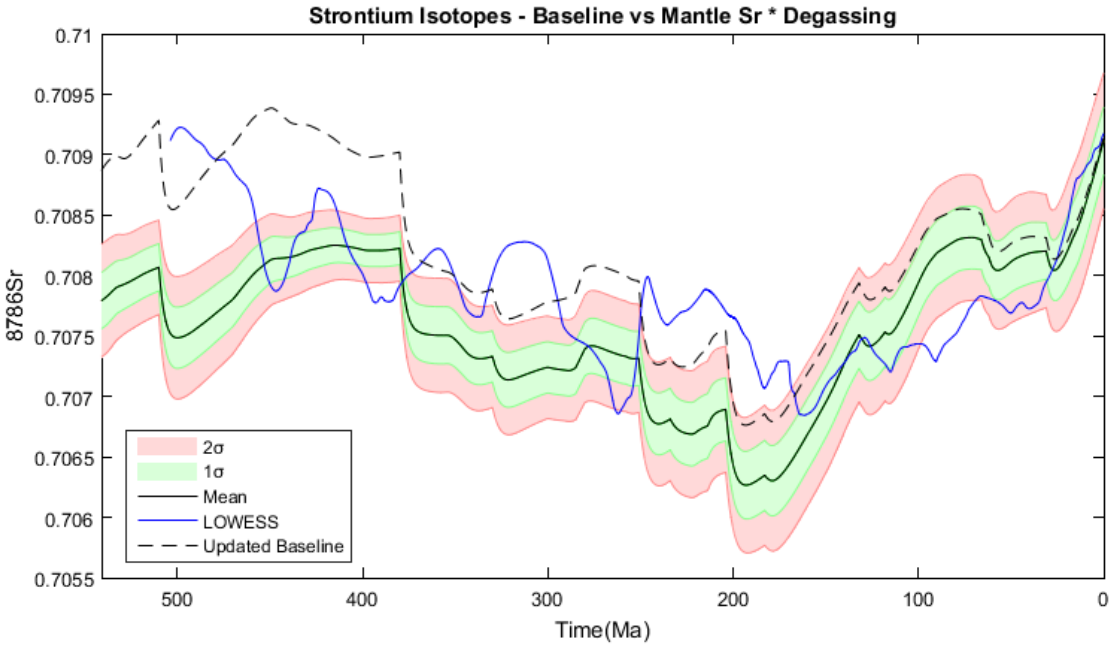

Figure 7.17. Phanerozoic $^{87}Sr/^{86}Sr$ prediction of the updated COPSE model with the mantle strontium flux linked to degassing (seafloor spreading), compared to the updated baseline and LOWESS proxy dataset (McArthur et al., 2012), following a Monte Carlo simulation of 100 runs. The error range is denoted as ±1 and ±2 standard deviations (σ) from the mean.

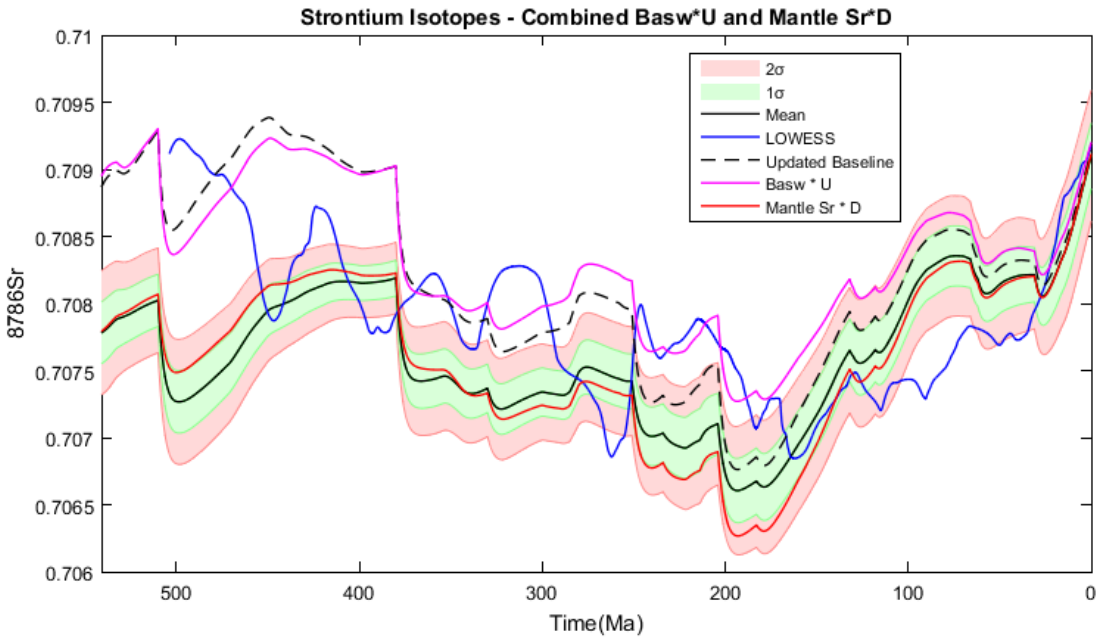

Figure 7.18. Phanerozoic $^{87}Sr/^{86}Sr$ predictions of the updated COPSE model when LIP basalt area is linked to uplift and the mantle strontium flux linked to degassing (seafloor spreading). This is compared to the updated baseline and LOWESS proxy dataset (McArthur et al., 2012), as well as the constituent runs displayed in Figures 7.16 and 7.17, following Monte Carlo simulations of 100 runs. The error range is denoted as ±1 and ±2 standard deviations (σ) from the mean.

Beyond this, recent work has shown that there appears to be a coupling between neodymium and strontium isotopes during the Ordovician (Saltzman, pers. comm.). This coupling rules out a role for an enhanced seafloor hydrothermal flux in causing the Ordovician $^{87}Sr/^{86}Sr$ decline as this flux should not affect neodymium (i.e. Cox et al., 2016).

Consequently, it has been put forward that a peak in volcanic rock abundance could have increased the weathering of basalts (Young et al., 2009), argued to be responsible for an estimated 33% of Ordovician cooling (Nardin et al., 2011). Moreover, it has been hypothesised that a low-latitude mantle superplume (Barnes, 2004; Courtillot and Olsen, 2007; Lefebvre et al., 2010) may have occurred during the Katian.

As the basaltic area forcing is constructed from the LIP record, it may be that due to incomplete preservation, such an LIP is missing from the record. To investigate this, basaltic area is perturbed with a spike in the Ordovician such that the strontium curve is reproduced, as displayed in Figure 7.19**.** However, as no direct geological evidence exists for such an event (Lefebvre et al., 2010), far too large a basaltic area increase is required, totalling 16,116,000km^2, although it could be argued that a smaller province would be required to reproduce the LOWESS curve under a more complex strontium isotope system, as suggested by Figures 7.14 through 7.16. Despite this, it is argued that given far smaller provinces have been preserved, at least to an extent, that should such a province have occurred during the Ordovician, it would not have gone unnoticed in the geologic record.

Nardin et al (2011) attribute the majority of Ordovician climate cooling through enhanced weathering as a result of continental movement through the ITCZ. Through the mapping of LIP latitude, it is indeed clear that the majority of basaltic rock was located in the tropics and sub-tropics during the Ordovician.

However as the weathering of basalts is linked to this, at least on a first-order level, the downward spike in $^{87}Sr/^{86}Sr$ is therefore assumed not to be solely as a result of plate movement, although the enhancement of basaltic weathering as a function of LIP latitude during this period acts as to reduce mean $^{87}Sr/^{86}Sr$.

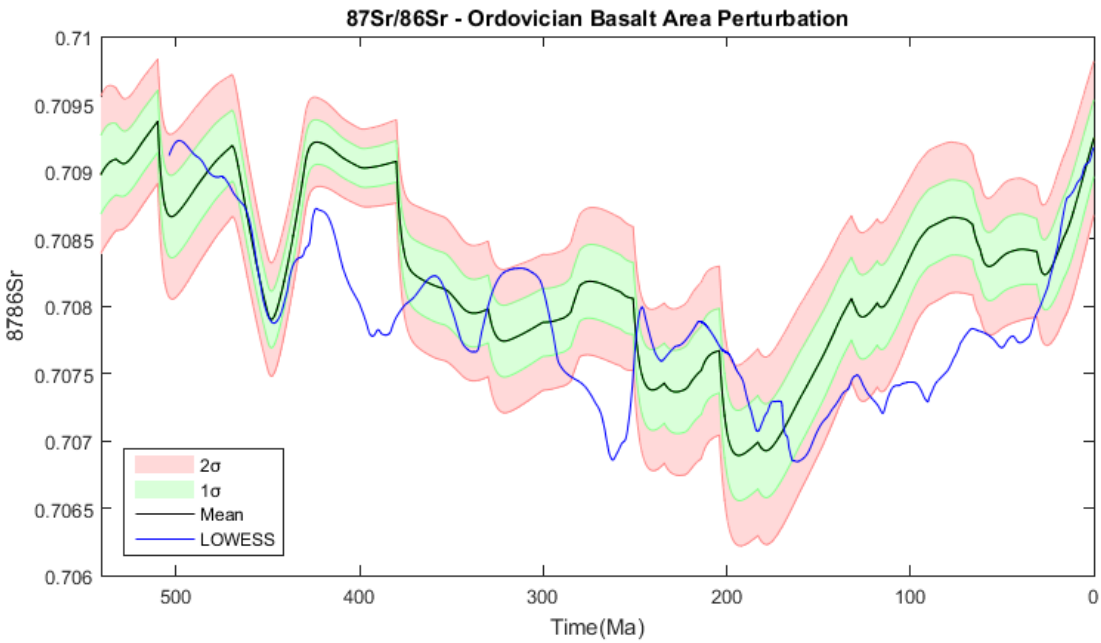

Figure 7.19. Phanerozoic $^{87}Sr/^{86}Sr$ prediction of the updated COPSE model when an arbitrary spike in basalt area is applied in the Ordovician in order to reproduce the known proxy record for this period. This is compared to the updated baseline and LOWESS proxy dataset (McArthur et al., 2012), following a Monte Carlo simulation of 100 runs. The error range is denoted as ±1 and ±2 standard deviations (σ) from the mean.

Sea-level change is not considered by the updated model, however it can exert an important control on strontium fluxes to the ocean (Shields et al., 2003) as it can alter the type and age of rock that is exposed to continental silicate weathering. For example, a peak in eustatic sea level prior to the Hirnantian Glaciation may have flooded radiogenic source areas, resulting in a reduced riverine input of radiogenic strontium (Saltzman et al., 2014; Edwards et al., 2015).

In addition, sea-level change has a large impact on carbonate strontium. Biogenic carbonate that accumulates on continental shelves act as a major sink and source of strontium in the ocean (Schlanger, 1988). During sea-level high-stands, they act as to store strontium, and following their exposure during low-stands, a transient pulse of carbonate strontium is added to the ocean as a result of carbonate diagenesis (Schlanger, 1988; Stoll and Schrag, 1998). This can affect the seawater $^{87}Sr/^{86}Sr$ ratio if it is out of equilibrium – the addition of carbonate strontium acts as to buffer seawater strontium towards ~0.7080, the average Phanerozoic seawater value, and so flattens the slope of any increase or decrease in seawater $^{87}Sr/^{86}Sr$ (Stoll and Schrag, 1998).

As sea level changes are not considered, and carbonate strontium is set to constant throughout the Phanerozoic, it offers, at least in part, an explanation for the shorter-term dynamics of the strontium isotope curve throughout the Phanerozoic that are not predicted by the model.

Similarly to the Ordovician, the Silurian $^{87}Sr/^{86}Sr$ proxy record displays rapid short-term variation, notably the major increase in the rate of $^{87}Sr/^{86}Sr$ increase in the Ludlow (Cramer et al., 2011; McArthur et al., 2012). This Ludlow excursion falls below two standard deviations of the mean, and the sinuosity of the proxy data is not predicted by the model. As with the Ordovician decline, this increase can be attributed to orogenic events associated with a peak in continental assembly (Cramer et al., 2011), reductions in seafloor spreading and so hydrothermal input (Stanley and Hardie, 1998), or sea level change, all of which, as discussed, are not represented in sufficient detail to account for such short term variability.

What the model does do well, however, is to account for changes in the long term carbon cycle and subsequent impacts on the long term pattern of Phanerozoic $^{87}Sr/^{86}Sr$, even if the exact values themselves are under/overestimated. This is apparent in the Mid to Late-Devonian through the Carboniferous, following a large fall in $^{87}Sr/^{86}Sr$ in the Early Devonian. Whilst the Early Devonian minimum pre-dates the predicted fall of the strontium isotope curve, the Mid to Late Devonian curve falls within one standard deviation of the mean.

Following an $^{87}Sr/^{86}Sr$ maxima at the Silurian/Devonian boundary associated with the Caledonian Orogeny and intense weathering of equatorial mountain belts (van Geldern et al., 2006), there is a fall in proxy $^{87}Sr/^{86}Sr$ of a similar magnitude to that which characterises the Ordovician. This correlates with the end of the Acadian phase of the Caledonian Orogeny (McKerrow et al., 2000), as well as with suggestions of substantially increased volcanism and oceanic hydrothermal activity (Denison et al., 1997). Moreover, significant sea level transgressions are argued to have reduced the exposure of ^{87}Sr-rich continental rocks, thus reducing the riverine input of ^{87}Sr (van Geldern et al., 2006).

In the updated model, the uplift forcing is a large simplification and doesn't capture individual orogenic events. As such, it is argued that the emplacement

of the Kola-Dnieper and Yakutsk-Vilyui LIPs, consistent with a suggested increase in volcanic rocks (Nardin et al., 2011) as displayed in Figure 7.7, is the major factor causing a fall in the predicted $^{87}Sr/^{86}Sr$ ratio. As this post-dates the Early-Devonian, the predicted fall in $^{87}Sr/^{86}Sr$ occurs after that predicted by the LOWESS data.

The Mid to Late Devonian is characterised by continental flood basalts located largely in equatorial latitudes, further amplifying the weathering of basaltic rocks and the supply of non-radiogenic strontium to the ocean. A peak in carbonate exposure (Bluth and Kump, 1991) could have resulted in enhanced carbonate weathering regime, acting as to buffer seawater strontium towards the average Phanerozoic seawater ratio of ~0.7080, although carbonate strontium is set to constant in the baseline model.

The large drop in the predicted $^{87}Sr/^{86}Sr$ ratio to the predicted lowest level of the Palaeozoic may be as a result of the combination of increased basaltic area due to LIP emplacement, combined with the enhancement of weathering of basalts due to vascular plants evolution, as well as the latitudinal location of the majority of LIP basalt during this period. Moreover, plants require rock-derived minerals in order to grow (Lenton, 1998; Lenton et al., 2012), and as basalts are rich in Calcium and Magnesium, as well as Phosphorus, they are often preferentially colonised by rock-weathering flora (i.e. Quirk et al., 2012).

In addition, whilst the initial fall in $^{87}Sr/^{86}Sr$ is argued to reflect an increase in basaltic rock area through LIP emplacement, and weathering rate through the evolution of vascular plants, the maintenance of the low predicted curve through the Carboniferous may relate to its correlation with the Permo-Carboniferous Glaciation (i.e. Crowley and Baum, 1992; Scheffler et al., 2003; Poulsen et al., 2007; Fielding et al., 2008; Frank et al., 2008; Royer, 2014; Zhuang et al., 2014; Algeo et al., 2015). This glacial interval is the most prevalent of the Phanerozoic, lasting up to an estimated 90Myr (Scheffler et al., 2003).

As a result, the predicted Palaeozoic strontium isotope minima correlates well with the predicted Palaeozoic temperature and pCO_2 minima (Figures 7.1 and 7.2) resulting in a reduction in global silicate weathering rates as a function of reduced global temperature. As basaltic weathering is amplified by the LIP latitudinal forcing, whereas granitic weathering is not, this provides a

mechanism in the model whereby the basaltic weathering component of the silicate weathering flux can be maintained at a higher level than that of the granitic weathering flux as a function of the palaeogeographic location of the basaltic lithology, maintaining a supply of non-radiogenic strontium to the ocean during a period in which the supply of radiogenic strontium may be largely reduced.

This does not, however, consider the impact of glacial erosion, which has been argued to have increased weathering rates in the Neoproterozoic (i.e. Planavsky et al., 2010). Furthermore, the onset of the Permo-Carboniferous was characterised by extremely low sea levels (Haq and Schutter, 2008), exposing both radiogenic source areas and shelfal carbonates to chemical weathering. Combined, these processes offer an explanation as to why the Carboniferous peak in $^{87}Sr/^{86}Sr$ is overlooked, as neither are represented in the model itself.

Whilst the predicted $^{87}Sr/^{86}Sr$ curve does not necessarily follow the sinuosity of the LOWESS curve for the Mid Palaeozoic, the majority of the variation of the proxy record falls within two standard deviations of the mean. In contrast, during the Permian, the predicted curve displays an increasing trend, in opposition to the rapid decline to the lowest $^{87}Sr/^{86}Sr$ ratios of the Phanerozoic that characterise the LOWESS data (i.e. Gruszczynski et al., 1992; Veizer et al., 1999; McArthur and Howarth, 2004; McArthur et al., 2012; Kani et al., 2013). Along with the Ordovician $^{87}Sr/^{86}Sr$ minima, this is arguably the largest disagreement between the model prediction and the proxy record; whilst an offset between the two of similar magnitude is observed at ~100Ma, the curve of the model retains the shape of the proxy data during the Mesozoic and Cenozoic, which is not the case for the Permian.

The Capitanian $^{87}Sr/^{86}Sr$ minimum, reaching values as low as 0.7068-0.7069 (McArthur et al., 2012; Kani et al., 2013), has been attributed to Mid-Permian cooling, driving extensive ice cover over the continents, argued to suppress the continental weathering flux (Kani et al., 2013). In contrast, the model predicts a dramatic rise in temperature/pCO_2 (Figures 7.1 and 7.2) at the Carboniferous/Permian boundary, potentially enhancing the continental weathering flux through increased temperature, acting as to raise the predicted

curve to mean values of ~0.7081 to ~0.708. This is a major problem with the updated model, as discussed in Section 7.1.1.

On the other hand, the majority of studies argue that deglaciation began in the Sakmarian, approximately starting between 290-280Ma (i.e. Gibbs et al., 2002; Rothman, 2002; Isbell et al., 2003; Montanez et al., 2007; Zhuang et al., 2014), and ending in the Mid-Late Permian (~265Ma) (Montanez et al., 2007). As a consequence, the Early-Permian decline in $^{87}Sr/^{86}Sr$ is coincident with this deglaciation (Korte et al., 2006). As such, the previously high proxy $^{87}Sr/^{86}Sr$ ratios occurred under glacial conditions, as a result of tectonic uplift and glacial erosion (Frank et al., 2008), in contrast to the argument put forward by Kani et al (2013). Therefore, the decline in the proxy $^{87}Sr/^{86}Sr$ trend must be attributed to a process that acts alongside deglaciation, either as a forcing factor or as a resulting impact.

The opening of the Neotethys is argued to have resulted in widespread basaltic volcanism (Veizer et al., 1997; Korte et al., 2006). As displayed in Figure 6.13, the degassing forcing increases at ~300Ma, reaching a minor peak at ~280Ma, and as discussed for the Ordovician decline, the simplified strontium system assumes constant mantle input and so doesn't scale with this. Moreover, as the basaltic area forcing is calculated from the LIP record, this doesn't necessarily represent basalt emplacement as a result of such tectonism, as seen in Figure 7.7, although ocean island basalts are considered as proportional to the degassing forcing. The model predicts a reduction in the percentage of volcanic rock area, and this temporally correlates well with the predicted increase in $^{87}Sr/^{86}Sr$ during the Permian.

Whilst other hypothesis exist for the Permian decline in $^{87}Sr/^{86}Sr$, for example a rapid change from stratified to well mixed ocean conditions (Gruszczynski et al., 1992), this suggests that the model predicts a shift away from a basaltic weathering regime, which may potentially contribute to the underestimation of the length of the Permo-Carboniferous glaciation.

Following the disagreement between model predictions and the LOWESS curve during the Permian, the Mesozoic and Cenozoic curves show a general good agreement, especially in their long-term shape, although the predicted curve lies far above that of the LOWESS data from ~170-30Ma.

At the Permian-Triassic boundary, both curves show a sharp negative spike. Whilst the model predicts a greater decrease in $^{87}Sr/^{86}Sr$ ratio, the LOWESS values fall within the error range of the model prediction. This fall is attributed to the emplacement of the Siberian Traps LIP (i.e. Renne et al., 1995; Joachimski et al., 2012; Romano et al., 2013) at 251Ma, resulting in a major increase in basaltic area and weathering. During the Mid to Late-Triassic, both the predicted curve and the LOWESS data show a concurrent increase in $^{87}Sr/^{86}Sr$, reaching a peak at the Triassic-Jurassic boundary, ~205.7Ma (McElwain et al., 1999). This period was characterised by extensive volcanism associated with the breakup of the Pangaea. The Central Atlantic Magmatic Province (CAMP) at ~201Ma (Marzoli et al., 1999) is the largest known LIP of the Phanerozoic, and so as with the Siberian Traps, resulted in a major basalt input, and so a large decrease in the $^{87}Sr/^{86}Sr$ ratio of seawater as a function of this basalt emplacement.

As the model assumes instantaneous LIP emplacement, the modelled curve falls more sharply than the LOWESS data. Despite this, both curves reach a minimum of ~0.7068-0.7070, although the LOWESS data shows an initial fall, before a small rise of 0.0002 at ~180Ma, before declining again to reach a minimum value in the Late Jurassic.

The increase in predicted $^{87}Sr/^{86}Sr$ ratio through the Jurassic and Early-Cretaceous in consistent with that of the LOWESS dataset, which also rises while remaining within two standard deviations of the predicted mean. This rise is consistent with uplift associated with that of the West Cordillera (Grocke et al., 2003; Dera et al., 2011), as well as reductions in sea level. Despite this, the predicted model increase is likely more to be as a result of decreasing basaltic area following the Triassic and Jurassic (Mills et al., 2014b), as the general predicted trend on a Phanerozoic scale shows a good long term agreement with the predicted volcanic rock abundance, as seen in Figure 7.15.

During the majority of the Mesozoic, seafloor weathering acted as a negative feedback on atmospheric CO_2 due to increased hydrothermal CO_2 consumption (Coogan and Gillis, 2013), whereas through the Cretaceous and Cenozoic, continental weathering increased and the seafloor weathering flux decreased (Gills and Coogan, 2011). Degassing is also seen to increase in the Mesozoic, before falling through the Cenozoic (Mills et al., 2014b; Van Der Meer et al.,

2014). Although showing good agreement with the general trend of the proxy data, through the Cretaceous and Cenozoic, the predicted curve rises far above that of the LOWESS data.

Whilst the predicted curve is consistent with the reduction in seafloor weathering and degassing, the simplified strontium isotope system results in the predicted curve being too radiogenic from ~170-30Ma, as the flux of non-radiogenic strontium through enhanced seafloor spreading is not included, and in turn the seafloor weathering flux is decoupled from seafloor spreading to remain consistent. Despite the updated degassing forcing of Mills et al (in preparation) showing less degassing for the Mesozoic and Cenozoic than that of Van Der Meer et al (2014) (Figure 6.3), it is still greater than at present, falling from relative values of 1.5 to 1.0 over this interval. As a consequence, it is argued that the discrepancy in Late Mesozoic to Early Cenozoic $^{87}Sr/^{86}Sr$ (as much as 0.0011 at ~100Ma) between the model prediction and proxy data may be as a result of the simplified model strontium system regarding both hydrothermal input and seafloor weathering, acting as to enhance the impact of a reduced basaltic weathering contribution to the global silicate weathering flux.

Excellent agreement between the predicted and LOWESS curves exists for the last 30Ma of the Cenozoic, which is characterised by a rapid increase in $^{87}Sr/^{86}Sr$ ratio. This is argued to be as a function of Himalayan uplift (Galy et al., 1999; Mills et al., 2014b), and is captured in the model by increasing the $^{87}Sr/^{86}Sr$ value of old igneous rocks from 0.715 to 0.718 during the last 30Ma to account for this, following the extremely radiogenic strontium source of Himalayan rivers discussed by Galy et al (1999). This kind of source rock alteration may have been important during other parts of the Phanerozoic.

7.1.4. $\delta^{13}C$

The Phanerozoic $\delta^{13}C_{carb}$ record is characterised by major short-term fluctuations (Saltzman and Thomas, 2012). As the aim of this study is to improve long-term predictions, such rapid variation is not captured. Despite this, Figure 7.20 shows that the modelled $\delta^{13}C_{carb}$ record follows the proxy data of Saltzman and Thomas (2012). In addition, some peaks are captured, even if the magnitude is less than that of the proxy data.

The Lower-Cambrian is characterised by considerable variability, with two large shifts between 540 and 535Ma (Saltzman and Thomas, 2012), before the global Steptoean Positive Carbon Isotope Excursion (SPICE) at ~495Ma, though this is clearly overlooked.

Whilst the updated model predictions follows suggestions of a relatively steady Tremadocian $\delta^{13}C_{carb}$ record (Saltzman, 2005), the Early-Ordovician is characterised by unusually light values, below 0‰, which are not captured by the model.

Major positive $\delta^{13}C_{carb}$ excursions take place in the later Ordovician, namely the Mid-Darriwilian Isotopic Carbon Excursion (MDICE) (Bergstrom et al., 2009; Rasmussen et al., 2016), Guttenberg Isotopic Carbon Excursion (GICE) (i.e. Bergstrom et al., 2010; Cooper and Sadler, 2012; Lenton et al., 2012; Melchin et al., 2013), and Hirnantian Isotopic Carbon Excursion (HICE) (i.e. Kaljo et al., 2004; 2007; Ainsaar et al., 2007; 2010; Bergstrom et al., 2009; 2010; Bauert et al., 2014).

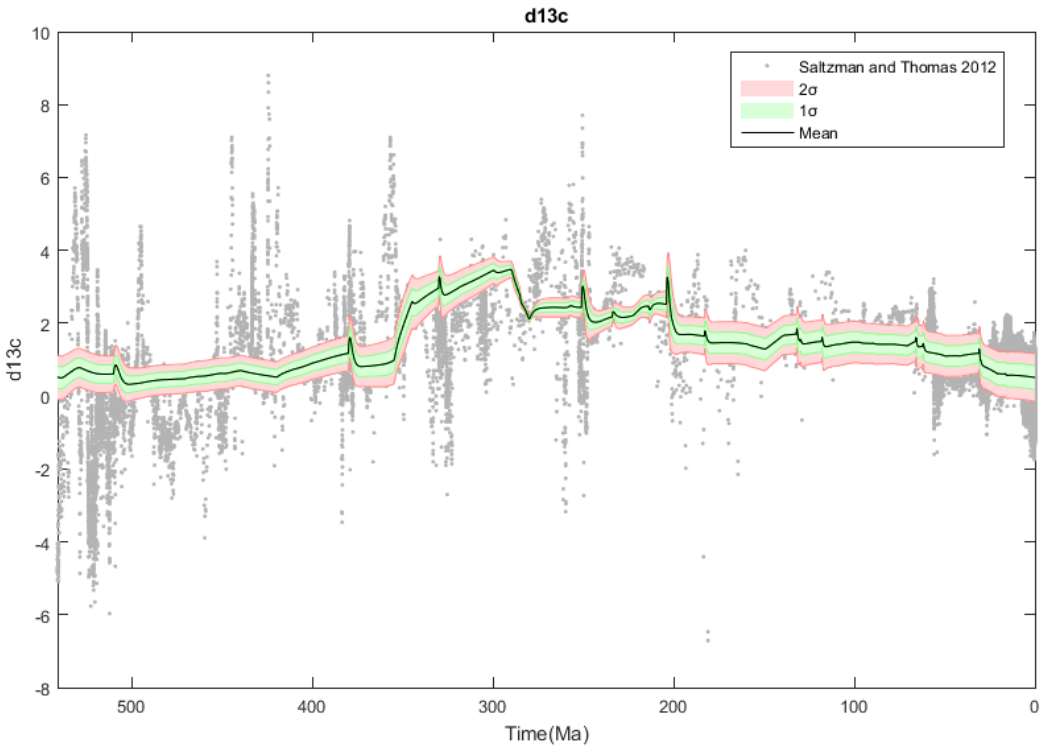

Figure 7.20. Phanerozoic $\delta^{13}C_{carb}$ prediction of the updated COPSE model compared to the proxy data of Saltzman and Thomas (2012), following a Monte Carlo simulation of 100 runs. The error range is denoted as ±1 and ±2 standard deviations (σ) from the mean.

The GICE correlates with cooling attributed to explosive volcanism (Buggisch et al., 2010; Sell, 2011), however there is no direct evidence that GICE is coeval with a period of extensive glaciation (Bergstrom et al., 2010). HICE is a global positive $\delta^{13}C_{carb}$ excursion of +6-7‰ (i.e. Ainsaar et al., 2007; 2010; Lenton et al., 2012), indicative of a major carbon cycle perturbation, for example enhanced organic carbon burial (Brenchley et al., 1994), through the glacial interval (i.e. Brenchley et al., 2003; Hammarlund et al., 2012; Jones and Fike, 2013).

In the work of Lenton et al (2012), both GICE and HICE are reproduced by perturbing the phosphorus weathering flux. As this is not done in the updated baseline model, these peaks are not predicted by the model.

The model predicts a gradual minor increase in $\delta^{13}C_{carb}$ through the Silurian. To reproduce the positive excursions, the inclusion of phosphorus weathering by early plants is required (Lenton et al., in press), as with the Ordovician (Lenton et al., 2012). Multiple positive $\delta^{13}C_{carb}$ excursions characterise the Devonian (Saltzman and Thomas, 2012). The excursion across the Frasnian/Famennian boundary, ~372Ma, is argued to be captured by the model, although not in the same magnitude as the proxy data. This excursion is associated with a major extinction episode (Joachimski, 1997; Kaiho et al., 2013).

As discussed in Section 7.1.2, the Permo-Carboniferous was characterised by a peak in organic carbon burial (i.e. Robinson, 1990) in widespread peat forming environments. This sequestration of isotopically light ^{12}C resulted in an increase in $\delta^{13}C_{carb}$, as predicted by the updated model. This is consistent with the proxy data of Saltzman and Thomas (2012), with model values in the range of +2-4‰ following the Early-Carboniferous increase.

Such positive $\delta^{13}C_{carb}$, and thus reduced organic carbon burial, allows the inference of iceage conditions, as seen in the temperature and pCO_2 predictions, especially given the co-variance with $\delta^{18}O$ (i.e. Veizer et al., 1999; Frank et al., 2008) and $\delta^{13}C_{org}$ (Scheffler et al., 2003) proxy data.

Agreement between the model prediction and proxy data is also seen in the Permian, which is characterised by heavy $\delta^{13}C_{carb}$ values (Saltzman and Thomas, 2012). Whilst recent studies argue for a negative excursion during the Capitanian (Wignall et al., 2009; Bond et al., 2010), the model predicts a fall in

$\delta^{13}C_{carb}$ in the Asselian through Sakmarian. This likely relates to the abrupt decline in predicted organic carbon burial that results in an underestimation of the length of the Permo-Carboniferous glaciation, as discussed previously.

The model predicts a positive excursion, followed by a decrease in $\delta^{13}C_{carb}$ at the Permian/Triassic boundary, in good agreement with the proxy data. This negative shift is associated with the influx of isotopically light carbon from Siberian Traps volcanism (Joachimski et al., 2012), and is thus coincident with the End-Permian extinction (i.e. Jin et al., 2000; Payne et al., 2004). A similar increase in $\delta^{13}C_{carb}$ followed by a fall is observed at the emplacement of CAMP.

Following this, predicted $\delta^{13}C_{carb}$ generally falls within two standard deviations of the proxy data through to the present day.

7.1.5. $\delta^{34}S$

As displayed in Figure 7.21, it is argued that the updated model shows excellent long term agreement with the $\delta^{34}S$ proxy data of Algeo et al (2015), although shorter-term dynamics are not captured. This may be as a result of elements of the sulphur cycle, notably marine pyrite burial, being difficult to quantify (Bergman et al., 2004), with pyrite burial related the concentration of ocean sulphate, as well as organic carbon burial and atmospheric O_2 levels.

The Cambrian displays the maximum $\delta^{34}S$ values of the Phanerozoic (Strauss, 1999; Paytan and Gray, 2012; Algeo et al., 2015), both in the proxy data and model prediction. There is slight disagreement in the values themselves, with proxies estimating $\delta^{34}S$ values in the region of ~34-36‰ compared to the ~28-31‰ of the model prediction, and the steep decline from the Cambrian to the Ordovician (Algeo et al., 2015) also goes unpredicted by the model. An influx of strongly ^{34}S-enriched water masses via the overturn of a stratified water body has been suggested as an explanation of the Cambrian peak in $\delta^{34}S$ (Kampschulte and Strauss, 2004), and as such ocean dynamics are beyond the scope of the COPSE model, it is clear that the simplification of the Sulphur cycle and isotope system offers a reason behind such disagreement with the proxy data.

Following the Cambrian, $\delta^{34}S$ declines through the remainder of the Palaeozoic, reaching the Phanerozoic minimum during the Permian (Paytan and Gray, 2012; Algeo et al., 2015). A fall from ~30‰ to ~24‰ is stated to have characterised the Ordovician (Kampschulte and Strauss, 2004), however the more recent proxy data shows excellent agreement with model predictions in the region of ~26-28‰ for this period.

These reasonably high values coincide with a period of enhanced pyrite burial (Prokoph et al., 2008), as displayed in Figure 7.9. Moreover, the peak in pyrite burial roughly coincides with the peak in pyrite weathering (Figure 7.22), and so the supply of freshly weathered pyrite, depleted in ^{34}S, to the ocean (Kampschulte and Strauss, 2004). The peak in pyrite weathering follows the uplift forcing, which predicts a peak in orogenic uplift during the Ordovician associated with the Taconic and Caledonian orogenies.

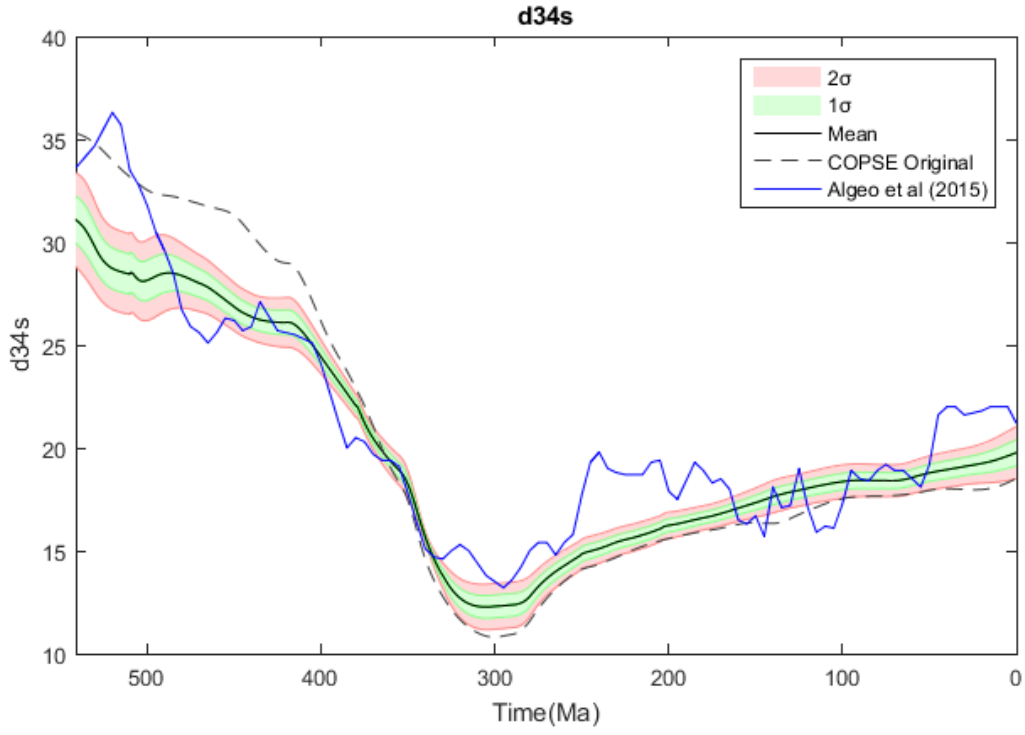

Figure 7.21. Phanerozoic $\delta^{34}S$ prediction of the updated COPSE model compared to COPSE Original (Bergman et al., 2004) and the proxy data of Algeo et al (2015), following a Monte Carlo simulation of 100 runs. The error range is denoted as ±1 and ±2 standard deviations (σ) from the mean.

As displayed in Figures 7.11 and 7.22, both pyrite burial and pyrite weathering are much higher in the early Phanerozoic in the updated model than in COPSE original. This causes a reduction in $\delta^{34}S$ values for the Cambrian and Ordovician that are more consistent with proxy data than the original COPSE model of Bergman et al (2004), with pyrite weathering showing excellent agreement with the curve of Berner (2004b).

It has been argued that a large negative $\delta^{34}S$ perturbation occurred during the Ordovician, consistent with deglaciation, as a result of rapid transgression and consequent increased ^{32}S transport from deep waters into shallow waters, perturbing the Sulphur cycle (Zhang et al., 2009). Whilst substantial variation can occur over shorter timescales (Kampschulte and Strauss, 2004), this negative spike is not recognised in the proxy data or the model prediction.

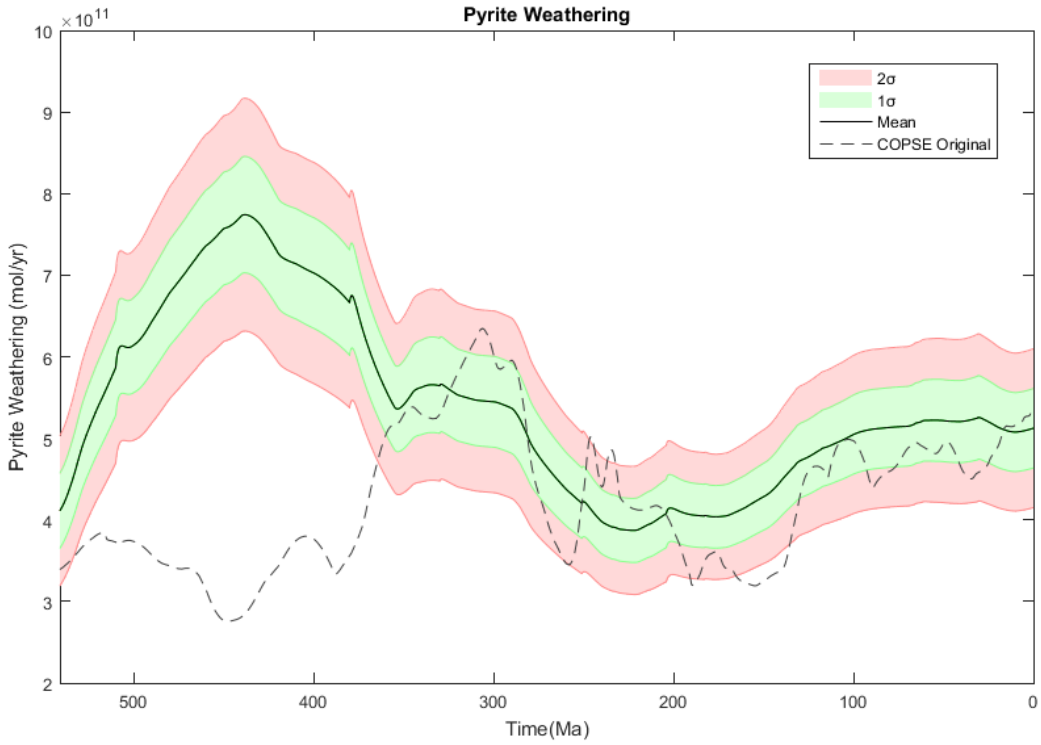

Figure 7.22. Phanerozoic pyrite weathering prediction of the updated COPSE model compared to COPSE Original (Bergman et al., 2004), following a Monte Carlo simulation of 100 runs. The error range is denoted as ±1 and ±2 standard deviations (σ) from the mean.

The intermediate values of the Ordovician continue through the Silurian until the Early-Devonian (Algeo et al., 2015), following which a fall of >10‰ occurs (Paytan and Gray, 2012), with both the model and proxy data reaching a minimum in $\delta^{34}S$ during the Carboniferous to Early-Permian. This sharp decline mirrors that of other model outputs such as CO_2 and temperature, as well as the increase in atmospheric O_2. As such, it is suggested that the rise of vascular land plants caused an indirect reduction in marine pyrite burial (i.e. Kampschulte and Strauss, 2004), as observed in Figure 7.11 – as this flux is inversely dependent upon atmospheric O_2 (Bergman et al., 2004), and O_2 dramatically increases as a result of the colonisation of the continents by land plants, it therefore follows that pyrite burial is reduced. This provides evidence for a regulating mechanism for atmospheric O_2 (Berner, 2006a; Archer, 2010), whereby periods of high organic carbon burial tend to be offset by reduced pyrite burial.

In reality, this fall in $\delta^{34}S$ may relate to the efficiency of microbial sulphate reduction (MSR) (Strauss, 1999). Strongly positive $\delta^{34}S$ values characterise the early Phanerozoic, indicating that MSR proceeded both rapidly and efficiently. In contrast, the evolution of vascular land plants led to a change in the organic substrate away from purely marine algal matter to increased land plant input, which is more difficult for sulphate-reducing bacteria to metabolise (Strauss, 1999). Whilst this process is not represented in the model, it is clear that the fall in $\delta^{34}S$ is as a result of the evolution of land plants.

Seawater $\delta^{34}S$ reaches its minimum value during the Permo-Carboniferous (i.e. Strauss, 1997; 1999; Kampschulte and Strauss, 2004; Paytan and Gray, 2012; Algeo et al., 2015). Whilst this minima is traditionally stated to have occurred at the Permian-Triassic boundary (i.e. Strauss, 1999; Paytan and Gray, 2012), more recent proxy data suggests that the minima took place from the Mid-Mississippian to the Early-Permian (Algeo et al., 2015), consistent with model predictions. A range of $\delta^{34}S$ values have been measured for this period, however they generally fall into the range of ~11-16‰ (Strauss, 1999; Paytan and Gray, 2012; Algeo et al., 2015). Whilst the model prediction falls below the proxy data by more than two standard deviations, the predicted value of ~12.5‰ is consistent with published data.

Although Zhang et al (2009) argue for a negative $\delta^{34}S$ excursion as a result of sea level transgression following the Hirnantian Glaciation, Algeo et al (2015) argue that the reduction in pyrite burial during the Permo-Carboniferous was at least partly related to reduced sea levels, causing a reduction in shelf area available for sulphate reduction (i.e. Halevy et al., 2012; Algeo et al., 2014). This brings about the question as to whether low $\delta^{34}S$ characterises icehouse periods. Comparing the Permo-Carboniferous to the Late-Cretaceous/Cenozoic shows enriched $\delta^{34}S$ values in the latter, however this may be as a result of a long-term increase in total seawater sulphate (Algeo et al., 2015), as discussed in Section 7.1.6, and so the impact of glaciation on $\delta^{34}S$ remains uncertain.

The Mesozoic is characterised by a slow increase with $\delta^{34}S$ values generally in the range of 14-20‰. This trend is clearly followed by the model, although predictions lie below the values presented by Algeo et al (2015) until the Cretaceous. A sharp increase to ~20‰ characterises the Early Triassic. This prominent shift is overlooked by the model, reaching values >~5‰ larger than the mean model value. Anoxic bottom waters favour MSR, thus acting as to shift $\delta^{34}S$ to a more positive value. Flooding of shelf areas subsequently transports this anoxic water into regions of carbonate and evaporate precipitation, allowing the positive $\delta^{34}S$ signal to be deposited in sediments (Kampschulte and Strauss, 2004). The End-Permian mass extinction (i.e. Erwin 1994; Joachimski et al., 2012) has been attributed to widely documented shallow water anoxia (i.e. Wignall and Hallam, 1992; Knoll et al., 1996; 2007). As discussed, such processes are not represented in the updated COPSE model, and the strong agreement with the long term $\delta^{34}S$ proxy trend allows for confidence with, for example, atmospheric O_2 predictions, despite the lack of representation of short term excursions.

A similar maximum in proxy $\delta^{34}S$ is observed in the Toarcian (Kampschulte and Strauss, 2004), which is characterised by the global deposition of black shales (Rampino and Caldeira, 1993; Kampschulte and Strauss, 2004), reflecting the flooding of continental shelves with anoxic waters.

The long-term $\delta^{34}S$ trend predicted by the model shows excellent agreement with the proxy data for the majority of the Phanerozoic, though especially the Cretaceous and Early-Cenozoic. A similar gradual increase is observed in pyrite burial (Figure 7.9) following the Permo-Carboniferous, and as previously

discussed, this relates to a fall in atmospheric O_2 following the Phanerozoic maximum in the Carboniferous. A rapid increase in proxy $\delta^{34}S$ from ~17-22‰ takes place during the Eocene (Paytan et al., 1998; Algeo et al., 2015), with values subsequently stabilising in the region of 21-23‰.

A criticism of the model is that mean $\delta^{34}S$ does not return to the present day value of ~21.2‰ of the proxy data (Algeo et al., 2015). Despite this, it is clear that the long term prediction of $\delta^{34}S$ displays excellent agreement with the proxy curve, with a negative feedback mechanism on atmospheric O_2 with respect to pyrite burial strongly represented by, and thus acting as a major control on, $\delta^{34}S$.

7.1.6. Ocean Sulphate

As introduced in Section 4.4, the history of past oceanic sulphate concentrations is of interest due to its intrinsic link to the oxygenation of the Earth System (Algeo et al., 2015). Therefore, it essentially acts as a proxy for atmospheric O_2. Oceanic sulphate is argued to have been characterised by a two-step increase since the Neoproterozoic. Although the first step is not displayed due to its pre-Phanerozoic initiation, the second stepwise increase in oceanic sulphate concentration clearly characterises the Permo-Carboniferous (Algeo et al., 2015), as displayed in Figure 7.23.

This increase in oceanic sulphate concentration is a result of two-interlinked processes. Firstly, increased oxidation of the Earth System, notably through the rise of plants, results in increasing oxidation of marine sulphides, thus increasing the marine sulphate concentration (Kah et al., 2004). Secondly, the main removal pathway for ocean sulphate is via pyrite burial, with some burial as gypsum in evaporites (i.e. Berner and Raiswell, 1983; Canfield and Farquhar, 2009; Halevy et al., 2012). As discussed in the preceding section, pyrite burial decreases with increasing atmospheric O_2 (Algeo et al., 2015). Therefore, the increase in atmospheric O_2 through the Mid-Late Palaeozoic coincides with a reduction in pyrite burial, as displayed in Figure 7.9, thus increasing the size of the oceanic sulphate reservoir.

In contrast to the results of the updated model, additional published curves (i.e. Berner, 2004b; Algeo et al., 2015) argue for a peak in ocean sulphate during the Triassic. This can be explained through sulphate deposition as gypsum becoming a significant sulphate-removal pathway at enhanced ocean sulphate concentrations (Canfield and Farquhar, 2009), and so following the rise of ocean sulphate through the Permian, it is expected that gypsum deposition would increase, acting as to reduce the ocean sulphate reservoir. This is consistent with a Mesozoic peak in evaporite deposits (Hay et al., 2006).

Despite this, there is large variation between curves (i.e. Berner, 2004b; Wortmann and Chernyavsky, 2007; Halevy et al., 2012; Wortmann and Paytan, 2012; Algeo et al., 2015), and a major success of the model is the capturing of the Permo-Carboniferous rise in oceanic sulphate.

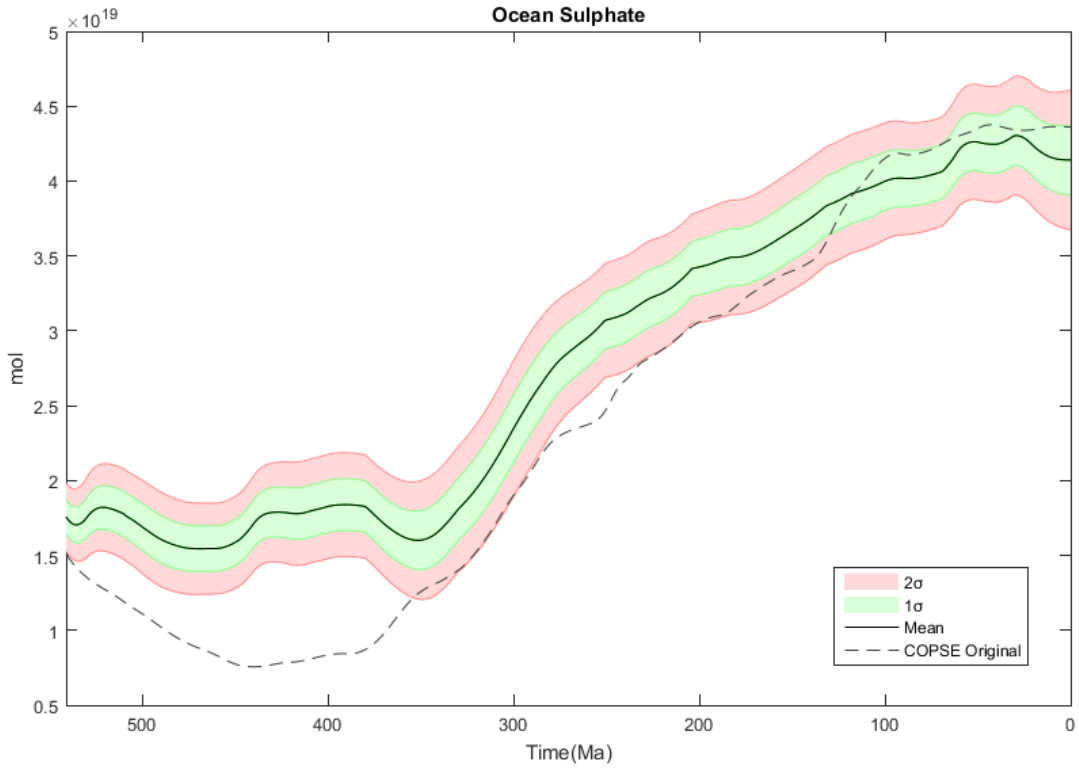

Figure 7.23. Phanerozoic ocean sulphate concentration prediction of the updated COPSE model compared to COPSE Original (Bergman et al., 2004), following a Monte Carlo simulation of 100 runs. The error range is denoted as ±1 and ±2 standard deviations (σ) from the mean.

8. Impact of Additional and Updated Forcings

8.1. Increasing the Complexity of the Model

8.1.1. Land Area

Following numerous revisions of Phanerozoic palaeomaps, a land area forcing is developed from the COPSE forcing that was essentially based upon data from Ronov (1994), to a forcing calculated from the palaeomaps of Blakey (2011).

Changes in land area are dominantly forced by eustatic sea level change (i.e. Miller et al., 2005; Haq and Schutter, 2008; Nardin et al., 2011), which is in turn dominated by the growth and decay of continental ice sheets, producing high amplitude and potentially rapid eustatic change (Miller et al., 2005). For example, the maximum sea level in the Phanerozoic was observed in the Mid-Ordovician (Haq and Schutter, 2008), ~225m higher than present, before a prominent fall through the Hirnantian glaciation.

Whilst changes in total land area may affect silicate weathering rates, as changes in total land area are dominated by sea level fluctuations, this effect is oft-considered minor as continental margins are typically low-relief areas containing highly-weathered minerals (Berner, 1994; 2004a). Despite this, Monte Carlo simulations lead Royer et al (2014) to argue that land area has a similar effect on atmospheric CO_2 as runoff, continental temperature, relief and seafloor spreading rates, amongst other factors, at least for GEOCARBSULF model simulations.

Furthermore, Montanez et al (1996) argue that Cambrian strontium isotope variations correspond to sea level change, leading to suggestions that weathering rates may also change in response to variations in continental surface area governed by marine transgressions and regressions, for example through the incision of rivers as a result of changes in base level, and through the exposure of fine grained, ^{87}Sr-rich phyllosilicates, as well as shelfal carbonates, to increased physical and chemical weathering.

Whilst the use of the updated land area forcing following COPSE (Section 5.2.1.4), whereby it is used to calculate the granitic component of the total silicate area at any given time, has thus been argued to have a potentially

limited effect on the long term carbon cycle, Figure 8.1 displays the clear impact through running a Phanerozoic simulation with a ±10% range of total land area.

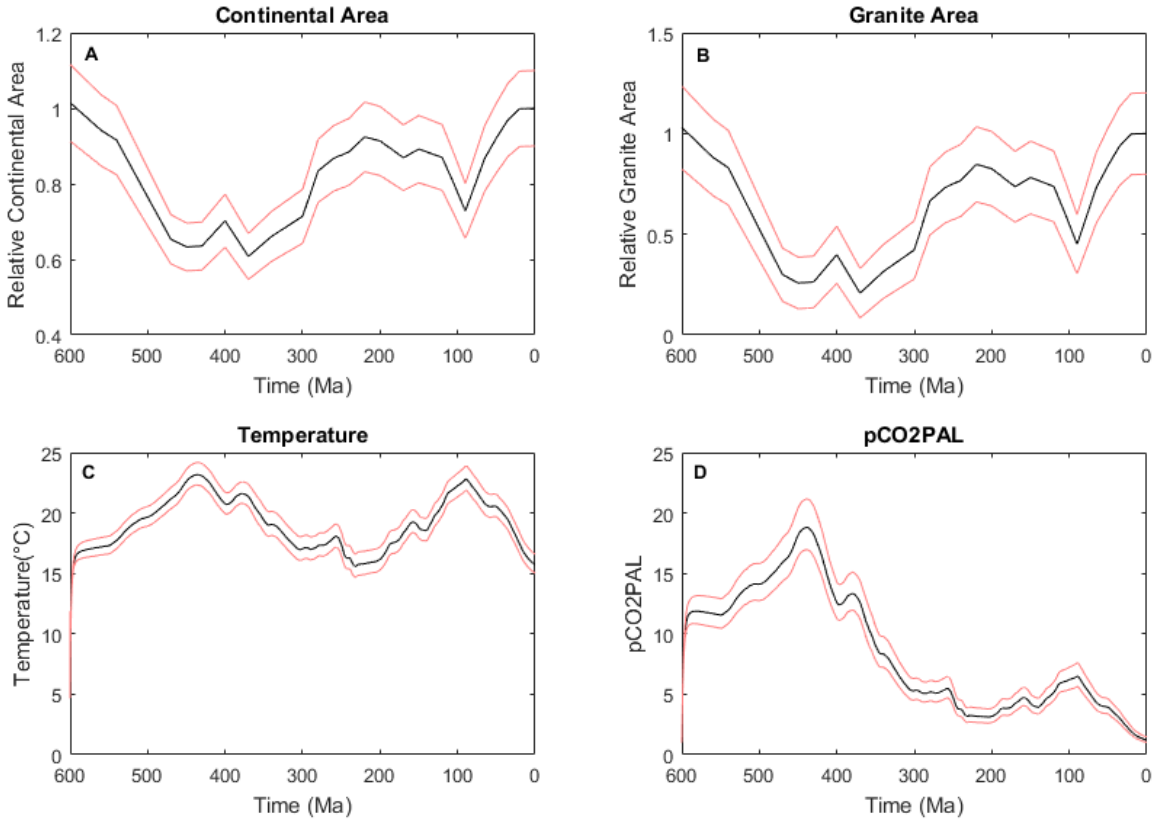

Figure 8.1. Impact of a +/- 10% change in land area (a), and hence granite area (b), on global surface temperature (c) and atmospheric pCO2PAL (d) over the course of the Phanerozoic, with all other forcings under COPSE baseline conditions. Maximum (+10%) and minimum (-10%) limits are displayed in red, with the updated Blakey (2011) land area forcing used.

As with the development of the LIP palaeogeography forcing, palaeomaps were georeferenced to a standard Mollweide projection. This projection is appropriate for the derivation of this forcing as plates and other areas of finite size, i.e. continental surface area, are represented in correct proportion (Varga et al., 2012).

Land area was also calculated from the more recent palaeomaps of Scotese (2015), however, as is clear in Figure 8.2, the edge of the continental shelf is displayed rather than the edge of the continental land surface itself, resulting in extremely large land areas. In an attempt to correct for this, Phanerozoic shelf areas were taken from Walker et al (2002) and subtracted from the initial

calculated land area, however this was deemed too inaccurate an approach, and as such the Blakey (2011) based forcing is used.

A summary of the methodology used to derive land areas from the palaeomaps of Blakey (2011) is displayed in Figure 8.3, with Table 8.1 displaying a catalogue of maps, and thus the temporal resolution of the forcing. Due to the 'time slice' nature of the palaeomap catalogue, linear change in land area is assumed between maps, and so shorter term variation, such as sea level fluctuations, is not captured by this forcing. It is, however, representative on a geologic time scale.

The updated land area forcing is compared to that of Berner (1994) in Figure 8.4.

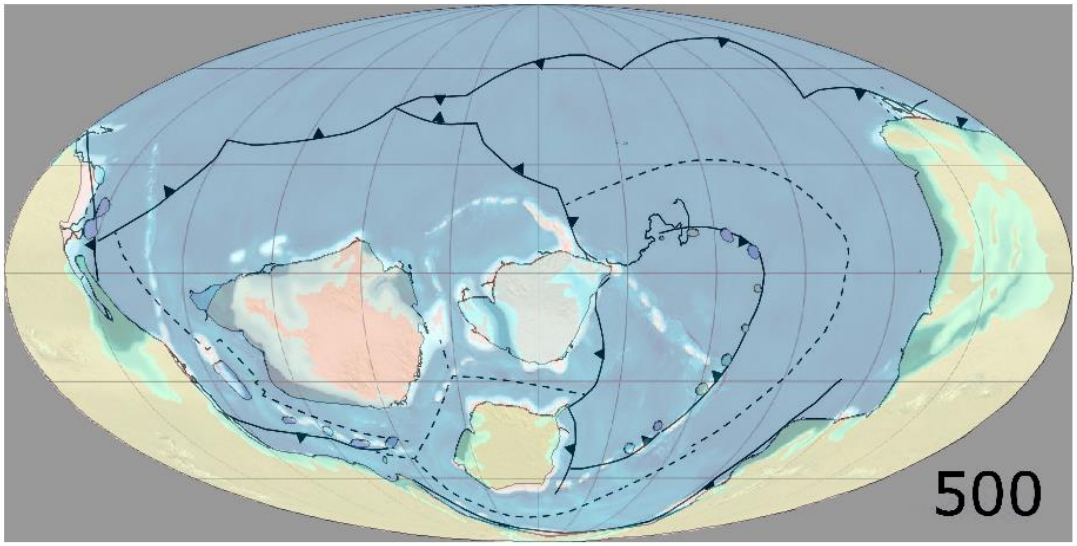

Figure 8.2. Comparison of Blakey (2011) and Scotese (2015) palaeomaps for the calculation of land area, using 500Ma as an example. The land area polygons of the Scotese (2015) map are transparently overlain above the Blakey (2011) map – not only does this show the differences between the two reconstructions, but it is also clear that the Scotese (2015) map has mapped the edge of the shelf, whereas the Blakey (2011) map more accurately represents continental area.

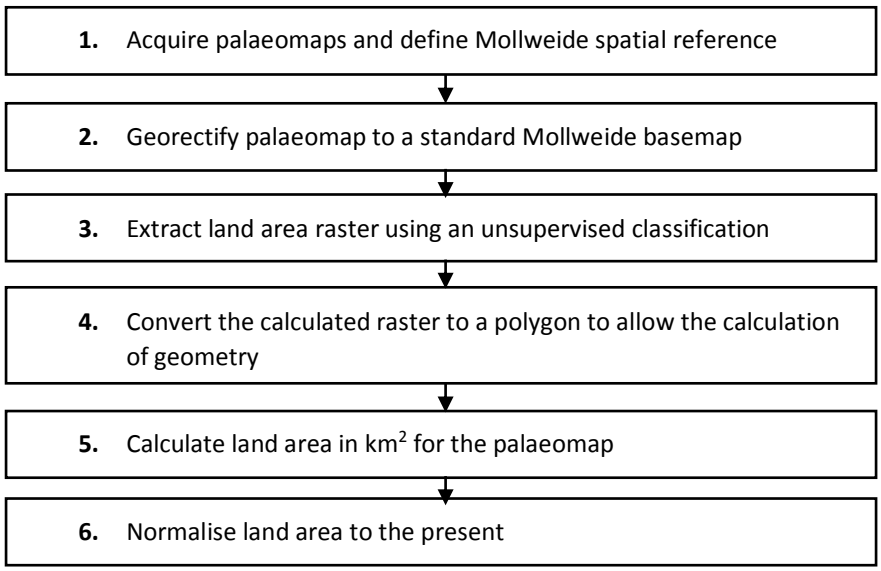

Figure 8.3. Flow chart displaying a summary of the method used to extract a land area forcing for the Phanerozoic from the palaeomaps of Blakey (2011).

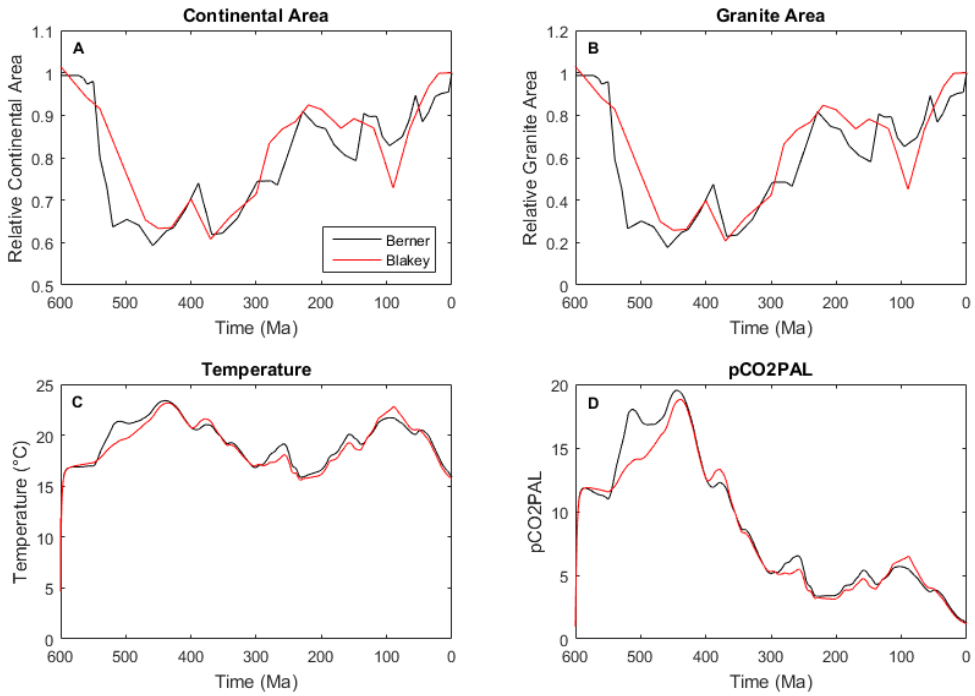

Figure 8.4. Comparison between Berner (1994) and Blakey (2011) land area (a), and hence granite area (b), and the effects on global surface temperature (c) and atmospheric pCO2PAL (d) over the course of the Phanerozoic, with all other forcings under COPSE baseline conditions.

Geologic Time Period	Time (Ma)
Late Proterozoic	600
Latest Proterozoic	560
Early Cambrian	540
Late Cambrian	500
Mid Ordovician	470
Late Ordovician	450
Silurian	430
Early Devonian	400
Late Devonian	370
Mississippian	340
Pennsylvanian	300
Early Permian	280
Late Permian	260
Early-Mid Triassic	240
Late Triassic	220
Early Jurassic	200
Mid Jurassic	170
Late Jurassic	150
Early Cretaceous	120
Late-Early Cretaceous	105
Late Cretaceous	90
Cretaceous/Palaeogene Boundary (K-T)	65
Eocene	50
Oligocene	35
Miocene	20
Present	0

Table 8.1. Catalogue of palaeomaps used to calculate the updated land area forcing for the Phanerozoic, following Blakey (2011).

8.1.2. Accounting for Incomplete Preservation of LIPs

To account for the potential error involved regarding the incomplete preservation of LIPs, a suggested maximum initial areal extent for the continental flood basalts is calculated following the reconstruction of original masses of sediment deposited through the Phanerozoic by Hay et al (2006). They argue that the mass-age distribution of ancient sediment masses resembles an exponential decay, as younger sediments are formed mostly by the erosion of older sediments (Hay et al., 2006). This decay function can be standardised as follows (Wold and Hay, 1990):

$$y = Ae^{-bt} \quad (8.1)$$

Here, 'y' represents the remnant of original sediment deposited at time 't' (Myr), after tMyr of cycling at a constant rate of erosion 'b', the decay constant of Veizer and Jansen (1985). The constant 'A' is the long term average rate at which sediment was deposited (Hay et al., 2006).

The reconstruction of Hay et al (2006) uses the decay equation displayed in Equation 8.2:

$$y = 9.5496e^{(-0.0031t)} \quad (8.2)$$

To apply this to the continental flood basalt database, the time of emplacement for each LIP is taken as 't', and following the application of Equation 8.2, the resulting y value is divided by the constant (A = 9.5496) as displayed in Equation 8.3 to give a factor by which the initial area estimate (at the time of emplacement, t) is multiplied by to give a revised upper estimate (Equation 8.4).

$$z = \frac{y}{9.5496} \quad (8.3)$$

$$Revised\ Area\ (t) = Initial\ Area\ (t) * z \quad (8.4)$$

As an example, for the Columbia River province, Equation 8.2 gives a y value of 10.0507702, which results in a z value of 1.052480754 following the application of Equation 8.3. This shows that the revised upper areal estimate will be ~105% that of the initial area (240000km^2) estimate. Consequently, following Equation 8.4, the revised area equates to 252595km^2. The revised areas for the continental flood basalt database following the application of this process are displayed in Table 8.2.

Time of Emplacement (Ma)	Name of Province	Initial Continental Area (km^2)	Z	Revised Continental Area (km^2)
16.5	Columbia River	240000	1.052480754	252595
30	Sierra Madre Occidental	400000	1.097461735	438985
31	Afro-Arabia	2000000	1.100869145	2201738
62	North Atlantic Igneous Province	1300000	1.211912875	1575487
66	Deccan Traps	1800000	1.227034153	2208661
90	Madagascar Event	260000	1.321807344	343670
110	Marie Byrd Land Event	160000	1.406353241	225017
118	Kerguelen Plateau	1540000	1.44166688	2220167
118	Rajmahal/Sylhet Province	200000	1.44166688	288333
130	Queen Elizabeth Islands	275000	1.496306892	411484
130	High Arctic Large Igneous Province	500000	1.496306892	748153
132	Comei-Bunbury LIP	100000	1.505612813	150561
132	Parana-Etendeka Event	2050000	1.505612813	3086506
140	South West Greenland Trap	20000	1.543418868	30868
160	North West Australian Margin	160000	1.642139558	262742
183	Karoo-Ferrar Event	1560000	1.76349917	2751059
204	Central Atlantic Magmatic Province	7000000	1.882122257	13174856
251	Siberian Traps	5000000	2.177331403	10886657
258	Emeishan Event	250000	2.225095865	556274
280	Qiangtang Panjal	40000	2.382141802	95286
280	Himalaya-Neotethys Event	200000	2.382141802	476428
280	Tarim Block Event	250000	2.382141802	595535
300	European-Northwest Africa Event	150000	2.534509178	380176
330	Tianshan	1700000	2.78152684	4728596
380	Yakutsk-Vilyui	800000	3.247871959	2598298
380	Kola-Dneiper	3000000	3.247871959	9743616
400	Panzhihua	5000	3.455613465	17278
510	Antrim Event	450000	4.859813195	2186916
510	Kalkarindji	2100000	4.859813195	10205608

Table 8.2. Revised estimates of the initial areas of the LIP database, following the application of Equations 8.2 through 8.4. The value of Z is seen to increase exponentially with age of initial emplacement.

Time of Emplacement (Ma)	Name of Province	Initial Continental Area (km^2)	Z	Revised Continental Area (km^2)
540	Wichita Mountains Event	40000	5.333459022	213338
575	Late Central-Iapetus Event	7000	5.944699606	41613
592	Middle Central-Iapetus Event	140000	6.266387298	877294
620	Early Central-Iapetus Event	105000	6.834614037	717634
650	Volyn Event	140000	7.500727381	1050102
720	Gannakouriep Event	30000	9.318484424	279555
720	Franklin Province	2250000	9.318484424	20966590
720	Dovyren-Kingash	130000	9.318484424	1211403
720	Mutare	50000	9.318484424	465924
750	Muggamurra Event	140000	10.22668009	1431735
758	Mundine Well Event	180000	10.48347282	1887025
760	Shaba and Ogcheon Event	330000	10.54867226	3481062
760	Malani Event	20000	10.54867226	210973
760	Mt. Rogers Event	60000	10.54867226	632920
780	Gunbarrel Event	200000	11.22339007	2244678
780	Kangding Event	1160000	11.22339007	13019132
800	Niquelandia	30000	11.94126442	358238
830	Willouran-Gairdner Event	210000	13.10508077	2752067
850	Bir El Khzaim Event	520000	13.94331246	7250522

Table 8.2.cotd. Revised estimates of the initial areas of the LIP database, following the application of Equations 8.2 through 8.4. The value of Z is seen to increase exponentially with age of initial emplacement.

Due to the exponential nature of Equation 8.2, the older LIPs will have much larger revised estimates, as displayed in Figure 8.5.

Following the revision of the initial areas of the LIP database, new decay constants are required to be calculated. The ‘major’ events, as termed by Mills et al (2014b), have individual decay constants calculated to recover their present areas, and as before a single decay constant is applied to the rest of the LIPs such that the present basaltic area is recovered. This constant is calculated as 0.017933, with the revised LIP areas displayed in Figure 8.6.

Regardless of whether the initial or revised areas are used, basaltic area is calculated at a temporal resolution of 0.1Myr, and this is normalised to the present to give a forcing file. Both approaches use the same ocean island

basalt/island arc contribution as calculated from the subduction zone data of Mills et al (in preparation).

Figure 6.5 displays the initial basalt area calculation, with error bars displaying the +50%/-20% range applied by Mills et al (2014b). In comparison, following the application of the decay equation of Hay et al (2006), Figures 8.7 and 8.8 display the extremely large increase in basalt area for the Late Proterozoic, although for the most recent periods of the Phanerozoic the +50% error on the initial estimate gives a greater area than the revised areal data.

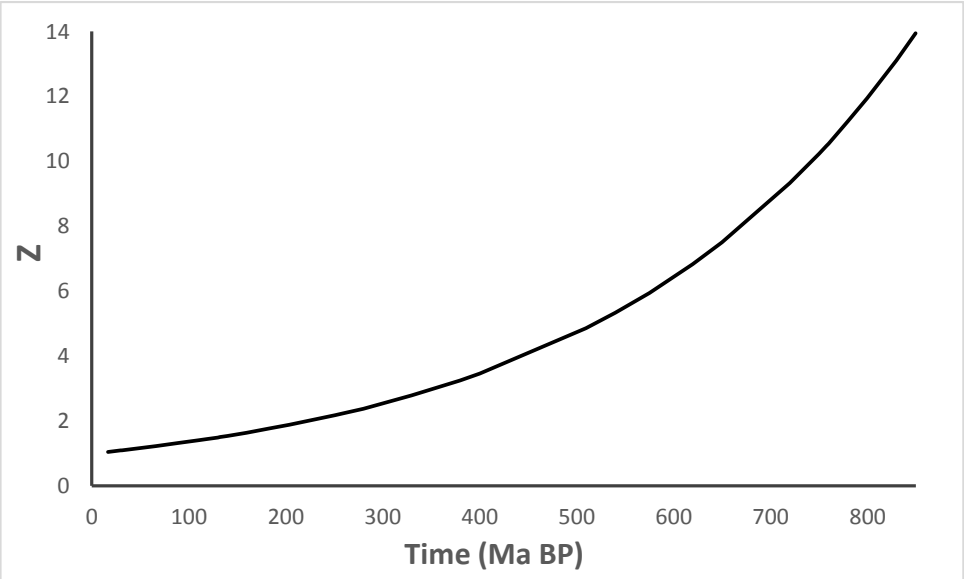

Figure 8.5 Exponential decay curve displaying the change in 'z' values over the past 850Ma by which the initial areas at time of emplacement 't' are multiplied by for each LIP to give a revised upper initial area estimate, following Hay et al (2006).

As the geological accuracy of the 'Hay' basalt area forcing cannot, as of yet, be verified by revised estimates of LIP area in the literature, it is therefore not used in the updated baseline model configuration, which instead favours the use of the average basalt area forcing following the use of the unrevised initial areas. Despite this, it offers a method for investigating the impacts of enhanced basaltic area through the majority of the Phanerozoic.

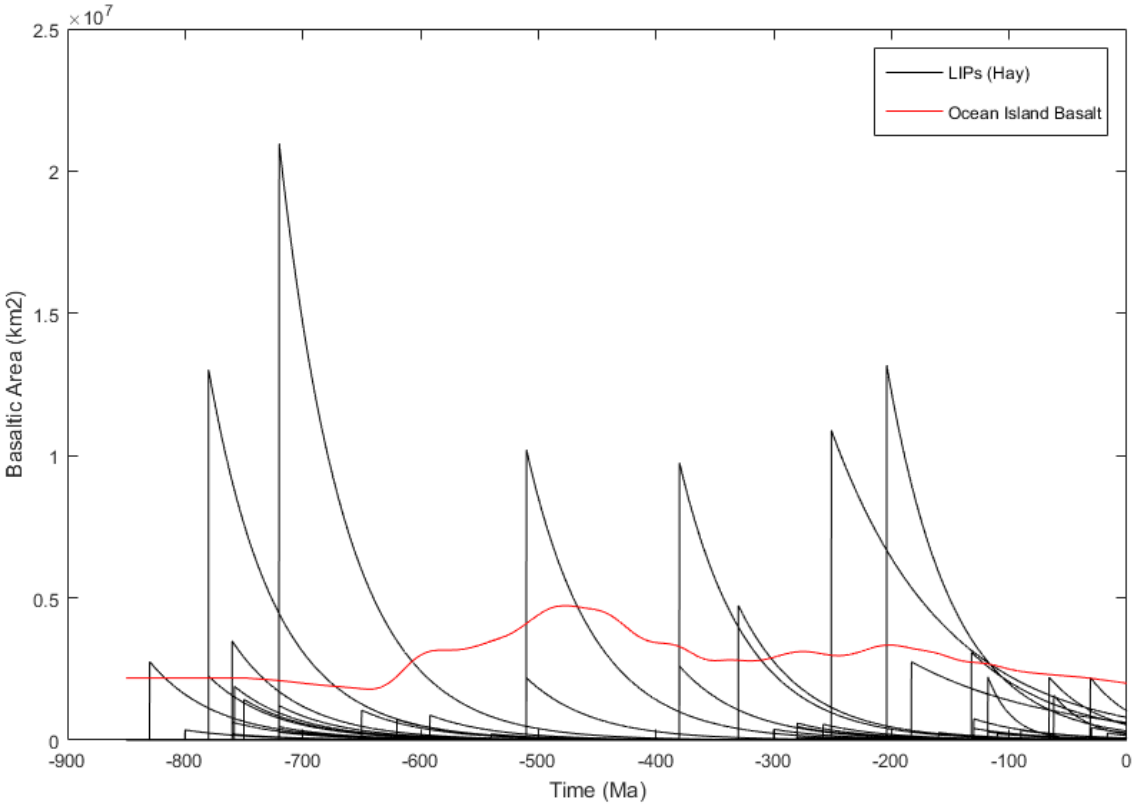

Figure 8.6. Reconstruction of basaltic area from 850Ma to present following the Hay et al (2006) revision, with the black curves displaying the contribution of individual LIPs, and the red curve showing the contribution from ocean island basalts, assumed proportional to subduction zone lengths.

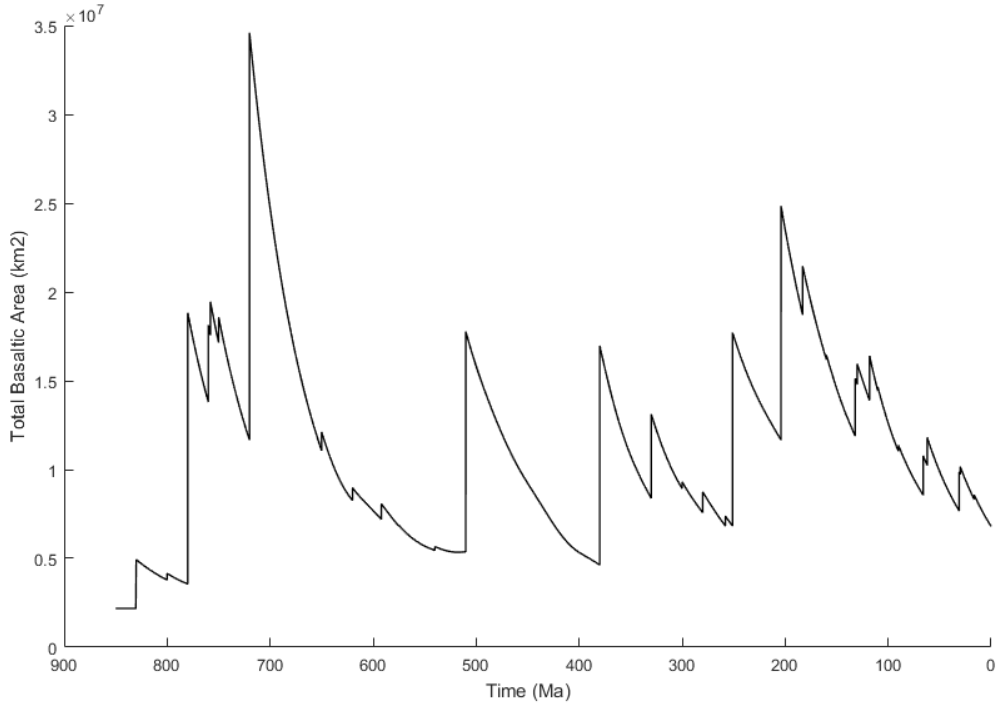

Figure 8.7. Reconstruction of total basaltic area from 850Ma to present, combining both the LIP and ocean island basalt contributions, following Hay et al (2006) revision of LIP areas.

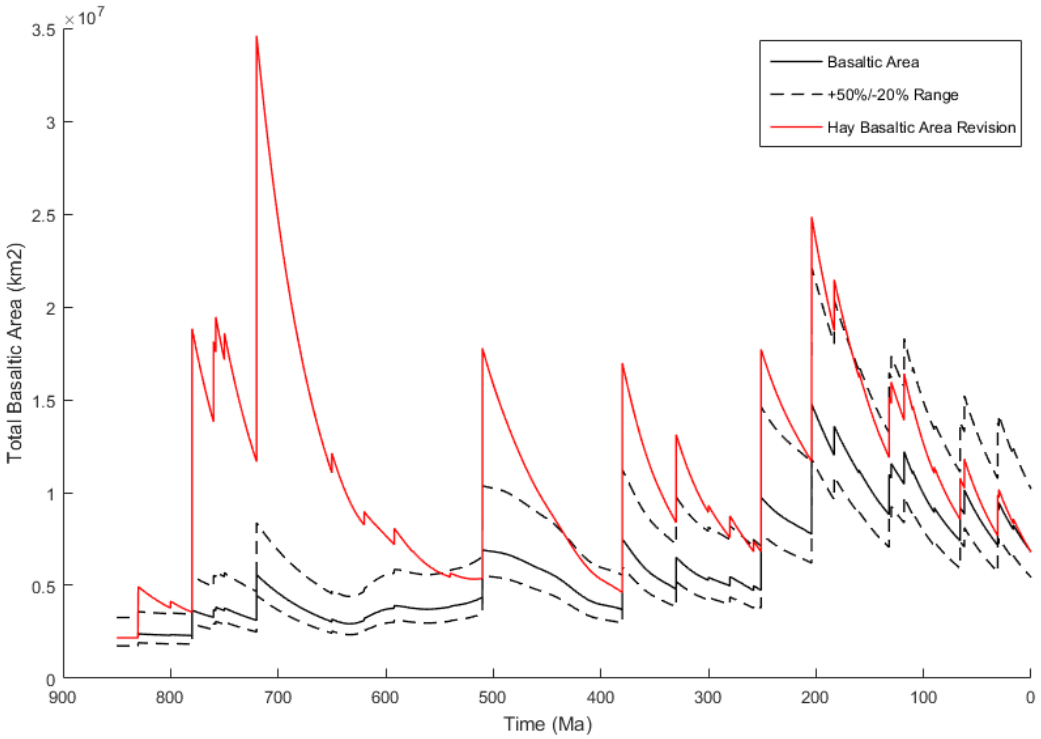

Figure 8.8. Comparison of reconstructions of total basaltic area from 850Ma to present, forming the four basalt area forcings used in this study.

8.1.3. Linking Seafloor Weathering to Spreading Rates

As discussed, seafloor spreading rates are also suggested as a dominant control on the low temperature alteration process (Steuber and Veizer, 2002). As such, the temperature-based function is updated to scale with the degassing forcing following Mills et al (in preparation), as this is derived from subduction zone lengths throughout the Phanerozoic. The updated flux equation is displayed in Equation 8.5:

$$sfw = sfw_t * k_{sfw} * D \quad (8.5)$$

An increase in subduction is argued to be indicative of an increase in seafloor spreading (i.e. Berner et al., 1983; Archer, 2010), and so scaling the temperature-based seafloor weathering dependence with the degassing forcing of Mills et al (in press) is seen as an appropriate method of approximating the additional dependence of seafloor weathering upon seafloor spreading rates.

To retain consistency, when seafloor weathering is linked to spreading rates, the mantle hydrothermal strontium flux is also coupled to spreading rates.

8.1.4. Increasing the Complexity of the Strontium Isotope System

The strontium isotope system presented in Section 6.1.3 is a vast simplification of not only reality, but also other model approaches (i.e. Francois and Walker, 1992; Mills et al., 2014b). Consequently, should a more complex system offer a similar range of predictions to the simplified system, the updated COPSE model will offer greater comparability with both stratigraphic data, as well as other biogeochemical models.

The system is essentially reverted to that of Mills et al (2014b); following the coupling of seafloor weathering to spreading rates through the degassing forcing of Mills et al (in preparation), consistency is maintained by linking the mantle strontium input to the same forcing. The decay of ^{87}Rb is switched back on, and sediment strontium is allowed to fluctuate over time.

8.2. Results

8.2.1. Inclusion of a Dynamic Land Area

Granitic area is calculated following the basaltic area, carbonate area, and total land area forcings. The granite weathering component of the total silicate weathering flux is then calculated using this areal variability.

As displayed in Figure 8.1, incorporating a land area forcing based on the palaeomaps of Blakey (2011) should therefore cause reduced granitic area throughout the Phanerozoic, especially during the Palaeozoic and Late-Mesozoic. Consequently, it is expected that the inclusion of such a palaeo-land area forcing will thus lower the $^{87}Sr/^{86}Sr$ curve due to reduced ^{87}Sr input from the reduced weathering of old rocks given the expected fall in granitic weathering.

Moreover, as granitic weathering is expected to decline, the total silicate weathering flux must therefore be expected to fall, and so pCO_2 and temperature are expected to increase.

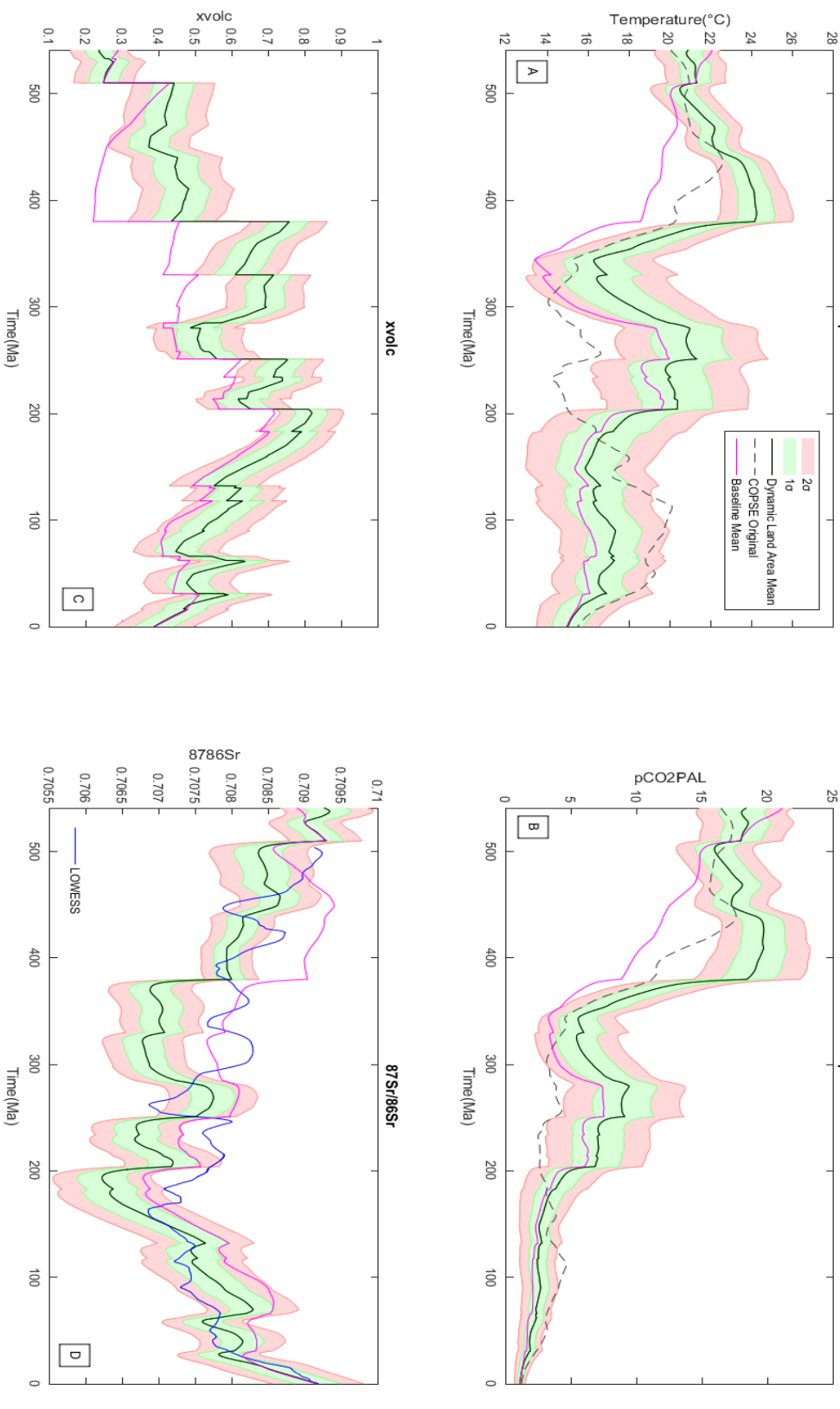

Figure 8.9. Phanerozoic predictions of (A) temperature, (B) pCO_2, (C) xvolc, and (D) $^{87}Sr/^{86}Sr$ following the inclusion of a dynamic land area forcing. These predictions are compared to the mean prediction of the baseline run, as well as proxy data. A Monte Carlo simulation of 100runs was used for the two model configurations, with error displayed as ±1 and ±2 standard deviations (σ) from the mean.

Figure 8.9 shows that such expectations are met when a dynamic land area is included within the model. Both predicted global temperature and pCO_2 are consistently greater than that of the baseline model as a result of the large reduction in silicate weathering on a reduced land area. Confusingly, xvolc increases which is generally associated with increased basaltic weathering and thus reductions in temperature and pCO_2. This is the case as basalt area is calculated independently of land area, and so the proportion of basaltic area increases under a reduction in land area as land area only affects granitic area.

Figure 8.9D shows a consistent decrease in the predicted $^{87}Sr/^{86}Sr$ ratio through the Phanerozoic. This follows the suggestion of reduced radiogenic ^{87}Sr input as a result of reduced granite area.

Including a dynamic land area gives a much better agreement with the LOWESS curve in the Ordovician and Silurian, as well as from 150Ma to present, fixing some of the key issues with the baseline model. However, the Devonian through Carboniferous is characterised by an $^{87}Sr/^{86}Sr$ prediction that is far too low, invalidating the predicted curve. Moreover, whilst the use of a dynamic land area does improve the $^{87}Sr/^{86}Sr$ prediction in some intervals of the Phanerozoic, the temperature and pCO_2 predictions are argued to be worse than that of the baseline model – for example the Ordovician is characterised by a steadily increasing temperature whereas proxy data (Trotter et al., 2008) implies a gradual decline.

8.2.2. Impacts of Accounting for Incomplete Preservation of LIPs

As a result of the modified basalt area forcing following the sediment deposition data of Hay et al (2006), it is clear in Figure 8.10 that LIP emplacement has a far more pronounced impact, especially regarding xvolc and $^{87}Sr/^{86}Sr$. As such, falls in $^{87}Sr/^{86}Sr$ associated with LIP emplacement have much greater magnitudes.

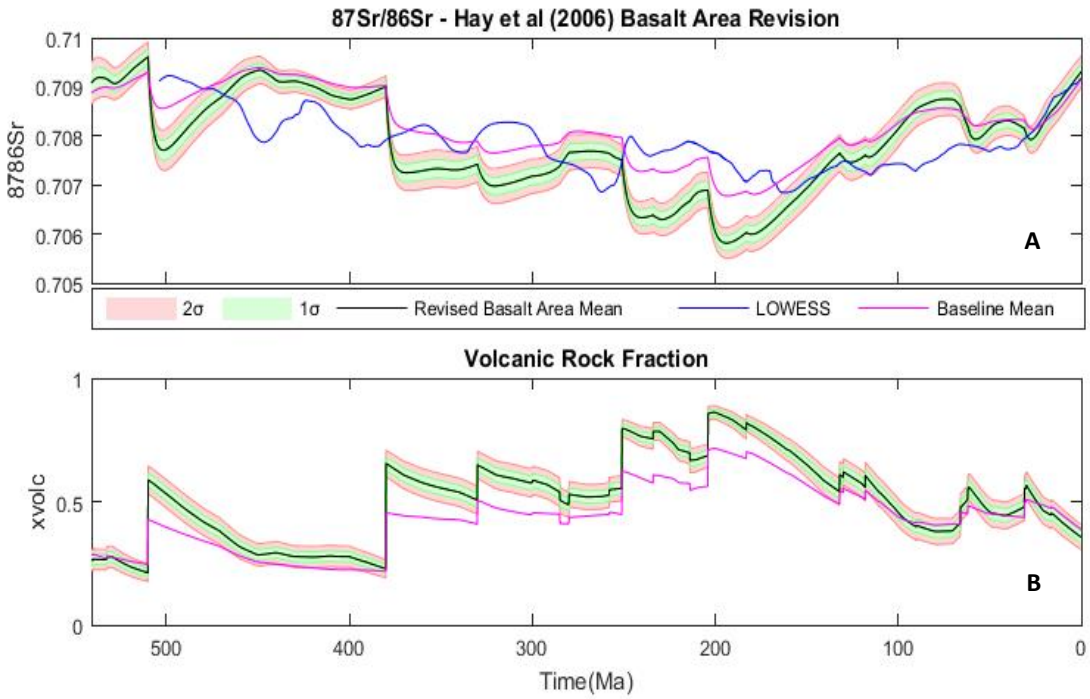

Figure 8.10. Phanerozoic predictions of (A) $^{87}Sr/^{86}Sr$, and (B) xvolc following the upwards revision of basaltic area. These predictions are compared to the mean prediction of the baseline run, as well as proxy data. A Monte Carlo simulation of 100runs was used for the two model configurations, with error displayed as ±1 and ±2 standard deviations (σ) from the mean.

Despite this, LIP decay occurs rapidly in order to recover the present LIP basalt area and so the length of the perturbation is rather short, allowing $^{87}Sr/^{86}Sr$ to recover to higher values somewhat. This is clear in the Ordovician and Silurian, whereby the large areal increase of the Antrim and Kalkarindji LIPs cause a dramatic drop in $^{87}Sr/^{86}Sr$ in the Mid-Cambrian, however by the Early-Mid Ordovician, the predicted mean $^{87}Sr/^{86}Sr$ recovers to values similar to those of the baseline model. This follows the decline in xvolc between 510 and 380Ma, a period in which no LIPs are emplaced.

Individual decay constants cannot be calculated for such old LIPs as there remains no basalt from these events at present day. As such, the true impact of such dramatic increases in LIP area, especially in the Palaeozoic, may be offset or hidden, at least to an extent, by the assumption of exponential decay.

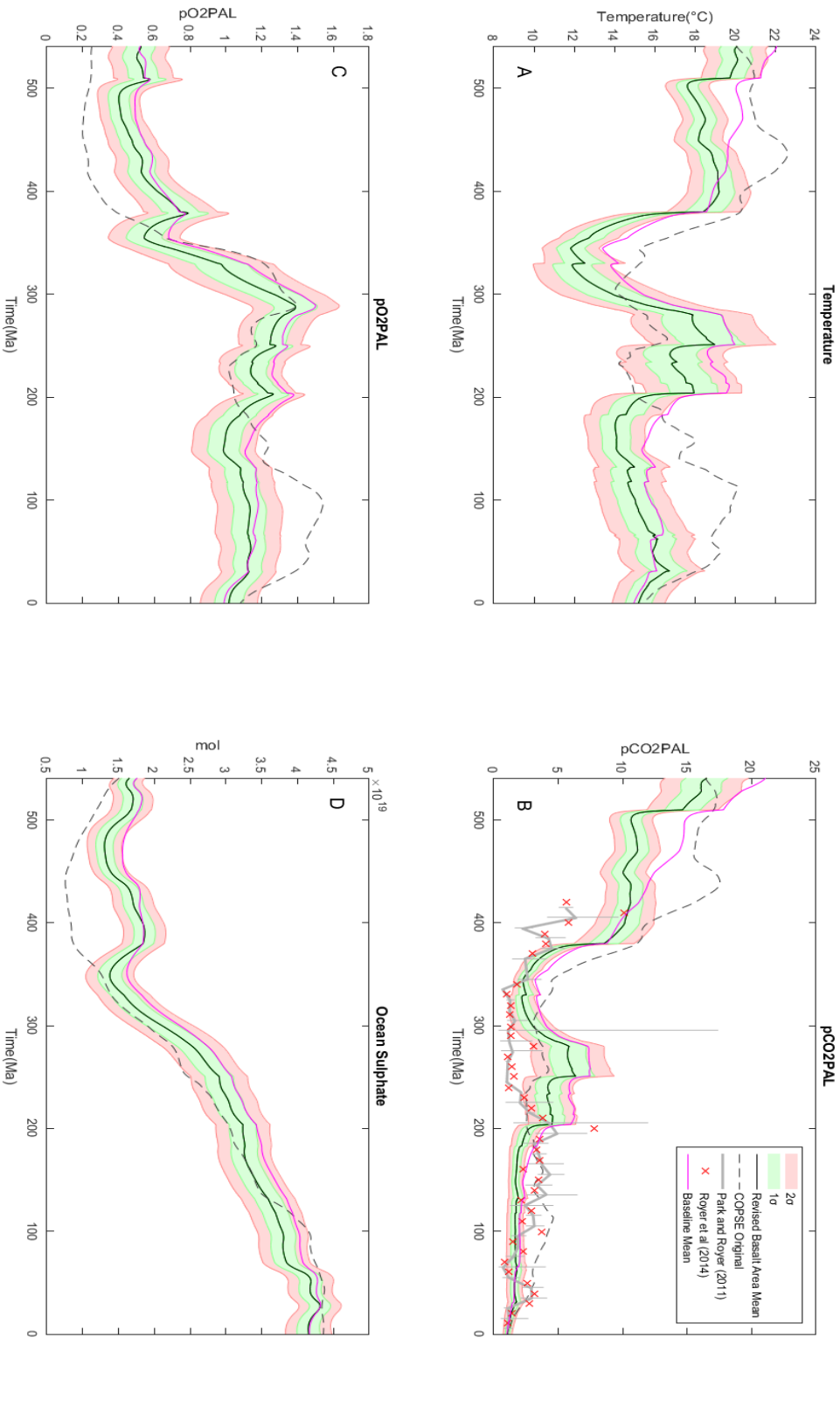

Figure 8.11. Phanerozoic predictions of (A) temperature, (B) pCO_2, (C) pO_2, and (D) ocean sulphate concentration following the upwards revision of basalt area after Hay et al (2006). These predictions are compared to the mean prediction of the baseline run, as well as proxy data. A Monte Carlo simulation of 100runs was used for the two model configurations, with error displayed as ±1 and ±2 standard deviations (σ) from the mean.

Regardless, there are clear impacts upon predicted global temperature, pCO_2 and pO_2 as seen in Figure 8.11. Temperature and pCO_2 show a minor reduction through the Early-Palaeozoic, however the Permo-Carboniferous is characterised by ~1PAL and ~1.5^{0}C decreases in pCO_2 and temperature respectively compared to the baseline run, given the large increase in basaltic, and thus silicate, weathering. This shows better agreement with the pCO2 proxy data of both Park and Royer (2011) and Royer et al (2014), and approaches the ~2PAL pCO_2 suggested by Crowley and Berner (2001) for this period. Despite this, the length of the Permo-Carboniferous glaciation remains underestimated as no additional LIPs are added.

Given the increased frequency of LIP emplacement from 380Ma to present compared to the Early-Palaeozoic, the upwards revision of initial LIP area results in a consistently increased basalt area from ~380Ma to ~100Ma. As a consequence, this period is characterised by mean $^{87}Sr/^{86}Sr$, pO_2, temperature, pCO_2, and ocean sulphate concentration consistently lower than mean baseline predictions.

As discussed, pCO_2 and global temperature are lower than baseline from the Permo-Carboniferous, with this trend continuing to the Late-Mesozoic. Whilst the Permo-Carboniferous is characterised by improved agreement with the proxy data, the predicted pCO_2 falls below the proxy data for the majority of the Mesozoic, with the baseline run showing better agreement during this interval. Reductions in pCO_2 and temperature thus cause a reduction in pO_2 as a function of the reduced phosphorus weathering flux limiting marine productivity and thus organic carbon burial. Reduced pO_2 thus explains the coincident reduction in ocean sulphate concentration, as the marine sulphate concentration is increased by increased oxidation of sulphides under enhanced pO_2 (Kah et al., 2004).

Although this revision of LIP area has notable impacts upon the key environmental variables of temperature, pCO_2 and pO_2, following the Kalkarindji and Antrim LIPs at 380Ma, the increased frequency of LIP emplacement results in an invalidation of the $^{87}Sr/^{86}Sr$ prediction. The mean predicted isotopic ratio falls far below that of the LOWESS dataset (McArthur et al., 2012) until ~150Ma, with a minor positive excursion during the Permian that, whilst bringing

the mean predicted $^{87}Sr/^{86}Sr$ value more in line with the LOWESS data, is in opposition to the negative inflection displayed by the proxy data.

Consequently, whilst revising LIP initial areas following the sediment deposition data of Hay et al (2006) causes notable changes in the model predictions, as it invalidates the $^{87}Sr/^{86}Sr$ prediction it cannot be included in the baseline model.

8.2.3. Impacts of Linking Seafloor Weathering to Spreading Rates

As discussed in Section 5.2.2.2, both seafloor spreading and seafloor temperature have been suggested as dominant controls on the seafloor weathering flux (i.e. Brady and Gislason, 1997; Gillis and Coogan, 2011; Coogan and Gillis, 2013; Farahat et al., 2013). Coupling seafloor weathering and the mantle strontium flux to degassing has clear impacts on model predictions across the Phanerozoic, as displayed in Figures 8.12 and 8.13.

The degassing forcing of Mills et al (in preparation) peaks in the Early-Palaeozoic. As a consequence, this period is characterised by an increased magnitude of the seafloor weathering flux, as well as hydrothermal strontium input. Therefore, the predicted mean $^{87}Sr/^{86}Sr$ ratio falls dramatically compared to the baseline run, nearing the Ordovician minima.

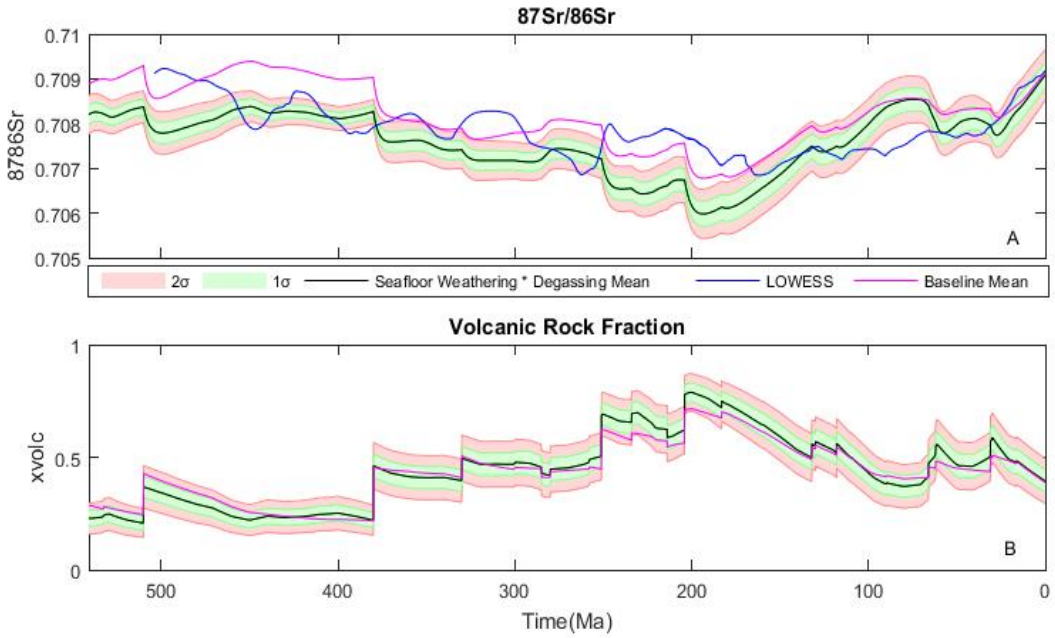

Figure 8.12. Phanerozoic predictions of (A) $^{87}Sr/^{86}Sr$, and (B) xvolc following coupling of seafloor weathering to degassing (and so the mantle strontium flux to degassing). These predictions are compared to the mean prediction of the baseline run, as well as proxy data. A Monte Carlo simulation of 100runs was used for the two model configurations, with error displayed as ±1 and ±2 standard deviations (σ) from the mean.

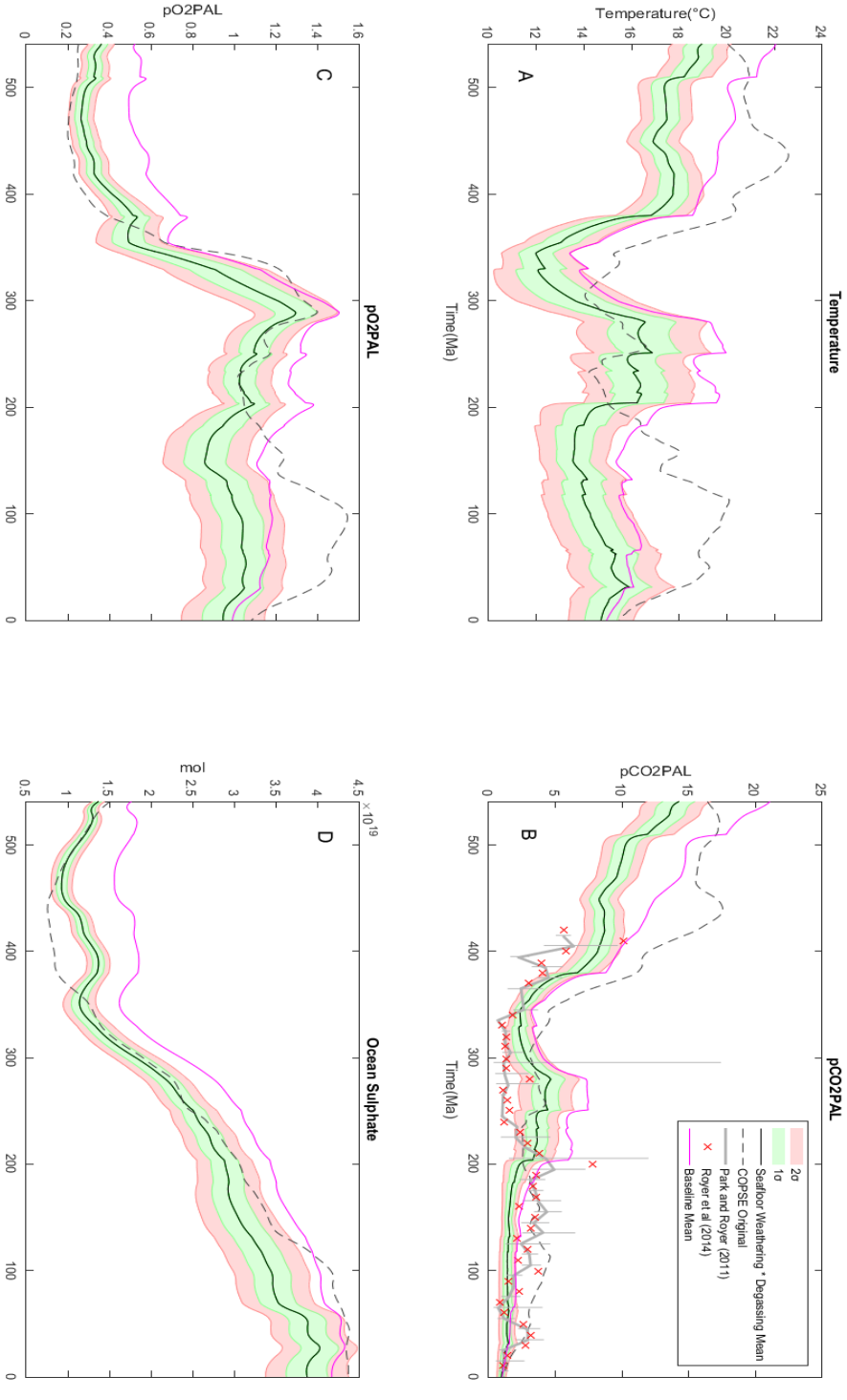

Figure 8.13. Phanerozoic predictions of (A) temperature, (B) pCO_2, (C) pO_2, and (D) ocean sulphate concentration following the coupling of seafloor weathering to degassing (and so the mantle strontium flux to degassing). These predictions are compared to the mean prediction of the baseline run, as well as proxy data. A Monte Carlo simulation of 100runs was used for the two model configurations, with error displayed as ±1 and ±2 standard deviations (σ) from the mean.

When compared to the impact of an upwards revision of LIP area, as displayed in Figure 8.14, it suggests that the coupling of mantle strontium and seafloor weathering to spreading rates may be more important than increasing basaltic area with relation to the Ordovician $^{87}Sr/^{86}Sr$ minimum. On the other hand, recent research puts forward the argument that the coupled shifts in neodymium and strontium isotopes rules out a role of the seafloor weathering hydrothermal flux in causing the Ordovician $^{87}Sr/^{86}Sr$ decline as this shouldn't affect neodymium isotope ratios (Saltzman, pers. comm.).

In addition, Early-Palaeozoic temperature and pCO_2 are below that of the baseline run, with pCO_2 falling below 10PAL in the Mid-Ordovician. Accompanying this is a fall in pO_2 to levels similar to that of COPSE original. Unlike when basalt area is enhanced, these changes are not as a result of a large increase in xvolc. The peak in seafloor weathering (Figure 8.15), given the peak in degassing, acts as to increase the output flux of carbon from the atmosphere, rather than an increased basalt weathering flux.

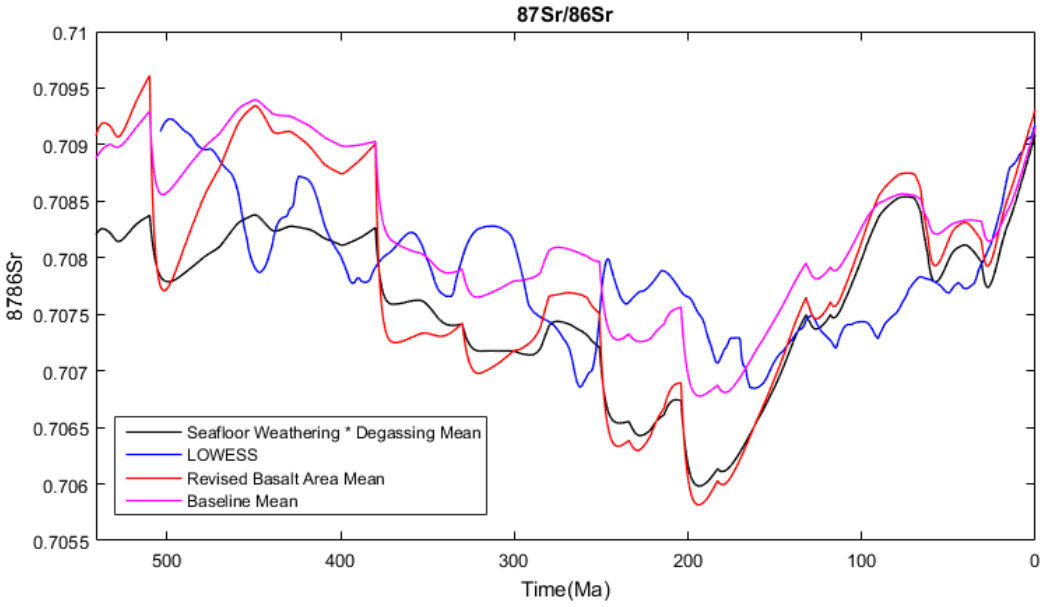

Figure 8.14. Comparison of the impacts of an upwards revision of basalt area and those following the coupling of seafloor weathering to degassing (and so the mantle strontium flux to degassing). The mean predictions are displayed following Monte Carlo simulations of 100 runs, and the runs are compared to both the mean baseline prediction and LOWESS proxy data (McArthur et al., 2012).

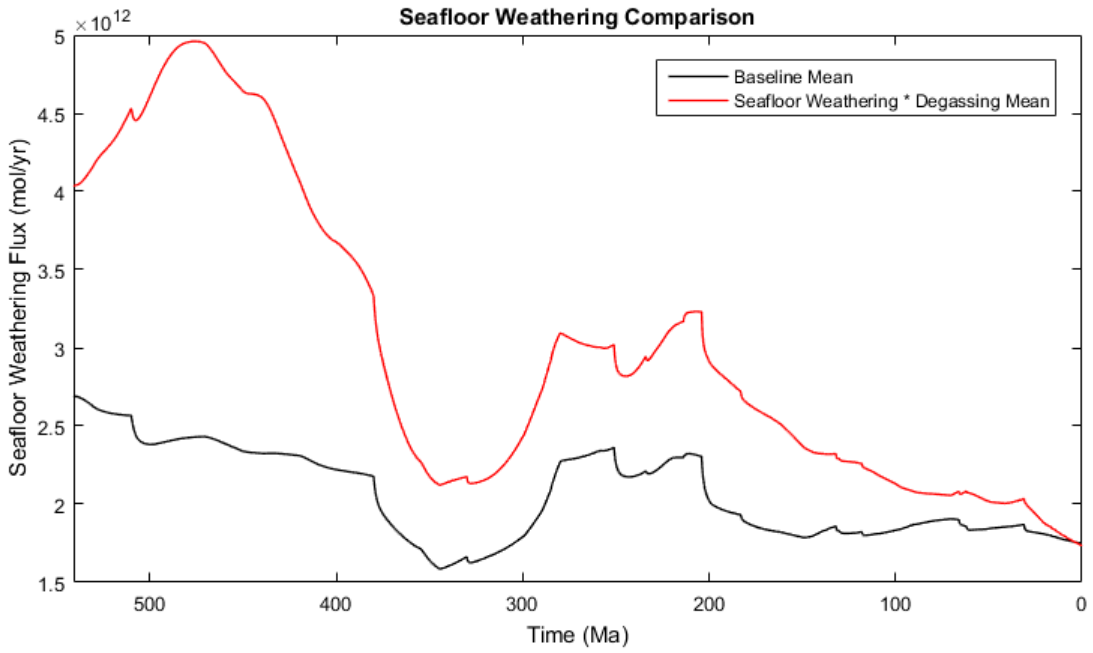

Figure 8.15. Mean Phanerozoic predictions of the seafloor weathering flux under the baseline configuration whereby seafloor weathering is only a function of seafloor temperature, and under a configuration whereby seafloor weathering is also coupled to seafloor spreading, represented by the degassing forcing.

As degassing decreases, the impacts of a coupled seafloor weathering-seafloor spreading system show high similarity with those following an enhancement of LIP area. With respect to pCO_2 and temperature, except for the Permian through Triassic, the model predictions show only minor differences between the two runs, with both showing better agreement with CO_2 proxies during the Permo-Carboniferous, but worse agreement in the Mid-Mesozoic.

Ocean sulphate concentration and pO_2 display a greater decrease from the baseline run compared to the impact of enhanced basaltic area, with Mid-Mesozoic pO_2 values falling to similar levels predicted by other biogeochemical models (i.e. Berner and Canfield, 1989; Berner, 2001; Arvidson et al., 2006; Royer et al., 2014).

8.2.4. Combined Impact of Additional and Updated Forcings

Combining these updates, as is clear in Figures 8.16 and 8.17, results in predicted minimum values for temperature, pCO_2, pO_2, ocean sulphate concentration and $^{87}Sr/^{86}Sr$ across the Phanerozoic, as the impact of the additional and updated forcings all act in the same direction. As stated, such a fall in pCO_2 offers better agreement with the proxy data for the Permo-Carboniferous, however the majority of other predictions are not as well constrained.

The post-glacial fall in pO_2, whilst offering better agreement with other modelling studies, contradicts recent research into insect wing lengths (Clapham and Karr, 2012), and so it is argued that the baseline pO_2 prediction is a better representation of Phanerozoic atmospheric oxygen trends. During this interval, predicted global temperature and pCO_2 are also far too low, falling to levels consistently similar too, if not below present day.

Moreover, predicted $^{87}Sr/^{86}Sr$ levels are extremely low, resulting from both the enhanced basaltic weathering flux as well as enhanced hydrothermal input, both of which increase the flux of non-radiogenic ^{86}Sr to the ocean. Such predictions invalidate the predicted $^{87}Sr/^{86}Sr$ record.

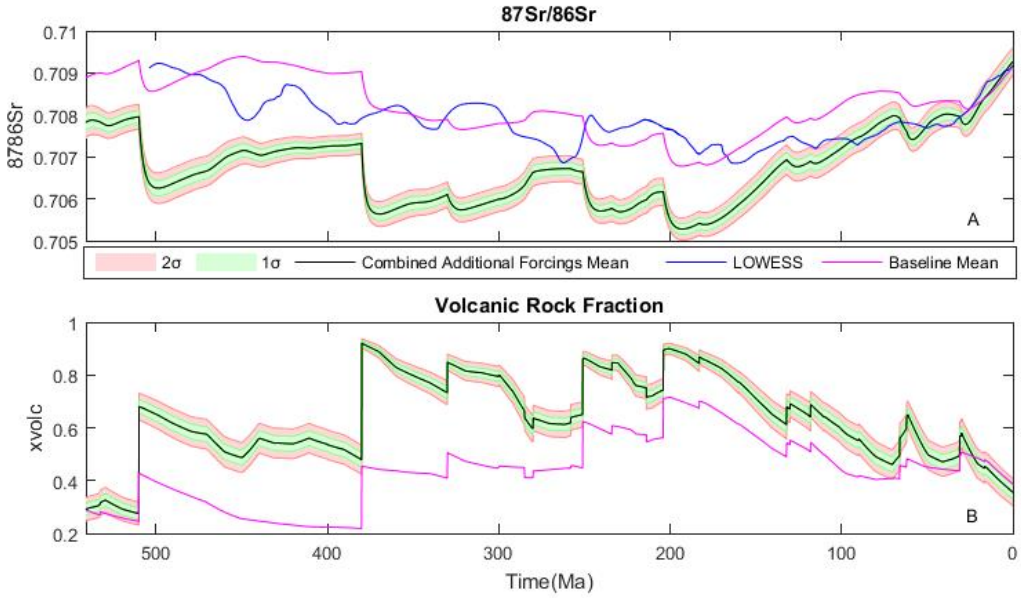

Figure 8.16. Phanerozoic predictions of (A) $^{87}Sr/^{86}Sr$, and (B) xvolc following combination of all three additional forcings; the inclusion of a dynamic land area, the upwards revision of basaltic area and the coupling of seafloor weathering to degassing. These predictions are compared to the mean prediction of the baseline run, as well as proxy data. A Monte Carlo simulation of 100runs was used for the two model configurations, with error displayed as ±1 and ±2 standard deviations (σ) from the mean.

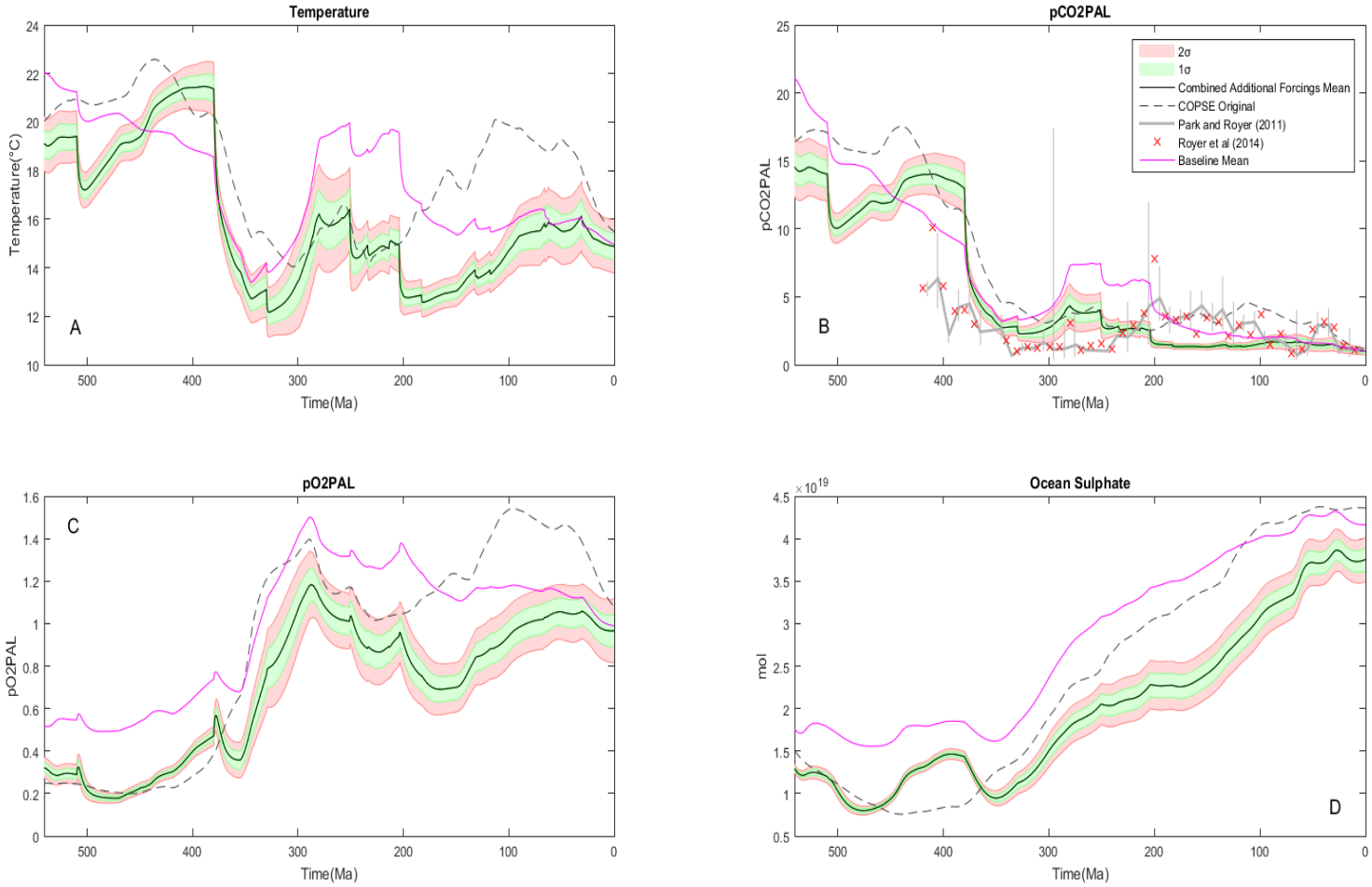

Figure 8.17. Phanerozoic predictions of (A) temperature, (B) pCO_2, (C) pO_2, and (D) ocean sulphate concentration following combination of all three additional forcings; the inclusion of a dynamic land area, the upwards revision of basaltic area and the coupling of seafloor weathering to degassing. These predictions are compared to the mean prediction of the baseline run, as well as proxy data. A Monte Carlo simulation of 100runs was used for the two model configurations, with error displayed as ±1 and ±2 standard deviations (σ) from the mean.

In addition, whilst the inclusion of such forcing updates significantly alters the magnitude of the predicted variables, the major Phanerozoic trends remain. The length of the Permo-Carboniferous glaciation remains underestimated, the Permian is still characterised by an associated peak in $^{87}Sr/^{86}Sr$ that is not recorded in the LOWESS record, and the Late-Cretaceous through to present day is still predicted to have an $^{87}Sr/^{86}Sr$ ratio far above that of the proxy data.

Consequently, although the baseline run is subject to large simplifications, increases in complexity through updating model forcings result in model predictions that are not only invalidated by the $^{87}Sr/^{86}Sr$ record, but may also be less accurate than the simplified baseline run in other areas, notably Mid to Late-Mesozoic temperature, pCO_2 and pO_2.

8.2.5. Increased Complexity of the Strontium Isotope System

As discussed, the major impact of adding complexity to the baseline model is to invalidate the predicted $^{87}Sr/^{86}Sr$ record by largely increasing the supply of non-radiogenic strontium, thus drawing the predicted curve far below that of the LOWESS data. However, as discussed, the modelled strontium isotope system is subject to large simplifications – both the decay of ^{87}Rb to ^{87}Sr, as described in Section 5.2.3 and Equation 5.4, as well as a dynamic carbonate strontium component, are not included.

The impact of Rubidium decay is to increase the supply of radiogenic ^{87}Sr, and so raise the $^{87}Sr/^{86}Sr$ curve, thus offering a potential method by which strontium isotope predictions are validated against the LOWESS data under the updated model forcings discussed previously.

However, as Figure 8.18 clearly displays, incorporating rubidium decay and a dynamic carbonate strontium subsystem, either individually or in conjunction, does not fix the discrepancies between the predicted curve and the LOWESS data under additional forcings. Rubidium decay acts as to raise the predicted $^{87}Sr/^{86}Sr$ curve far above that of the LOWESS data, whereas a dynamic carbonate strontium subsystem reduces the predicted curve to a new minimum level. As a consequence, it is thus argued that for a zero-dimensional biogeochemical modelling study of the Phanerozoic such as this one, a

simplified strontium isotope system offers the best prediction of the $^{87}Sr/^{86}Sr$ record that is largely consistent with the LOWESS proxy data, even though it is missing key components of the known strontium isotope system.

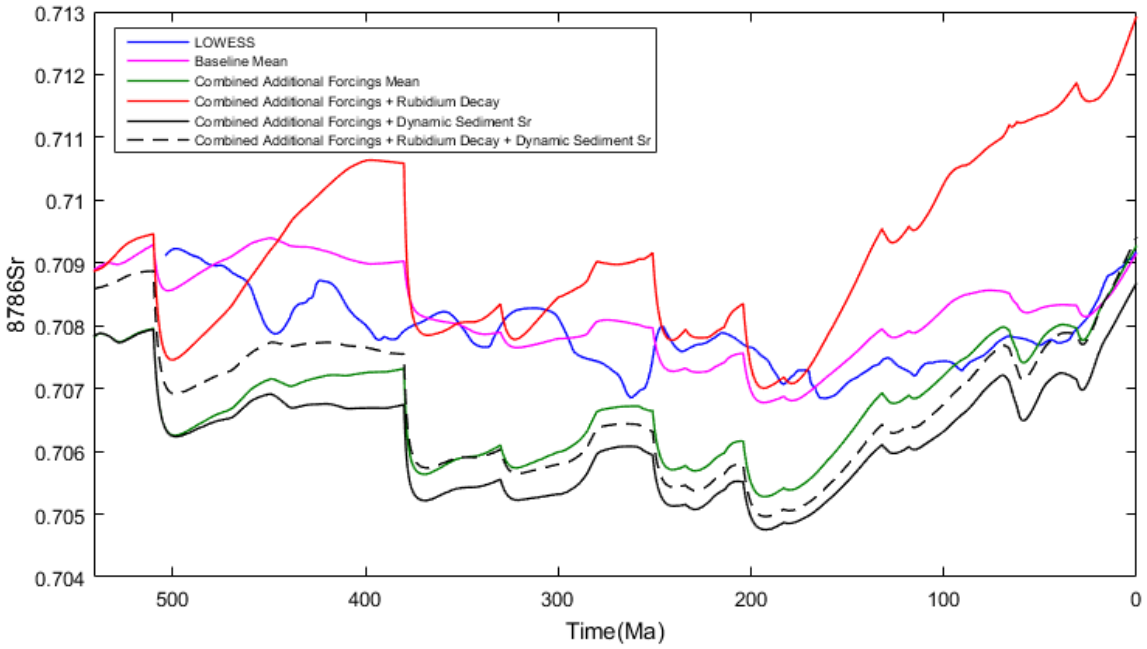

Figure 8.18. Comparison of mean model $^{87}Sr/^{86}Sr$ predictions under varying degrees of strontium isotope system complexity, with all three additional forcings implemented into the model run. These mean curves are compared to the mean prediction of the baseline run and the LOWESS proxy dataset (McArthur et al., 2012).

9. Conclusions

The major aim of this study was to update geologic forcings of the COPSE model, such that the model leads to improved predictions of the major environmental variables of temperature, pCO_2 and pO_2 across the Phanerozoic, but also reproduces, and is thus validated by, the broad-scale strontium isotope record.

Following the revision of the uplift, degassing and basaltic area forcings, as well as the incorporation of basalt weatherability functions, the updated model predictions display clear differences from COPSE original (Bergman et al., 2004).

Temperature and pCO_2 show a gradual decline in the Early Phanerozoic, consistent with the $\delta^{18}O$ record of Trotter et al (2008) – this is argued to be much improved over COPSE original which displays consistently higher global temperatures through this interval. Despite this, the Hirnantian glaciation remains unrepresented under purely geologic forcing factors. Whilst both a peak in uplift (Kump et al., 1999) and, under a simplified approach, continental drift (Nardin et al., 2011) are considered, this likely relates to the LIP-driven nature of the model, with no such province recorded for the Ordovician. As such, geologic processes alone seems insufficient to drive pCO_2 down sufficiently to initiate glacial conditions, acting instead to drive the long term cooling trend.

However, modelled pCO_2 in the Ordovician approaches the 8-10PAL threshold (i.e. Poussart et al., 1999; Herrmann et al., 2004; Pohl et al., 2014; 2015) suggested to separate warm and cool climate modes in the Ordovician. Consequently, it suggests that geologic forcing factors may have been necessary to cool the climate sufficiently to approach this threshold, but an additional factor, for example the weathering by early non-vascular plants (Lenton et al., 2012), may have been required to push the climate past the threshold, thus initiating icehouse conditions. Such hypotheses are beyond the realms of this study, and offer an interesting opportunity to further the work undertaken.

As with other biogeochemical models, the evolution of vascular plants causes a dramatic fall in temperature and pCO_2, leading into the Permo-Carboniferous

glaciation (i.e. Veevers and Powell, 1987; Isbell et al., 2003; Frank et al., 2008; Royer, 2014). This glaciation, whilst represented in the updated model, is largely underestimated in length. Whilst an increase in degassing and a concurrent decrease in uplift, alongside a reduction in basaltic weathering may have played a part, the major factor forcing the early post-glacial rise in temperature and pCO_2 is the dramatic fall in organic carbon burial attributed to the reduction in the C:P burial ratio of plant biomass following the evolution of lignolytic organisms (i.e. Robinson, 1990).

This is an arbitrary decrease, and recent work (Nelsen et al., 2016) argues that these organisms were present much earlier in the Phanerozoic, with unique climatic conditions acting as to permit vast coal accumulation in the Carboniferous/Permian. As a result, whilst a major issue with the updated model as it currently stands, the fact that this is an arbitrary decrease means that following future research into the Phanerozoic history, and importance, of lignin and associated lignolytic organisms, the model can be revised which should improve temperature and pCO_2 predictions during the Permo-Carboniferous.

Through the Mesozoic there is excellent agreement with CO_2 proxies, especially from 200Ma to present, although shorter term trends, for example the Eocene maximum (Royer, 2014), are not represented.

The revised prediction of the Phanerozoic history of atmospheric O_2 is argued to be improved. An increase through the Early-Palaeozoic compared to COPSE original is consistent with recent research (i.e. Yan et al., 2009; 2012; Lenton et al., in press), yet the mean prediction of ~0.6PAL remains consistent with the lack of fossil charcoal for this interval. Other models predict pO_2 levels >15-17% (i.e. Berner and Canfield, 1989; Berner, 1999; Berner and Kothavala, 2001; Arvidson et al., 2006) for this interval, for which there is currently no supporting geological data.

The rise of vascular plants leads to a peak in pO_2 in the Carboniferous. Whilst the updated model increases the magnitude of this increase over COPSE original by ~0.7-1PAL, the predicted peak in pO_2 remains lower than the overestimates of Berner and Canfield (1989), Berner and Kothavala (2001), and

Arvidson et al (2006). This is consistent with the known persistence of forests through this interval.

Following the peak in pO_2, atmospheric O_2 declines gradually, offering a better agreement with the fossil wing length data of Clapham and Karr (2012) than the GEOCARBSULF prediction (Berner, 2006; 2009). Later in the Mesozoic and Cenozoic, the updated model is largely consistent with other biogeochemical models, and fixes a major issue in COPSE original whereby Mesozoic pO_2 rises above Carboniferous levels.

The revision and development of forcings directly from geologic data allows model predictions of the broad-scale Phanerozoic strontium isotope record, which when compared to proxy data offers a method for validating model predictions.

The modelled strontium isotope system is simplified from that of Mills et al (2014b), and offers generally good broad-scale agreement with the LOWESS dataset across the Phanerozoic. Excellent agreement is observed from the Mid-Devonian through Carboniferous, the Early to Mid-Mesozoic and the Mid to Late-Cenozoic, with the LOWESS proxy dataset falling within two standard deviations of the mean prediction.

There are however, some key disagreements, notably in the Ordovician, Devonian, Permian and Mesozoic. The lack of a recorded LIP in the Ordovician means that the $^{87}Sr/^{86}Sr$ minimum is not represented by the model. Attempts to address this resulted in an invalidation of the predicted curve later in the Phanerozoic, as was the case under a more complex strontium isotope system, or too large a basalt area perturbation that should, if it had occurred, be present in the geologic record.

Emplacement of the Yakutsk-Vilyui and Kola-Dnieper LIPs postdates the proxy decline in Devonian $^{87}Sr/^{86}Sr$, resulting in model disagreement with the LOWESS record given the dependence of the modelled strontium isotope system on the LIP record.

The Permian is characterised by a contradictory prediction of the model compared to the $^{87}Sr/^{86}Sr$ proxy data, which temporally correlates with the underestimation of the Permo-Carboniferous glaciation. This implies that

reduced basaltic weathering may have played a role somewhat in raising Permian global temperature and pCO_2 in the updated model.

Whilst the values of the predicted strontium isotope record disagree with the LOWESS dataset during the Late Mesozoic, the broad scale trend is reproduced. The discrepancy in values may be linked to the initially simplified seafloor weathering flux that doesn't scale with seafloor spreading, suggested to be important during the Mesozoic (Gills and Coogan, 2011; Coogan and Gillis, 2013).

Increasing the complexity of the strontium isotope system by coupling the mantle strontium flux to degassing, and linking the weathering of continental flood basalts to uplift results in a reduction in $^{87}Sr/^{86}Sr$ values throughout the Phanerozoic. Whilst this offers improved predictions in some intervals, it invalidates the prediction in others. As such, a simplified strontium isotope system is seen to offer the best approximation of the Phanerozoic record in the updated COPSE model.

As with the $^{87}Sr/^{86}Sr$ record, the broad-scale Phanerozoic trends in both $\delta^{13}C_{carb}$ and $\delta^{34}S$ are also well reproduced by the updated model, with proxy data falling within two standard deviations of the predicted mean throughout the majority of the Phanerozoic, although shorter term variations are not represented. A notable improvement in the $\delta^{34}S$ record over COPSE original is seen in the Early-Palaeozoic, which in the updated model is characterised by large increases in both the weathering and burial in pyrite. Ocean sulphate concentrations show a stepwise increase in the Permo-Carboniferous, consistent with proxy data and atmospheric pO_2 predictions (Algeo et al., 2015).

Following the initial analyses, the model is increased in complexity to investigate whether an inclusion of additional and updated geologic forcings acts as to improve model predictions. A dynamic land area forcing is added to the model, the basaltic area forcing is revised to account for incomplete preservation and seafloor weathering is coupled to degassing.

Whilst arguably a better representation of reality, all three of these updates act as to at some point invalidate the predicted $^{87}Sr/^{86}Sr$ curve, and combining them acts as to draw the $^{87}Sr/^{86}Sr$ curve to lower values as all the additional forcings act in the same direction with respect to $^{87}Sr/^{86}Sr$.

In an attempt to address this, the strontium isotope system is increased in complexity to account for both the decay of ^{87}Rb to ^{87}Sr, and a dynamic sediment strontium subsystem. Rubidium decay causes a dramatic increase in the predicted strontium isotope record through the majority of the Phanerozoic, even from initially minimum levels, with this increase causing a far too radiogenic system. Combining this with a dynamic sediment strontium subsystem overrides this, causing too large a reduction in the predicted record.

Consequently, it is argued that a simplified strontium isotope system offers the best approximation of the broad-scale $^{87}Sr/^{86}Sr$ record for the Phanerozoic in such a simple biogeochemical model.

There are several reasons as to why the more complex model largely performs more poorly than the simplified model. Although the LIP weatherability forcing aims to correct for this to an extent, the distribution of rock weathering is assumed uniform. Consequently, the impact of a dynamic land area, in which the land area is almost always lower than present, is to reduce global granite weathering given that there is less rock available to weather. This in turn offers an explanation for why the resultant $^{87}Sr/^{86}Sr$ prediction is too low as the riverine flux of ^{87}Sr-rich material is reduced. In reality, it is argued that at present, ~70% of the global weathering flux derives from ~10% of the land area (Hartmann et al., 2014), with soil shielding reducing chemical weathering over large areas. As a result, given the simplicity of the uplift forcing, the model would be improved by considering the area of highly-weatherable regions through the Phanerozoic. Such an improvement would be beneficial as an increased flux of radiogenic strontium would allow the incorporation of a dynamic carbonate strontium subsystem without drawing the projected record too low.

This feeds in to an additional factor affecting the model – the forcings themselves may be too oversimplified. This isn't an issue with the simplified model as the aim is to investigate the long-term trends, however when the complexity is increased in an attempt to improve the structure of the predicted strontium isotope record, this becomes a problem. To reproduce the sinusoidal structure of the strontium isotope record (i.e. McArthur et al., 2012), it may be that sinusoidal uplift/degassing forcings are required.

Moreover, a major factor affecting the modelled strontium isotope system is the supply of non-radiogenic strontium from the weathering of LIP basalts. However, in the present model the areal coverage of basalts is a dominant factor affecting this supply, rather than the actual amount of basalt undergoing weathering. As such, the emplacement of LIPs results in potential overestimations in the drawdowns in $^{87}Sr/^{86}Sr$ that follows such emplacement. Should an LIP be emplaced in a largely non-weatherable region, it follows that the flux of non-radiogenic strontium would be smaller than otherwise. The LIP weatherability forcing looks to offer a simple consideration for this, however an improvement would be to incorporate a dynamic basalt area forcing, with the areal coverage of basalts changing as a response to their weathering, and a more detailed quantification of the weatherability of their locations (i.e. distance from coastlines, relief). The essentially instantaneous modelled drawdowns in the predicted $^{87}Sr/^{86}Sr$ record are observed to have major effects on the prediction, and, given that the more complex model is invalidated by drawing the predicted $^{87}Sr/^{86}Sr$ record below the LOWESS curve, an improved quantification of this major source of non-radiogenic strontium may act to offset the drawdowns by the inclusion of a dynamic carbonate subsystem, the linking of degassing and seafloor spreading, and the inclusion of a dynamic land area forcing.

In addition, granite area is a function of the basalt, carbonate and land area forcings. Consequently, the major flux of radiogenic strontium is subject to the uncertainties involved with the derivation of these forcings. Carbonate area follows Berner and Kothavala (2001), and so in turn Bluth and Kump (1991), a study in which the reconstructed palaeogeology is somewhat erroneous, for example the large overestimation of sandstone area. Given the quantification of granite area, the emplacement of an LIP, given the generally slower changes in carbonate area, must essentially remove an area of granite of the same size, thus potentially exaggerating the drawdown in $^{87}Sr/^{86}Sr$ as a result of a large drop in the radiogenic flux, which in reality may not be affected to such a degree. Therefore, an improvement to the model would be to derive a distinct forcing for the area of granite over the Phanerozoic.

Thus, it may not be the increased complexity of the model that is the issue, but the forcings affecting the fluxes of strontium to the ocean. As the impact of the

complex model is to drawdown the predicted $^{87}Sr/^{86}Sr$ curve, improvements acting as to increase the radiogenic flux from continental weathering would allow the complex model to run without invalidation of the predicted $^{87}Sr/^{86}Sr$ record.

In summary, this study provides a platform upon which the COPSE model can be further developed, with a variety of opportunities for future work presented. It is clear that whilst geologic factors exert a major control on the long-term carbon cycle, shorter term dynamics, for example the Hirnantian glaciation, are underrepresented, and the model is largely simplified, especially the LIP weatherability functions and strontium isotope systems. Moreover, an improved representation of key factors affecting the strontium isotope system may allow the use of a model of increased complexity.

Despite this, many of the model predictions are argued to be much improved over both COPSE original and other zero-dimensional biogeochemical modelling studies, with the nature and scale of these differences indicative of the strength of the impact of geologic factors on the Phanerozoic long-term carbon cycle.

Bibliography

Abbot, D.S., Farahat, N.X. and Archer, D.E. (2015) Seafloor Weathering Dependence on Temperature and Dissolved Organic Carbon [abstract], in AGU Fall Meeting, 2015, 14/12 - 18/12, San Francisco, CA.

Ainsaar, L., Meidla, T., Tinn, O., Martma, T. and Dronov, A. (2007) Darriwilian (Middle Ordovician) carbon isotope stratigraphy in Baltoscandia, *Acta Palaeontologica Sinica*, 46, pp.1-8.

Ainsaar, L., Kaljo, D., Martma, T., Meidla, T., Mannik, P., Nolvak, J. and Tinn, O. (2010) Middle and Upper Ordovician carbon isotope chemostratigraphy in Baltoscandia: A correlation standard and clues to environmental history, *Palaeogeography, Palaeoclimatology, Palaeoecology*, 294, pp.189-201.

Algeo, T.J and Scheckler, S.E. (1998) Terrestrial-marine teleconnections in the Devonian: links between the evolution of land plants, weathering processes, and marine anoxic events, *Phil. Trans. R. Soc. Land. B*, 353, pp.113-130.

Algeo, T.J. and Ingall, E. (2007) Sedimentary C_{org}:P ratios, paleocean ventilation, and Phanerozoic atmospheric pO_2, *Palaeogeography, Palaeoclimatology, Palaeoecology*, 256, pp.130-155.

Algeo, T.J., Meyers, P.A., Robinson, R.S., Rowe, H. and Jiang, G.Q. (2014) Icehouse-greenhouse variations in marine denitrification, *Biogeosciences*, 11, pp.1273-1295.

Algeo, T.J., Luo, G.M., Song, H.Y., Lyons, T.W. and Canfield, D.E. (2015) Reconstruction of secular variation in seawater sulfate concentrations, *Biogeosciences*, 12, pp.2131-2151.

Allègre, C.J., Louvat, P., Gaillardet, J., Meynadier, L., Rad, S. and Capmas, F. (2010) The fundamental role of island arc weathering in the oceanic Sr isotope budget, *Earth and Planetary Science Letters*, 292(1-2), pp.51–56.

Amiotte-Suchet, P., Probst, J-L. and Ludwig, W. (2003) Worldwide distribution of continental rock lithology: Implications for the atmospheric/soil CO 2 uptake by continental weathering and alkalinity river transport to the oceans, *Global Biogeochemical Cycles*, 17(2), http://doi.org/10.1029/2002GB001891.

Andrews, J.A. and Schlesinger, W.H. (2001) Soil CO_2 dynamics, acidification, and chemical weathering in a temperate forest with experimental CO_2 enrichment, *Global Biogeochemical Cycles,* 15(1), pp.149-162.

Archer, D. (2010) *The Global Carbon Cycle*, Princeton Primers in Climate, Princeton University Pres, 216pp.

Armstrong, H.A. and Harper, D.A.T. (2014) An earth system approach to understanding the end-Ordovician (Hirnantian) mass extinction, *Geological Society of America Special Papers*, 505, pp.287–300.

Arvidson, R.S., Mackenzie, F.T. and Guidry, M. (2006) MAGic: A Phanerozoic Model for the Geochemical Cycling of Major Rock-Forming Components, *American Journal of Science*, 306(3), pp.135-190.

Barham, M., Murray, J., Joachimski, M.M. and Williams, D.M. (2012) The onset of the Permo-Carboniferous glaciation: reconciling global stratigraphic evidence with biogenic apatite $\delta^{18}O$ records in the late Visean, *Journal of the Geological Society*, 169(2), pp.119-122.

Barnes, C. (2004) Was there an Ordovician superplume event?, in Webby, B.D., Paris, F., Droser, M. and Percival, I. eds. *The Great Ordovician Biodiversification Event*, Columbia University Press, New York, pp.77-80.

Bauert, H., Ainsaar, L., Poldsaar, K. and Sepp, S. (2014) $\delta^{13}C$ chemostratigraphy of the Middle and Upper Ordovician succession in the Tartu-453 drillcore, southern Estonia, and the significance of the HICE, *Estonian Journal of Earth Sciences*, 63(4), pp.195-200.

Baum, S.K. and Crowley, T.J. (1991) Seasonal snowline instability in a climate model with realistic geography: Application to Carboniferous (~300Ma) glaciation, *Geophysical Research Letters*, 19, pp.1719-1722.

Belcher, C.M. and McElwain, J.C. (2008) Limits for combustion in low O_2 redefine paleoatmospheric predictions for the Mesozoic, *Science*, 321, pp.1197-1200.

Belcher, C.M., Mander, L., Rein, G., Jervis, F.X., Haworth, M., Hesselbo, S.P., Glasspool, I.J. and McElwain, J.C. (2010) Increased fire activity at the Triassic/Jurassic boundary in Greenland due to climate-driven floral change, *Nature Geoscience*, 3, pp.426-429.

Benton, M.J., Tverdokhlebov, V.P. and Surkov, M.V. (2004) Ecosystem remodelling among vertebrates at the Permian-Triassic boundary in Russia, *Nature*, 432, pp.97-100.

Bergström, S.M., Chen, X., Gutierrez-Marco, J.C. and Dronov, A. (2009) The new chronostratigraphic classification of the Ordovician System and its relations to major regional series and stages and to $\delta^{13}C$ chemostratigraphy, *Lethaia*, 42(1), pp.97-107.

Bergström, S.M., Schmitz, B., Saltzman, M.R. and Huff, W.D. (2010) *The Ordovician Earth System*. *Geological Society of America Special Papers* (Vol. 466), Geological Society of America, http://doi.org/10.1130/2010.2466(04).

Berner, R.A. and Raiswell, R. (1983) Burial of organic carbon and pyrite sulfur in sediments over Phanerozoic time: A new theory, *Geochimica et Cosmochimica Acta*, 47, pp.855-862.

Berner, R.A., Lasaga, A.C. and Garrels, R.M. (1983) The Carbonate-Silicate Geochemical Cycle and its Effect on Atmospheric Carbon Dioxide over the past 100 Million Years, *American Journal of Science*, 283, pp.641-683.

Berner, R.A. (1987) Models for carbon and sulfur cycles and atmospheric oxygen; application to Paleozoic geologic history, *American Journal of Science*, 287(3), pp.177-196.

Berner, R.A. and Canfield, D.E. (1989) A new model for atmospheric oxygen over Phanerozoic time, *American Journal of Science*, 289, pp.333-361.

Berner, R.A. (1990) Atmospheric carbon dioxide levels over Phanerozoic time, *Science*, 249(4975), pp.1382-1386.

Berner, R.A. (1991) A model of atmospheric CO_2 over Phanerozoic time, *American Journal of Science*, 291, pp.339-376.

Berner, R.A. (1994) GEOCARB II: A Revised Model of Atmospheric CO_2 over Phanerozoic Time, *American Journal of Science*, 294, pp.56-91.

Berner, R.A. (1997) The Rise of Plants and Their Effect on Weathering and Atmospheric CO_2, *Science*, 276(5312), pp.544-546.

Berner, R.A. and Caldeira, K. (1997) The need for mass balance and feedback in the geochemical carbon cycle, *Geology*, 25(10), pp.955-956.

Berner, R.A. (1998) The carbon cycle and CO_2 over Phanerozoic time: the role of land plants, *Philosophical Transactions of the Royal Society Series B*, 353, pp.75-82.

Berner, R.A. (1999) Atmospheric oxygen over Phanerozoic time, *Proceedings of the National Academy of Sciences of the United States of America*, 96(20), pp.10955-10957.

Berner, R.A. (2001) Modeling atmospheric O2 over Phanerozoic time. *Geochimica et Cosmochimica Acta*, 65(5), pp.685–694.

Berner, R.A. and Kothavala, Z. (2001) GEOCARB III: A Revised Model of Atmospheric CO_2 over Phanerozoic Time, *American Journal of Science*, 301, pp.182-204.

Berner, R.A. (2003) The long-term carbon cycle, fossil fuels and atmospheric composition, *Nature*, 426, pp.323-326.

Berner, R.A., Beerling, D.J., Dudley, R., Robinson, J.M. and Wildman Jr., R.A. (2003) Phanerozoic Atmospheric Oxygen, *Annu. Rev. Earth Planet. Sci.*, 31, pp.105-134.

Berner, R.A. (2004a) *The Phanerozoic Carbon Cycle*, Oxford University Press, New York.

Berner, R.A. (2004b) A model for calcium, magnesium and sulfate in seawater over Phanerozoic time, *American Journal of Science*, 304(5), pp.438-453.

Berner, R.A. (2006a) GEOCARBSULF: A combined model for Phanerozoic atmospheric O2 and CO2. *Geochimica et Cosmochimica Acta*, 70(23), pp.5653–5664.

Berner, R.A. (2006b) Inclusion of the Weathering of Volcanic Rocks in the GEOCARBSULF Model, *American Journal of Science*, 306, pp.295-302.

Berner, R.A., VandenBrooks, J.M. and Ward, P.D. (2007) Oxygen and Evolution, *Science*, 316, pp.557-558.

Berner, R.A. (2009) Phanerozoic atmospheric oxygen: New results using the GEOCARBSULF model, *American Journal of Science*, 309(7), pp.603-606.

Blakey, R.C. (2011) *Mollweide Plat Tectonic Maps*, http://www.cpgeosystems.com/mollglobe.html.

Bluth, G J.S. and Kump, L.R. (1994). Lithologic and climatologic controls of river chemistry. *Geochimica et Cosmochimica Acta*, 58(10), pp.2341–2359.

Bond, D.P.G., Wignall, P.B., Wang, W., Izon, G., Jiang, H-S., Lai, X-L., Sun, Y-D., Newton, R.J., Shao, L-Y., Vedrine, S. and Cope, H. (2010) The mid-Capitanian (Middle Permian) mass extinction and carbon isotope record of South China, *Palaeogeography, Palaeoclimatology, Palaeoecology*, 292, pp.282-294.

Bond, D.P.G. and Wignall, P.B. (2014) Large igneous provinces and mass extinctions: An update, *Geological Society of America Special Papers*, 505, pp.29–55.

Bottrell, S.H. and Newton, R.J. (2006) Reconstruction of changes in global sulfur cycling from marine sulfate isotopes, *Earth-Science Reviews*, 75, pp.59-83.

Boucot, A.J. and Gray, J. (2001) A critique of Phanerozoic climatic models involving changes in the CO_2 content of the atmosphere, *Earth-Science Reviews*, 56, pp.1-159.

Bowring, S.A., Erwin, D.H., Jin, Y.G., Martin, M.W., Davidek, K. and Wang, W. (1998) U/Pb zircon geochronology and tempo of the End-Permian mass extinction, *Science*, 280(5366), pp.1039-1045.

Brady, P.V. and Gislason, S.R. (1997) Seafloor weathering controls on atmospheric CO_2 and global climate, *Geochimica et Cosmochimica Acta*, 61, pp.965-973.

Braiser, M.D., Shields, G., Kuleshov, V.N. and Zhegallo, E.A. (1996) Integrated chemo-and biostratigraphic calibration of early animal evolution: Neoproterozoic-early Cambrian of southwest Mongolia, *Geological Magazine*, 133(4), pp.445-485.

Brass, G.W. (1976) The variation of the marine 87Sr86Sr ratio during Phanerozoic time: interpretation using a flux model, *Geochimica et Cosmochimica Acta*, 40(7), pp.721-730.

Breecker, D.O., Sharp, Z.D. and McFadden, L.D. (2010) Atmospheric CO2 concentrations during ancient greenhouse climates were similar to those predicted for A.D. 2100, *Proceedings of the National Academy of Sciences*, 107(2), pp.576–580.

Breecker, D.O. and Retallack, G.J. (2014) Refining the pedogenic carbonate atmospheric CO_2 proxy and application to Miocene CO_2, *Palaeogeography, Palaeoclimatology, Palaeoecology*, 406, pp.1-8.

Brenchley, P.J., Marshall, J.D., Carden, G.A.F., Robertson, D.B.R., Long, D.G.F., Meidla, T., Hints, L. and Anderson, T.F. (1994) Bathymetric and isotopic evidence for a short-lived Ordovician glaciation in a greenhouse period, *Geology*, 22(4), pp.295-298.

Brenchley, P.J., Carden, G.A., Hints, L., Kaljo, D., Marshall, J.D., Martma, T., Meidla, T. and Nolvak, J. (2003) High-resolution stable isotope stratigraphy of Upper Ordovician sequences: Constraints on the timing of bioevents and environmental changes associated with mass extinction and glaciation, *GSA Bulletin*, 115(1), pp.89-104.

Briggs, D.E.G. and Crowther, P.R. eds. (2001) *Palaeobiology II*, Blackwell Science Ltd., Malden, MA, USA.

Bryan, S. and Ferrari, L. (2013) Large Igneous Provinces and Silicic Large Igneous Provinces: progress in our understanding over the last 25 years, *Geological Society of America Bulletin*, 125, pp.1053-1078.

Budkyo, M.I. (1969) The effect of solar radiation variations on the climate of the Earth, *Tellus*, 21(5), pp.611-619.

Buggisch, W., Joachimski, M.M., Lehnert, O., Bergstrom, S.M., Repetski, J.E. and Webers, G.F. (2010) Did intense volcanism trigger the first Late Ordovician icehouse?, *Geology*, 38(4), pp.327–330.

Burke, W.H., Denison, R.E., Hetherington, E.A., Koepnick, R.B., Nelson, H.F. and Otto, J.B. (1982) Variation of seawater 87Sr/86Sr throughout Phanerozoic time, *Geology*, 10(10), pp.516–519.

Caldeira, K. and Kasting, J.F. (1992) The lifespan of the biosphere revisited, *Nature*, 360, pp.721-723.

Canfield, D.E. (2001) Biogeochemistry of Sulfur Isotopes, *Reviews in Mineralogy and Geochemistry*, 43(1), pp.607-636.

Canfield, D.E. (2004) The evolution of the Earth surface sulfur reservoir, *American Journal of Science*, 304(10), pp.839-861.

Canfield, D.E. (2005) The early history of atmospheric oxygen: Homage to Robert. M. Garrels., *Annu. Rev. Earth. Planet. Sci.*, 33, pp.1-36.

Canfield, D.E., Poulton, S.W. and Narbonne, G.M. (2007) Late-Neoproterozoic deep-ocean oxygenation and the rise of animal life, *Science,* 315(5808), pp.92–95.

Canfield, D.E. and Farquhar, J. (2009) Animal evolution, bioturbation, and the sulfate concentration of the oceans, *Proceedings of the National Academy of Sciences of the United States of Americs*, 106(2), pp.8123-8127.

Chadwick, J.P., Troll, V.R., Ginibre, C., Morgan, D., Gertisser, R., Waight, T.E. and Davidson, J.P. (2007) Carbonate Assimilation at Merapi Volcano, Java, Indonesia: Insights from Crystal Isotope Stratigraphy, *Journal of Petrology*, 48(9), pp.1793-1812.

Chan, L., Edmond, J., Thompson, G. and Gillis, K. (1992) Lithium isotopic composition of submarine basalts: implications for the lithium cycle in the oceans, *Earth and Planetary Science Letters*, 108(1-3), pp.151–160.

Cherns, L., Wheeley, J.R., Popov, L.E., Ghobadi Pour, M., Owens, R.M. and Hemsley, A. R. (2013) Long-period orbital climate forcing in the early Palaeozoic?, *Journal of the Geological Society*, 170(5), pp.707–710.

Chumakov, N.M. and Zharkov, M.A. (2003) Climate during the Permian-Triassic Biosphere Reorganizations. Article 2. Climate of the Late Permian and Early Triassic: General Inferences, *Stratigraphy and Global Correlation*, 11(4), pp.361-375.

Clapham, M.E. and Karr, J.A. (2012) Environmental and biotic controls on the evolutionary history of insect body size, *Proceedings of the National Academy of Sciences*, 109(27), pp. 10927-10930.

Clarkson, M.O., Kasemann, S.A., Wood, R.A., Lenton, T.M., Daines, S.J., Richoz, S., Ohnemueller, F., Meixner, A., Poulton, S.W. and Tipper, E.T. (2015) Ocean acidification and the Permo-Triassic mass extinction, *Science,* 348(6231), pp.229–232.

Cleal, C.J. and Thomas, B.A. (2005) Palaeozoic tropical rainforests and their effect on global climates: is the past the key to the present?, *Geobiology*, 3(1), pp.13-31.

Cleveland, W.S. (1981) Robust locally weighted regression and smoothing scatterplots, *Journal of the American Statistical Association*, 74(368), pp.829-836.

Compton, J, Mallinson, D., Glenn, C.R., Filippelli, G., Follmi, K., Shields, G. and Zanin, Y. (2000) Variations in the Global Phosphorus Cycle, *Marine Authigenesis: From Global to Microbial, SEPM Special Publication No. 66*, pp.21-33.

Coogan, L.A. and Gillis, K.M. (2013) Evidence that low-temperature oceanic hydrothermal systems play an important role in the silicate-carbonate weathering cycle and long-term climate regulation, *Geochemistry, Geophysics, Geosystems*, 14(6), pp.1771-1786.

Cooper, R.A. and Sadler, P.M (2012) The Ordovician Period, in Gradstein, F.M., Ogg, J.G., Schmitz, M.D. and Ogg, G.M. eds. *The Geologic Time Scale 2012*, Elsevier, pp.489-523.

Cooper, R.A., Sadler, P.M., Munnecke, A. and Crampton, J.S. (2014) Graptoloid evolutionary rates track Ordovician-Silurian global climate change, *Geological Magazine*, 151(2), pp.349-364.

Correia, C.T., Sinigoi, S., Girardi, V.A.V., Mazzucchelli, M., Tassinari, C.C.G. and Giovanardi, T. (2012) The growth of large mafic intrusions: Comparing Niquelandia and Ivrea large igneous complexes, *Lithos*, 155, pp.167-182.

Courtillot, V.E. and Olson, P. (2007) Mantle plumes link magnetic superchrons to phanerozoic mass depletion events, *Earth and Planetary Science Letters*, 260(3-4), pp.495–504.

Cox, G.M., Halverson, G.P., Stevenson, R.K., Vokaty, M., Poirier, A., Kunzmann, M., Li, Z-X., Denyszyn, S.W., Strauss, J.V. and Macdonald, F.A. (2016) Continental flood basalt weathering as a trigger for Neoproterozoic Snowball Earth, *Earth and Planetary Science Letters*, 446, pp.89-99.

Craig, H. (1953) The geochemistry of the stable carbon isotopes, *Geochimica et Cosmochimica Acta*, 3(2-3), pp.53-92.

Cramer, B.D. and Saltzman, M.R. (2005) Sequestration of ^{12}C in the deep ocean during the early Wenlock (Silurian) positive carbon isotope excursion, *Palaeogeography, Palaeoceanography, Palaeoclimatology*, v. 219, pp. 333-349.

Cramer, B.D., Munnecke, A., Schofield, D.I., Haase, K.M. and Haase-Schramm, A. (2011) A Revised 87 Sr/ 86 Sr Curve for the Silurian: Implications for Global Ocean Chemistry and the Silurian Timescale, *The Journal of Geology*, 119(4), pp.335–349.

Cressler, W.L. (2001) Evidence of earliest known wildfires, *PALAIOS*, 16(2), pp.171-174.

Crowley, T.J. and Baum, S.K. (1991) Toward Reconciliation of Late Ordovician (~440Ma) Glaciation with Very High CO_2 Levels, *Journal of Geophysical Research*, 96(D12), pp.22597-22610.

Crowley, T.J. and Baum, S.K. (1992) Modeling late Paleozoic glaciation, *Geology*, 20, pp.507-510.

Crowley, T.J. (1998) Significance of tectonic boundary conditions for paleoclimate simulations, *Oxford Monographs on Geology and Geophysics*, 39, pp.3-20.

Crowley, T.J. (2001) PALEOCLIMATE: Enhanced: CO2 and Climate Change, *Science*, 292(5518), pp.870–872.

Crowley, T.J. and Berner, R.A. (2001) CO_2 and Climate Change, *Science*, 292(5518), pp.870-872.

Cuneo, N.R. (1996) Permian phytogeography in Gondwana, *Palaeogeography, Palaeoclimatology, Palaeoecology*, 125, pp.75-104.

Dabard, M.P., Loi, A., Paris, F., Ghienne, J.F., Pistis, M. and Vidal, M. (2015) Sea-level curve for the Middle to early Late Ordovician in the Armorican Massif (western France): Icehouse third-order glacio-eustatic cycles, *Palaeogeography, Palaeoclimatology, Palaeoecology*, 436, pp.96–111.

Dahl, T.W., Hammarlund, E.U., Anbar, A.D., Bond, D.P.G., Gill, B.C., Gordon, G.W., Knoll, A.H., Nielsen, A.T., Schovsbo, N.H. and Canfield, D. E. (2010) Devonian rise in atmospheric oxygen correlated to the radiations of terrestrial plants and large predatory fish, *Proceedings of the National Academy of Sciences of the United States of America*, 107(42), pp.17911–17915.

Delabroye, A. and Vecoli, M. (2010) The end-Ordovician glaciation and the Hirnantian stage: A global review and questions about Late Ordovician event stratigraphy, *Earth-Science Reviews*, 98(3-4), pp.269-282.

Denison, R., Koepnick, R., Burke, W. and Hetherington, E. (1998) Construction of the Cambrian and Ordovician seawater 87Sr/86Sr curve, *Chemical Geology*, 152(3-4), pp.325–340.

Denison, R., Koepnick, R., Burke, W., Hetherington, E. and Fletcher, A. (1997) Construction of the Silurian and Devonian seawater 87Sr/86Sr curve, *Chemical Geology*, 140(1-2), pp.109–121.

Dera, G., Brigaud, B., Monna, F., Laffont, R., Puceat, E., Deconinck, J-F., Pellenard, P., Joachimski, M.M. and Durlet, C. (2011) Climate ups and downs in a disturbed Jurassic world, *Geology*, 39(3), pp.215-218.

Derry, L.A., Braiser, M.D., Corfield, R.M., Rozanov, A.Y. and Zhuravlev, A.Y. (1994) Sr and C isotopes in Lower Cambrian carbonates from the Siberian craton: A paleoenvironmental record during the 'Cambrian explosion', *Earth and Planetary Science Letters*, 128, pp.671-681.

Desrochers, A., Ghienne, J.-F., Vandenbroucke, T.R.A., Achab, A., Asselin, E., Dabard, M.-P., Farley, C., Loi, A., Paris, F., Wickson, S. and Veizer, J. (2015). A Cenozoic-Style Scenario for the End-Ordovician Glaciation. *EGU General Assembly 2015*.

Dessert, C., Dupre, B., Francois, L.M., Schott, J., Gaillardet, J., Chakrapani, G. and Bajpai, S. (2001) Erosion of Deccan Traps determined by river geochemistry: impact on the global climate and the $^{87}Sr/^{86}Sr$ ratio of seawater, *Earth and Planetary Science Letters*, 188(3-4), pp.459-474.

Dessert, C., Dupre, B., Francois, L.M., Gaillardet, J. and Allegre, C. (2003) Basalt weathering laws and the impact of basalt weathering on the global carbon cycle, *Chemical Geology*, 202(3-4), pp.257-273.

Donnadieu, Y., Godderis, Y., Pierrehumbert, R., Dromart, G., Fluteau, F. and Jacob, R. (2006) A GEOCLIM simulation of climatic and biogeochemical consequences of Pangea breakup, *Geochemistry, Geophysics, Geosystems*, 7(11), doi:0.1029/2006GC001278.

Donnadieu, Y., Dromart, G., Goddéris, Y., Pucéat, E., Brigaud, B., Dera, G., Dumas, C. and Olivier, N. (2011) A mechanism for brief glacial episodes in the Mesozoic greenhouse, *Paleoceanography*, 26(3), http://doi.org/10.1029/2010PA002100.

Dorrington, G.E. (2012) On flying insect size and Phanerozoic atmospheric oxygen, *Proceedings of the National Academy of Sciences of the United States of America*, 109(50), doi:10.1073/pnas.1215611109.

Duarte, C.M., Lenton, T.M., Wadhams, P. and Wassmann, P. (2012) Abrupt climate change in the Arctic, *Nature Climate Change*, 2(2), pp.60–62.

Dudley, R. (1998) Atmospheric oxygen, giant Paleozoic insects and the evolution of aerial locomotor performance, *J. Exp. Biol.*, 201, pp.1043-1050.

Ebelmen, J.J. (1845) Sur les produits de la décomposition des espèces minérales de la famille des silicates, *Annu. Rev. Moines*, 12, pp.627-654.

Edmond, J.M. and Huh, Y. (2003) Non-steady state carbonate recycling and implications for the evolution of atmospheric P_{CO2}, *Earth and Planetary Science Letters*, 216, pp.125-139.

Edwards, C.T., Saltzman, M.R., Leslie, S.A., Bergström, S.M., Sedlacek, A.R.C., Howard, A., Bauer, J.A., Sweet, W.C. and Young, S. A. (2015) Strontium isotope ($^{87}Sr/^{86}Sr$) stratigraphy of Ordovician bulk carbonate: Implications for preservation of primary seawater values, *Geological Society of America Bulletin*, B31149.1, http://doi.org/10.1130/B31149.1.

Elliott, T., Thomas, A., Jeffcoate, A. and Niu, Y. (2006) Lithium isotope evidence for subduction-enriched mantle in the source of mid-ocean-ridge basalts, *Nature*, 443(7111), pp.565–568.

Engelder, T. and Whittaker, A. (2006) Early jointing in coal and black shale: Evidence for an Appalachian-wide stress field as a prelude to the Alleghanian orogeny, *Geology*, 34(7), pp.581-584.

Ernst, R.E. and Buchan, K.L. (2001) The use of mafic dike swarms in identifying and locating mantle plumes, in Ernst, R.E. and Buchan, K.L. eds. *Mantle Plumes: Their Identification Through Time*, Geol. Soc. America Spec. Paper 352, pp.247-265.

Ernst, R.E. (2007) Mafic-ultramafic large igneous provinces (LIPs): importance of the Pre-Mesozoic record, *Episodes 30*, pp.108-114.

Ernst, R.E. and Bleeker, W. (2010) Large igneous provinces (LIPs), giant dyke swarms, and mantle plumes: significance for breakup events within Canada and adjacent regions from 2.5Ga to present, *Canadian Journal of Earth Sciences*, 47(5), pp.695-739.

Ernst, R.E. (2014) *Large Igneous Provinces*, Cambridge University Press, Cambridge, UK.

Erwin, D.H. (1994) The Permo-Triassic extinction, *Nature*, 367, pp.231-236.

Evans, M.J., Derry, L.A., & France-Lanord, C. (2008) Degassing of metamorphic carbon dioxide from the Nepal Himalaya, *Geochemistry, Geophysics, Geosystems*, 9(4), http://doi.org/10.1029/2007GC001796.

Farahat, N.X., Archer, D.E. and Abbot, D.S. (2013) Seafloor weathering buffering climate: numerical experiments [abstract], in AGU Fall Meeting, 2013, 09/12 – 13/12, San Francisco, CA.

Farahat, N.X., Abbot, D.S. and Archer, D.E. (2014) Seafloor Weathering as a Long-Term Climate Regulation Mechanism [abstract], in AGU Fall Meeting, 2014, 15/12 – 19/12, San Francisco, CA.

Farquhar, G.D., Ehleringer, J.R. and Hubick, K.T. (1989) Carbon isotope discrimination and photosynthesis, *Annu. Rev. Plant. Physiol. Mol. Biol.*, 40, pp.503-537.

Fielding, C.R., Frank, T.D. and Isbell, J.L. (2008) The late Paleozoic ice age – A review of current understanding and synthesis of global climate patterns, *Geological Society of America Special Papers*, 441, pp.343-354.

Fike, D.A., Grotzinger, J.P., Pratt, L.M. and Summons, R. E. (2006) Oxidation of the Ediacaran ocean, *Nature*, 444(7120), pp.744–747.

Filippelli, G.M. (2002). The Global Phosphorus Cycle, *Reviews in Mineralogy and Geochemistry*, 48(1), pp.391–425.

Finlay, A.J., Selby, D. and Gröcke, D.R. (2010) Tracking the Hirnantian glaciation using Os isotopes, *Earth and Planetary Science Letters*, 293(3-4), pp.339–348.

Finnegan, S., Bergmann, K., Eiler, J.M., Jones, D.S., Fike, D.A., Eisenman, I., Hughes, N.C., Tripati, A.K. and Fischer, W.W. (2011) The Magnitude and Duration of Late Ordovician-Early Silurian Glaciation, *Science*, 311, pp.903-906.

Finney, S.C. (2005) Global Series and Stages for the Ordovician System: A Progress Report, *Geologica Acta*, 3, pp.309-316.

Fortey, R.A. and Cocks, L.R.M. (2005) Late Ordovician global warming—The Boda event, *Geology*, 33(5), pp.405-408.

François, L.M. and Walker, J.C. (1992) Modelling the Phanerozoic carbon cycle and climate: constraints from the 87Sr/86Sr isotopic ratio of seawater, *American Journal of Science*, 292(2), pp.81–135.

Francois, L.M., Grard, A. and Godderis, Y. (2005) Modelling atmospheric CO2 changes at geologic time scales, in Steemans, P. and Javaux, E. eds. *Pre-Cambrian to Palaeozoic Palaeopalynology and Palaeobotany*, Carnets de Geologie, Brest.

Frazier, M.R., Woods, H.A. and Harrison, J.F. (2001) Interactive effects of rearing temperature and oxygen on the development of Drosophila melanogaster, *Physiological and Biochemical Zoology*, 74(5), pp.641-650.

Frýda, J., Hladil, J., & Vokurka, K. (2002) Seawater strontium isotope curve at the Silurian/Devonian boundary: a study of the global Silurian/Devonian boundary stratotype, *Geobios*, 35(1), pp.21–28.

Gaillardet, J., Dupre, B., Louvat, P. and Allegre, C.J. (1999) Global silicate weathering and CO_2 consumption rates deduced from the chemistry of large rivers, *Chemical Geology*, 159(1), pp.3-30.

Galy, A., France-Lanord, C. and Derry, L.A. (1999) The strontium isotopic budget of Himalayan Rivers in Nepal and Bangladesh, *Geochimica et Cosmochimica Acta*, 63(13/14), pp.1905-1925.

Gambacorta, G., Caronni, V., Antonielli, E., Previde Massara, E., Riva, A., Scotti, P., Trincianti, E. and Erba, E. (2016) Hot shale in an ice world: paleoceanographic evolution of the northern Gondwana margin during the early Paleozoic (Tanezzuft Formation, Tunisia), *Marine and Petroleum Geology*, 72, pp.393–411.

Ganis, G.R. and Wise, D.U. (2008) Taconic events in Pennsylvania: Datable phases of a 20 m.y. orogeny, *American Journal of Science*, 308(2), pp.167–183.

Garrels, R.M. and Lerman, A. (1981) Phanerozoic Cycles of Sedimentary Carbon and Sulfur, *Proceedings of the National Academy of Sciences of the United States of America*, 78(8), pp.4652-4656.

Garrels, R.M. and Lerman, A. (1984) Coupling of the sedimentary carbon and sulfur cycles: an improved model, *American Journal of Science*, 284, pp.989-1007.

Geurot, C. and Peucat, J.J. (1990) U-Pb geochronology of the Upper Proterozoic Cadomian orogeny in the northern Armorican Massif, France, in D'Lemos, R.S., Strachan, R.A. and Topley, C.G. eds. *The Cadomian Orogeny*, Geological Society Special Publication No. 51, pp.13-26.

Ghienne, J.-F., Desrochers, A., Vandenbroucke, T R.A., Achab, A., Asselin, E., Dabard, M.-P., Farley, C., Loi, A., Paris, F., Wickson, S. and Veizer, J. (2014) A Cenozoic-style scenario for the end-Ordovician glaciation, *Nature Communications*, 5, 4485, doi:10.1038/ncomms5485.

Gillis, K.M. and Coogan, L.A. (2011) Secular variation in carbon uptake into the ocean crust, *Earth and Planetary Science Letters*, 302(3-4), pp.385-392.

Glass, L.M. and Phillips, D. (2006) The Kalkarindji continental flood basalt province: A new Cambrian large igneous province in Australia with possible links to faunal extinctions, *Geology*, 34(6), pp.461-464.

Glasspool, I.J., Edwards, D. and Axe, L. (2004) Charcoal in the Silurian as evidence for the earliest wildfire, *Geology*, 32, pp.381-383.

Godderis, Y. and Francois, L.M. (1995) The Cenozoic evolution of the strontium and carbon cycles: relative importance of continental erosion and mantle exchanges, *Chemical Geology*, 126, pp.169-190.

Godderis, Y., Donnadieu, Y., Tombozafy, M. and Dessert, C. (2008) Shield effect on continental weathering: Implication for climatic evolution of the Earth at the geological timescale, *Geoderma*, 145(3-4), pp.439-448.

Goddéris, Y., Donnadieu, Y., Lefebvre, V., Le Hir, G. and Nardin, E. (2012) Tectonic control of continental weathering, atmospheric CO2, and climate over Phanerozoic times, *Comptes Rendus Geoscience*, 344(11-12), pp.652–662.

Goddéris, Y., Donnadieu, Y., Le Hir, G., Lefebvre, V. and Nardin, E. (2014) The role of palaeogeography in the Phanerozoic history of atmospheric CO2 and climate, *Earth-Science Reviews*, 128, pp.122–138.

Goldstein, S.J. and Jacobsen, S.B. (1988) Nd and Sr isotopic systematics of river water suspended material: implications for crustal evolution, *Earth and Planetary Science Letters*, 87, pp.249-265.

Gradstein, F.M. and Ogg, J.G. (2012) The Chronostratigraphic Scale, in Gradstein, F.M., Ogg, J.G., Schmitz, M.D. and Ogg, G.M. eds. *The Geologic Time Scale 2012*, Elsevier, pp.31-42.

Gradstein, F.M., Ogg, J.G., Schmitz, M.D. and Ogg, G.M. (2012a) *The Geologic Time Scale 2012*, Elsevier, 1144pp.

Gradstein, F.M., Ogg, J.G. and Hilgen, F.J. (2012b) On The Geologic Time Scale, *Newsletters on Stratigraphy*, 45(2), pp.171-188.

Grafarend, E.W. and Krumm, F.W. (2006) *Map Projections: Cartographic Information Systems*, Springer-Verlag, Berlin.

Graham, J., Dudley, R., Aguilar, N. and Gans, C. (1995) Implication of the late Paleozoic oxygen pulse for physiology and evolution, *Nature*, 375, pp.117-120.

Gray, J., Chaloner, W.G. and Westoll, T.S. (1985) The microfossil record of early land plants: Advances in understanding of early terrestrialization, 1970-1984, *Phil. Trans. Of. R. Soc. Lond. B.*, 309, pp.167-195.

Grocke, D.R., Price, G.D., Ruffell, A.H., Mutterlose, J. and Baraboshkin, E. (2003) Isotope evidence for Late Jurassic-Early Cretaceous climate change, *Palaeogeography, Palaeoclimatology, Palaeoecology*, 202(1-2), pp.97-118.

Gruszczynski, M., Hoffman, A., Malkowski, K. and Veizer, J. (1992) Seawater strontium isotope perturbation at the Permian-Triassic boundary, West Spitsbergen, and its implications for the interpretation of strontium isotopic data, *Geology*, 20, pp.779-782.

Guy, R.D., Fogel, M.L. and Berry, J.A. (1993) Photosynthetic fractionation of the stable isotopes of oxygen and carbon, *Plant Physiol.*, 101, pp.37-47.

Halevy, I., Peters, S.E. and Fischer, W.W. (2012) Sulfate Burial Constraints on the Phanerozoic Sulfur Cycle, *Science*, 337(6092), pp.331-334.

Halverson, G.P., Dudás, F.Ö., Maloof, A.C. and Bowring, S.A. (2007) Evolution of the 87Sr/86Sr composition of Neoproterozoic seawater, *Palaeogeography, Palaeoclimatology, Palaeoecology*, 256(3-4), pp.103–129.

Hammarlund, E.U., Dahl, T.W., Harper, D.A.T., Bond, D.P.G., Nielsen, A.T., Bjerrum, C.J., Schovsbo, N.H., Schonlaub, H.P., Zalasiewicz, J.A. and Canfield, D.E. (2012) A sulfidic driver for the end-Ordovician mass extinction, *Earth and Planetary Science Letters*, 331, pp.128-139.

Harper, D.A.T., Hammarlund, E.U. and Rasmussen, C.M.Ø. (2014) End Ordovician extinctions: A coincidence of causes, *Gondwana Research*, 25(4), pp.1294–1307.

Harper, D.A.T., Zhan, R.-B. and Jin, J. (2015) The Great Ordovician Biodiversification Event: Reviewing two decades of research on diversity's big bang illustrated by mainly brachiopod data, *Palaeoworld*, 24(1-2), pp.75–85.

Hartmann, J., Dürr, H.H., Moosdorf, N., Meybeck, M. and Kempe, S. (2011) The geochemical composition of the terrestrial surface (without soils) and comparison with the upper continental crust, *International Journal of Earth Sciences*, 101(1), pp.365–376.

Hartmann, J., Moosdorf, N., Lauerwald, R., Hinderer, M. and West, A.J. (2014) Global chemical weathering and associated P-release — The role of lithology, temperature and soil properties, *Chemical Geology*, 363, pp.145–163.

Hathorne, E. and James, R. (2006).Temporal record of lithium in seawater: A tracer for silicate weathering?, *Earth and Planetary Science Letters*, 246(3-4), pp.393–406.

Hay, W.W., Migdisov, A., Balukhovsky, A.N., Wold, C.N., Flögel, S. and Söding, E. (2006) Evaporites and the salinity of the ocean during the Phanerozoic: Implications for climate, ocean circulation and life, *Palaeogeography, Palaeoclimatology, Palaeoecology*, 240(1-2), pp.3–46.

Hayes, J.M., Strauss, H. and Kaufman, A.J. (1999) The abundance of ^{13}C in marine organic matter and isotopic fractionation in the global biogeochemical cycle of carbon during the past 800Ma, *Chemical Geology*, 161(1-3), pp.103-125.

Herrmann, A.D., Haupt, B.J., Patzkowsky, M.E., Seidov, D. and Slingerland, R.L. (2004) Response of Late Ordovician paleoceanography to changes in sea level, continental drift, and atmospheric pCO_2: potential causes for long-term cooling and glaciation, *Palaeogeography, Palaeoclimatology, Palaeoecology*, 210, pp.385-401.

Herrmann, A.D., Macleod, K. G. and Leslie, S.A. (2010) Did a volcanic mega-eruption cause global cooling during the Late-Ordovician? *PALAIOS*, 25(12), pp.831–836.

Hodell, D.A., Mead, G.A. and Mueller, P.A. (1990) Variation in the strontium isotopic composition of seawater (8Ma to present): Implications for chemical weathering rates and dissolved fluxes to the oceans, *Chemical Geology: Isotope Geoscience section*, 80(4), pp.291-307.

Holland, H.D. (1984) *The Chemical Evolution of the Atmosphere and Oceans*, Princeton Series in Geochemistry, Princeton, Princeton University Press.

Holmden, C., Mitchell, C.E., LaPorte, D.F., Patterson, W.P., Melchin, M.J. and Finney, S.C. (2013) Nd isotope records of late Ordovician sea-level change—Implications for glaciation frequency and global stratigraphic correlation, *Palaeogeography, Palaeoclimatology, Palaeoecology*, 386, pp.131–144.

Horton, D.E., Poulsen, C.J., Montanez, I.P. and DiMichele, W.A. (2012) Eccentricity-paced late Paleozoic climate change, *Palaeogeography, Palaeoclimatology, Palaeoecology*, 331-332, pp.150-161.

Horton, F. (2015) Did phosphorus derived from the weathering of large igneous provinces fertilize the Neoproterozoic ocean?, *Geochemistry, Geophysics, Geosystems*, 16(6), pp.1723–1738.

Huang, C., Tong, J., Hinnov, L. and Chen, Z.Q. (2011) Did the great dying of life take 700k.y.? Evidence from global astronomical correlation of the Permian-Triassic boundary interval, *Geology*, 39(8), pp.779-782.

Huff, W.D. (2005) Ordovician K-Bentonites, in Ludvigson, G.A. and Bunker, B.J. eds. *Facets of the Ordovician geology of the Upper Mississippi Valley region: Iowa Geological Society Guidebook Ser. No. 24: Guidebook for the 35th Annual Field Conference of the Great Lakes Section*, Society for Sedimentary Geology (SEPM), pp.50-53.

Huff, W.D. (2008) Ordovician K-bentonites: Issues in interpreting and correlating ancient tephras, *Quaternary International*, 178(1), pp.276–287

Huff, W.D., Bergström, S.M. and Kolata, D.R. (2010) *The Ordovician Earth System*, *Geological Society of America Special Papers* (Vol. 466), Geological Society of America, http://doi.org/10.1130/2010.2466(02).

Isbell, J.L., Miller, M.F., Wolfe, K.L. and Lenaker, P.A. (2003) Timing of late Paleozoic glaciation in Gondwana: Was glaciation responsible for development of northern hemisphere cyclotherms?, *Geological Society of America Special Paper 370*, pp.5-24.

Jahn, B. (2004) The Central Asian Orogenic Belt and growth of the continental crust in the Phanerozoic, *Geological Society London Special Publications*, 226, pp.73-100.

James, R.H. and Palmer, M.R. (2000) The lithium isotope composition of international rock standards, *Chemical Geology*, 166(3-4), pp.319–326.

Jin, Y.G., Wang, Y., Wang, W., Shang, Q.H., Cao, C.Q. and Erwin, D.H. (2000) Pattern of Marine Mass-Extinction Near the Permian-Triassic Boundary in South China, *Science*, 289, pp.432-436.

Joachimski, M.M. (1997) Comparison of organic and inorganic carbon isotope patterns across the Frasnian-Famennian boundary, *Palaeogeography, Palaeoclimatology, Palaeoecology*, 132(1-4), pp.133-145.

Joachimski, M.M., Lai, X., Shen, S., Jiang, H., Luo, G., Chen, B., Chen, J. and Sun, Y. (2012) Climate warming in the latest Permian and the Permian-Triassic mass extinction, *Geology*, 40(3), pp.195-198.

Johnston, D.T. (2011) Multiple sulfur isotopes and the evolution of Earth's surface sulfur cycle, *earth-Science Reviews*, 106, pp.161-183.

Jones, A.T. and Fielding, C.R. (2004) Sedimentological record of the Late Paleozoic glaciation in Queensland, Australia, *Geology*, 32, pp.153-156.

Jones, D.S. and Fike, D.A. (2013) Dynamic sulfur and carbon cycling through the end-Ordovician extinction revealed by paired sulfate-pyrite $\delta^{34}S$, *Earth and Planetary Science Letters*, 363, pp.144-155.

Kah, L.C., Lyons, T.W. and Frank, T.D. (2004) Low Marine Sulphate and Protracted Oxygenation of the Proterozoic Biosphere, *Nature*, 431, pp.834-838.

Kaiho, K., Yatsu, S., Oba, M., Gorjan, P., Casier, J-G. and Ikeda, M. (2013) A forest fire and soil erosion event during the Late Devonian mass extinction, *Palaeogeography, Palaeoclimatology, Palaeoecology*, 392, pp.272-280.

Kaiser, A., Klok, J.C., Socha, J.J., Lee, W-K., Quinlan, M.C. and Harrison, J.F. (2007) Increase in tracheal investment with beetle size supports hypothesis of oxygen limitation on insect gigantism, *Proceedings of the National Academy of Sciences of the United States of America*, 104(32), pp.13198-13203.

Kaljo, D., Hints, L., Martma, T., Nolvak, J. and Oraspold, A. (2004) Late Ordovician carbon isotope trend in Estonia, its significance in stratigraphy and environmental analysis, *Palaeogeography, Palaeoclimatology, Palaeoecology*, 210(2-4), pp.165-185.

Kaljo, D., Martma, T. and Saadre, T. (2007) Post-Hunnebergian Ordovician carbon isotope trend in Baltoscandia, its environmental implications and some similarities with that of Nevada, *Palaeogeography, Palaeoclimatology, Palaeoecology*, 245(1-2), pp.138-155.

Kampschulte, A. and Strauss, H. (2004) The sulfur isotopic evolution of Phanerozoic seawater based on the analysis of structurally substituted sulfate in carbonates, *Chemical Geology*, 204, pp.255-286.

Kani, T., Hisanabe, C. and Isozaki, Y. (2013) The Capitanian (Permian) minimum of $^{87}Sr/^{86}Sr$ ratio in the mid-Panthalassan paleo-atoll carbonates and its demise by the deglaciation and continental doming, *Gondwana Research*, 24(1), pp.212-221.

Kasting, J.F. (1989) Long-term stability of the Earth's climate, *Global and Planetary Change*, 1(1-2), pp.83-95.

Katz, M.E., Miller, K.G., Wright, J.D., Wade, B.S., Browning, J.V., Cramer, B.S. and Rosenthal, Y. (2008) Stepwise transition from the Eocene greenhouse to the Oligocene icehouse, *Nature Geoscience*, 1, pp.329-334.

Kearsey, T., Twitchett, R.J., Price, G.D. and Grimes, S.T. (2009) Isotope excursions and palaeotemperature estimates from the Permian/Triassic boundary in the Southern Alps (Italy), *Palaeogeography, Palaeoclimatology, Palaeoecology*, 279, pp.29-40.

Kenrick, P., Wellman, C.H., Schneider, H. and Edgecombe, G.D. (2012) A timeline for terrestrialization: consequences for the carbon cycle in the Palaeozoic, *Phil. Trans. R. Soc. B*, 367, pp.519-536.

Kerrick, D.M. (2001) Present and past nonanthropogenic CO_2 degassing from the solid Earth, *Reviews of Geophysics*, 39(4), pp.565-585.

Kidder, D.L. and Worsley, T.R. (2004) Causes and consequences of extreme Permo-Triassic warming to globally equable climate and relation to the Permo-Triassic extinction and recovery, *Palaeogeography, Palaeoclimatology, Palaeoecology*, 203, pp.207-237.

Kiehl, J.T. and Shields, C.A. (2005) Climate simulation of the latest Permian: Implications for mass extinction, *Geology*, 33(9), pp.757-760.

Kirschvink, J.L. (1992) Late Proterozoic low-latitude global glaciation: the snowball Earth, in Schopf, J.W. and Klein, C. eds., *The Proterozoic Biosphere*, Cambridge University Press, Cambridge, pp.51-52.

Knoll, A.H., Bambach, R.K., Canfield, D.E. and Grotzinger, J.P. (1996) Comparative earth history and Late Permian mass extinction, *Science*, 273(5274), pp.452-457.

Knoll, A.H., Bambach, R.K., Payne, J.L., Pruss, S. and Fischer, W.W. (2007) Paleophysiology and end-Permian mass extinction, *Earth and Planetary Science Letters*, 256, pp.295-313.

Korte, C., Kozur, H.W. and Veizer, J. (2005) $\delta^{13}C$ and $\delta^{18}O$ values of Triassic brachiopods and carbonate rocks as proxies for coeval seawater and palaeotemperature, *Palaeogeography, Palaeoclimatology, Palaeoecology*, 226, pp.287-306.

Korte, C., Jasper, T., Kozur, H.W. and Veizer, J. (2006) $^{87}Sr/^{86}Sr$ record of Permian seawater, *Palaeogeography, Palaeoclimatology, Palaeoecology*, 240(1-2), pp.89-107.

Krug, A.Z. and Patzkowsky, M.E. (2007) Geographic variation in turnover and recovery from the Late Ordovician mass extinction, *Paleobiology*, 33(3), pp.435–454.

Kump, L.R. and Garrels, R.M. (1986) Modeling atmospheric O_2 in the global sedimentary redox cycle, *American Journal of Science*, 286, pp.337-360.

Kump, L.R. and Arthur, M.A. (1997) Global chemical erosion during the Cenozoic: weatherability balances the budget, in Ruddiman, W. eds., *Tectonics, Uplift and Climate Change*, Plenum Publishing Co., pp.399-426.

Kump, L.R., Arthur, M.A., Patzkowsky, M.E., Gibbs, M.T., Pinkus, D.S. and Sheehan, P.M. (1999) A weathering hypothesis for glaciation at high atmospheric pCO_2 during the Late Ordovician, *Palaeogeography, Palaeoclimatology, Palaeoecology,* 152(1-2), pp.173-187.

Kump, L.R., Pavlov, A. and Arthur, M.A. (2005) Massive release of hydrogen sulfide to the surface ocean and atmospheric during intervals of oceanic anoxia, *Geology*, 33(5), pp.397-400.

Kutzbach, J.E. and Gallimore, G. (1989) Pangaean climates: Megamonsoons of the megacontinent, *Journal of Geophysical Research Atmospheres*, 94(D3), pp.3341-3357.

Kutzbach, J.E., Guetter, P.J., Ruddiman, W.F. and Prell, W.L. (1989) Sensitivity of climate to late Cenozoic uplift in southern Asia and the American west: Numerical experiments, *Journal of Geophysical Research: Atmospheres*, 94(D15), pp.18393-18407.

Le Heron, D.P. and Dowdeswell, J.A. (2009) Calculating ice volumes and ice flux to constrain the dimensions of a 440 Ma North African ice sheet, *Journal of the Geological Society*, 166(2), pp.277–281.

Le Hir, G., Donnadieu, Y., Goddéris, Y., Meyer-Berthaud, B., Ramstein, G. and Blakey, R.C. (2011) The climate change caused by the land-plant invasion, *Earth and Planetary Science Letters*, 310, pp.203–221.

Le Hir, G., Teitler, Y., Fluteau, F., Donnadieu, Y. and Philippot, P. (2014) The faint young Sun problem revisited with a 3-D climate-carbon model - Part 1, *Climate of the Past*, 10, pp.697-713.

Leavitt, W.D., Halevy, I., Bradley, A.S. and Johnston, D.T. (2013) Influence of sulfate reduction rates on the Phanerozoic sulfur isotope record, *Proceedings of the National Academy of Sciences of the United States of America*, 110(28), pp.11244-11249.

Lee, C-T. A., Shen, B., Slotnick, B.S., Liao, K., Dickens, G.R., Yokoyama, Y., Lenardic, A., Dasgupta, R., Jellinek, M., Lackey, J.S., Schneider, T. and Tice, M.M. (2013) Continental arc-island arc fluctuations, growth of crustal carbonates, and long-term climate change, *Geosphere*, 9(1), pp.21-36.

Lee, C-T.A., Thurner, S., Paterson, S. and Cao, W. (2015) The rise and fall of continental arcs: Interplays between magmatism, uplift, weathering, and climate, *Earth and Planetary Science Letters*, 425, pp.105-119.

Lefebvre, V., Servais, T., Francois, L. and Averbuch, O. (2010) Did a Katian large igneous province trigger the Late Ordovician glaciation? A hypothesis tested with a carbon cycle model, *Palaeogeography, Palaeoclimatology, Palaeoecology*, 296, pp.310-319.

Lenton, T.M. (1998) Gaia and natural selection, *Nature*, 394, pp.439-447.

Lenton, T.M. (2001) The role of lands plants, phosphorus weathering and fire in the rise and regulation of atmospheric oxygen, *Global Change Biology*, 7, pp.613-629.

Lenton, T.M., Myerscough, R.J., Marsh, R., Livina, V.N., Price, A.R. and Cox, S.J. (2009) Using GENIE to study a tipping point in the climate system, *Philosophical Transactions. Series A, Mathematical, Physical, and Engineering Sciences*, 367(1890), pp. 871–84.

Lenton, T.M. (2011) Early warning of climate tipping points, *Nature Climate Change*, 1(4), pp.201–209.

Lenton, T.M. and Watson, A.J. (2000a) Redfield Revisited 1. Regulation of nitrate, phosphate, and oxygen in the ocean, *Global Biogeochemical Cycles*, 14(1), pp.225-248.

Lenton. T.M. and Watson, A.J. (2000b) Redfield Revisited 2. What regulates the oxygen content of the atmosphere?, *Global Biogeochemical Cycles*, 14(1), pp.249-268.

Lenton, T.M. and Watson, A.J. (2011) *Revolutions That Made the Earth*, Oxford University Press, Oxford, 440pp.

Lenton, T.M., Crouch, M., Johnson, M., Pires, N. and Dolan, L. (2012) First plants cooled the Ordovician, *Nature Geoscience,* 5(2), pp.86–89.

Lenton, T.M., Dahl, T.W., Daines, S.J., Mills, B.J.W., Ozaki, K., Saltzman, M. and Porada, P. (in press) A mid-Paleozoic oxygenation event driven by early land plants.

Libby, W. (1946) Atmospheric helium three and radiocarbon from cosmic radiation, *Phys. Rev.*, 69, pp.671.

Linnemann, U., Pereira, F., Jeffries, T.E., Drost, K. and Gerdes, A. (2008) The Cadomian Orogeny and the opening of the Rheic Ocean: The diacrony of tectonic processes constrained by LA-ICP-MS U-Pb zircon dating (Ossa-Morena and Saxo-Thuringian Zones, Iberian and Bohemian Massifs), *Tectonophysics*, 461(1-4), pp.21-43.

Lorimer, G.H. (1981) The carboxylation and oxygenation of ribulose-1,5-biphosphate: the primary event in photosynthesis and photorespiration, *Annu. Rev. Plant Physiol.*, 32, pp.349-383.

Lovelock, J.E. and Whitfield, M. (1982) Life span of the biosphere, *Nature*, 296, pp.561-563.

Luo, G., Algeo, T.J., Zhan, R., Yan, D., Huang, J., Liu, J. and Xie, S. (2015) Perturbation of the marine nitrogen cycle during the Late Ordovician glaciation and mass extinction, *Palaeogeography, Palaeoclimatology, Palaeoecology*, 448, pp.339-348.

Lyons, T.W., Reinhard, C.T. and Planavsky, N.J. (2014) The rise of oxygen in Earth's early ocean and atmosphere, *Nature*, 506, pp.307-315.

Macdonald, F.A., Ryan-Davis, J., Coish, R.A., Crowley, J.L. and Karabinos, P. (2014). A newly identified Gondwanan terrane in the northern Appalachian Mountains: Implications for the Taconic orogeny and closure of the Iapetus Ocean, *Geology*, 42(6), pp.539–542.

Maher, K. and Chamberlain, C.P. (2014) Hydrologic regulation of chemical weathering and the geologic carbon cycle, *Science*, 343, pp.1502-1504.

Marshall, J.D., Brenchley, P.J., Mason, P., Wolff, G.A., Astini, R.A., Hints, L. and Meidla, T. (1997) Global carbon isotopic events associated with mass extinction and glaciation in the late Ordovician, *Palaeogeography, Palaeoclimatology, Palaeoecology*, 132(1-4), pp.195–210.

Marzoli, A., Renne, P.R., Piccirillo, E.M., Ernesto, M., Bellieni, G. and De Min, A. (1999) Extensive 200-Million-Year-Old Continental Flood Basalts of the Central Atlantic Magmatic Province, *Science*, 284, pp.616-618.

McArthur, J.M., Howarth, R J. and Bailey, T.R. (2001) Strontium Isotope Stratigraphy: LOWESS Version 3: Best Fit to the Marine Sr-Isotope Curve for 0–509 Ma and Accompanying Look-up Table for Deriving Numerical Age, *The Journal of Geology*, 109(2), pp.155-170.

McArthur, J.M. and Howarth, R.J. (2004) Sr-isotope stratigraphy: the Phanerozoic $^{87}Sr/^{86}Sr$-curve and explanatory notes, in Gradstein, F.M., Ogg, J.G. and Smith, A.G. eds. *A Geological Timescale 2004*, Elsevier.

McArthur, J.M., Howarth, R.J. and Shields, G.A. (2012) Strontium isotope stratigraphy, in Gradstein, F.M., Ogg, J.G., Schmitz, M.D. and Ogg, G.M. eds. *The Geologic Time Scale*, Elsevier, pp.127–144.

McClellan, E. and Gazel, E. (2014) The Cryogenian intra-continental rifting of Rodinia: Evidence from the Laurentian margin in eastern North America, *Lithos*, 206-207, pp.321-337.

McElwain, J.C., Beerling, D.J. and Woodward, F.I. (1999) Fossil Plants and Global Warming at the Triassic-Jurassic Boundary, *Science*, 285(5432), pp.1386-1390.

McKenzie, N.R., Hughes, N.C., Gill, B.C. and Myrow, P.M. (2014) Plate tectonic influences on Neoproterozoic-early Paleozoic climate and animal evolution, *Geology*, 42(2), pp.127–130.

McKenzie, N.R., Horton, B.K., Loomis, S.E., Stockli, D.F., Planavsky, N.J. and Lee, C.T. (2016) Continental arc volcanism as the principal driver of icehouse-greenhouse variability, *Science*, 352(6284), pp.444-447.

McKerrow, W.S., Mac Niocaill, C. and Dewey, J.F. (2000) The Caledonian Orogeny redefined, *Journal of the Geological Society, London*, 157, pp.1149-1154.

Melchin, M.J., Mitchell, C.E., Holmden, C. and Storch, P. (2013) Environmental changes in the Late Ordovician-early Silurian: Review and new insights from black shales and nitrogen isotopes, *Geological Society of America Bulletin*, 125(11-12), pp.1635–1670.

Meert, J.G. (2012) Whats in a name? The Columbia (Palaeopangaea/Nuna) supercontinent, *Gondwana Research*, 21(4), pp.987-993.

Meybeck, M. (1987) Global chemical weathering of surficial rocks estimated from river dissolved loads, *American Journal of Science*, 287, pp.401-428.

Miller, K.G., Kominz, M.A., Browning, J.V., Wright, J.D., Mountain, G.S., Katz, M.E., Sugarman, P.J., Cramer, B.S., Christie-Blick, N. and Pekar, S.F. (2005) The Phanerozoic Record of Global Sea-Level Change, *Science*, 310, pp.1293-1298.

Milliman, J.D. (1993) Production and accumulation of calcium carbonate in the ocean: budget of a nonsteady state, *Global Biogeochemical Cycles*, 7(4), pp.927-957.

Mills, B.J.W., Watson, A.J., Goldblatt, C., Boyle, R. and Lenton, T.M. (2011) Timing of Neoproterozoic glaciations linked to transport-limited global weathering, *Nature Geoscience*, 4(12), pp.861–864.

Mills, B.J.W., Lenton, T.M. and Watson, A.J. (2014a) Proterozoic oxygen rise linked to shifting balance between seafloor and terrestrial weathering, *Proceedings of the National Academy of Sciences of the United States of America*, 111(25), pp.9073–9078.

Mills, B.J.W., Daines, S.J. and Lenton, T.M. (2014b) Changing tectonic controls on the long-term carbon cycle from Mesozoic to present, *Geochemistry, Geophysics, Geosystems*, 15(12), pp.4866–4884.

Mills, B.J.W., Scotese, C.R., Walding, N.G. and Lenton, T.M. (2016) Subduction Zones, CO_2 Degassing, and Recovery from the Cryogenian Icehouse [abstract], in Goldschmidt Conference, 2016, 26/06-01/07, Yokohama, Japan.

Mills, B.J.W., Scotese, C.R., Walding, N.G. and Lenton, T.M. (in preparation) Increasing length of subduction zones drives recovery from the Cryogenian icehouse.

Misra, S. and Froelich, P.N. (2012) Lithium Isotope History of Cenozoic Seawater: Changes in Silicate Weathering and Reverse Weathering, *Science*, 335(6070), pp.818–823.

Molnar, P., Boos, W.R. and Battisti, D.S. (2010) Orographic controls on climate and paleoclimate of Asia: Thermal and mechanical roles for the Tibetan Plateau, *Annual Review of Earth and Planetary Sciences*, 38, pp.77-10.

Montanez, I.P., Banner, J.L., Osleger, D.A., Borg, L.E. and Bosserman, P.J. (1996) Integrated Sr isotope variations and sea-level history of Middle to Upper Cambrian platform carbonates: Implications for the evolution of Cambrian seawater 87Sr/86Sr, *Geology*, 24(10), pp.917–920.

Montanez, I.P., Tabor, N.J., Niemeier, D., DiMichele, W.A., Frank, T.D., Fielding, C.R., Isbell, J.L., Birgenheier, L. and Rygel, M.C. (2007) CO_2-Forced Climate and Vegetation Instability During Late-Paleozoic Deglaciation, *Science*, 315(5808), pp.87-91.

Montanez, I.P. (2016) A Late Paleozoic climate window of opportunity, *Proceedings of the National Academy of Sciences of the United States of America*, 113(9), pp.2334–2336.

Moore, P.D. (1989) The ecology of peat-forming processes: a review, *International Journal of Coal Geology*, 12, pp.89-103.

Moore, T.L. and Worsley, T.R. (1994) *Pangea: Paleoclimate, Tectonics, and Sedimentation During Accretion, Zenith, and Breakup of a Supercontinent*. *Geological Society of America Special Papers* (Vol. 288), Geological Society of America, http://doi.org/10.1130/SPE288.

Mora, C.I., Driese, S.G. and Seager, P.G. (1991) Carbon dioxide in the Paleozoic atmosphere: Evidence from carbon-isotope compositions of pedogenic carbonate, *Geology*, 19(10), pp.1017-1020.

Mora, C.I., Driese, S.G. and Colarusso, L.A. (1996) Middle to late Paleozoic atmospheric CO2 levels from soil carbonate and organic matter, *Science*, 271(5252), pp.1105-1107.

Munnecke, A., Calner, M., Harper, D.A.T. and Servais, T. (2010) Ordovician and Silurian sea–water chemistry, sea level, and climate: A synopsis, *Palaeogeography, Palaeoclimatology, Palaeoecology*, 296(3-4), pp.389–413.

Murphy, J.B., van Staal, C.R. and Keppie, J.D. (1999) Middle to late Paleozoic Acadian orogeny in the northern Appalachians: A Laramide-style plume-modified orogeny?, *Geology*, 27(7), pp.653-656.

Murphy, J.B. and Keppie, J.D. (2005) The Acadian Orogeny in the Northern Appalachians, *International Geology Review*, 47(7), pp.663-687.

Nance, R.D. and Murphy, J.B. (2013) Origins of the supercontinent cycle, *Geoscience Frontiers*, 4(4), pp.439-448.

Nance, R.D., Murphy, J.B. and Santosh, M. (2014) The supercontinent cycle: A retrospective essay, *Gondwana Research*, 25(1), pp.4-29.

Nardin, E., Godderis, Y., Donnadieu, Y., Le Hir, G., Blakey, R.C., Puceat, E. and Aretz, M. (2011) Modelling the early Paleozoic long-term climatic trend, *Geological Society of America Bulletin*, 123(5/6), pp.1181-1192.

Nehlich, O. (2015) The application of sulfur isotope analyses in archaeological research: A review, *Earth-Science Reviews*, 142, pp.1–17.

Nelsen, M.P., DiMichele, W.A., Peters, S.E. and Boyce, C.K. (2016) Delayed fungal evolution did not cause the Paleozoic peak in coal production, *Proceedings of the National Academy of Sciences*, 113(9), pp.2442-2447.

Newman, M.J. and Rood, R.T. (1977) Implications of solar evolution for the Earth's early atmosphere, *Science*, 198(4321), pp.1035-1037.

Newton, R.C., Smith, J.V. and Windley, B.F. (1980) Carbonic metamorphism, granulites and crustal growth, *Nature*, 288, pp.45-50.

Nicholas, C.J. (1996) The Sr isotopic evolution of the oceans during the 'Cambrian Explosion', *Journal of the Geological Society, London*, 153, pp.243-254.

North, G.R., Cahalan, R.F. and Coakley, J.A. (1981) Energy balance climate models, *Reviews of Geophysics*, 19(1), pp.91-121.

North, G.R. (1984) The small ice cap instability in diffusive climate models, *Journal of the Atmospheric Sciences*, 41(23), pp.3390-3395.

Notz, D. (2009) The future of ice sheets and sea ice: between reversible retreat and unstoppable loss, *Proceedings of the National Academy of Sciences of the United States of America*, 106(49), pp.20590–20595.

Ohno, T., Komiya, T., Ueno, Y., Hirata, T. and Maruyama, S. (2008) Determination of $^{88}Sr/^{86}Sr$ mass-dependent isotopic fractionation and radiogenic isotopic variation of $^{87}Sr/^{86}Sr$ in the Neoproterozoic Doushantuo Formation, *Gondwana Research*, 14(1-2), pp.126-133.

Otto-Bliesner, B.L. (1995) Continental drift, runoff, and weathering feedbacks: Implications from climate model experiments, *Journal of Geophysical Research: Atmospheres*, 100(D6), pp.11537-11548.

Page, A.A., Zalasiewicz, J.A., Williams, M. and Popov, L.E. (2007) Were transgressive black shales a negative feedback modulating glacioeustasy in the Early Palaeozoic Icehouse?, in Williams, M., Haywood, A.M., Gregory, J.F. and Schmidt, D.N. eds. *Deep Time Perspectives on Climate Change: Marrying the Signal from Computer Models and Biological Proxies*, Micropalaeontological Society Special Publications, Geological Society of London, London, pp.123-156.

Palmer, M.R. and Elderfield, H. (1985) Sr isotopic composition of sea water over the past 75Myr, *Nature*, 314, pp.526-528.

Palmer, M.R. and Edmond, J.M. (1989) The strontium isotope budget of the modern ocean, *Earth and Planetary Science Letters*, 92(1), pp.11-26.

Papanastassiou, D.A. and Wasserburg, G.J. (1968) Initial strontium isotope abundances and the resolution of small time differences in the formation of planetary objects, *Earth and Planetary Science Letters*, 5, pp.361-376.

Park, J. and Royer, D.L. (2011) Geologic Constraints on the Glacial Amplification of Phanerozoic Climate Sensitivity, *American Journal of Science*, 311, pp.1-26.

Paris, F., Verniers, J., Miller, M.A., Al-Hajri, S., Melvin, J. and Wellman, C.H. (2015) Late Ordovician–earliest Silurian chitinozoans from the Qusaiba-1 core hole (North Central Saudi Arabia) and their relation to the Hirnantian glaciation, *Review of Palaeobotany and Palynology*, 212, pp.60–84.

Parnell, J. and Foster, S. (2012) Ordovician ash geochemistry and the establishment of land plants, *Geochemical Transactions*, 13(1), http://doi.org/10.1186/1467-4866-13-7.

Payne, J.L., Lehrmann, D.J., Wei, J., Orchard, M.J., Schrag, D.P. and Knoll, A.H. (2004) Large Perturbations of the Carbon Cycle During Recovery from the End-Permian Extinction, *Science*, 305, pp.506-509.

Paytan, A., Kastner, M., Campbell, D. and Thiemens, M.H. (1998) Sulfur isotope composition of Cenozoic seawater sulfate, *Science*, 282, pp.1459-1462.

Paytan, A. and Gray, E.T. (2012) Sulfur Isotope Stratigraphy, in Gradstein, F.T., Ogg, J.G., Schmitz, M.D. and Ogg, G.M. eds. *The Geologic Time Scale 2012*, Elsevier, pp.167-180.

Perrier, V., Meidla, T., Tinn, O. and Ainsaar, L. (2012) Biotic response to explosive volcanism: Ostracod recovery after Ordovician ash-falls, *Palaeogeography, Palaeoclimatology, Palaeoecology*, 365-366, pp.166–183.

Peucker-Ehrenbrink, B. and Miller, M.W. (2006) Marine 87Sr/86Sr record mirrors the evolving upper continental crust, *Geochimica et Cosmochimica Acta*, 70(18), DOI: 10.1016/j.gca.2006.06.1437.

Planavsky, N.J., Rouxel, O.J., Bekker, A., Lalonde, S.V., Konhauser, K.O., Reinhard, C.T. and Lyons, T.W. (2010) The evolution of the marine phosphate reservoir, *Nature*, 467(7319), pp.1088–1090.

Pogge von Strandmann, P.A.E., Stüeken, E.E., Elliott, T., Poulton, S.W., Dehler, C.M., Canfield, D.E. and Catling, D.C. (2015) Selenium isotope evidence for progressive oxidation of the Neoproterozoic biosphere, *Nature Communications*, 6, 10157, doi:10.1038/ncomms10157.

Pohl, A., Donnadieu, Y., Le Hir, G., Buoncristiani, J.-F. and Vennin, E. (2014) Effect of the Ordovician paleogeography on the (in)stability of the climate, *Climate of the Past*, 10(6), pp.2053–2066.

Pohl, A., Nardin, E., Vandenbroucke, T.R.A. and Donnadieu, Y. (2015) High dependence of Ordovician ocean surface circulation on atmospheric CO2 levels, *Palaeogeography, Palaeoclimatology, Palaeoecology*, http://doi.org/10.1016/j.palaeo.2015.09.036.

Porada, P., Weber, B., Elbert, W., Pöschl, U. and Kleidon, A. (2013) Estimating global carbon uptake by lichens and bryophytes with a process-based model, *Biogeosciences Discussions*, 10(2), pp.3735–3847.

Porada, P., Weber, B., Elbert, W., Pöschl, U., & Kleidon, A. (2014) Estimating impacts of lichens and bryophytes on global biogeochemical cycles, *Global Biogeochemical Cycles*, 28(2), pp.71–85.

Porada, P., Lenton, T.M., Pohl, A., Weber, B., Mander, L., Donnadieu, Y., Beer, C., Poschl, U. and Kleidon, A. (2016) High potential for weathering and climate effects of non-vascular vegetation in the Late Ordovician, *Nature Communications*, 7, doi:10.1038/ncomms12113.

Poulsen, C.J., Pollard, D., Montanez, I.P. and Rowley, D. (2007) Late Paleozoic tropical climate response to Gondwanan deglaciation, *Geology*, 35(9), pp.771-774.

Poulsen, C.J., Tabor, C. and White, J.D. (2015) Long-term climate forcing by atmospheric oxygen concentrations, *Science*, 348(6240), pp.1238-1241.

Poussart, P.F., Weaver, A.J. and Barnes, C.R. (1999) Late Ordovician glaciation under high atmospheric CO_2 : A coupled model analysis, *Paleoceanography*, 14(4), pp.542–558.

Probst, J-L. and Tardy, Y. (1989) Global Runoff Fluctuations During the Last 80 Years in Relation to World Temperature Change, *American Journal of Science*, 289, pp.267-285.

Prokoph, A., Shields, G.A. and Veizer, J. (2008) Compilation and time-series analysis of a marine carbonate δ18O, δ13C, 87Sr/86Sr and δ34S database through Earth history, *Earth-Science Reviews*, 87(3-4), pp.113–133.

Qing, H., Barnes, C.R., Buhl, D. and Veizer, J. (1998) The strontium isotopic composition of Ordovician and Silurian brachiopods and conodonts: relationships to geological events and implications for coeval seawater, *Geochimica et Cosmochimica Acta*, 62(10), pp.1721–1733.

Quirk, J., Beerling, D.J., Banwart, S.A., Kakonyi, G., Romero-Gonzalez, M.E. and Leake, J.R. (2012) Evolution of trees and mycorrhizal fungi intensifies silicate mineral weathering, *Biology Letters*, 8(6), 10.1098/rsbl.2012.0503.

Quirk, J., Leake, J.R., Johnson, D.A., Taylor, L.L., Saccone, L. and Beerling, D.J. (2015) Constraining the role of early land plants in Palaeozoic weathering and global cooling, *Proc. R. Soc. B*., 282(1813), http://doi.org/10.1098/rspb.2015.1115.

Raevskaya, E., Dronov, A., Servais, T. and Wellman, C.H. (2016) Cryptospores from the Katian (Upper Ordovician) of the Tungus basin: The first evidence for early land plants from the Siberian paleocontinent, *Review of Palaeobotany and Palynology*, 224, pp.4–13.

Rampino, M.R. and Caldeira, K. (1993) Major episodes of geologic change: Correlations, time structure and possible causes, *Earth and Planetary Science Letters*, 114, pp.215-227.

Rasmussen, C.M.Ø., Ullmann, C.V, Jakobsen, K.G., Lindskog, A., Hansen, J., Hansen, T., Eriksson, M.E., Dronov, A., Frei, R., Korte, C., Nielsen, A.T. and Harper, D.A.T. (2016) Onset of main Phanerozoic marine radiation sparked by emerging Mid Ordovician icehouse, *Scientific Reports*, 6, http://doi.org/10.1038/srep18884.

Raven, J.A. and Andrews, M. (2010) Evolution of tree nutrition, *Tree Physiology*, 30(9), pp.1050-1071.

Renne, P.R., Zichao, Z., Richards, M.A., Black, M.T. and Basu, A.R. (1995) Synchrony and Causal Relations between Permian-Triassic Boundary Crisis and Siberian Flood Volcanism, *Science*, 269, pp.1413-1416.

Retallack, G.J. (1997) Early forest soils and their role in Devonian climate change, *Science*, 276, pp.583-585.

Retallack, G.J. (2013) Ediacaran Gaskiers Glaciation of Newfoundland reconsidered, *Journal of the Geological Society*, 170(1), pp.19–36.

Robinson, J.M. (1990) Lignin, land plants, and fungi: Biological evolution affecting Phanerozoic oxygen balance, *Geology*, 15, pp.607-610.

Roeske, C.A. and O'Leary, M.H. (1984) Carbon isotope effects on the enzyme-catalysed carboxylation of ribulose biphosphate, *Biochemistry*, 23(25), pp.6275-6284.

Romano, C., Goudemand, N., Vennemann, T.W., Ware, D., Schneebeli-Hermann, E., Hochuli, P.A., Bruhwiler, T., Brinkmann, W. and Bucher, H. (2013) Climatic and biotic upheavals following the end-Permian mass extinction, *Nature Geoscience*, 6, pp.57-60.

Ronov, A.B. (1994) Phanerozoic transgressions and regressions on the continents: a quantitative approach based on areas flooded by the sea and areas of marine and continental deposition, *American Journal of Science*, 294(7), pp.777-801.

Roscher, M., Stordal, F. and Svensen, H. (2011) The effect of global warming and global cooling on the distribution of the latest Permian climate zones, *Palaeogeography, Palaeoclimatology, Palaeoecology*, 309, pp.186-200.

Rose, B.E.J., Ferreira, D. and Marshall, J. (2013) The Role of Oceans and Sea Ice in Abrupt Transitions between Multiple Climate States, *Journal of Climate*, 26(9), pp.2862–2879.

Rose, B.E.J. and Marshall, J. (2009) Ocean Heat Transport, Sea Ice, and Multiple Climate States: Insights from Energy Balance Models, *Journal of the Atmospheric Sciences,* 66(9), pp.2828-2843.

Rosenbaum, G. and Lister, G. (2002) Relative motions of Africa, Iberia and Europe during Alpine orogeny, *Tectonophysics*, 359, pp.117-129.

Rothman, D.H. (2002) Atmospheric carbon dioxide levels for the last 500 million years, *Proceedings of the National Academy of Sciences*, 99, pp.4167-4171.

Rowe, N.P. and Jones, T.P. (2000) Devonian charcoal, *Palaeogeography, Palaeoclimatology, Palaeoecology*, 164, pp.347-354.

Royer, D.L. (2006) CO2-forced climate thresholds during the Phanerozoic, *Geochimica et Cosmochimica Acta*, 70(23), pp.5665–5675.

Royer, D.L. (2014) Atmospheric CO_2 and O_2 during the Phanerozoic: Tools, Patterns, and Impacts, in Holland, H.D. and Turekian, K. eds. *Treatise on Geochemistry (Second Edition)*, Elsevier Science.

Royer, D.L., Donnadieu, Y., Park, J., Kowalczyk, J., & Godderis, Y. (2014) Error analysis of CO2 and O2 estimates from the long-term geochemical model GEOCARBSULF, *American Journal of Science*, 314(9), pp.1259–1283.

Rubinstein, C.V, Gerrienne, P., de la Puente, G.S., Astini, R.A. and Steemans, P. (2010) Early Middle Ordovician evidence for land plants in Argentina (eastern Gondwana), *The New Phytologist*, 188(2), pp.365–369.

Sadler, P.M. and Cooper, R.A. (2004) Calibration of the Ordovician Timescale, in Webby, B.W., Paris, F., Droser, M.L. and Percival, I.G. eds., *The Great Ordovician Biodiversification Event*, Columbia University Press, pp.48-51.

Sadler, P.M., Cooper, R.A. and Melchin, M. (2009) High-resolution, early Paleozoic (Ordovician-Silurian) time scales, *GSA Bulletin*, 121(5/6), pp.887-906.

Sagan, C. and Mullen, G. (1972) Earth and Mars: Evolution of atmospheres and surfaces temperatures, *Science*, 177(4043), pp.52-56.

Saltzman, M.R. (2005) Phosphorus, nitrogen, and the redox evolution of the Paleozoic oceans, *Geology*, 33(7), pp.573-576.

Saltzman, M.R. and Thomas, E. (2012) Carbon Isotope Stratigraphy, in Gradstein, F., Ogg, J., Schmitz, M.D. and Ogg, G. eds. *The Geologic Time Scale 2012*, Elsevier, pp.207-232.

Saltzman, M.R., Edwards, C.T., Leslie, S.A., Dwyer, G.S., Bauer, J.A., Repetski, J.E., Harris, A.G. and Bergström, S.M. (2014) Calibration of a conodont apatite-based Ordovician $^{87}Sr/^{86}Sr$ curve to biostratigraphy and geochronology: Implications for stratigraphic resolution, *Geological Society of America Bulletin*, 126(11-12), pp.1551–1568.

Scheffler, K., Hoernes, S. and Schwark, L. (2003) Global changes during Carboniferous-Permian glaciation of Gondwana: Linking polar and equatorial climate evolution by geochemical proxies, *Geology*, 31(7), pp.605-608.

Schlanger, S.O. (1988) Strontium Storage and Release During Deposition and Diagenesis of Marine Carbonates Related to Sea-Level Variations, in Lerman, A. and Meybeck, M. eds. *Physical and Chemical Weathering in Geochemical Cycles*, Kluwer Academic Publishers, pp.323-339.

Schmid, S.M., Fugenschuh, B., Kissling, E. and Schuster, R. (2004) Tectonic map and overall architecture of the Alpine orogeny, *Eclogae Geologicae Helvetiae*, 97(1), pp.93-117.

Schmitz, B., Harper, D.A.T., Peucker-Ehrenbrink, B., Stouge, S., Alwmark, C., Cronholm, A., Bergström, S.M., Tassinari, M. and Xiaofeng, W. (2008) Asteroid breakup linked to the Great Ordovician Biodiversification Event, *Nature Geoscience*, 1(1), pp.49–53.

Schneebeli-Hermann, E. (2012) Extinguishing a Permian World, *Geology*, 40(3), pp.287-288.

Schwartzman, D.W. and Volk, T. (1989) Biotic enhancement of weathering and the habitability of Earth, *Nature*, 340, pp.457-460.

Scotese, C.R. (2015) Plate Tectonic Flipbook, Van der Voo Retirement Symposium, August 26-27, Ann Arbury, MI.

Scott, A.C. and Glasspool, I.J. (2006) The diversification of Paleozoic fire systems and fluctuations in atmospheric oxygen concentration, *Proceedings of the National Academy of Sciences of the United States of America*, 103(29), pp.10861-10865.

Sell, B.K. (2011) Intense Volcanism and Ordovician Icehouse Climate, in Gutierrez-Marco, J.C., Rabano, I. and Garcia-Bellido eds. *Ordovician of the World*, Cuadernos del Mussel Geominero, 14. Instituto Geológico y Minero de España, Madrid. ISBN 978-84-7840-857-3.

Sell, B.K., Ainsaar, L. and Leslie, S. (2013) Precise timing of the Late Ordovician (Sandbian) super-eruptions and associated environmental, biological, and climatological events, *Journal of the Geological Society, London*, doi: 10.1144/jgs2012-148.

Sellers, W.D. (1969) A Global Climatic Model Based on the Energy Balance of the Earth-Atmosphere System, *Journal of Applied Meteorology*, 8, pp.392-400.

Servais, T., Harper, D.A.T., Munnecke, A., Owen, A.W. and Sheehan, P.M. (2009) Understanding the Great Ordovician Biodiversification Event (GOBE): Influences of paleogeography, paleoclimate, or paleoecology, *GSA Today*, 19(4), pp.4-10.

Sheehan, P.M. (2001) The Late Ordovician Mass Extinction, *Annual Review of Earth and Planetary Sciences*, 29, pp.331-364.

Shen, S., Crowley, J.L., Wang, Y., Bowring, S.A., Erwin, D.H., Sadler, P.M., Cao, C., Rothman, D.H., Henderson, C.H., Ramezani, J., Zhang, H., Shen, Y., Wang, X., Wang, W., Mu, L., Li, W., Tang, Y., Liu, X., Liu, L., Zeng, Y., Jiang, Y. and Jin, Y. (2011) Calibrating the End-Permian Mass Extinction, *Science*, 334(6061), pp.1367-1372.

Shields, G.A., Carden, G.A. ., Veizer, J., Meidla, T., Rong, J.-Y. and Li, R.-Y. (2003) Sr, C, and O isotope geochemistry of Ordovician brachiopods: a major isotopic event around the Middle-Late Ordovician transition, *Geochimica et Cosmochimica Acta*, 67(11), pp.2005–2025.

Shields, G.A. (2007) A normalised seawater strontium isotope curve: possible implications for Neoproterozoic-Cambrian weathering rates and the further oxygenation of the Earth, *eEarth*, 2(2), pp.35-42.

Simancas, J.F., Tahiri, A., Azor, A., Lodeiro, F.G., Martinez Poyatos, D.J., El Hadi, H. (2005) The tectonic frame of the Variscan-Alleghanian orogeny in Southern Europe and Northern Africa, *Tectonophysics*, 398, pp.181-198.

Simon, L., Bousquet, J., Levesque, R. and Lalonde, M. (1993) Origin and diversification of endomycorrhizal fungi and coincidence with vascular land plants, *Nature*, 363, pp.67-69.

Snyder, J. (1987) *Map Projections: A Working Manual*, U.S. Geological Survey Professional Paper 1395, United States Government Printing Office, Washington.

Steuber, T. and Veizer, J. (2002) Phanerozoic record of plate tectonic control of seawater chemistry and carbonate sedimentation, *Geology*, 30(12), pp.1123–1126.

Stoll, H.M. and Schrag, D.P. (1998) Effects of Quaternary sea level cycles of strontium in seawater, *Geochimica et Cosmochimica Acta*, 62(7), pp.1107-1118.

Strauss, H. (1997) The isotopic composition of sedimentary sulfur through time, *Palaeogeography, Palaeoclimatology, Palaeoecology*, 132(1-4), pp.97–118.

Strauss, H. (1999) Geological evolution from isotopic proxy signals – sulfur, *Chemical Geology*, 161(1-3), pp.89-101.

Stanley, S.M. and Hardie, L.A. (1998) Secular oscillations in the carbonate mineralogy of reef-building and sediment-producing organisms driven by tectonically forced shifts in seawater chemistry, *Palaeogeography, Palaeoclimatology, Palaeoecology*, 114, pp.3-19.

Sturt, B.A., Pringle, I.R. and Ramsay, D.M. (1978) The Finnmarkian phase of the Caledonian orogeny, *Journal of the Geological Society, London*, 135, pp.597-610.

Sun, Y., Joachimski, M.M., Wignall, P.B., Yan, C., Chen, Y., Jiang, H., Wang, L. and Lai, X. (2012) Lethally hot temperatures during the Early Triassic greenhouse, *Science*, 338(6105), pp.366-370.

Sutcliffe, O.E., Dowdeswell, J.A., Whittington, R.J., Theron, J.N. and Craig, J. (2000) Calibrating the Late Ordovician glaciation and mass extinction by the eccentricity cycles of Earth's orbit, *Geology*, 28(11), pp.967-970.

Tajika, E. and Matsui, T. (1993) Evolution of seafloor spreading rate based on ^{40}Ar degassing history, *Geophysical Research Letters*, 20(9), pp.851-854.

Taylor, E.L., Taylor, T.N. and Cuneo, N.R. (1992) The present is not the key to the past: A Permian petrified forest in Antarctica, *Science*, 257, pp.1675-1677.

Taylor, A. and Lasaga, A. (1999) The role of basalt weathering in the Sr isotope budget of the oceans, *Chemical Geology*, 161(1-3), pp.199–214.

Tobin, K.J., Bergstrom, S.M. and De La Garza, P. (2005) A mid-Caradocian (453Ma) drawdown in atmospheric pCO_2 without ice sheet development?, *Palaeogeography, Palaeoclimatology, Palaeoecology*, 226(3-4), pp.187-204.

Trexler, J.C. and Travis, J. (1993) Nontraditional regression analyses, *Ecology*, 74(6), pp.1629-1637.

Trotter, J.A., Williams, I.S., Barnes, C.R., Lecuyer, C. and Nicoll, R.S. (2008) Did cooling oceans trigger Ordovician biodiversification? Evidence from conodont thermometry, *Science*, 321, pp.550-554.

Underwood, C.J., Crowley, S.F., Marshall, J.D. and Brenchley, P.J. (1997) High-Resolution carbon isotope stratigraphy of the basal Silurian Stratotype (Dob's Linn, Scotland) and its global correlation, *Journal of the Geological Society*, 154, pp.709-718.

Urey, H.C. (1952) On the Early Chemical History of the Earth and the Origin of Life, *Proceedings of the National Academy of Sciences of the United States of America*, 38(4), pp.351-363.

Van Cappellen, P. and Ingall, E.D. (1994) Benthic phosphorus regeneration, net primary production, and ocean anoxia: A model of the coupled marine biogeochemical cycles of carbon and phosphorus, *Paleoceanography,* 9(5), pp.677-692.

Van Cappellen, P. and Ingall, E.D. (1996) Redox stabilization of the atmosphere and oceans by phosphorus-limited marine productivity, *Science*, 271(5248), pp.493-496.

Van de Schootbrugge, B. (2010) Palaeoclimate: A fiery start to the Jurassic, *Nature Geoscience*, 3(6), pp.381-382.

Van Geldern, R., Joachimski, M.M., Day, J., Jansen, U., Alvarez, F., Yolkin, E A. and Ma, X.-P. (2006) Carbon, oxygen and strontium isotope records of Devonian brachiopod shell calcite, *Palaeogeography, Palaeoclimatology, Palaeoecology*, 240(1-2), pp.47–67.

Vandenbroucke, T.R.A., Armstrong, H.A., Williams, M., Paris, F., Zalasiewicz, J.A., Sabbe, K., Nolvak, J., Challands, T.J., Verniers, J. and Servais, T. (2010) Polar front shift and atmospheric CO2 during the glacial maximum of the Early Paleozoic Icehouse, *Proceedings of the National Academy of Sciences of the United States of America*, 107(34), pp.14983–14986.

Vandenbroucke, T.R.A., Emsbo, P., Munnecke, A., Nuns, N., Duponchel, L., Lepot, K., Quijada, M., Paris, F., Servais, T. and Kiessling, W. (2015) Metal-induced malformations in early Palaeozoic plankton are harbingers of mass extinction, *Nature Communications*, 6, 7966, http://doi.org/10.1038/ncomms8966.

Van Der Meer, D.G., Zeebe, R.E., van Hinsbergen, D.J.J., Sluijs, A., Spakman, W. and Torsvik, T.H. (2014) Plate tectonic controls on atmospheric CO_2 levels since the Triassic, *Proceedings of the National Academy of Sciences*, 111(12), pp.4380-4385.

Varga, P., Krumm, F.W., Doglioni, C., Grafarend, E.W., Panza, G., Riguzzi, F., Schreider, A.A. and Sneeuw, N. (2012) Did a change in tectonic regime occur between the Phanerozoic and earlier Epochs?, *Rendiconti Lincei*, 23(2), pp.139–148.

Veevers, J.J. and Powell, C.M. (1987) Late Paleozoic glacial episodes in Gondwanaland reflected in transgressive-regressive depositional sequences in Euramerica, *Geological Society of America Bulletin*, 98, pp.475-487.

Veizer, J. and Jansen, S.L. (1985) Basement and sedimentary cycling – 2: Time dimension to global tectonics, *Journal of Geology*, 93, pp.625-664.

Veizer, J., Buhl, D., Diener, A., Ebneth, S., Podlaha, O.G., Bruckshen, P., Jasper, T., Korte, C., Schaaf, M., Ala, D. and Azmy, K. (1997) Strontium isotope stratigraphy: potential resolution and event correlation, *Palaeogeography, Palaeoclimatology, Palaeoecology*, 132(1-4), pp.65-77.

Veizer, J., Ala, D., Azmy, K., Bruckshen, P., Buhl, D., Bruhn, F., Carden, G.A.F., Diener, A., Ebneth, S., Godderis, Y., Jasper, T., Korte, C., Pawellek, F., Podlaha, O.G. and Strauss, H. (1999) $^{87}Sr/^{86}Sr$, $\delta^{13}C$ and $\delta^{18}O$ evolution of Phanerozoic seawater, *Chemical Geology*, 161(1-3), pp.59-88.

Veizer, J., Godderis, Y. and François, L.M. (2000) Evidence for decoupling of atmospheric CO2 and global climate during the Phanerozoic eon, *Nature*, 408(6813), pp.698–701.

Volk, T. (1989) Sensitivity of climate and atmospheric CO_2 to deep-ocean and shallow-ocean carbonate burial, *Nature*, 337, pp.637-640.

Vollstaedt, H., Eisenhauer, A., Wallmann, K., Böhm, F., Fietzke, J., Liebetrau, V., Krabbenhoft, A., Farkas, J., Tomasovych, A., Raddatz, J. and Veizer, J. (2014) The Phanerozoic δ88/86Sr record of seawater: New constraints on past changes in oceanic carbonate fluxes. *Geochimica et Cosmochimica Acta*, 128, pp.249–265.

Wadhams, P. (2012) Arctic ice cover, ice thickness and tipping points, *Ambio*, 41(1), pp.23–33.

Walker, J.C.G., Hays, P.B. and Kasting, J.F. (1981) A negative feedback mechanism for the long-term stabilization of Earth's surface temperature, *Journal of Geophysical Research*, 86(C10), pp.9776-9782.

Walker, L.J., Wilkinson, B.H. and Ivany, L.C. (2002) Continental Drift and Phanerozoic Carbonate Accumulation in Shallow-Shelf and Deep-Marine Settings, *The Journal of Geology*, 110(1), pp.75–87.

Webby, B.W., Cooper, R.A., Bergstrom, S.M. and Paris, F. (2004) Stratigraphic Framework and Time-Slices, in Webby, B.W., Paris, F., Droser, M.L. and Percival, I.G. eds., *The Great Ordovician Biodiversification Event*, Columbia University Press, pp.41-47.

Wellman, C.H., Edwards, D. and Axe, L. (1998) Permanent dyads in sporangia and spore masses from the Lower Devonian of the Welsh Borderland, *Botanical Journal of the Linnean Society*, 127(2), pp.117-147.

Wellman, C.H. (2010) The invasion of the land by plants: when and where?, *New Phytologist*, 188(2), pp.306–309.

Wellman, C.H., Steemans, P. and Miller, M.A. (2015) Spore assemblages from Upper Ordovician and lowermost Silurian sediments recovered from the Qusaiba-1 shallow core hole, Qasim region, central Saudi Arabia, *Review of Palaeobotany and Palynology*, 212, pp.111-126.

Wenzel, B. and Joachimski, M.M. (1996) Carbon and oxygen isotopic composition of Silurian brachiopods (Gotland/Sweden): palaeoceanographic implications, *Palaeogeography, Palaeoclimatology, Palaeoecology*, 122, pp.143-166.

Wheat, C.G., Elderfield, H., Mottl, M.J. and Monnin, C. (2000) Chemical composition of basement fluids within an ocean ridge flank: implications for along-strike hydrothermal circulation, *Journal of Geophysical Research*, 105, pp.13437-13447.

Wheat, C.G. and Fischer, A.T. (2008) Massive, low-temperature hydrothermal flow from a basaltic outcrop on 23Ma seafloor of the cocos plate: chemical constraints and implications, *Geochemistry, Geophysics, Geosystems*, 9(12), *Q12O14, doi:10.1029/2008GC002136.*

Wignall, P.B. and Hallam, A. (1992) Anoxia as a cause of the Permian/Triassic extinction: facies evidence from northern Italy and the western United States, *Palaeogeography, Palaeoclimatology, Palaeoecology,* 93, pp.21-46.

Wignall, P.B., Sun, Y-D., Bond, D.P.G., Izon, G., Newton, R.J., Vedrine, S., Widdowson, M., Ali, J.R., Lai, X-L., Jiang, H-S., Cope, H. and Bottrell, S.H. (2009) Volcanism, mass extinction and carbon isotope fluctuations in the Middle Permian of China*, Science,* 324, pp.1179-1182*.*

Wilde, P. (1991) Oceanography in the Ordovician, in Barnes, C.R. and Williams, S.H. eds.*, Advances in Ordovician Geology*, Geological Survey of Canada Paper 90-9, pp.283-298.

Wold, C.N. and Hay, W.W. (1990) Estimating ancient sediment fluxes*,* *American Journal of Science*, 290, pp.1069-1089.

Worsley, T.R. and Kidder, D.L. (1991) First-order coupling of paleogeography and CO_2 with global surface temperature and its latitudinal contrast, *Geology*, 19, pp.1161-1164.

Wortmann, U.G. and Chernyavsky, B.M. (2007) Effect of evaporate deposition on Early Cretaceous carbon and sulphur cycling, *Nature*, 446, pp.654-656.

Wortmann, U.G. and Paytan, A. (2012) Rapid Variability of Seawater Chemistry Over the Past 130 Million Years, *Science*, 337(6092), pp.334-336.

Yan, D., Chen, D., Wang, Q., Wang, J. and Wang, Z. (2009) Carbon and sulfur isotopic anomalies across the Ordovician–Silurian boundary on the Yangtze Platform, South China, *Palaeogeography, Palaeoclimatology, Palaeoecology*, 274(1-2), pp.32–39.

Yan, D., Chen, D., Wang, Q. and Wang, J. (2010) Large-scale climatic fluctuations in the latest Ordovician on the Yangtze block, south China, *Geology*, 38(7), pp.599–602.

Yan, D., Chen, D., Wang, Q. and Wang, J. (2012) Predominance of stratified anoxic Yangtze Sea interrupted by short-term oxygenation during the Ordo-Silurian transition, *Chemical Geology*, 291, pp.69–78.

Yang, Q.H., Snyder, J. and Tobler, W. (1999) *Map Projection Transformation: Principles and Application*, CRC Press, USA.

Yapp, C.J. and Poths, H. (1992) Ancient atmospheric CO_2 pressures inferred from natural goethites, *Nature*, 355, pp.342-344.

Yapp, C.J. and Poths, H. (1996) Carbon isotopes in continental weathering environments and variations in ancient atmospheric CO_2 pressure, *Earth and Planetary Science Letters*, 137(1-4), pp.71-82.

Young, S.A., Saltzman, M.R., Foland, K.A., Linder, J.S., & Kump, L.R. (2009) A major drop in seawater 87Sr/86Sr during the Middle Ordovician (Darriwilian): Links to volcanism and climate?, *Geology*, 37(10), pp.951–954.

Young, S.A., Saltzman, M.R., Ausich, W.I., Desrochers, A., & Kaljo, D. (2010) Did changes in atmospheric CO2 coincide with latest Ordovician glacial–interglacial cycles?, *Palaeogeography, Palaeoclimatology, Palaeoecology*, 296(3-4), pp.376–388.

Zachos, J.C., Wara, M.W., Bohaty, S., Delaney, M.L., Petrizzo, M.R., Brill, A., Bralower, T.J. and Premoli-Silva, I. (2003) A transient rise in tropical sea surface temperature during the Paleocene-Eocene Thermal Maximum, *Science*, 302, pp.1551-1554.

Zachos, J.C., Rohl, U., Schellenberg, S.A., Sluijs, A., Hodell, D.A., Kelly, D.C., Thomas, E., Nicolo, M., Raffi, I., Lourens, L.J., McCarren, H. and Kroon, D. (2005) Rapid acidification of the ocean during the Paleocene-Eocene Thermal Maximum, *Science*, 308, pp.1611-1615.

Zachos, J.C., Schouten, S., Bohaty, S., Quattlebaum, T., Sluijs, A., Brinkhuis, H., Gibbs, S.J. and Bralower, T.J. (2006) Extreme warming of mid-latitude coastal ocean during the Paleocene-Eocene Thermal Maximum: Inferences from TEX_{86} and isotope data, *Geology*, 34(9), pp.737-740.

Zagorevski, A., McNicoll, V.J., Rogers, N. and van Hees, G.H. (2016) Middle Ordovician disorganized arc rifting in the peri-Laurentian Newfoundland Appalachians: implications for evolution of intra-oceanic arc systems, *Journal of the Geological Society*, 173(1), pp.76-93.

Zanchi, A., Zanchetta, S., Berra, F., Mattei, M., Garzanti, E., Molyneux, S., Nawab, A. and Sabouri, J. (2009) The Eo-Cimmerian (Late? Triassic) orogeny in North Iran, *Geological Society London Special Publications*, 312, pp.31-55.

Zhai, Q., Jahn, B., Su, L., Ernst, R.E., Wang, K., Zhang, R., Wang, J. and Tang, S. (2013) SHRIMP zircon U-Pb geochronology, geochemistry and Sr-Nd-Hf isotopic compositions of a mafic dyke swarm in the Qiangtang terrane, northern Tibet, and geodynamic implications, *Lithos*, 174, pp.28-43.

Zhang, T., Shen, Y., Zhan, R., Shen, S. and Chen, X. (2009) Large perturbations of the carbon and sulfur cycle associated with the Late Ordovician mass extinction in South China, *Geology*, 37(4), pp.299–302.

Zhao, Y-Y., Zheng, Y-F., and Chen, F. (2009) Trace element and strontium isotope constraints on sedimentary environment of Ediacaran carbonates in southern Anhui, South China, *Chemical Geology*, 265(3-4), pp.345-362.

Zhou, L., Algeo, T.J., Shen, J., Hu, Z., Gong, H., Xie, S., Huang, J. and Gao, S. (2015) Changes in marine productivity and redox conditions during the Late Ordovician Hirnantian glaciation, *Palaeogeography, Palaeoclimatology, Palaeoecology*, 420, pp.223–234.

Zhuang, K., North, G.R. and Giardino, J.R. (2014) Hysteresis of glaciations in the Permo-Carboniferous, *Journal of Geophysical Research: Atmospheres*, 119(5), pp.2147-2155.

Ziegler, A.M., Hulver, M.L. and Rowley, D.B. (1997) Permian world topography and climate, in Martini, I.P. eds. *Late glacial and postglacial environmental changes: Quaternary, Carboniferous-Permian and Proterozoic*, Oxford University Press, Oxford, pp.111-146.